PHYSIK-DEPARTMENT

Neutron Spin Precession in Samples of Polarised Nuclei and Neutron Spin Phase Imaging

Dissertation

von

Florian Michael Piegsa

Technische Universität München

Lehrstuhl für Physik E18, Physik-Department
Technische Universität München

Neutron Spin Precession in Samples of Polarised Nuclei and Neutron Spin Phase Imaging

Dipl.-Phys. Univ. Florian Michael Piegsa

Vollständiger Abdruck der von der Fakultät für Physik der Technischen Universität München zur Erlangung des akademischen Grades eines

Doktors der Naturwissenschaften (Dr. rer. nat.)

genehmigten Dissertation.

Vorsitzender: Univ.-Prof. Dr. Andrzej J. Buras

Prüfer der Dissertation:

1. Univ.-Prof. Dr. Oliver Zimmer
2. Univ.-Prof. Dr. Peter Böni

Die Dissertation wurde am 09.04.2009 bei der Technischen Universität München eingereicht und durch die Fakultät für Physik am 09.07.2009 angenommen.

Neutron Spin Precession in Samples of Polarised Nuclei and Neutron Spin Phase Imaging

Dissertation am Physik-Department
der Technischen Universität München

vorgelegt von
Florian Michael Piegsa
aus München

München, den 26. März 2009

This thesis work was performed in the Sample Environment and Polarised Targets Group of the Paul Scherrer Institute in Switzerland.

PAUL SCHERRER INSTITUT

"Dieses Experiment ist so elegant, dass man es durchführen muss,
selbst wenn nichts dabei heraus kommt."

W.E. Fischer – *Former Head of the Department for*
Condensed Matter Research with Neutrons and Muons of PSI

"How can you know what things are worth,
if your hands won't move to do a days work?"

Editors – *when anger shows*

Abstract

The doublet neutron-deuteron (nd) scattering length $b_{2,\mathrm{d}}$, which is at present only known with an accuracy of 5%, is particularly well suited to fix three-body forces in novel effective field theories at low energies. The understanding of such few-nucleon systems is essential, e.g. for predictions of element abundances in the big-bang and stellar fusion. $b_{2,\mathrm{d}}$ can be obtained via a linear combination of the spin-independent nd scattering length $b_{\mathrm{c,d}}$ and the spin-dependent one, $b_{\mathrm{i,d}}$.
The aim of this thesis was to perform a high-accuracy measurement of the latter to improve the relative accuracy of $b_{2,\mathrm{d}}$ below 1%. The experiment was performed at the fundamental neutron physics beam line FUNSPIN at the Paul Scherrer Institute in Switzerland. It utilises the effect that the spin of a neutron passing through a target with polarised nuclei performs a pseudomagnetic precession proportional to the spin-dependent scattering length of the nuclei. An ideal method to measure this precession angle very accurately is Ramsey's atomic beam technique, adapted to neutrons.
The most crucial part of the experimental setup is the so-called frozen spin target, which consists of a specially designed dilution refrigerator and contains a sample with dynamically polarised nuclear spins. The polarisation of the sample is determined by nuclear magnetic resonance (NMR) techniques. It turned out that the relaxation of the nuclear spins during the necessary "cross-calibration" of the two employed NMR systems is ultimately limiting the achievable accuracy of $b_{\mathrm{i,d}}$.

During the extensive use of the Ramsey resonance method in the neutron-deuteron experiment, an idea emerged that the applied technique could be exploited in a completely different context, namely polarised neutron radiography. Hence, the second part of the thesis covers the development of a novel neutron radiography technique, based on the spin-dependent interaction of the neutron with ferromagnetic samples and magnetic fields. For the first time, quantitative imaging of such samples could be performed using a dedicated compact Ramsey apparatus. First results of this spin-off project as well as the principle idea of the imaging technique are presented.

Zusammenfassung

Die doublet Neutron-Deuteron (nd) Streulänge $b_{2,\mathrm{d}}$, welche zurzeit nur mit einer Genauigkeit von 5% bekannt ist, eignet sich besonders gut um Dreikörperkräfte in Effektiven Feldtheorien zu beschreiben. Das Verstehen derartiger Systeme mit wenigen Nukleonen ist von essentiellem Interesse zum Beispiel für die Vorhersage von Isotopenhäufigkeiten während des Big-Bang und der Kernfusion in Sternen. $b_{2,\mathrm{d}}$ kann aus der Linearkombination der spin-unabhängigen $b_{\mathrm{c,d}}$ und der spin-abhängigen $b_{\mathrm{i,d}}$ Neutron-Deuteron Streulänge gewonnen werden.
Das Ziel dieser Arbeit bestand darin Letztere mit hoher Präzision zu messen, um insgesamt eine relative Genauigkeit von $b_{2,\mathrm{d}}$ von unter 1% zu erzielen. Das Experiment wurde an der Strahllinie für fundamentale Neutronenphysik FUNSPIN am Paul Scherrer Institut in der Schweiz durchgeführt. Es verwendet den Effekt, dass der Spin eines Neutrons, welches eine Probe mit polarisierten Kernen durchdringt, eine pseudomagnetische Präzession vollführt, welche wiederum proportional zu $b_{\mathrm{i,d}}$ ist. Eine ideale Methode um eine derartige Präzession möglichst genau zu vermessen ist die auf Neutronen adaptierte Atomstrahl Technik nach Ramsey.
Der wichtigste Bestandteil des Experiments ist das sogenannte "frozen spin target", welches aus einem speziellen Mischkryostaten besteht in dem eine Probe mit Hilfe der Methode der dynamischen Kernpolarisation polarisiert werden kann. Die Polarisation der Probe wird mittels Kernspinresonanz untersucht. Es stellte sich jedoch heraus, dass die erreichbare Genauigkeit von $b_{\mathrm{i,d}}$, aufgrund der Relaxation der Kernspins während der notwendigen "Kreuz-Kalibration" der beiden verwendeten NMR-Systeme, limitiert ist.

Während der umfangreichen Arbeit mit der Ramsey Resonanzmethode für das Neutron-Deuteron Experiment, entstand die Idee, dass die angewandte Technik auch in einem völlig anderen Zusammenhang genutzt werden könnte, nämlich der Radiographie mit polarisierten Neutronen. Der zweite Teil der Arbeit beschreibt deshalb die Entwicklung einer neuartige Neutronenradiographie-Technik, welche auf der spin-abhängigen Wechselwirkung von Neutronen mit ferromagnetischen Materialien und magnetischen Feldern beruht. Damit konnten zum ersten Mal quantitative Bilder von derartigen Materialien und Feldern durchgeführt werden. Es werden sowohl erste Ergebnisse als auch die zugrundeliegende Methodik dieser Radiographie-Technik vorgestellt.

Contents

1. Preface

The quantum mechanical property of the spin of a particle plays an important role in almost all areas of modern physics:
In condensed matter research the spins of the electrons give rise to new phenomena and interesting properties in semiconductors, magnetic materials and superconductors etc.
The nuclear spins and the shifts of their resonance frequency due to chemical bindings are used in nuclear magnetic resonance (NMR) to identify chemical substances and element isotopes. The effect of nuclear magnetic resonance of liquids and solids was first observed by Bloch in Stanford [Blo46] and by Purcell in Harvard [Pur46] both in 1946. On the other hand, Rabi already discovered the nuclear magnetic resonance in atomic beams in 1938 [Rab38].
In medicine magnetic resonance imaging (MRI) employs the nuclear spins, mainly of the protons, to obtain visual information, which is complementary to X-ray imaging. MRI is especially suited to perform metabolic imaging and to image human tissue and organs, e.g. ligaments and the brain (see Fig. 1.1). Also polarised noble gases, as ^{3}He and Xenon, can be utilised for medical purposes in the diagnostic of lung diseases (e.g. Ref. [Alb94]).
In nuclear and particle physics the spin provides another degree of freedom, which can for instance lead to a distinctive behaviour of reactions depending on the initial spin-states of the nuclei and/or particles (e.g. spin-dependent absorption of neutrons, spin-dependent scattering of nuclei due to spin-orbit coupling, the muon decay, the charged pion decay etc.).
High energy experiments as the COMPASS experiment at CERN even aim for the exploration of the origin of the spin of fundamental particles, i.e. protons and neutrons. So far it is not fully understood from where the spin of the nucleons ultimately emerges (*spin puzzle*). But it is safe to say that the quarks only carry part of the nucleon spin. It is assumed that other contributions come from the polarisation of the gluons and from the angular momentum of the quarks and the gluons, respectively [Fri07].

Quantum mechanics makes a clear distinction between particles, which possess integer spin, so-called *Bosons* with spin $s \in \{0, 1, 2, ...\}$, and particles with half-integer spin, *Fermions* with $s \in \{1/2, 3/2, ...\}$. Their total wave functions Ψ_B and Ψ_F need to be symmetric and anti-symmetric under permutation of two particles, respectively [Sch00]. This causes that two Fermions of the same species cannot possess the exact same quantum numbers and have the exact same wave function. This after Pauli named principle prohibits for instance that even at absolute zero temperature the conduction electrons in a metal join together in the energetic ground-state. Instead, they fill up all energy levels up to the so-called Fermi-energy E_F. Bosons on the other hand can collapse into a common lowest quantum state and form a

Figure 1.1: Magnet resonance image of the ankle of the author's left foot, taken at the Kantonsspital Baden AG in Switzerland.

so-called Bose-Einstein condensate. The latter phenomenon appears for example in laser-cooled rubidium or sodium atoms [Dav95] and in superfluid ^{4}He (see section 4.1).

The present work is devoted to the spin of the neutron. Two experiments are presented, in which the neutron serves, due to its electronically neutral character, as a very sensitive probe for pseudomagnetic and magnetic interactions. The thesis is divided into two main parts:

I. **Neutron Spin Precession in Samples of Polarised Nuclei:**
An experiment with the aim to measure the spin-dependent (incoherent) scattering length of the neutron on the deuteron is described. The experiment has been carried out in collaboration with the *Sample Environment and Polarised Targets Group* of the *Paul Scherrer Institute* (PSI), H. Glättli from the *CEA Saclay* and O. Zimmer from the *Institut Laue-Langevin* (ILL). The actual measurements have been performed at the polarised cold neutron beam line FUNSPIN at the spallation neutron source SINQ at PSI in Switzerland.

II. **Neutron Spin Phase Imaging (NSPI):**
This part introduces a novel neutron radiography technique, which is sensitive to samples that cause a change of the neutron spin precession frequency. First results of the method are presented, which were obtained during one week of beam time at the small angle neutron scattering instrument SANS-I at PSI.

Part I.

Neutron Spin Precession in Samples of Polarised Nuclei

The first main part of the thesis focuses on the experiment with the aim to perform an accurate measurement of the spin-dependent neutron scattering length $b_{\mathrm{i,d}}$ of the deuteron, which was proposed in Ref. [Bra04].

In chapter 2 the motivation for the measurement is briefly explained. Chapter 3 presents the theoretical background of the scattering of a neutron on a single nucleus and of the experiment, while chapter 4 summarises some basic knowledge of low temperature physics. In chapters 5 and 6 the instrumental setup of the experiment and the individual beam times and their findings are described in detail. Finally, the results, possible improvements and future options are discussed in chapter 7.

2. Introduction

2.1. The Neutron-Deuteron Experiment

An accurate direct determination of the spin-dependent (incoherent) neutron scattering length of the deuteron $b_{\mathrm{i,d}}$ is of great importance. Combining the value with the well-known coherent neutron-deuteron scattering length $b_{\mathrm{c,d}}$ [Sch03] will provide a new value of the doublet neutron-deuteron scattering length $b_{2,\mathrm{d}}$, which represents a crucial input parameter for modern effective field theories of low-energy interactions among nucleons (compare section 2.2). Presently, $b_{2,\mathrm{d}}$ is known only with 5% accuracy from an indirect determination of $b_{\mathrm{i,d}}$ dating back to the 1970s [Dil71]. The goal of the nd-experiment is to achieve a relative accuracy of $b_{2,\mathrm{d}}$ of about 1%, which requires an improvement of the accuracy of $b_{\mathrm{i,d}}$ from presently 0.8% to better than 0.13% (see section 3.2.7).

The here presented experiment was carried out at the cold, polarised neutron beam line FUNSPIN at the spallation neutron source SINQ at the Paul Scherrer Institute in Switzerland. Its aim was to determine $b_{\mathrm{i,d}}$ directly using the phenomenon of *pseudomagnetic precession* [Abr731, Bar65]: owing to the spin-dependent refractive index, the spin of a neutron passing through a polarised target precesses around the axis of nuclear polarisation with the precession angle φ^* being proportional to the bound incoherent scattering length of the nuclear species present in the sample. The precisely known value of the proton incoherent scattering length $b_{\mathrm{i,p}}$ allows to adopt a method proposed in Ref. [Bra04], which relies on a relative measurement employing a sample containing both protons and deuterons. This way the experimental difficulties associated with absolute measurements of neutron wavelength, number density and nuclear polarisation, which would limit considerably the final accuracy, can be avoided.
The pseudomagnetic precession angle φ^* can be measured very accurately using Ramsey's well-known atomic beam technique [Ram56], adapted to neutrons [Abr82]. Originally introduced as a molecular beam resonance method, *Ramsey's technique of separated oscillating fields* has become a well-established tool in many areas of research. It is sensitive to spin-dependent interactions of particles with external fields. For slow neutrons the method is employed in various ways. Most longstanding is the search for a non-vanishing electric dipole moment (EDM) of the neutron, which serves as a tool to investigate CP violation beyond the CKM mechanism. Another application is the above mentioned measurement of the spin-dependent, incoherent neutron scattering length b_{i} of atomic nuclides. The method was pioneered by a group from Saclay in the 1970s and provided values for more than 30 nuclides with applications in neutron scattering and for tests of nuclear models [Abr75, Abr82, Glä79, Mal81, Rou74].

The accurate measurement of the spin-dependent neutron scattering length of the deuteron requires that several experimental techniques and R&D-topics have to be carefully addressed. This includes the following points, which are fully covered in the present thesis:

- Set up of a neutron Ramsey apparatus, which has to run very stable (radio frequency fields, magnetic fields etc.) to achieve a high accuracy in the determination of the pseudomagnetic precession angle.
- This includes a carefully prepared neutron beam in terms of polarisation, collimation, wavelength selection etc.
- Design of a spin polarised nuclear target, i.e. a dilution refrigerator with several special features as well as sample preparation and the study of sample materials.
- Provide a reliable and highly sensitive system to measure the nuclear polarisation of small samples.

2.2. Motivation of the Neutron-Deuteron Experiment

In this section we introduce the motivation of the presented neutron-deuteron experiment, which originates from the demand for more accurate experimental input parameters by theoretical nuclear physics and effective field theories, respectively.

2.2.1. The Nucleon-Nucleon Potential

Nucleons and nuclei prove an outstanding scientific challenge even after many decades of nuclear physics [Gri05]. Nucleons themselves are composite objects and interact with each other mainly via the strong interaction, while gravitation and electro-weak interaction can be neglected on the same length scale of 10^{-15} m = 1 fm.[1] The range of the interaction is very short and on the order of the radius of a nucleus. To study the nucleon-nucleon interaction, one investigates not only bound few nucleon system, namely the deuteron, triton and helium, but also elastic nucleon-nucleon scattering at various energies. The measured cross-sections of these scattering processes can be described theoretically by the so-called scattering phases δ_l of the corresponding partial waves (compare *partial wave expansion* in section 3.2.2). They describe the phase shift between the scattered wave and the incoming wave and thus deliver information about the strength and the shape of the nucleon-nucleon potential. For instance, an attractive (repulsive) potential results in a positive (negative) scattering phase [Kam79, Pov01].

Fig. 2.1 shows qualitatively the radial dependence of a potential, which reproduces the results of a scattering phase analysis. It has a characteristic short range repulsive and a long range attractive nature. Since the repulsive part of the potential increases rapidly at small distances, it is known as the *hard core*. The long range part of the

---

[1] This is of course true for all hadrons, i.e. mesons and baryons.

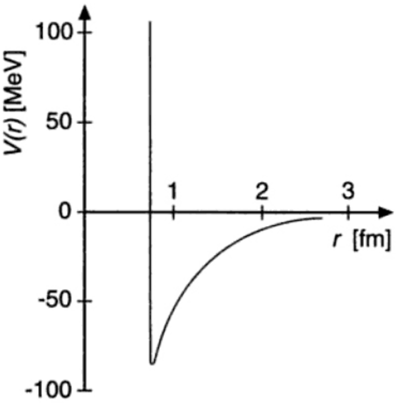

Figure 2.1: Sketch of the radial dependence of the nucleon-nucleon potential for $l = 0$. Taken from Ref. [Pov01].

potential ($r > 4$ fm) can be explained by the one-pion-exchange and the attributed attractive Yukawa potential with the pion mass $m_\pi = 140\ \mathrm{MeV}/c^2$.[2]
However, the intermediate and short range behaviour of the potential is usually described by phenomenological models, where the parameters of these models, usually more than 30, are determined by fitting to experimental data. The most widely used models are the *Paris potential*, the *Argonne AV18 potential*, the *CD-Bonn potential* and the *Nijmegen potentials*. A dissatisfying aspect is that they cannot be derived from fundamental principles and that although they lead to accurate descriptions of particular processes, it is often not clear how related phenomena can be explained in the same framework.
A more recent approach is the development of *effective field theories*, which provide a consistent description of nucleon-nucleon and three-nucleon forces and allow perturbative calculations of the interactions between nucleons.

2.2.2. From QCD to Effective Field Theories

Quantum Chromodynamics (QCD) is the theory of strong interaction. QCD describes all hadrons as built out of point-like spin 1/2 particles: quarks and anti-quarks, where the force between them is mediated by gluons. The dynamics of QCD is highly non-linear because gluons as well as the quarks possess a colour charge and thus interact amongst themselves. As a result, the strong interaction strength, which is described by the strong coupling "constant" α_s becomes weak or *asymptotically free* at high energies, while it is large at energies below 1 GeV. The latter is known as *confinement* and causes that at large distances the binding between the quarks becomes infinitely large and that a single quark cannot be removed from a hadron (compare also *hadronisation*).
Hence, at high energies, i.e. short distances, one can apply standard perturbation theory to calculate hadronic properties directly from the dynamics of quarks and gluons as $\alpha_\mathrm{s} \ll 1$. However, at the energy scales of nuclear physics of less than 1 GeV, i.e. distances of more than approximately 0.2 fm, the perturbative expansion breaks

---

[2] Due to Heisenberg's uncertainty principle nucleons can emit and absorb virtual pions and other mesons. According to the theory of Yukawa, these massive bosons mediate the interaction between two nucleons, in analogy with the photons which mediate the electro-magnetic interaction.

down because α_s becomes large. As a result, quarks and gluons are hidden from direct observation; instead, hadrons and atomic nuclei are detected in experiments. These effective low-energy degrees of freedom interact and are bound together by what can be considered the "residual" QCD-interaction [Gri05].[3] In the past few years, a new and very promising strategy has been developed to describe this residual interaction between the hadronic degrees of freedom by effective field theories (EFT) at low energies. Thereby, these EFT's require much less experimental input than traditional potential models to reach comparable accuracies and they provide the possibility to describe phenomena in a systematic way (compare Ref. [Bed03, Phi02] for reviews).

In general, an effective theory is an systematic approximation to some underlying theory, which includes appropriate degrees of freedom to describe physical phenomena occurring at a chosen energy, while ignoring substructures and degrees of freedom at higher energies. Effective theories are largely used in many branches of physics where a separation exists between high- and low-energy scales.[4,5] Thereby, an effective theory is not a model, since its systematic character allows to make predictions with reliable, high accuracy. However, if this is to be true then a small parameter, such as the coupling constant α of QED, must govern the systematical approximation scheme [Phi02].

EFT's are characterised by their dimensionless expansion parameter Q_{EFT}, on which the ordering scheme is based. The parameter is defined by

$$Q_{\text{EFT}} = \frac{\text{typical excitation energy or mass scale of the process}}{\Lambda_{\text{EFT}}} \ll 1 \ , \qquad (2.1)$$

where Λ_{EFT} is the so-called breakdown-scale of the theory beyond which the theory cannot be applied anymore. Besides others, one successfully employs the following two EFT's in nuclear physics:

- The *Chiral Effective Field Theory* (χEFT), which can be interpreted as the low energy version of QCD with the breakdown-scale of about 600 to 1000 MeV. Hence, in χEFT the nucleons, the pions and the $\Delta(1232)$, as the lowest-lying nucleon-resonance, form the degrees of freedom of the theory. All other mesons and nucleon-resonances involve much higher energies and are thus integrated out.

- The *Pion-less Effective Field Theory* ($\not{\pi}$EFT), which can be interpreted as the low energy version or a special case of the χEFT [Bed02, Gri05, Phi02]. Its breakdown-scale is of the order 100 MeV, i.e. approximately the pion mass. $\not{\pi}$EFT contains only protons and neutrons as degrees of freedom and the only appearing forces are point-like two- and more-nucleon interactions.

---

[3] Similar situations arise in other branches of physics, e.g. for neutral atoms: They can be bound in molecules by the van-der-Waals force as a residual force of the more fundamental electro-magnetic interactions between the more fundamental degrees of freedom, namely the electrons and nuclei. Another example is given in classical mechanics: on the astronomical scale, it does not make sense to describe the planets as made of 10^{30} molecules. Instead, a point with the mass of the planet becomes a more efficient description.

[4] Further examples are: Fermi's theory of the β-decay and the BCS theory of superconductivity.

[5] A very intuitive example of an effective theory is given in Ref. [Phi02]: the gravitational potential above the Earth's surface.

Although the restriction to low energies might seem severe, a wealth of pivotal physical processes takes place in this range, which are important for astrophysical applications and fundamental questions, e.g. big-bang nucleo-synthesis, stellar evolution, neutrino astro-physics, parity violating effects in the standard model, the solar Hep-process etc.[6]

Moreover, EFT's provide an answer of finite accuracy because higher order corrections are systematically calculable and suppressed in powers of Q_{EFT}. Hence, the power counting allows for an error estimate of the final result, with the natural size of all neglected terms known to be of higher order. And relativistic effects, chiral dynamics and external currents are included systematically.

2.2.3. Three-Nucleon Forces

Every description of low-energy nuclear physics which is not directly employing quarks and gluons but different "effective" degrees of freedom will necessarily have to include few-nucleon forces, namely forces which are mediated only when nucleons are within one nucleonic radius of each other. One example is the "hard-core" nucleon-nucleon force mentioned above. When three nucleons interact at very small distances, they can interact with three-nucleon forces. Therefore, every theoretical description will incorporate three-nucleon forces. Their strengths cannot be determined by two-body observables, but have to be inferred from data taken on systems with at least three nucleons. Clearly, these data must be as good as possible, so that the error associated with the experimental input is as small as possible. The binding energies of the triton and ^{3}He are known with very high accuracy but do not suffice to constrain all three-nucleon forces. Measuring highly accurate three-nucleon scattering lengths, as undertaken in this thesis, provides therefore stringent constraints and crucial input for nuclear theory.

For example, three-nucleon forces are introduced for conceptual reasons in $\not{\pi}$EFT already at leading order to ensure that physical observables do not depend on the details of the short-distance physics chosen for the theoretical calculation [Gri06, Gri08]. Thereby, the strengths of the three-body forces have to be fixed by experimentally well-determined input parameters. Best suited, due to the absence of the Coulomb force, are the binding energy of the triton, which is known with an accuracy of 5×10^{-7}, and the doublet neutron-deuteron scattering length $b_{2,\mathrm{d}}$. The reason of the high sensitivity of the latter to three-nucleon forces is the absence of Pauli blocking in the doublet channel, since the incident neutron has its spin anti-parallel to the one bound in the deuteron.[7]

Thereby, the $\not{\pi}$EFT can be in principle pushed to a quite high accuracy of below 1%, i.e. high orders of expansion, because it is considerably simpler than potential models or the more complex χEFT with pions. This allows for exploring processes at very low energies with considerable less effort, and testing of the universal properties of systems, i.e. how much of them can be explained with only scattering lengths and effective ranges as input. However, this accuracy can only be attained if the experimental input parameters are known with a sufficient precision. As already mentioned

---

[6] The Hep process is a weak-interaction reaction, which occurs in the sun: $^3\mathrm{He} + \mathrm{p} \longrightarrow {}^4\mathrm{He} + \mathrm{e}^+ + \nu_\mathrm{e}$ [Kub04].

[7] Hence, the triton binding energy is employed at leading order (LO), while one utilises $b_{2,\mathrm{d}}$ at next-to-next-to leading order (N^{2}LO), as the second three-body datum.

in section 2.1, at present the doublet nd-scattering length $b_{2,\mathrm{d}}$ is known only with 5% accuracy, which is considerably worse than the theoretical uncertainty. This has motivated the present development to determine this crucial quantity with high-accuracy in the so-called neutron-deuteron experiment [Bra04].

3. Neutron Scattering and Ramsey's Method

In this chapter the theoretical background of the nd-experiment is presented. Section 3.1 briefly summarises the properties and the production of neutrons, while section 3.2 describes the scattering of neutrons on nuclei and introduces scattering lengths, the Fermi potential and the neutron refractive index. In the following section 3.3 an idealised Ramsey resonance apparatus is considered and simulated using quantum mechanical time evolution operators. Finally, section 3.4 describes the principle of the intended relative measurement of $b_{\mathrm{i,d}}$.

3.1. Neutrons

Neutrons are electronically neutral fermionic particles with spin 1/2. They are produced for research purposes in a nuclear fission process in a nuclear research reactor (e.g. FRM 2 @ TU München) or at a spallation source (e.g. SINQ @ Paul Scherrer Institute [Fis97]). These reactions produce high energetic neutrons of several MeV. For most applications the velocities of the neutrons have to be reduced by means of moderation in:

- Heavy water (D_2O at 300 Kelvin - **thermal neutrons** - peak velocity of the neutron Maxwell-Boltzmann distribution $v_{\mathrm{p}} \approx 2200$ m/s).
- Liquid deuterium (D_2 at 25 Kelvin - **cold neutrons** - $v_{\mathrm{p}} \approx 850$ m/s).
- Solid deuterium or liquid ^{4}He below one Kelvin (super-thermal source - **ultra cold neutrons** - velocities of down to 10 m/s), e.g. Ref. [Atc05, Zim07].

In all cases, the obtained neutrons are not polarised, that means that half of the neutrons will have their spin parallel/anti-parallel to an externally applied magnetic field $\vec{B}_0$. Their polarisation P_{n} is given by

$$P_{\mathrm{n}} = \frac{N_+ - N_-}{N_+ + N_-} \ , \tag{3.1}$$

where N_+ (N_-) denotes the number of neutrons with spin parallel (anti-parallel) to $\vec{B}_0$. Equ. (3.1) is of course valid for all spin 1/2 particles. The two spin states are separated by the Zeeman energy

$$\Delta E_{\mathrm{Z,n}} = \frac{\vec{\mu}_{\mathrm{n}}}{|\vec{s}|} \cdot \vec{B}_0 = \gamma_{\mathrm{n}} \hbar B_0 \ , \tag{3.2}$$

where $\vec{\mu}_\mathrm{n} = \gamma_\mathrm{n}\hbar\vec{s}$ is the magnetic moment of the neutron, which is oriented along its spin $\vec{s}$ and $\gamma_\mathrm{n} = -2\pi \times 29.1647$ MHz/T is the gyromagnetic ratio of the neutron.
A neutron beam can be polarised ($P_\mathrm{n} \neq 0$) by filtering neutrons of one spin-state. This is usually done by scattering of the unpolarised neutron beam on magnetic multilayers (polarising supermirror) [Bön99, Kri04, Pie083, Sch89], by spin-dependent absorption in polarised ^{3}He-gas [Hei99] or by spin-dependent scattering on targets containing polarised protons [Asw08, Zim99].

3.2. Neutron Scattering on Nuclei

3.2.1. Solution of the Scattering Problem

We consider elastic scattering of a single neutron on a single nucleus with spin $\vec{I}$ as presented in Fig. 3.1 in the centre of mass system.[1],[2] The relative coordinate $\vec{r}$ describes the distance between the neutron and the nucleus. First, we will neglect the spin of the neutron and of the nucleus. The interaction between the two particles is purely strong interaction and is given by the potential $V(\vec{r})$. The range of the interaction is of order fm = 10^{-15} m, which is about five orders of magnitude smaller than the *de Broglie* wavelength λ of the neutron. The Schrödinger equation of the system is given by:

$$\hat{H}\psi(\vec{r}) = \left[-\frac{\hbar^2\Delta}{2m} + V(\vec{r})\right]\psi(\vec{r}) = \frac{\hbar^2 k^2}{2m}\psi(\vec{r}) \tag{3.3}$$

$$\left(\Delta + k^2\right)\psi(\vec{r}) = \frac{2m}{\hbar^2}V(\vec{r})\psi(\vec{r}) \tag{3.4}$$

m is the reduced mass of the system: $m = m_\mathrm{N} m_\mathrm{n}/(m_\mathrm{N} + m_\mathrm{n})$, where m_N is the mass of the nucleus and $m_\mathrm{n} = 1.6726 \times 10^{-27}$ kg is the neutron mass. k is the modulus of the relative wave vector, which is connected to the neutron wave vector $\vec{k}_0$ in the laboratory frame via:

$$\vec{k} = \vec{k}_0 \cdot \frac{m_\mathrm{N}}{m_\mathrm{N} + m_\mathrm{n}} = \vec{k}_0 \cdot \left(\frac{A}{A+1}\right) , \tag{3.5}$$

where A is the mass ratio of the nucleus and the neutron, which can be approximated by the number of nucleons in the nucleus. Therefore it holds that $k \approx k_0$ for $A \gg 1$.
Equ. (3.4) represents an inhomogeneous Helmholtz equation, which is solved using its Green's function presented in appendix A.1. The solution is given by:

$$\psi(\vec{r}) = e^{i\vec{k}\cdot\vec{r}} - \frac{m}{2\pi\hbar^2}\int_{-\infty}^{+\infty} d^3r'\ V(\vec{r}')\psi(\vec{r}') \cdot \frac{e^{ik|\vec{r}-\vec{r}'|}}{|\vec{r}-\vec{r}'|} . \tag{3.6}$$

This equation can be interpreted as follows. The total wave consists of the incoming plane wave and a scattered wave. In the second term, the amplitude of the incident wave times the potential at $\vec{r}'$ acts as a source for the scattered wave. The Green's function $G(\vec{r},\vec{r}')$ is the amplitude of the scattered wave at $\vec{r}$ due to the source $\vec{r}'$. Hence, the total scattered wave at $\vec{r}$ is given by the integral over all source points [Bay69].

---

[1] A similar derivations of the scattering problem can be found in Ref. [Gol91, Sea89].

[2] Compare also chapter 6.4 in Ref. [Sch88].

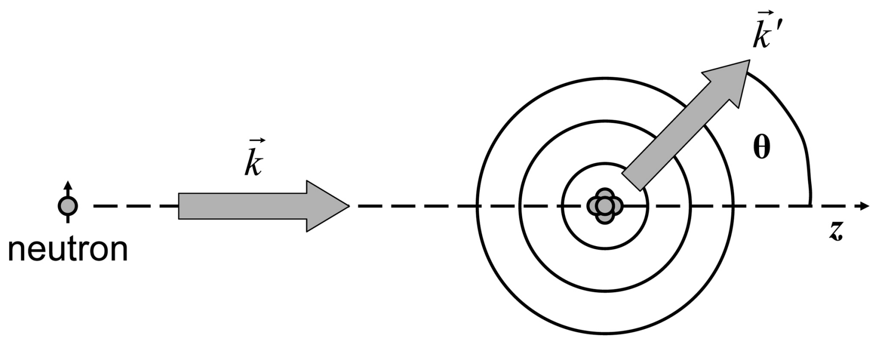

Figure 3.1: Elastic scattering of a neutron on nucleus. The neutron with its initial wave vector $\vec{k}$ is scattered under the angle θ from the nucleus. The final wave vector is $\vec{k'}$.

For distance far away from the nucleus, i.e. $|\vec{r}| \gg |\vec{r'}|$, the solution can be approximated using $|\vec{r}-\vec{r'}| \approx r - (\vec{r} \cdot \vec{r'}/r)$, with $r = |\vec{r}|$ and $r' = |\vec{r'}|$.[3] It follows:

$$\begin{aligned} \psi(\vec{r}) &\approx e^{i\vec{k}\cdot\vec{r}} + f(\theta)\frac{e^{ikr}}{r} \qquad (3.7) \\ \text{with: } f(\theta) &= -\frac{m}{2\pi\hbar^2}\int d^3r'\ V(\vec{r'})\psi(\vec{r'}) \cdot e^{-i\vec{k'}\cdot\vec{r'}} \end{aligned}$$

$\vec{k'} = k\frac{\vec{r}}{r}$ represents the wave vector of the scattered neutron in the direction of $\vec{r}$. Hence, the solution given in Equ. (3.7) represents the sum of an in-coming plane wave and an out-going spherical wave, which is weighted with the so-called *scattering amplitude* $f(\theta)$, where θ is the angle between $\vec{k}$ and $\vec{k'}$.

We end up with a recursively defined wave function $\psi(\vec{r})$ as a solution for the Schrödinger equation. As already mentioned, the nuclear potential $V(\vec{r})$ has a very short range R_0 and therefore vanishes at distances much shorter than λ. Hence, the exponential function $e^{-i\vec{k'}\cdot\vec{r'}}$ in the above formula can be replaced by unity:

$$f = -\frac{m}{2\pi\hbar^2}\int d^3r'\ V(\vec{r'})\psi(\vec{r'}) \qquad (3.8)$$

The isotropic scattering corresponds to so-called *s-wave scattering*, with orbital momentum $l = 0$. This can also be regarded in the sense that the angular momentum transfer $\hbar k R_0 = hR_0/\lambda$ is very small compared to $\hbar$.

---

[3] Compare section A.2 in the appendix.

3.2.2. Scattering Lengths

As the scattering potential $V(\vec{r})$ is assumed to be a central potential and independent of the azimuthal angle, the scattering amplitude $f(\theta)$ in Equ. (3.7) can be expressed in Legendre polynomials (partial wave expansion) [Sea89]:

$$f(\theta) = \frac{1}{2ik}\sum_{l=0}^{\infty}(2l+1)\cdot(e^{2i\delta_l(k)}-1)\cdot P_l(\cos\theta)\ , \tag{3.9}$$

where $\delta_l(k)$ is the phase shift (scattering phase) of the l-th partial wave and $P_l(\cos\theta)$ is the l-th Legendre polynomial. For s-wave scattering this expression reduces to:

$$f(\theta) = \frac{1}{2ik}\left(e^{2i\delta_0(k)}-1\right) \approx \frac{1}{2ik}\left(2i\delta_0(k) + \frac{(2i\delta_0(k))^2}{2!} + ...\right) \tag{3.10}$$

using $P_0(\cos\theta) = 1$ and the Taylor expansion of the exponential function. For low energies, i.e. small k, it holds that $\delta_l(k) \propto k^{2l+1}$ [Sch88]. Hence, one can write $\delta_0(k) = -ak$, where the proportionality factor a has the dimension of a length and is therefore called *free scattering length*. This yields

$$f(\theta) = -a + ia^2k + \mathcal{O}(k^2) \tag{3.11}$$

with a being complex: $a = a' - ia''$. The imaginary part a'' describes absorption processes of the neutron. The *optical theorem*

$$\sigma_{\text{tot}} = \sigma_{\text{s}} + \sigma_{\text{a}} = \frac{4\pi}{k}\text{Im}[f(0)] \tag{3.12}$$

relates the total cross-section σ_{tot} to the imaginary part of the forward scattering amplitude [New76], where σ_{s} is the *scattering cross-section* and σ_{a} is the *absorption cross-section*. Note, while a' may be either positive or negative[4], a'' is always positive. For almost all nuclei, except strongly absorbing ones, it also holds that $a'/a'' > 10^5$. Inserting the result of Equ. (3.11) in the Equ. (3.12) leads to:

$$\sigma_{\text{tot}} = 4\pi\,|a|^2 \ + \ \frac{4\pi}{k}a''(1-2a''k) \tag{3.13}$$

The scattering cross-section of $\sigma_{\text{s, free}} = 4\pi\,|a|^2$ corresponds to the scattering on a hard sphere with a radius a [Lan74]. For all practical cases the absorption cross-section can be reduced to $\sigma_{\text{a, free}} = \frac{4\pi}{k}a''$, as even for strong neutron absorbers like ^{6}Li or ^{10}B the factor $2a''k$ is negligible compared to unity.

For the scattering of neutrons on rigidly bound nuclei (e.g. in a crystal or a molecule), one often uses the so-called *bound scattering length* b, which is related to the free scattering length in the following way:[5]

$$b = b' - ib'' = \frac{m_{\text{n}}}{m}\ a = \left(\frac{A+1}{A}\right)a \tag{3.14}$$

---

[4] There are only a few examples of nuclei with a negative scattering length, e.g. hydrogen ^{1}H and titanium ^{48}Ti. $a' < 0$ ($a' > 0$) corresponds to a attractive (repulsive) interaction between the neutron and the nucleus.

[5] This corresponds to a transformation from the centre of mass system to the laboratory frame (compare chapter 2.3 in Ref. [Gol91]).

Hence, the *bound cross-sections* are given by:

$$\text{Scattering: } \sigma_{\text{s,bound}} = \left(\frac{A+1}{A}\right)^2 \sigma_{\text{s,free}} = 4\pi\,|b|^2 \tag{3.15}$$

$$\text{Absorption: } \sigma_{\text{a,bound}} = \frac{4\pi}{k_0} b'' \tag{3.16}$$

Equ. (3.16) is usually called the $1/v$-law, meaning that the absorption of a neutron is inversely proportional to its velocity or its wave vector k_0. Note, absorption cross-sections are normally tabulated for thermal neutrons with $\lambda = 1.8$ Å or $v = 2200$ m/s.

3.2.3. Spin Dependent Scattering

To take the effect of the spins of the neutron and of the nucleus into account, one introduces a spin-dependent part of the bound scattering length:

$$b = b_{\text{c}} + \frac{2b_{\text{i}}}{\sqrt{I(I+1)}}\, \vec{s}\cdot\vec{I} \tag{3.17}$$

with: b_{c} = coherent, spin-independent scattering length
b_{i} = incoherent, spin-dependent scattering length

$\vec{s}$ is the spin of the neutron and $\vec{I}$ the spin of the nucleus, respectively. The total spin of the system is $\vec{J} = \vec{l} + \vec{s} + \vec{I}$, with l being the orbital momentum (here: $\vec{l} = 0$). Hence, the total spin can either be $I + 1/2$ or $I - 1/2$ leading to the two scattering lengths $b_\pm$:

$$J = I + \frac{1}{2} \quad \rightarrow \quad b_+ = b_{\text{c}} + \sqrt{\frac{I}{I+1}}\, b_{\text{i}} \tag{3.18}$$

$$J = I - \frac{1}{2} \quad \rightarrow \quad b_- = b_{\text{c}} - \sqrt{\frac{I+1}{I}}\, b_{\text{i}} \tag{3.19}$$

The inversion of these two equation yields:

$$b_{\text{c}} = \frac{1}{2I+1}\left[(I+1)b_+ + I b_-\right] \tag{3.20}$$

$$b_{\text{i}} = \frac{\sqrt{I(I+1)}}{2I+1}\left[b_+ - b_-\right] \tag{3.21}$$

Also the scattering cross-section can be distinguished in a coherent and an incoherent part:

$$\sigma_{\text{s,bound}} = \sigma_{\text{c,bound}} + \sigma_{\text{i,bound}} = 4\pi\left[|b_{\text{c}}|^2 + |b_{\text{i}}|^2\right] \tag{3.22}$$

$$\text{also: } \sigma_{\text{s,bound}} = \frac{4\pi}{2I+1}\left[(I+1)\,|b_+|^2 + I\,|b_-|^2\right] \tag{3.23}$$

In table 3.1 the scattering lengths and the cross-sections of some light nuclei are presented.

	I	b_c [fm]	b_i [fm]	$\sigma_{\mathrm{c,bound}}$	$\sigma_{\mathrm{i,bound}}$	σ_a
^{1}H	1/2	-3.7423(12)	25.217(6)	1.7599(11)	79.91(4)	0.3326(7)
^{2}H	1	6.674(6)	4.033(32)	5.597(10)	2.04(3)	0.000519(7)
^{3}H	1/2	4.94(8)	0.00(37)	3.07(10)	0.00(2)	0
^{3}He	1/2	6.000(9) -i 1.483(2)	-2.365(20) +i 2.568(3)	4.80(1)	1.53(1)	5333(7)
^{4}He	0	3.26(3)	0	1.34(2)	0	0
^{6}Li	1	2.0(1) -i 0.261(1)	-1.79(24) +i 0.257(11)	0.51(5)	0.41(11)	940(4)
^{7}Li	3/2	-2.22(1)	-2.49(5)	0.619(6)	0.78(3)	0.0454(3)
^{13}C	1/2	6.19(9)	-0.52(9)	4.81(14)	0.034(12)	0.00137(4)

Table 3.1: Scattering lengths and cross-sections of light nuclei. The cross-sections are given in barn=10^{-28} m^2=10^{-24} cm^2 (taken from [Sea92] and [Ket04] for ^{3}He).

3.2.4. The Fermi Potential

As the potential in Equ. (3.8) is usually unknown, it is impossible to determine the scattering length from first principles. Hence, Enrico Fermi introduced a pseudo potential V_F, which in combination with the *Born-Approximation*[6] correctly describes the scattering of the neutron on the nucleus:

$$V_\mathrm{F}(\vec{r}) = \frac{2\pi\hbar^2}{m_\mathrm{n}}\; b\;\delta(\vec{r})\;, \tag{3.24}$$

where $\delta(\vec{r})$ is the Dirac delta function (see appendix A.1). $V_\mathrm{F}(\vec{r})$ is called *Fermi Potential* and depends only on one parameter, which can be determined experimentally.

Inserting Equ. (3.17) into Equ. (3.24) delivers the Fermi potential of a nucleus, which is situated at $\vec{r_j}$ with the nuclear spin $\vec{I_j}$:

$$V_\mathrm{F}(\vec{r};\vec{r_j}) \;=\; \frac{2\pi\hbar^2}{m_\mathrm{n}}\,\delta(\vec{r}-\vec{r_j})\left[b_\mathrm{c} + \frac{2b_\mathrm{i}}{\sqrt{I(I+1)}}\;\vec{s}\cdot\vec{I_j}\right] \tag{3.25}$$

Now we consider a solid with N equal nuclei, which are distributed homogeneously in a volume V. Hence, the nuclear number density is $\rho = N/V$. The degree of nuclear spin polarisation is given by $\vec{P} = \left\langle\vec{I_j}\right\rangle/I$, where $\langle\ldots\rangle$ represents an average over all nuclei. Therefore the resulting potential V_F averaged over the volume is:

$$V_\mathrm{F} = \frac{2\pi\rho\hbar^2}{m_\mathrm{n}}\left[b_\mathrm{c} + \frac{2b_\mathrm{i}}{\gamma_\mathrm{n}\hbar}\sqrt{\frac{I}{I+1}}\vec{\mu}_\mathrm{n}\cdot\vec{P}\right] \tag{3.26}$$

---

[6] The Born-Approximation assumes a weak interaction potential, which allows to substitute $\psi(\vec{r}')$ under the integral by an unperturbed plane wave $e^{i\vec{k}\cdot\vec{r}'}$.

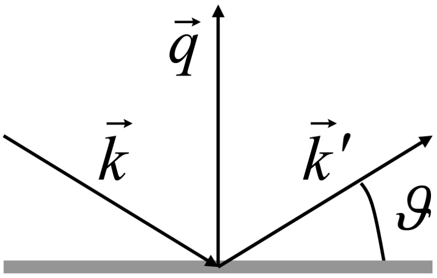

Figure 3.2: Specular reflection of a neutron with an incident wave vector $\vec{k}$ on a surface under the angle ϑ. The momentum transfer is given by $\vec{q} = \vec{k}' - \vec{k}$.

Hereby $\vec{\mu}_\mathrm{n} = \gamma_\mathrm{n}\hbar\vec{s}$ was used, where $\vec{\mu}_\mathrm{n}$ is the magnetic moment of the neutron and $\gamma_\mathrm{n} = -2\pi \times 29.1647$ MHz/T is the gyromagnetic ratio of the neutron.
Although one could continue with the whole expression given in Equ. (3.26), we will consider the two parts separately in the following two sections, divided up in the spin-independent potential $V_\mathrm{F,c}$ and the spin-dependent potential $V_\mathrm{F,i}$.

3.2.5. Neutron Refractive Index and Total Reflection

The interaction of a neutron passing through a solid with the spin-independent potential

$$V_\mathrm{F,c} = \frac{2\pi\hbar^2}{m_\mathrm{n}} \cdot \rho b_\mathrm{c} \ , \tag{3.27}$$

can be expressed by the neutron refractive index n, analogue to the refractive index in optics [Mai63]. The kinetic energy of neutrons with a de Broglie wavelength λ is $E_\mathrm{kin} = \frac{4\pi^2\hbar^2}{2m_\mathrm{n}\lambda^2}$. Thus the refractive index can be written as

$$n^2 = 1 - V_\mathrm{F,c}/E_\mathrm{kin} \tag{3.28}$$

$$= 1 - \frac{\lambda^2}{\pi}\rho b_\mathrm{c} \tag{3.29}$$

The quantity $1 - n^2$ is for all nuclear species of order 10^{-5} for cold neutrons and can be approximated using the Taylor expansion (see appendix A.3):

$$n \approx 1 - \frac{\lambda^2}{2\pi}\rho b_\mathrm{c} \tag{3.30}$$

Note, that the refractive index of neutrons is defined reciprocal compared to the index of refraction of light, i.e. $n_\mathrm{neutron} = v_\mathrm{medium}/v_\mathrm{vacuum}$ and $n_\mathrm{light} = v_\mathrm{vacuum}/v_\mathrm{medium}$, with v being the group velocity of the neutrons and light, respectively.
We now consider the reflection of a neutron on a surface as depicted in Fig. 3.2. For neutrons with a kinetic energy perpendicular to the surface which is lower than the potential $V_\mathrm{F,c}$, we expect total reflection up to a critical angle ϑ_c or up to a critical momentum transfer $q_\mathrm{c} = |\vec{q}_\mathrm{c}|$:

$$V_\mathrm{F,c} = \frac{\hbar^2 q_\mathrm{c}^2}{8m_\mathrm{n}} \tag{3.31}$$

Material	ρ [10^{28} m^{-3}]	b_c [fm]	ρb_c [10^{-6} Å^{-2}]	$1-n$ [10^{-6}]	$V_{F,c}$ [neV]	ϑ_c [°]
Be	12.3	7.74	9.5	1.52	247	0.099
Al	6.03	3.5	2.1	0.34	54.9	0.047
Si	5.19	4.15	2.2	0.34	55.9	0.047
Ni	9.14	10.3	9.4	1.50	244	0.0992
^{58}Ni	9.14	14.4	13.2	2.09	335	0.117
Ti	5.66	-3.4	-1.9	-0.31	-50	-
Pb	3.30	9.4	3.1	0.49	80	0.057
H_2O	3.35	-1.68	-0.6	-0.090	-14.6	-
D_2O	3.35	19.14	6.4	1.02	167	0.082

Table 3.2: Number densities ρ, bound coherent scattering lengths b_c and Fermi potentials $V_{F,c}$ of some selected materials, taken from [Kle83]. Here, the refractive index n and the critical angle ϑ_c are tabulated for neutrons with a wavelength of 1 Å.

The critical angle is given by $\cos\vartheta_c = n$, which yields:

$$\vartheta_c \text{ [rad]} \approx \sqrt{\frac{\rho b_c}{\pi}}\lambda \tag{3.32}$$

In table 3.2 some values for the refractive index and the Fermi potential are summarised.

3.2.6. Pseudomagnetic Precession

The spin-dependent potential

$$V_{\mathrm{F,i}} = \frac{4\pi\hbar}{m_{\mathrm{n}}\gamma_{\mathrm{n}}} \cdot \rho b_{\mathrm{i}} \cdot \sqrt{\frac{I}{I+1}}\vec{\mu}_{\mathrm{n}} \cdot \vec{P} \ , \tag{3.33}$$

can also be written in the following way, analogue to a magnetic interaction of the neutron magnetic moment:

$$V_{\mathrm{F,i}} = -\vec{\mu}_{\mathrm{n}} \cdot \vec{B}^{*} \tag{3.34}$$

$$\text{with: } \vec{B}^{*} = -\frac{4\pi\hbar}{m_{\mathrm{n}}\gamma_{\mathrm{n}}} \cdot \rho b_{\mathrm{i}} \cdot \sqrt{\frac{I}{I+1}}\vec{P} \tag{3.35}$$

Because of this similarity $\vec{B}^{*}$ is called *pseudomagnetic field*[7] and the associated precession is called *pseudomagnetic Larmor precession* with the angular frequency:

$$\omega^{*} = \frac{4\pi\hbar}{m_{\mathrm{n}}} \cdot \rho b_{\mathrm{i}} P \cdot \sqrt{\frac{I}{I+1}} \tag{3.36}$$

For instance, the protons in solid polystyrene have a number density of about 0.08 mol/ml, which will create a pseudomagnetic field of approximately $B^{*}_{\mathrm{p}} = 3.0$ Tesla$\times P_{\mathrm{p}}$. For deuterons with the same density this yields a field of about $B^{*}_{\mathrm{d}} = 0.58$ Tesla $\times P_{\mathrm{d}}$. The spin of a neutron with a wavelength λ, which passes through a nuclear polarised target with a thickness d and a polarisation P, would therefore perform a precession of:

$$\varphi^{*}[\mathrm{rad}] = 2d\lambda\rho b_{\mathrm{i}} P \cdot \sqrt{\frac{I}{I+1}} \tag{3.37}$$

By measuring the angle φ^{*} one can in principle directly obtain the bound incoherent scattering length b_{i}, although the absolute determination of the number density, the wavelength etc. will cause a limitation on the accuracy. As we will see later this can be avoided by a relative measurement of two nuclear species in the same sample.
The precession angles caused by polarised protons, deuterons and ^{13}C nuclear spins are:

$$\begin{aligned} \varphi^{*}_{\mathrm{p}}\ [^\circ] &= (1004.6 \pm 0.3)^\circ \cdot d\ [\mathrm{mm}] \cdot \lambda\ [\text{Å}] \cdot P_{\mathrm{p}}\ [\%] \cdot \rho_{\mathrm{p}}\ [\mathrm{mol/ml}] \\ \varphi^{*}_{\mathrm{d}}\ [^\circ] &= (196.8 \pm 1.6)^\circ \cdot d\ [\mathrm{mm}] \cdot \lambda\ [\text{Å}] \cdot P_{\mathrm{d}}\ [\%] \cdot \rho_{\mathrm{d}}\ [\mathrm{mol/ml}] \\ \varphi^{*}_{\mathrm{C}}\ [^\circ] &= (-20.7 \pm 3.6)^\circ \cdot d\ [\mathrm{mm}] \cdot \lambda\ [\text{Å}] \cdot P_{\mathrm{C}}\ [\%] \cdot \rho_{\mathrm{C}}\ [\mathrm{mol/ml}] \end{aligned} \tag{3.38}$$

The errors are caused by the limited accuracy of the incoherent scattering lengths.

---

[7] The existence of a pseudomagnetic field was predicted by Barishevskii and Podgoretskii from an analysis of the neutron optical properties of a polarised target [Bar65]. A resonance experiment by Abragam et al. [Abr731] provided the first experimental demonstration using a sample of dynamically polarised protons in lanthanum magnesium nitrate ($La_2Mg_3(NO_3)_{12} \cdot 24H_2O$). Later pseudomagnetic precession detected with a Ramsey apparatus became a standard tool to determine incoherent scattering lengths (e.g. Ref. [Abr732]).

3.2.7. Neutron-Deuteron Scattering Lengths

Applying Equ. (3.18) and (3.19) for the deuteron yields (using the data given in table 3.1):

$$b_{+,\mathrm{d}} = b_{4,\mathrm{d}} = b_{\mathrm{c,d}} + \sqrt{\frac{1}{2}}\, b_{\mathrm{i,d}} = (9.53 \pm 0.02)\ \mathrm{fm} \tag{3.39}$$

$$b_{-,\mathrm{d}} = b_{2,\mathrm{d}} = b_{\mathrm{c,d}} - \sqrt{2}\, b_{\mathrm{i,d}} = (0.97 \pm 0.05)\ \mathrm{fm} \tag{3.40}$$

where $b_{4,\mathrm{d}}$ and $b_{2,\mathrm{d}}$ are the so-called neutron-deuteron quadruplet and doublet scattering length. The latter one is only known with a relative accuracy of about 5%.
In the latest measurement of the doublet scattering length [Dil71], $b_{\mathrm{i,d}}$ was determined indirectly via the bound scattering cross-section and the coherent scattering length of the deuteron, with the following results:[8]

$$\sigma_{\mathrm{s,\ bound}} = (7.623 \pm 0.027)\ \mathrm{barn} \tag{3.41}$$

$$b_{\mathrm{c,d}} = (6.672 \pm 0.007)\ \mathrm{fm} \tag{3.42}$$

$$b_{2,\mathrm{d}} = (0.96 \pm 0.06)\ \mathrm{fm} \tag{3.43}$$

Recently a group from the National Institute of Standards and Technology (NIST) achieved an improved measurement of $b_{\mathrm{c,d}}$ using a neutron interferometer [Sch03]:

$$b_{\mathrm{c,d}} = (6.665 \pm 0.004)\ \mathrm{fm} \tag{3.44}$$

But without a new value for $\sigma_{\mathrm{s,\ bound}}$ or $b_{\mathrm{i,d}}$ this does yields almost no improvement in the accuracy of $b_{2,\mathrm{d}}$.

The goal of the here presented work was to achieve a better accuracy by measuring $b_{\mathrm{i,d}}$ directly for the first time. To reach $\delta b_{2,\mathrm{d}}/b_{2,\mathrm{d}}$ of less than 1%, one needs $\delta b_{\mathrm{i,d}}/b_{\mathrm{i,d}} \leq$ 0.13%, i.e. an improvement by about a factor 6 compared to the present value.

---

[8] For the determination of the scattering cross-section, Dilg et al. performed measurements on D_2O, SiO_2 and Si using epithermal neutrons. From these measurements they deduced the total cross-sections of oxygen and the deuteron. The coherent scattering length of D_2O was determined by means of mirror reflection using slow neutrons with a gravity refractometer.

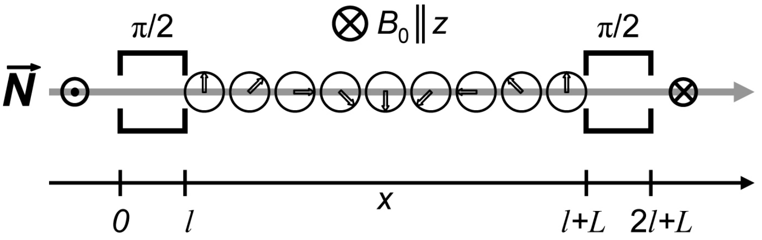

Figure 3.3: Ramsey's resonance method of separated oscillating fields for cold neutrons at resonance condition. Polarised neutrons ($\vec{N}$) travel in x-direction through a constant magnetic field $\vec{B}_0$ pointing in z-direction. The neutron spins precess freely with their Larmor frequency $\omega_0 = -\gamma_n B_0$ across a distance L between two $\pi/2$-resonance spin flippers of the length l where their spin gets turned by 90° each.

3.3. Theory of a Ramsey Apparatus

This section has been taken from Ref. [Pie082]. It recalls the basic features of Ramsey's method [Ram56] and provides formulas for the dependence of the observed signals from geometrical parameters, field strength and the width of the neutron wavelength distribution (instrumental parameters). A sketch of the Ramsey apparatus is shown in Fig. 3.3. A polarised neutron beam passes through a static magnetic field $\vec{B}_0$ in which two phase-locked $\pi/2$-resonance spin flippers are situated. Their fields $\vec{B}_1$ oscillate perpendicularly to $\vec{B}_0$ ($B_1 \ll B_0$), with an angular frequency ω close to the neutron Larmor frequency $\omega_0 = -\gamma_n B_0$. The spin flippers have a length l and are separated by a distance L. The field amplitude B_1 is adjusted to result in a 90° rotation of the neutron spin in each spin flipper at resonance.

We first consider the ideal case of a fully polarised ($P_n = 1$) and perfectly monochromatic beam with the wavelength $\lambda_0 = \frac{h}{m_n v_0}$, where h is the Planck constant, v_0 is the neutron velocity, and m_n is the neutron mass. With the resonance condition $\Delta = \omega - \omega_0 = 0$ exactly fulfilled, the first spin flipper rotates the neutron spin into the plane perpendicular to $\vec{B}_0$. The subsequent Larmor precession stays in phase with the oscillating fields, and the second $\pi/2$-spin flipper thus completes the spin flip by 180°. For small deviations from $\Delta = 0$ the spin will still be rotated by about 90° in the first spin flipper, but subsequently run out of phase with the field in the second flipper. If, for example, an additional phase shift of 180° occurs, the neutron spin will be turned back in its initial direction[9]. As a function of ω, a characteristic wiggle pattern results. A simulation of such a pattern, called Ramsey signal, is shown in Fig. 3.4. The corresponding equation Equ. (B.11), derived in the appendix B, gives the probability $\mathcal{W}(\Delta)$ for a 180° spin flip. It is also shown that the theoretical difference Δf between two frequencies, where the probability for a 180° flip has a maximum, is given by

$$\Delta f \approx \frac{h}{m_n \lambda_0 L} \cdot \left(1 + \frac{4}{\pi}\frac{l}{L}\right)^{-1} \quad , \text{ for } L \gg l \; . \tag{3.45}$$

Further off resonance, one observes a damping of the amplitudes of the intensity oscillations because of the decreasing efficiency of the spin flippers. A formula for the "background resonance" part of the whole Ramsey signal is given in Equ. (B.14) and

---

[9] This is easily understood, if one considers the spin flip process in the reference frame rotating with the angular frequency ω.

shown as a dashed line in Fig. 3.4 and 3.5. Its width depends on the time τ the neutron spends in the spin flippers and is found numerically[10],

$$\text{FWHM [Hz]} \approx \frac{1.12}{\tau\ [\text{s}]} \approx \frac{4.43 \times 10^6}{\lambda_0\ [\text{Å}] \cdot l\ [\text{mm}]}\ . \tag{3.46}$$

So far we have not taken into account an additional precession angle φ^* of the neutron spin between the spin flippers, such as caused by the pseudomagnetic field of a nuclear polarised target. For a perfectly monochromatic beam it leads to a corresponding phase shift of the oscillatory part of the Ramsey signal, keeping the envelope of the wiggles unaffected.

Considering the case where the neutron beam has a wavelength distribution $p(\lambda)$, things become more complicated due to the velocity dependence of φ^*,

$$\varphi^*(\lambda) = \varphi_0^* \cdot \frac{\lambda}{\lambda_0}\ , \tag{3.47}$$

where φ_0^* is the precession angle of a neutron with wavelength λ_0. The resulting spread of φ^* around φ_0^* leads to a modification of the envelope of the Ramsey signal, whereas the phase shift of the wiggles within the envelope is still given by φ_0^* (for symmetric $p(\lambda)$). The corresponding probability $\mathcal{W}'$ for a 180° flip, given in Equ. (B.12), also takes a non-perfect neutron polarisation P_n into account. Examples of Ramsey signals for a wavelength distribution $\Delta\lambda/\lambda_0 = 0.06$ are shown in Fig. 3.5. As a result, the limited monochromacy of the beam imposes practical limits to the maximum phase shift, beyond which the wiggles become undetectable.

A perfectly homogeneous constant magnetic field B_0 is not possible to provide. Indeed it is only necessary that the average field along the neutron flight path L between the spin flippers is equal to the field $B_{0,\text{rf}}$ at the sites of the spin flippers,

$$\langle B_0 \rangle = \frac{1}{L} \int_l^{l+L} B_0(x) dx = B_{0,\text{rf}}\ , \tag{3.48}$$

because the validity of this equation already assures that the neutron spins precess on average in phase with the oscillatory fields of the spin flippers at $\Delta = 0$. This means that one has rather to cope with the stabilisation of the magnetic field than with providing a very high homogeneity.

---

[10] Calculated from Equ. (B.14) with $\mathcal{W} = 1/4$.

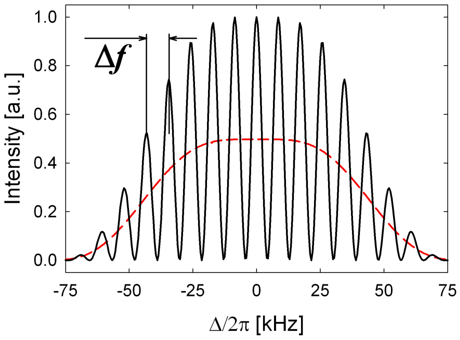

Figure 3.4: Simulated Ramsey resonance signal. Probability to detect a 180°-flipped neutron (solid line) and the corresponding background resonance curve (dashed line). Used simulation parameters: $P_{\mathrm{n}} = 1$, $\lambda_0 = 5$ Å, $l = 10$ mm, $L = 80$ mm → $\Delta f \approx 8.5$ kHz, FWHM ≈ 88.6 kHz.

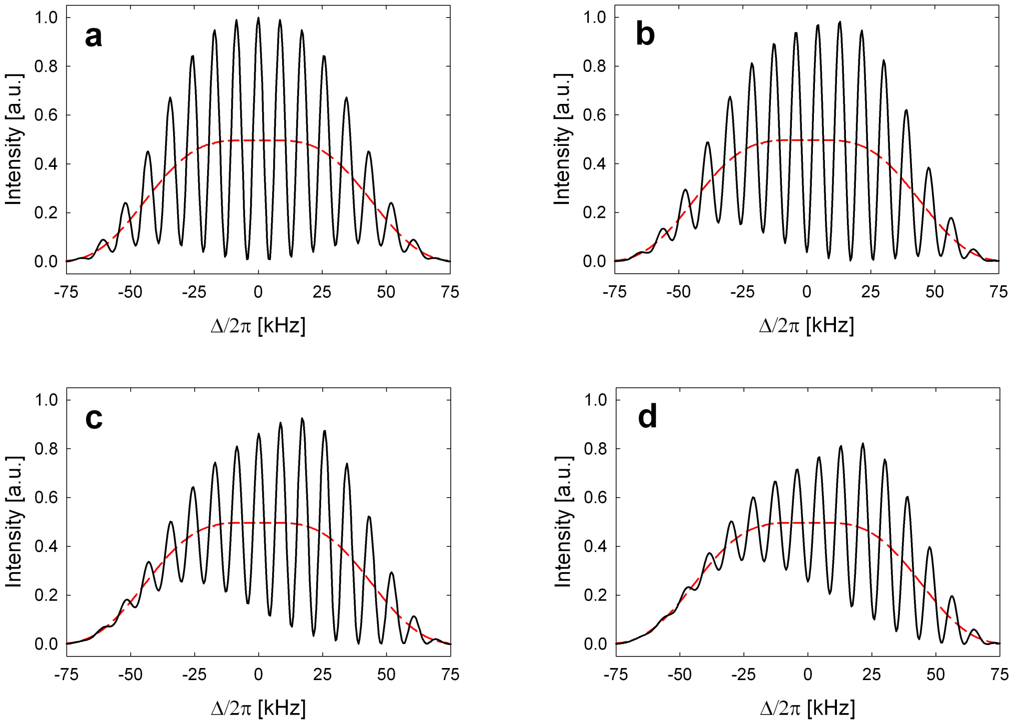

Figure 3.5: Simulated Ramsey signals with an assumed Gaussian wavelength distribution with $\Delta\lambda/\lambda_0 = 0.06$ (respectively: $\sigma_\lambda/\lambda_0 = 0.026$). The damped oscillations move along the background resonance curve (dashed line) if the additional precession angle increases. a) $\varphi_0^* = 0°$, b) $\varphi_0^* = 900°$, c) $\varphi_0^* = 1800°$ and d) $\varphi_0^* = 2700°$. Further simulation parameters: $P_{\mathrm{n}} = 1$, $\lambda_0 = 5$ Å, $l = 10$ mm, $L = 80$ mm.

3.4. Relative Measurement of $b_{\mathrm{i,d}}$

As already mentioned in sections 2.1 and 3.2.6 the nd-experiment foresees to measure the spin-dependent neutron scattering length of the deuteron $b_{\mathrm{i,d}}$ relative to the well-known scattering length of the proton $b_{\mathrm{i,p}}$ using a sample containing polarised protons and deuterons. This avoids the experimental difficulties associated with absolute measurements of the number density and nuclear polarisation.
In Ref. [Bra04] a formula was derived (Equ. (14)) for the case of three ideal measurement situations: 1) The protons and the deuterons are polarised. 2) Only one spin species is polarised with equal degree of polarisation as in the first situation. 3) The nuclear spins in the sample are completely unpolarised.
These three conditions cannot be perfectly prepared. Therefore, the previous equation has to be extended and additional terms have to be included to meet the experimental circumstances. Still, we make two reasonable assumptions:

- We assume that the sample only contains protons and deuterons and no other nuclei with spin-dependent scattering potentials, e.g. ^{13}C. The effect of other nuclear species can be easily corrected for and can be included in the following formulas.

- The magnetic field caused by the electrons of the paramagnetic centres and by the nuclear spins can be neglected (compare chapter C.1 in the appendix).

From Equ. (3.37) one can derive the pseudomagnetic precession angles of neutrons with a wavelength λ, due to polarised protons and deuterons respectively, in a sample with thickness d:

$$\varphi^{*}_{\mathrm{p},k} = 2d\lambda\rho_{\mathrm{p}}b_{\mathrm{i,p}}P_{\mathrm{p},k}\sqrt{\frac{1}{3}} \tag{3.49}$$

$$\varphi^{*}_{\mathrm{d},k} = 2d\lambda\rho_{\mathrm{d}}b_{\mathrm{i,d}}P_{\mathrm{d},k}\sqrt{\frac{1}{2}} \tag{3.50}$$

The total neutron spin precession angle will therefore be: $\phi_k = \varphi^{*}_{\mathrm{p},k} + \varphi^{*}_{\mathrm{d},k} + \phi_0$, where ϕ_0 is an intrinsic phase shift of the Ramsey apparatus, which also includes the precession angle due to the magnetic interaction with the paramagnetic centres.
To determine $b_{\mathrm{i,d}}$ one has to measure ϕ_k at least for two different degrees of nuclear polarisation, i.e. $k \in \{1, 2\}$. We define the ratio R_ϕ of the additional phase shifts as:

$$R_\phi \equiv \frac{\phi_1 - \phi_0}{\phi_2 - \phi_0} \tag{3.51}$$

Inserting Equ. (3.49) and (3.50) and solving for $b_{\mathrm{i,d}}$ yields:

$$b_{\mathrm{i,d}} = b_{\mathrm{i,p}} \cdot \sqrt{\frac{2}{3}} \cdot \left(1 - R_\phi \cdot \frac{P_{\mathrm{p},2}}{P_{\mathrm{p},1}}\right) \cdot \left(\frac{\rho_{\mathrm{p}}P_{\mathrm{p},1}}{R_\phi \cdot \rho_{\mathrm{d}}P_{\mathrm{d},2} - \rho_{\mathrm{d}}P_{\mathrm{d},1}}\right) \tag{3.52}$$

The missing product of the nuclear number density times the polarisation can be determined by the NMR absorption signals of the two nuclear species (see section 5.3 and Ref. [Hau04]):

$$\rho_j P_{j,k} = c_j \cdot \frac{I_j \cdot J_{j,k}}{g_j^2} \ , \tag{3.53}$$

where I_j is the spin, g_j is the g-factor[11] and $J_{j,k}$ is the area under the NMR absorption signal of the nuclear species $j \in \{\mathrm{p,d}\}$. The factor c_j includes constants and parameters which describe the NMR setup, e.g. filling factor of the coil etc. Hence, both nuclear species have to be measured with the same NMR setup at the same frequency, i.e. at different magnetic fields, in order to achieve that c_j cancels, when inserting Equ. (3.53) in Equ. (3.52):[12]

$$b_{\mathrm{i,d}} = -b_{\mathrm{i,p}} \cdot \sqrt{\frac{1}{6}} \cdot \left(\frac{g_{\mathrm{d}}}{g_{\mathrm{p}}}\right)^2 \cdot \left(\frac{R_\phi \cdot J_{\mathrm{p},2} - J_{\mathrm{p},1}}{R_\phi \cdot J_{\mathrm{d},2} - J_{\mathrm{d},1}}\right) \tag{3.54}$$

This means that one needs three phases (ϕ_0, ϕ_1 and ϕ_2) from three Ramsey signals and 4 NMR absorption signals for each relative measurement of $b_{\mathrm{i,d}}$. Actually the zero-phase measurement requires two further NMR signals with $J_{\mathrm{p},0} = J_{\mathrm{d},0} = 0$. Note, that it is not a trivial task to achieve a totally unpolarised sample and to confirm that the NMR signal is really zero. ϕ_0 is determined best by a separate measurement of several Ramsey signals for different sample temperatures with thermal equilibrium nuclear polarisation and by extrapolation to zero polarisation (see section 6.3).
Hence, the phases and the NMR signals have to be measured with an accuracy better than 10^{-3}, to reach the aimed precision of the spin-dependent scattering length of better than 0.13%.

Equ. (3.54) can be approximated for the special cases:

- $P_{\mathrm{p},2} = 0$:

$$b_{\mathrm{i,d}} = b_{\mathrm{i,p}} \cdot \sqrt{\frac{1}{6}} \cdot \left(\frac{g_{\mathrm{d}}}{g_{\mathrm{p}}}\right)^2 \cdot \left(\frac{J_{\mathrm{p},1}}{R_\phi \cdot J_{\mathrm{d},2} - J_{\mathrm{d},1}}\right) \tag{3.55}$$

- $P_{\mathrm{p},2} = 0$ and $P_{\mathrm{d},1} = P_{\mathrm{d},2}$:

$$b_{\mathrm{i,d}} = b_{\mathrm{i,p}} \cdot \sqrt{\frac{1}{6}} \cdot \left(\frac{g_{\mathrm{d}}}{g_{\mathrm{p}}}\right)^2 \cdot \frac{1}{R_\phi - 1} \cdot \left(\frac{J_{\mathrm{p},1}}{J_{\mathrm{d},1}}\right) \tag{3.56}$$

The later case corresponds to the derivation given in Ref. [Bra04], with $R_\phi - 1 = \varphi^*_{\mathrm{p},1}/\varphi^*_{\mathrm{d},1}$.

The best sensitivity for the determination of $b_{\mathrm{i,d}}$ is thus obtained for $R_\phi \approx 2$, i.e. the phase shift due to both isotopes is equal. Using Equ. (3.38), one finds this is the case when the residual proton concentration in a deuterated sample is approximately 4%, as at equal spin temperature it holds that $P_{\mathrm{p}}/P_{\mathrm{d}} \approx 5$ (compare section 5.4).
Further, Equ. (3.56) can be used to estimate the NMR absorption signals. For $R_\phi \approx 2$, this leads to $J_{\mathrm{p},1}/J_{\mathrm{d},1} \approx 4$.

---

[11] The g-factor is defined as the ratio between the magnetic moment of the nucleus and the nuclear magneton $\mu_{\mathrm{N}} = 0.505078 \times 10^{-26}$ Am^2. This yields: $g_{\mathrm{p}} = +2.79285$ and $g_{\mathrm{d}} = +0.85744$. Compare also table 5.1.

[12] We will see later that both signals will be measured at around 16 MHz, which corresponds to a magnetic field of about 0.4 Tesla (2.5 Tesla) for the protons (deuterons).

4. Some Basic Knowledge of Low Temperature Physics

4.1. The Helium Isotopes: ^{3}He and ^{4}He

Helium appears in nature in two stable isotopes: ^{3}He and ^{4}He. The natural abundance of the first is only 0.00014%. ^{4}He is nowadays obtained from helium-rich natural gas sources, whereas ^{3}He is a byproduct of tritium manufacure in a nuclear reaction:

$$\begin{aligned} {}^6_3\mathrm{Li} + \mathrm{n} &\longrightarrow {}^3_1\mathrm{T} + {}^4_2\mathrm{He} \\ {}^3_1\mathrm{T} &\longrightarrow {}^3_2\mathrm{He} + \mathrm{e}^- + \bar{\nu} \qquad T_{1/2} = 12.3 \text{ years} \end{aligned}$$

The liquefaction of ^{4}He was first achieved in 1908 by H. Kamerlingh Onnes in Leiden. A scheme of the used apparatus is presented in Fig. 4.1.
Fig. 4.2 illustrates the vapour pressures of the two helium isotopes as a function of the temperature. Below the drawn lines the corresponding isotope is gaseous and above liquid. In fact, such a diagram of a liquid, can be used for thermometry by measuring the vapour pressure above the liquid. The solid phases of helium have been omitted in the plot as they only appear at about ^{3}He: 34 bar and ^{4}He: 25 bar at $T \approx 0$ Kelvin, respectively. They can be found in complete phase-diagrams, for example in [Pob92].

One of the easiest ways to reach low temperatures is to pump on the vapour of a liquid helium bath (*^{3}He and ^{4}He evaporation cryostat*[1]). The achievable cooling power $\dot{Q}$ is proportional to the *latent heat of evaporation* L_{vap} of the gas and the amount of particles per unit of time moved from the liquid to the vapour $\dot{n}$, which is proportional to the vapour pressure $p_{\mathrm{vap}}(T)$ at temperature T:

$$\dot{Q}_{\mathrm{c}}(T) = \dot{n} \cdot L_{\mathrm{vap}} \propto p_{\mathrm{vap}}(T) \cdot L_{\mathrm{vap}} \tag{4.1}$$

$$\dot{Q}_{\mathrm{c}}(T) \propto e^{-1/T} \tag{4.2}$$

The last proportionality is given by the Clausius-Clapeyron equation[2] for the vapour pressure of an ideal gas with the approximation of $L_{\mathrm{vap}} \approx$ constant. It expresses that the cooling power depends exponentially on the inverse of the achievable temperature. Actually L_{vap} itself depends on the temperature, nevertheless one can assume for liquid helium an average latent heat of evaporation of ^{3}He: 25 J/mol = 0.5 kJ/l (liquid) and ^{4}He: 85 J/mol = 2.6 kJ/l (liquid). These values are one order of magnitude lower than for liquid hydrogen and two orders of magnitude compared to liquid nitrogen

---

[1] An example for a continuously operating ^{4}He evaporation bath cryostat can be found in Ref. [Del71].

[2] Compare appendix D.

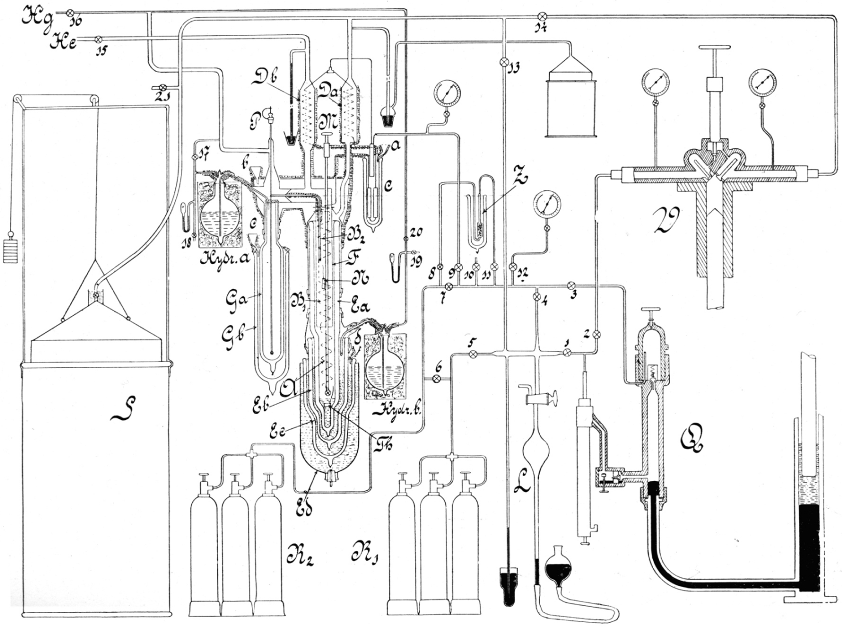

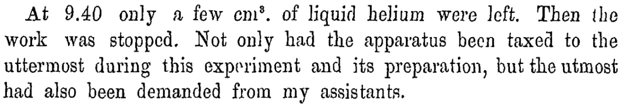
At 9.40 only a few cm³. of liquid helium were left. Then the work was stopped. Not only had the apparatus been taxed to the uttermost during this experiment and its preparation, but the utmost had also been demanded from my assistants.

Figure 4.1: Scheme of the ^{4}He liquefaction apparatus and citation of Kamerlingh Onnes, both taken from [Kam08].

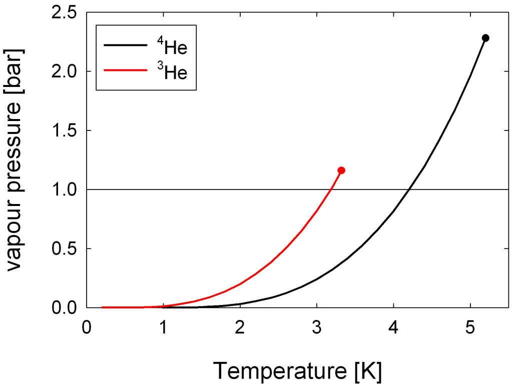

Figure 4.2: Temperature dependence of the vapour pressure of the two helium isotopes [Pob92]. The dots at the end of the curves are the critical points. ^{3}He: 3.32 Kelvin, 1.16 bar and ^{4}He: 5.20 Kelvin, 2.28 bar. The boiling temperatures T_b at 1 bar are ^{3}He: 3.19 Kelvin and ^{4}He: 4.21 Kelvin.

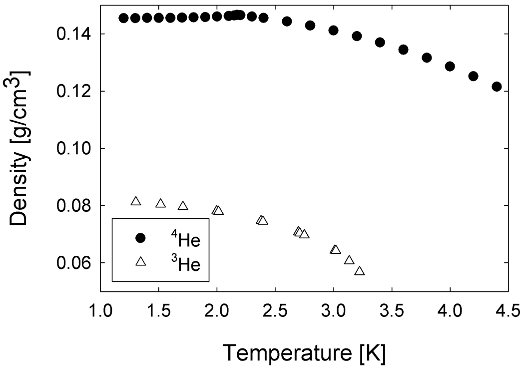

Figure 4.3: Temperature dependence of the density of liquid ^{3}He and ^{4}He under their own vapour pressure [Ker54, Ker57]. The density of ^{4}He reaches a maximum of about 0.1466 g/cm^3 at the λ-temperature $T_\lambda = 2.17$ Kelvin.

[Ens00]. In practice attainable temperatures by pumping on a helium bath are approximately ^{3}He: 0.3-0.4 Kelvin and ^{4}He: 1.0 Kelvin.
Using the latent heat of evaporation, one can also determine how much will be evaporated when a bath of liquid is exposed to heat, e.g. due to thermal radiation. One watt causes an evaporation of 7.5 l/h of liquid ^{3}He, 1.4 l/h of liquid ^{4}He or 0.023 l/h of liquid nitrogen N_2. Hence, to obtain long refill cycles of cryostats or dewars it is necessary to minimise the heat leak. This is done by means of an isolation vacuum, by using materials with a low thermal conductivity, as for example stainless steel or organic substances, and by avoiding thermal radiation. The latter is done by employing cooled radiation shields and baffles, e.g. highly polished metals or gold-plated surfaces, to avoid direct sight between parts cooled to liquid helium and surfaces at room temperature.
The radiation[3] of heat is described by the Stefan-Boltzmann equation:

$$\dot{Q}_{\text{Rad}}\ [\text{W}] = 5.67 \times 10^{-12} \cdot A\ [\text{cm}^2] \cdot \left(T_1^4 - T_2^4\right) \cdot \frac{\epsilon_1 \epsilon_2}{\epsilon_1 + \epsilon_2 - \epsilon_1 \epsilon_2}\ , \qquad (4.3)$$

where ϵ_i are the emissivities of the radiating and absorbing surfaces of size A.[4] For black body radiation with $\epsilon_{\text{max}} = 1$ and with $T_1 = 300$ Kelvin, $T_2 \approx 0$ Kelvin we find $\dot{Q}/A \approx 50$ mW/cm^2. For $T_1 = 100$ Kelvin this reduces already to about 0.6 mW/cm^2. However, also the use of the gas enthalpy is essential to minimise liquid helium consumption. The gas enthalpy of ^{4}He warming up from 4.2 Kelvin to 300 Kelvin is about 200 kJ/l (liquid), which is almost two orders of magnitude larger than the latent heat. The gas enthalpy can be exploited by heat exchangers between the warm gas that enters a cryostat and the cold outgoing gas that flows in opposite direction.

In Fig. 4.3 the density of the two helium isotopes is plotted as a function of the temperature[5]. At about 2.17 Kelvin ^{4}He reaches a maximum density of approximately 0.147 g/cm^3. This temperature is called λ-point, as ^{4}He undergoes a second

---

[3] Planck's law of black body radiation gives the spectrum of the radiation with the peak at the wavelength: $\lambda_{\text{max}} \approx \frac{hc}{2.82\, k_B T} \approx \frac{5.1\ \text{mm}}{T\ [\text{K}]}$ [Gre87].

[4] The emissivities strongly depend on the surfaces of the used materials. Typical values are: $\epsilon_{\text{Au}} = 0.01 - 0.03$, $\epsilon_{\text{Al}} = 0.02 - 0.3$ and $\epsilon_{\text{ss}} = 0.05 - 0.1$ for stainless steel.

[5] The molar volumes of the helium isotopes at $T \approx 0$ Kelvin and at saturated vapour pressure are: ^{3}He: 0.0368 l/mol and ^{4}He: 0.0276 l/mol [Pob92].

order phase transition (no latent heat), which causes a λ-shaped divergence in the specific heat capacity $C_V(T)$ (see Fig. 4.4).[6] This phase transition from the normal fluid He I to the superfluid He II is a consequence of the spin 0 of the ^{4}He atom (Bose-condensation). The transition temperature T_λ lowers slightly with increasing pressure - at the melting curve at about 30 bar it reduces to 1.77 Kelvin. Below the T_λ ^{4}He is often described with the *two fluid model* [Tis38]: at T_λ only *normal fluid* is present in He II. As the temperature is decreased, more and more normal fluid is transformed into *superfluid*. Finally, below 0.5 Kelvin, He II consists almost totally of superfluid. The superfluid has no entropy ($S = 0$) and no viscosity ($\eta = 0$). The latter enables superfluid helium to flow through tiny capillaries and so-called superleaks.[7] Another result of this special property is the thermo-mechanical effect, which says that superfluid helium flows towards areas where the He II is heated to restore the uniform mixture of normal and superfluid (fountain effect). This effect can also be turned around: if two reservoirs of He II are connected via a superleak and the first reservoir is put under pressure then only the superfluid helium can penetrate the superleak, which causes a cooling in the second reservoir.

Another consequence of the superfluidity is the superfluid film flow, which allows liquid ^{4}He to climb up the walls of a beaker against gravity. In a cryostat the liquid can climb up the pumping line to a height where the temperature is high enough to evaporate it. This causes two problems: firstly, this acts like a gas leak and reduces the effective amount of helium atoms, which are pumped from the surface of the liquid. Hence, it increases the lowest reachable vapour pressure and therefore increases the temperature. This effect becomes worse with a larger cross-section of the pumping line. Secondly, since the film is able to transport heat rather well, it acts like an additional heat leak [Bet76].

In analogy with the critical current or the critical magnetic field of a superconductor, superfluid helium has a critical velocity (*Landau velocity*). Above this certain velocity of about 30 cm/s excitations occur in He II (rotons, phonons and collective excitations), which cause that the liquid loses its superfluid properties (compare section 5.4 in Ref. [McC92]).[8]

Also ^{3}He has a superfluid phase, which appears at a temperature that is about three orders of magnitude lower than in ^{4}He. This is due to the fact that ^{3}He is a Fermion with spin 1/2 and its superfluidity can be seen analogue to the appearance of superconductivity in metals (compare electron *Cooper-pairs*).

For the sake of completeness, it shall be briefly mentioned how the liquefaction of gases is accomplished:

If a gas is caused to perform adiabatic ($\Delta Q = 0$) external work it must cool down, due to the first law of thermodynamics.[9] In practice, the gas is first isothermally compressed, before its internal kinetic energy is converted in performing work, e.g. against a turbine or piston, causing it to cool.

Another technique is the so-called *Joule-Thompson* isenthalpic ($dH = 0$) expansion,

---

[6] A very good summary of behaviours at phase transitions can be found chapter 17 of [Gre87].

[7] Unfortunately, it can also flow through tiny holes in liquid helium cells or tubes, which are hard to detect at room temperature (λ-leaks).

[8] The critical velocity may vary by more than one order of magnitude, if it is considered in a capillary instead of "bulk" helium [Wil67].

[9] Conservation of energy: $dU = \Delta Q + \Delta W$, i.e. the change in the internal energy dU of a closed thermodynamic system is equal to the sum of the amount of heat ΔQ supplied to the system and the work ΔW done on the system.

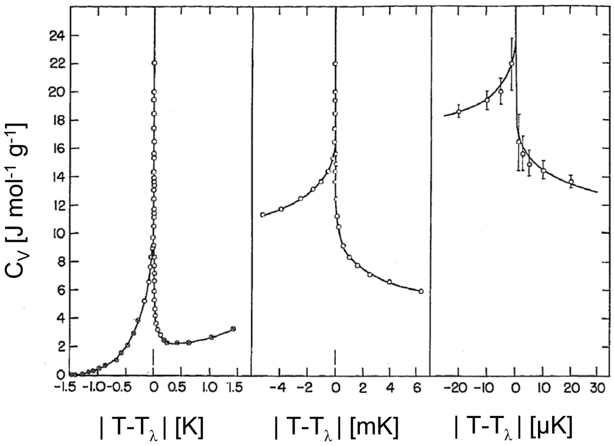

Figure 4.4: Specific heat capacity $C_V(T)$ close to the λ-temperature of liquid ^{4}He, taken from [Buc61]. The divergence of the curve is caused by a vertical tangent of the entropy at T_λ, as $C_V(T) = T\frac{\partial S}{\partial T}|_V$.

which exploits the attractive interatomic forces of a real gas.[10] This can be understood in the sense that during the expansion the gas performs work against these forces. The expansion can either cool or warm the gas depending on the initial pressure and the initial temperature of the gas (compare *inversion curve* and *Joule-Thompson coefficient*). Moreover, the Joule-Thompson effect works only for gases below their characteristic inversion temperature[11] T_{inv}, which makes it necessary that for instance helium has to be precooled by other means before this method can be applied for further cooling. A cryostat, which employs the Joule-Thompson effect for the liquefaction of ^{3}He is presented in Ref. [Wil72].

4.2. ^{3}He/^{4}He Mixtures and Dilution Refrigerators

Dilute solutions of ^{3}He and ^{4}He are of crucial importance for low temperature technology. Their special properties provide the basis of dilution refrigerators, which are considered the "easiest" possibility to reach steady temperatures in the millikelvin range, down to 2 mK [Fro78, Ver87].
The phase-separation x_3-T-diagram of liquid ^{3}He/^{4}He mixtures is depicted in Fig. 4.5, where x_3 is the ^{3}He concentration in the mixture. As we know already from section 4.1 ^{4}He undergoes a phase transition from He I to He II at the transition temperature T_λ. In the case of a mixture, T_λ depends now on the amount of ^{3}He. With increasing x_3 the transition temperature decreases down until it reaches $x_3 = 67\%$ and $T_\lambda = 0.87$ Kelvin (λ*-line* and *tricritical point*).
Below 0.87 Kelvin another characteristic of ^{3}He/^{4}He mixtures occurs. The liquid stops being a homogeneous mixture and separates into two phases with different ^{3}He contents and a visible interface between them (different optical refractive indices of the phases). The phase with a high concentration $x_{3,\text{c}}$ of ^{3}He (^{3}*He rich phase*) floats

---

[10] An ideal gas does not interact and therefore does not cool or warm under Joule-Thompson expansion. The van der Waals gas does, as it incorporates these forces in the term $\left(p + (N/V)^2\, a\right)$.

[11] The inversion temperatures of some gases: ^{4}He: 43 Kelvin, H_2: 204 Kelvin, N_2: 607 Kelvin and O_2: 893 Kelvin.

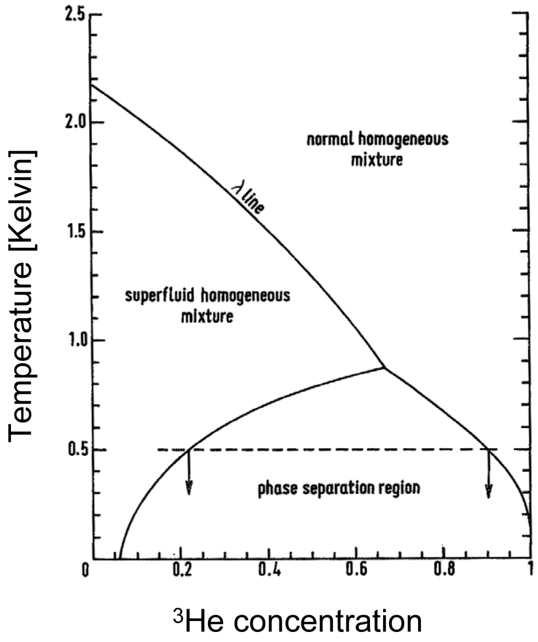

Figure 4.5: Phase diagram of liquid ^{3}He/^{4}He mixtures, taken from [Bet76].

on the dilute phase with only a small amount $x_{3,\mathrm{d}}$ (^{4}*He rich phase*), due to the different densities. An example is indicated by the dashed horizontal line at 0.5 Kelvin in Fig. 4.5: a mixture which is homogeneous above 0.87 Kelvin will separate into two phases with $x_{3,\mathrm{c}} \approx 90\%$ and $x_{3,\mathrm{d}} \approx 22\%$. With decreasing temperature the two helium isotopes do not totally separate, but reach finite values at $T \approx 0$ Kelvin of $x_{3,\mathrm{c}} = 100\%$ and $x_{3,\mathrm{d}} \approx 6.5\%$ [Edw65].

This finite solubility of ^{3}He in ^{4}He is caused by the fact that a ^{3}He atom has a lower energy when placed in pure liquid ^{4}He than it would have in pure liquid ^{3}He. This is a result of three effects:

- ^{3}He atoms with spin 1/2 obey Fermi statistics and are therefore correlated. In Ref. [Sch00] it is shown that even non-interacting Fermions feel an effective repulsion, if they have equal spin states due to the necessity of an anti-symmetric wave function (*exchange-correlation hole* and *Pauli principle*).

- In the diluted mixture, the ^{3}He atoms behave like a free degenerate Fermi gas[12] in the liquid ^{4}He, with an effective mass[13] $m_3^* \approx 2.5 \cdot m_3$. The Pauli principle causes that the energy levels of this Fermi gas are filled up till the Fermi energy E_F, which is proportinal to $(x_3)^{2/3}$ [Kit04]. Hence, any additional ^{3}He atom added to the mixture has to have an energy of at least E_F.

- On the other hand, ^{4}He atoms are Bosons and feel an attractive tendency as a result of their symmetric wave function (*Boson bunching*).

---

[12] The corresponding Fermi temperature with $x_3 = 6.5\%$ is approximately $T_\mathrm{F} = 0.38$ Kelvin [Lou74], which is very low compared to the Fermi temperature of electrons in a metal of about 10^4 Kelvin.

[13] The increased mass is caused by the ^{4}He atoms, which behave like a "massive vacuum" for the ^{3}He atoms. At this low temperatures the ^{4}He "solvent" is totally superfluid and has zero entropy, zero viscosity and no heat capacity - *inert superfluid background.*

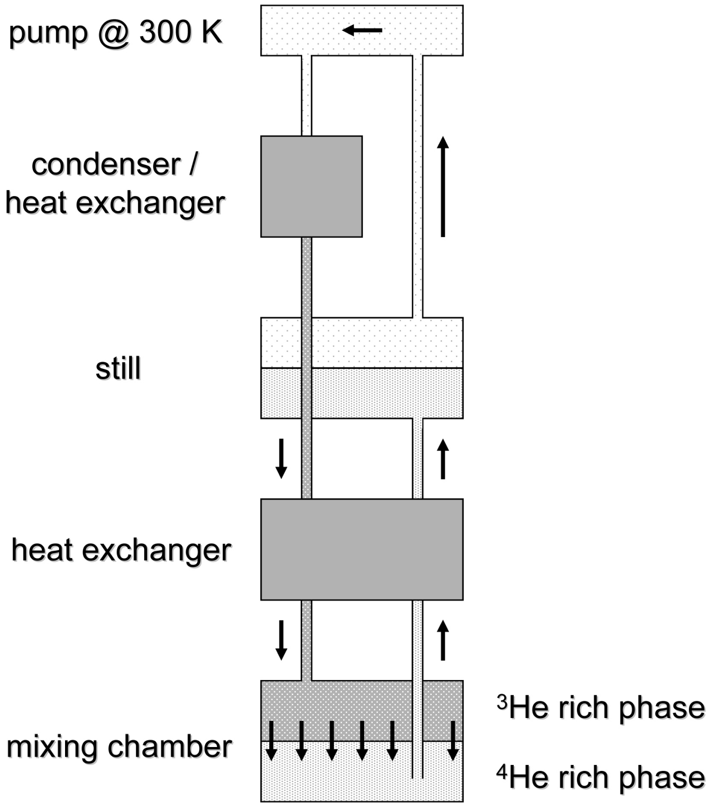

Figure 4.6: Scheme of a dilution refrigerator. The arrows indicate the flow direction of the ^{3}He atoms.

Hence, it is energetically advantageous at certain temperatures and concentrations, that ^{4}He atoms stay together in one phase and some of the ^{3}He atoms mix in this phase until the first two effects listed above balance each other. The latter is approximately the case at $x_{3,\mathrm{d}} \approx 6.5\%$.

But why is this special behaviour of ^{3}He/^{4}He mixtures important? To answer this question, we have to first understand how the cooling in a dilution refrigerator is achieved [Lou74]. A very schematic picture of a dilution refrigerator is presented in Fig. 4.6. The in-going helium gas is cooled by the counter flowing cold gas via several heat exchangers. It condenses and separates in two phases in the *mixing chamber*. In the *still*, which is at about 1 Kelvin, almost only ^{3}He atoms evaporate,[14] due to the different partial pressures of ^{3}He and ^{4}He in the mixture. The vapour in the still is removed by pumping, which causes a ^{3}He concentration gradient, resulting in an osmotic pressure gradient between still and mixing chamber. Hence, ^{3}He atoms penetrate the phase boundary in the mixing chamber and thereby cause cooling. This can be interpreted as the "evaporation" of ^{3}He atoms from the liquid to the "gas-like" ^{4}He rich phase. The temperature of the still can be regulated by a heater to establish a sufficient gas circulation rate.

We are therefore dealing with a kind of upside-down version of a ^{3}He evaporation cryostat mentioned in section 4.1. The important advantage is, that due to the finite solubility the amount of "evaporated" ^{3}He atoms $\dot{n}_3$ does not decrease exponentially but stays constant with temperature. In other words, the osmotic pressure gradient,

---

[14] E.g. at a temperature of 0.7 Kelvin and a ^{3}He concentration of 1% in the still the partial pressures are approximately ^{3}He: 0.080 mbar and ^{4}He: 0.003 mbar. Hence, in this case about 96% of the vapour in the still is ^{3}He. Compare equation (3.3) in [Bet76].

which can be seen as the analogous of the vapour pressure for an evaporation cryostat [Bet76], does not become zero, but instead approaches a finite value of about 22 mbar for $T \approx 0$ Kelvin [Ens00].[15]
The cooling power of an ideal dilution fridge (only ^{3}He circulates which is cooled by step heat exchangers) is explicitly derived in Ref. [Lou74]:

$$\dot{Q}_c(T)\ [\mathrm{W}] \quad = \quad \dot{n}_3\ [\mathrm{mol/s}] \ \cdot\ (96 \cdot T_{\mathrm{mix}}^2 - 12 \cdot T_{\mathrm{hx}}^2) \tag{4.4}$$

$$\dot{Q}_c(T)\ [\mathrm{W}] \quad \approx \quad 84 \cdot \dot{n}_3\ [\mathrm{mol/s}] \ \cdot\ T_{\mathrm{mix}}^2\ , \tag{4.5}$$

where T_{mix} and T_{hx} are the temperatures in the mixing chamber and the temperature of the last heat exchanger, respectively. In Equ. (4.5) it is assumed that $T_{\mathrm{mix}} \approx T_{\mathrm{hx}}$. Equ. (4.4) expresses that the cooling is proportional to the circulating ^{3}He flow $\dot{n}_3$, which is adjusted by means of a flow impedance (e.g. a needle valve) after the condenser above the still and by the still heater. On the other hand, it also expresses that the circulation introduces heat caused by the "warm" liquid coming from the last heat exchanger.
From the conservation of energy it follows that the cooling power is equal to the sum of the heat leak of the cryostat $\dot{Q}_{\mathrm{hl}}$ and the externally applied heating power $\dot{Q}_{\mathrm{ext}}$:

$$\dot{Q}_c(T) = \dot{Q}_{\mathrm{hl}} + \dot{Q}_{\mathrm{ext}} \tag{4.6}$$

Therefore, by plotting the square of the mixing chamber temperature T_{mix}^2 as a function of $\dot{Q}_{\mathrm{ext}}$, one can approximately determine the heat leak of a dilution cryostat (see section 5.2.1).

As an example we want to compare the theoretical cooling powers of a dilution refrigerator and of evaporation cryostats:
For instance, we consider a pump that can handle 1000 m^3/h, which corresponds to approximately 10 mol/s at 1 bar. This pump can then establish a ^{3}He gas flow of about 1 mmol/s in a dilution refrigerator, if we assume a partial pressure of ^{3}He of 0.1 mbar in the still. This yields a cooling power of approximately 0.8 mW (5 mW) at a mixing chamber temperature of 100 mK (250 mK).
With the same pump one can reach a cooling power of about 0.5 mW (8 mW) at 300 mK (400 mK) with a ^{3}He evaporation cryostat and about 0.3 W (0.7 W) at 1.1 K (1.2 K) with a ^{4}He evaporation cryostat (using Equ. (4.1)).

---

[15] This holds for temperatures below 200 mK and $x_{3,\mathrm{d}} = 6.5\%$ and $x_{3,\mathrm{still}} \leq 2\%$.

4.3. Thermal Conductivity

When designing low temperature apparatuses or cryostats, it is always essential to consider proper materials in terms of heat transfer and thermal conductivity, respectively. It is either necessary to couple two parts thermally as good as possible or to have them well-isolated from each other. The thermal conductivity of basically all materials depends very much on the temperature and can vary from room temperature to $T \approx 0$ Kelvin by several orders of magnitude. The heat is carried by lattice vibrations (phonons) and/or conduction electrons (in metals).

In general one can define the thermal conductivity κ in analogy with Ohm's law, by:

$$\kappa = \frac{L}{A} \cdot \frac{\dot{Q}_{\mathrm{tr}}}{\Delta T} \,, \tag{4.7}$$

where ΔT is the temperature difference and $\dot{Q}_{\mathrm{tr}}$ is the heat current transfered over a uniform rod of length L and cross-section A. Hence, $[\kappa] = \mathrm{W\ m^{-1}\ K^{-1}}$.

In this section we will only consider materials, which later will be of interest in the cryostat used to measure the incoherent neutron-deuteron scattering length. For a more detailed consideration on other materials consult Ref. [Lou74, Pob92].

4.3.1. Thermal Conductivity of Liquid ^{4}He

The thermal conductivity of helium is of great importance in our neutron-deuteron experiment, as the investigated sample is situated in a cell filled with liquid ^{4}He, which is thermally anchored to the mixing chamber of the cryostat (see section 5.2).

In section 4.1 it was already mentioned, that the specific heat capacity $C_{\mathrm{V}}(T)$ of ^{4}He diverges at 2.17 Kelvin and that below this phase transition temperature the liquid can be described with the two fluid model. Above 1 Kelvin, He II can transport enormous amounts of heat[16] by an internal convection process of normal and superfluid helium (thermo-mechanical effect). This flow is limited by the viscosity of the normal fluid, which increases drastically towards lower temperatures (see Fig. 5.9a in [Ens00]). Therefore, below about 0.6 Kelvin this process becomes negligible and the heat is then carried through liquid ^{4}He only by longitudinal phonons [Lou74]. Hence, the thermal conductivity $\kappa_{^4\mathrm{He}}$ close to $T \approx 0$ Kelvin is proportional to $D \cdot T^3$, where D is the diameter of the helium column (compare Debye's T^3-law in [Kit04]).

Fig. 4.7 shows a plot of the thermal conductivity of pure liquid ^{4}He taken from the publication of Abel and Wheatley [Abe68]. Note that the conductivity drops by approximately two orders of magnitude going from 200 mK to 50 mK. The admixture of small amounts of ^{3}He reduces the conductivity even further.

---

[16] This explains why liquid helium, which is cooled below T_λ, immediately stops boiling. This is due to the huge thermal conductivity, which prevents that temperature gradients in the liquid can occur.

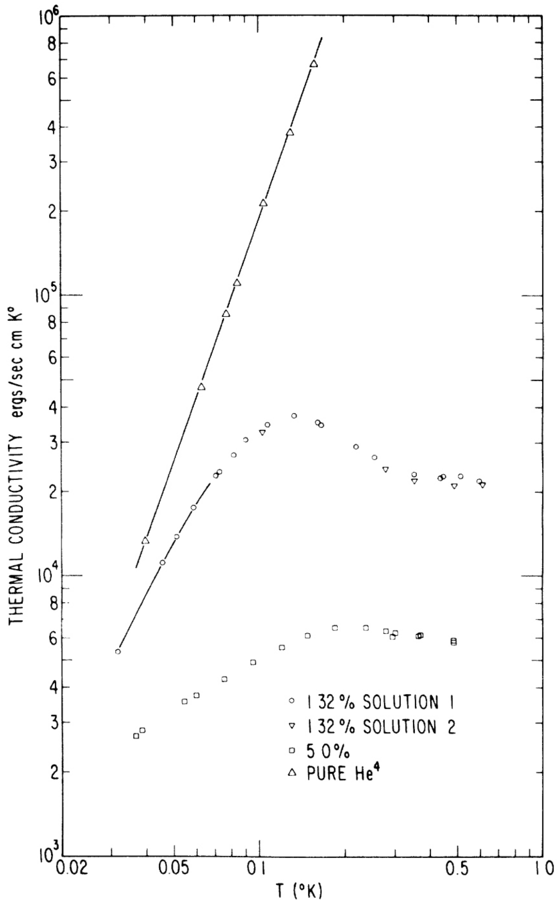

Figure 4.7: Thermal conductivity of two dilute solutions of ^{3}He in ^{4}He (1.3% and 5.0%) and of pure ^{4}He. The data is taken from [Abe68] and was obtained with a liquid helium column of 2.5 mm in diameter. Note that ergs/sec equals 10^{-7} W. A measurement of the thermal conductivity of pure liquid ^{3}He can be found in [Abe67].

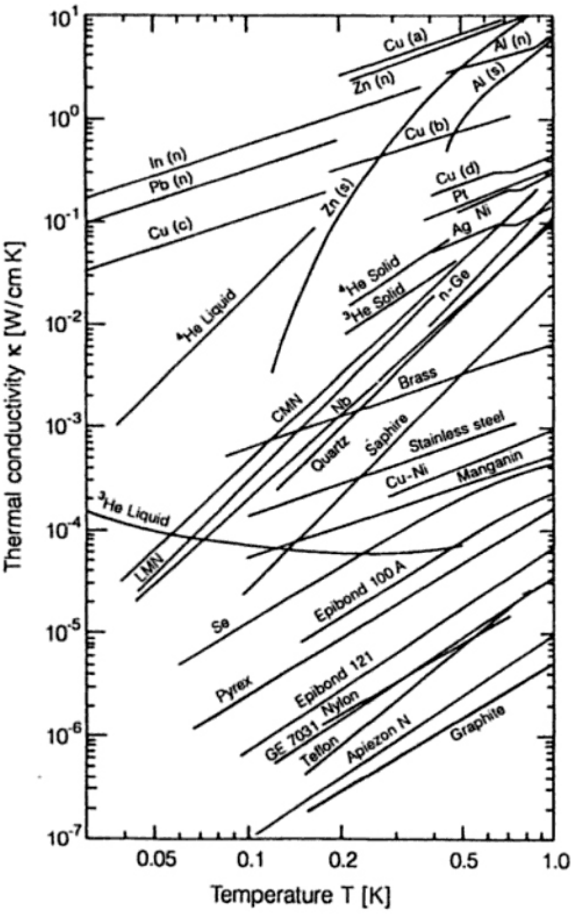

Figure 4.8: Thermal conductivities of various materials below 1 Kelvin, taken from [Lou74].

4.3.2. Thermal Conductivity of Metals

Nowadays most cryogenic apparatuses are made from metal. Often thin stainless steel is used because of its rigidity and the relatively bad thermal conductivity. On the other hand, copper is used, if one favours a good thermal contact.

In metals both, the phonons and the conduction electrons, contribute to the thermal conductivity. Usually, the electronic thermal conductivity κ_e in a metal is considerably larger than the thermal conductivity of the phonons κ_ph. This is caused by the much larger Fermi velocity of the electrons compared to the speed of sound of the lattice vibrations. At temperatures far below the Debye temperature[17] κ_ph is proportional to T^3 and below about 10 Kelvin κ_e is proportional to T. At higher temperatures the thermally excited phonons are limiting the thermal conductivity of the electrons due to scattering processes.

For instance, at 100 mK the thermal conductivity of copper of approximately 0.1 W K^{-1} cm^{-1} is almost three orders of magnitude larger than of stainless steel, while it is only 5 times larger than the thermal conductivity of liquid ^{4}He. For the temperature dependence of κ below 1 Kelvin of these and other materials see Fig. 4.8.

---

[17] Debye temperatures of several metals: Cu: 343 Kelvin, Ag: 226 Kelvin, Au: 162 Kelvin, Al: 428 Kelvin and Ti: 428 Kelvin [Kit04].

4.3.3. Kapitza Resistance

The term Kapitza resistance refers to the thermal boundary resistance between liquid helium and a solid body. This resistance, which is caused by a so-called acoustic mismatch between the two materials, becomes significant at temperatures well below 1 Kelvin. Its importance becomes clear if one considers the performance of heat exchangers in dilution refrigerators or as we will see later between the mixing chamber and a target cell filled with liquid ^{4}He, which are coupled via a sintered silver heat exchanger (see section 5.2.1).
A quantitative explanation of the Kapitza resistance is given in section 9.6 in Ref. [Lou74]. The gist is that due to Snell's law only a very small fraction of the longitudinal phonons in liquid helium may enter into the solid (critical cone of incidenting phonons).[18] And this amount is even further reduced by the transmission coefficient, which depends on the ratio of the acoustic impedances of the two materials. Therefore the phonon mismatch is especially great in the case of a liquid helium/solid boundary, due to the small density of the helium. The Kapitza thermal boundary resistivity is defined similarly to Equ. (4.7) by:

$$R_{\mathrm{K}} = \frac{A \cdot \Delta T}{\dot{Q}} \tag{4.8}$$

and is proportional to T^{-3}, i.e. the boundary resistance increases strongly with decreasing temperature.
Experiments show that the Kapitza resistance is extremely sensitive to the surface quality of the solid and that R_{K} is roughly the same for liquid ^{3}He, liquid ^{4}He and for dilute mixtures of ^{3}He in ^{4}He on one side and for different solids (metals and insulators) on the other [Lou74]. Hence, the simplest way to reduce the boundary resistivity is to increase the size of the surface, which is usually accomplished by using sintered metal sponges.

---

[18] This is caused by the fact that the velocity of phonons in liquid helium of about 200 m/s is 20-25 times slower than in metals.

5. Experimental Setup and DNP

The nd-experiment consists of three crucial parts, which will be dealt with in this chapter:

1. The neutronic part with the **Ramsey apparatus**, which is optimised to determine phase shifts due to pseudomagnetic interaction with an absolute accuracy of about ±1°. This is achieved by a careful stabilisation of the whole system, especially the radio frequency spin flippers and the magnetic field and by employing the so-called two beam method.

2. The **frozen spin target**, which consists of a dilution refrigerator with a high cooling power for dynamic nuclear polarisation and a target cell that is thermally anchored to the mixing chamber.

3. A highly sensitive **nuclear magnetic resonance (NMR)** setup to measure the nuclear spin polarisation of the polarised target.

These parts have to work all simultaneously to perform the measurement of the spin-dependent scattering length. They were constantly improved and changed during and in between the seven beam times (see section 6.1). Here, the focus will be on the latest versions of the parts, which corresponds to beam times six and seven. The individual developments will be mentioned and explained in the cases where it is necessary for the reader's understanding.

5.1. The Neutron Ramsey Apparatus

5.1.1. The FUNSPIN Beam Line

The nd-experiment was carried out at the fundamental neutron physics beam line FUNSPIN at PSI [Zej05]. Its polarised cold wavelength spectrum peaks at about 3.6 Å and the integrated neutron flux is about 2.5×10^8 neutrons cm^{-2} s^{-1} mA^{-1}, where mA refers to the proton current of the spallation source SINQ, which is typically around 1.2 – 1.4 mA (compare Fig. 5.1). The wavelength averaged beam polarisation is about 95% in the centre of the beam cross-section. The beam line features an adiabatic resonance π-spin flipper with a high efficiency of close to 100%.

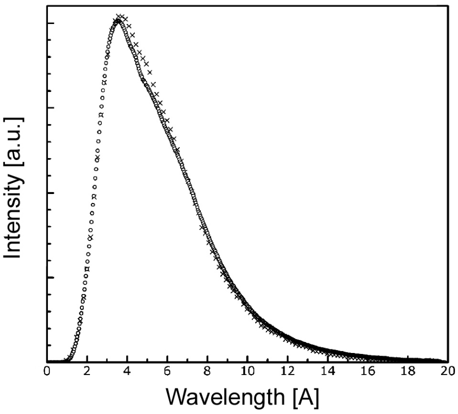

Figure 5.1: Neutron wavelength spectrum of the FUNSPIN beam line, taken from Ref. [Zej05].

5.1.2. Overview of the Ramsey Apparatus

A scheme of the neutron Ramsey apparatus is presented in Fig. 5.2. The white polarised cold neutron beam (N) is first collimated by several diaphragms and collimating devices (only in beam time seven) and afterwards reflected by an angle of $2 \cdot \theta_\mathrm{m} \approx 3°$ on a neutron NiTi bandpass supermirror (M). This produces a gaussian-shaped neutron wavelength spectrum with maximum at about 4 – 5 Å and a relative width $\Delta\lambda/\lambda_0$ of approximately 6% (FWHM). Along the beam path two radio frequency (rf) $\pi/2$-spin flippers (F_1 and F_2) are placed in the 48 mm wide gap between the pole pieces (P) of an electromagnet, which provides the static field $B_0 \approx 2.5$ Tesla.[1] The sample (S) is placed between the $\pi/2$-spin flippers, which are separated by a distance of about 80 mm.[2] The spin flippers are two matched resonant circuits for frequencies around 73 MHz, provided by a rf signal generator and two rf amplifiers. Their linear oscillating fields $B_1'(t) = 2B_1' \cos(\omega t)$ and $B_1''(t) = 2B_1'' \cos(\omega t + \vartheta_\mathrm{rf})$ are perpendicular to the static field and stabilised in phase and amplitude by a feedback loop (compare section 5.1.5). A field amplitude of about 1 mT is required for a $\pi/2$-flip, for which the rf amplifiers have to deliver a power of several watts each. Therefore both rf coils of the spin flippers have to be cooled with compressed air. Neutron polarisation analysis is performed with a supermirror bender (A), which has an analysing power of about 90% for 4 Å neutrons.[3] Finally, the neutrons are detected in a ^{3}He-gas detector (D). Actually, two detectors are used as the initial neutron beam is separated in front of the first spin flipper into two partial beams: the *sample beam*, which penetrates the polarised target and the *reference beam*, which passes by the target (compare two beam method in section 5.1.9). Count rates are normalised to the incident flux by a ^{235}U fission chamber (*monitor detector*) with a dead time of 2.4 μs and an efficiency of 1.5×10^{-3}. Due to the relatively low count rate in the monochromatic beam the monitor is placed after the collimation and before the monochromator mirror in the white beam (typically 10^3 counts s^{-1}).

In the following sections the individual components of the Ramsey apparatus are described. Another consideration of the setup can be found in Ref. [Pie082]. A photograph of the entire setup of the nd-experiment is shown in Fig. 5.3.

---

[1] This large magnetic field is required by the dynamic nuclear polarisation method employed to polarise the sample (see section 5.4).

[2] This distance corresponds roughly to the diameter of the pole shoes.

[3] This has been measured at the neutron reflectometer Morpheus at SINQ at the Paul Scherrer Institute.

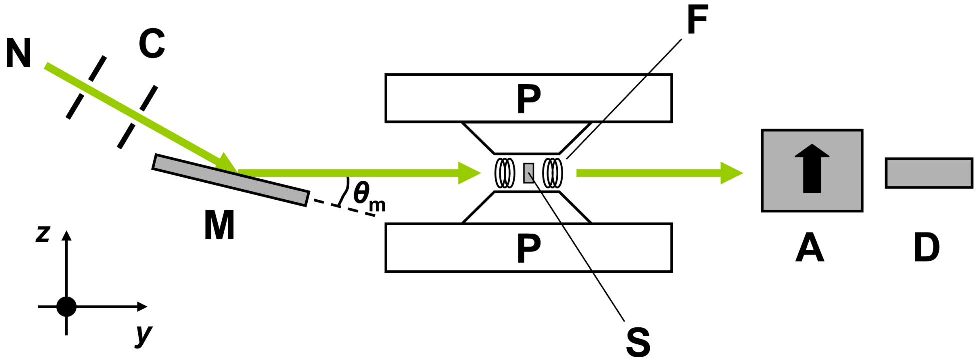

Figure 5.2: Scheme of the principle setup of the Ramsey apparatus. The white polarised neutron beam (N) is first collimated (C) and then monochromised by specular reflection on a monochromator mirror (M) under the angle θ_m. Afterwards it passes two radio frequency $\pi/2$-spin flippers (F: F_1 and F_2) and the sample (S), which are placed between the pole pieces of a magnet (P). Finally, the spins of the neutrons are analysed (A) and the neutrons are detected (D). The origin of the coordinate system is in centre between the pole pieces of the magnet.

5.1.3. Neutron Collimation

The beam collimation in front of the neutron monochromator mirror is of great importance. Firstly, the horizontal collimation is necessary to provide that the width of the neutron beam divergence distribution $\Delta\theta_h$ is of the same magnitude as the peak width of the reflectivity curve of the monochromator mirror (compare section 5.1.4), i.e.

$$\frac{\Delta\theta_h}{\theta_m} \approx \frac{\Delta q}{q_0} \approx 6\% \qquad \text{hence:} \quad \Delta\theta_h \approx 0.1^\circ \tag{5.1}$$

Secondly, the vertical collimation is crucial to separate the two partial beams well from each other. The necessary collimation $\Delta\theta_v$ is of the same order as $\Delta\theta_h$.
While during the first six beam times collimation was achieved by using ^{6}Li and B_4C diaphragms, in the last beam time an advanced setup of two specially developed Soller collimators has been used to provide larger beam cross-sections for the use of larger targets.

These collimators, which are adjusted using controllable motorised stages, are presented in Fig. F.1 and F.2. The horizontal collimator uses parallel aligned silicon wafers coated on both sides with a 1 μm thick absorption layer of TiGd ("*silicon collimator*"), whereas the vertical collimator uses thin aluminium sheets also coated with TiGd ("*aluminium collimator*").[4] The wafers and the aluminium sheets have a thickness of 0.4 mm and a rectangular shape with a length of 200 mm. They are aligned parallel at intervals of 0.8 mm using aluminium plates with eroded slits. The spacing between them causes that half of the passing neutrons travel in the 0.4 mm gaps, while the other penetrate through the 200 mm long wafers/sheets. This obviously increases the total neutron transmission compared to standard Soller type collimators using stacks of coated wafers [Kri00, Kri05, Cus01].

---

[4] The thickness of the coating ensures that the beam attenuation of the devices is sufficient for neutron wavelengths of down to 1 Å, i.e. the whole spectrum of a cold neutron source.

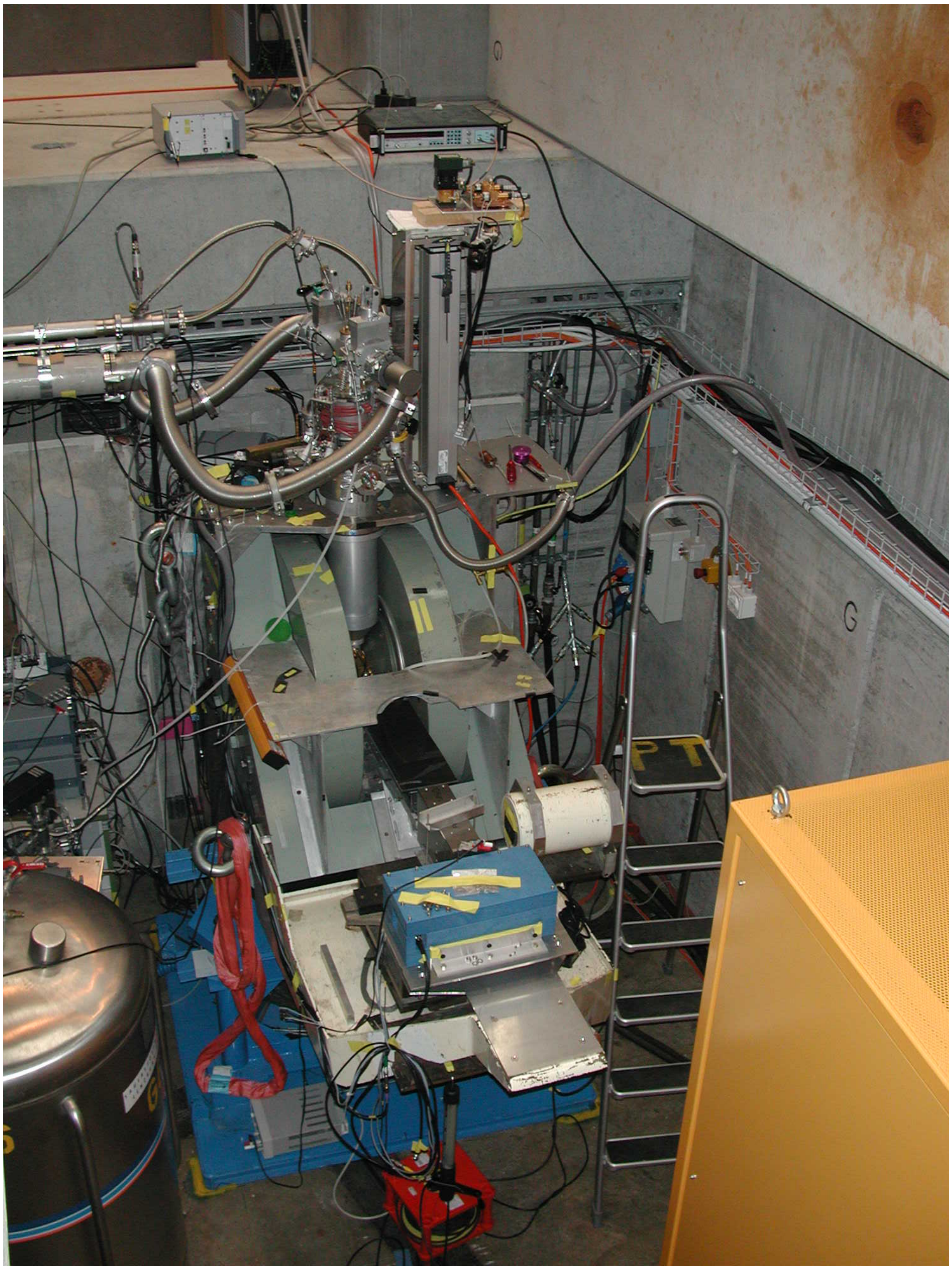

Figure 5.3: Photograph of the nd-experiment at the FUNSPIN beam line, taken after the third beam time in January 2006.

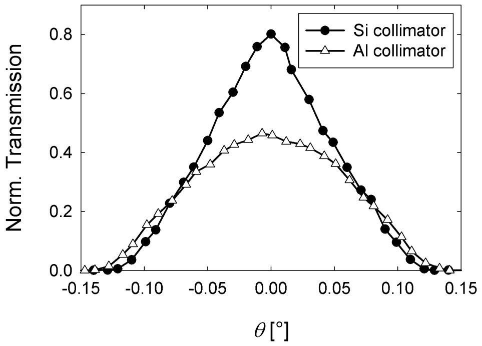

Figure 5.4: Transmission rocking curves of the two neutron collimators for 5 Å neutrons measured in steps of 0.01°: the silicon collimator (filled circles) and the aluminium collimator (white triangles).

The expected transmission of the two devices can be estimated using the absorption cross-sections of silicon and aluminium given in Ref. [Sea92]. Considering a perfectly parallel 5 Å neutron beam, yields an ideal transmission averaged over the beam cross-section of 81% for the silicon collimator and of 73% for the aluminium collimator.
The performance of the devices has been measured at the Narziss cold neutron reflectometer at the spallation neutron source SINQ at the Paul Scherrer Institute. The monochromator of the reflectometer provides a 5 Å neutron beam with $\Delta\lambda/\lambda_0 = 1.5\%$. The two collimating slits in front of the sample and the slit in front of the detector were set to a height of 20 mm and to a width of 0.5 mm such that a horizontal beam divergence of about 0.01° was achieved. The transmissions of the devices have been determined by performing a scan over the rocking angle θ (see Fig. 5.4). The plots show two acceptance distributions with a FWHM and a peak transmission of 0.11° and $(80 \pm 2)\%$ for the silicon collimator and of 0.15° and $(47 \pm 2)\%$ for the aluminium collimator, respectively.[5] The peak transmissions are normalised to the direct beam and give the average value over the whole cross-sections of the devices, obtained by a lateral scan at $\theta = 0°$. They have also been corrected taking the non-perfect collimation of the incoming neutron beam into account.[6]
A comparison between the experimentally found peak transmissions and the expected values given above shows that the mechanical setup of the silicon collimator works very well, whereas the aluminium collimator cannot meet the expectations. This is probably caused by the waviness of the aluminium sheets, which are far less rigid than the wafers. Hence, the use of two silicon collimators would have been advantageous, but was not possible due to lack of wafers and time.
A detailed description of the collimators can be found in Ref. [Pie093].

Independent from the method of collimation the resulting neutron beams are only of several square millimeters in cross-section. Hence, careful alignment of the whole Ramsey apparatus with a theodolite is indispensable, to ensure that the tiny beams fully illuminate the whole target and reach the detectors without being absorbed in a misadjusted aperture.

---

[5] The expected width of the distribution is given by $\arctan\left(\frac{0.4\text{mm}}{200\text{mm}}\right) = 0.115°$.

[6] The correction of the peak values is on a level of about 3.5% and is obtained by performing a convolution of two triangular functions of different widths.

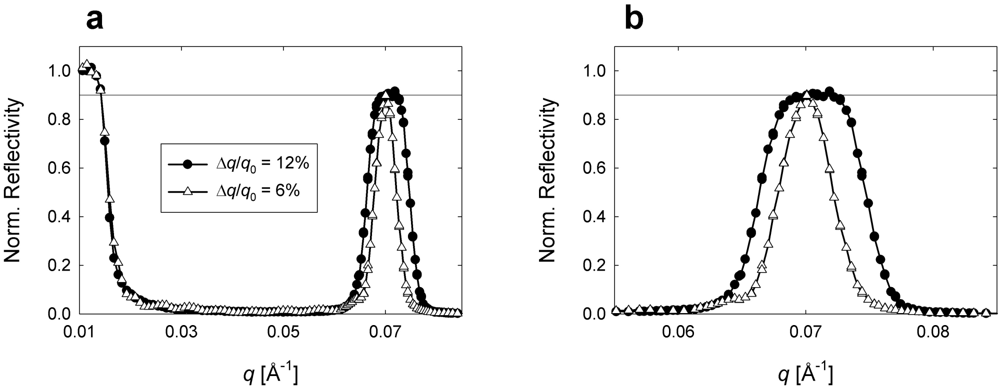

Figure 5.5: Normalised reflectivity of the two NiTi-supermirror monochromators measured at the cold neutron reflectometer Narziss at SINQ at the Paul Scherrer Institute. (a) The whole normalised reflectivity curve as a function of the momentum transfer q. (b) The peaks at 0.069 $Å^{-1}$ with a relative FWHM $\Delta q/q_0$ of 6% (white triangles) and 12% (filled circles) respectively and with a peak reflectivity of about 90% (horizontal line).

5.1.4. Neutron Monochromator

Two specially developed bandpass supermirrors with a length of 500 mm were produced to select a certain wavelength band of the incoming neutrons [Ay06]. The nickel titanium multilayers of the supermirrors are arranged such that the reflectivity peaks at $q_0 = 0.069$ $Å^{-1}$. The FWHM of the peak is 6% and 12%, respectively, while the peak reflectivity in the θ-2θ-scan was determined to be about 90% (compare Fig. 5.5). The angle θ_{m} and the reflected neutron wavelength λ_0 are linked via the relation:

$$\lambda_0 = \frac{4\pi}{q_0}\sin\theta_{\mathrm{m}} \tag{5.2}$$

Throughout all beam times, except the first one, the bandpass monochromator with $\Delta q/q_0 = 6\%$ was used.

5.1.5. $\pi/2$-Spin Flippers

Electrical and Mechanical Setup

Each of the two $\pi/2$-spin flippers consists of a matched radio frequency resonance circuit presented in Fig. 5.6, which is built into a brass housing. The inductance of the circuit, i.e. the coil, produces a rf field with the angular frequency ω perpendicular to the direction of the main magnetic field B_0. This rf field induces the spins of the passing neutron beam to turn, if the resonance condition $\omega = -\gamma_{\mathrm{n}} B_0$ is fulfilled. The process is similar to pulsed nuclear magnetic resonance, which is described in detail in Ref. [Sli96] (compare also *rotating frame*).

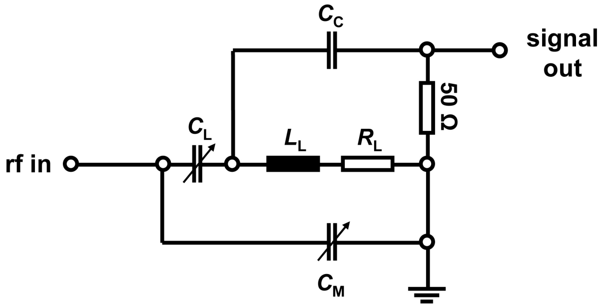

Figure 5.6: Scheme of the spin flipper resonance circuit. L_L and R_L are the inductance and the ohmic resistance of the spin flipper coil. C_L = 1...5 pF and C_M = 20...300 pF are the tunable capacitors and C_C serves as a coupling capacity to obtain a signal used for the feedback loop.

For the design of the spin flipper coils the following aspects needed to be considered:

- The size and the number of windings of the coil define the inductance. The size must be large enough to accommodate two partial neutron beams, while the inductance must be small enough to be able to tune the resonance circuit to the neutron Larmor frequency of about 73 MHz at 2.5 Tesla.

- The longitudinal length l of the coil in direction of the neutron beam affects the width of the background resonance curve of the Ramsey signal (compare Equ. (3.46) and section 5.1.8). It should be chosen as short as possible to obtain broad and non-distorted Ramsey signals, which can be fitted/analysed more accurate.

- On the other hand, the needed rf power for a $\pi/2$ flip is proportional to $(l \cdot \lambda_0)^{-2}$, leading for a few millimeter long coil and cold neutrons already to several watts of power. Hence, cooling of the coils as well as a proper choice of the material for the coil body and the windings is necessary.

Concerning the latter, we used silver coated copper wire and *Macor*® or PTFE for the coil bodies. During the beam times, two types of coils have been used:

- In the beam times two until six, we employed solenoid coils with a inner diameter of 11 mm and a nominal length of 7 mm, which produce a longitudinal rf field (along the y-axis, compare Fig. 5.2). The needed rf power for each spin flipper was about 5 W for 5 Å neutrons. A picture of one of these coils is presented in Fig. F.3. For more details see Ref. [Sch05].
  In the first beam time a similar but slightly smaller coil was used [Pie04, Abr733].

- In beam time seven, we aimed for a larger neutron beam cross-section. Therefore, flat box coils with the same length of 7 mm were chosen, which produce a rf field along the x-axis. Their cross-section is large enough to accommodate a neutron beam up to $20 \times 10\ \mathrm{mm}^2$. The needed rf power was between 20-25 W for 4.4 Å neutrons. A picture of one of these coils is presented in Fig. F.4a.

Each spin flipper (housing) is mounted on a support, which allows to precisely and reproducibly adjust the position of the flipper in all three dimensions (see Fig. F.4b).

Feedback Loop and Stability

The relative phase ϑ_{rf} and the individual rf field amplitudes B_1' and B_1'' of the two rf $\pi/2$-spin flipper coils are stabilised using a feedback loop, which is shown in Fig. 5.7. The rf signal of a signal generator is split into two branches by a 3 dB-splitter (*Minicircuits*® ZFSC-2-1). The signal in each branch passes an attenuator adjustable by means of a DC voltage (*Minicircuits*® ZMAS-1). The signal in branch one is then further attenuated to compensate the throughput loss of the controllable phase-shifter in branch two. Both signals then serve as inputs for two +50 dB rf power amplifiers feeding the matched resonant circuits of the spin flippers.

By capacitive coupling each spin flipper delivers a rf output signal. This allows us on one hand to determine the amplitudes of the oscillating magnetic fields using rf detector diodes. On the other hand the signal feeds a phase-detector, which produces a DC voltage proportional to $\sin \vartheta_{\mathrm{rf}}$. The three DC voltages, from the two diodes and the phase-detector, are permanently sampled by a data acquisition system, which controls the input voltages of the adjustable phase-shifter and the adjustable attenuators by means of a PID algorithm.

With this feedback loop the DC voltages corresponding to the field amplitudes (output lines 1 and 2 in Fig. 5.7) can routinely be held stable within better than ±0.2% for each spin flipper, while the DC voltage corresponding to the relative phase (output line 3 in Fig. 5.7) can be held zero within ±10 mV. By observing the phase of the Ramsey signal for systematically misadjusted settings for the amplitudes and the relative phase ϑ_{rf}, one can link these DC voltage stabilities to the phase stability of the Ramsey signal (see section 5.1.9). This leads to a conservatively estimated phase stability of the Ramsey signal, firstly of ±0.1° as a result of the stabilisation of ϑ_{rf}, and secondly of ±0.1° for each spin flipper due to the stabilisation of the oscillating field amplitude. This yields an overall stability of the Ramsey signal due to the spin flippers of about ±0.3°.

Spin Flipper Adjustment

At the beginning of an experiment, the resonance frequencies of the spin flippers have to be tuned to the neutron Larmor frequency in the static field, $\omega_0 = -\gamma_{\mathrm{n}} B_0$. Subsequently the amplitudes of the oscillating fields B_1' and B_1'' need to be adjusted separately such that each spin flipper turns the neutron spin by $\pi/2$. This is done by tuning the flipping ratio $FR = N_+/N_-$ to unity for one $\pi/2$-spin flipper, while the other $\pi/2$-spin flipper is turned off and vice versa (see Fig. 5.8). N_+ and N_- are the count rates for the adiabatic π-spin flipper of the beam line switched on and off, respectively.

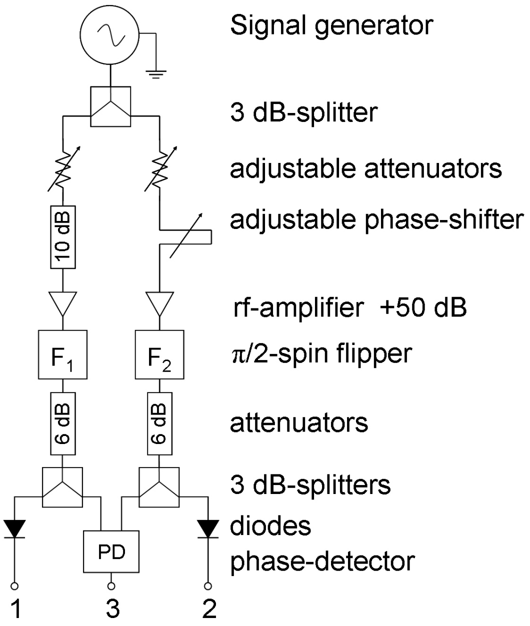

Figure 5.7: Feedback loop of the two rf $\pi/2$-spin flippers (F_1 and F_2). The loop stabilises the relative phase as well as the individual amplitudes of both flippers. The three output lines (1, 2 and 3) are continuously sampled by a data acquisition system and are used as a feedback to control the adjustable phase-shifter and the adjustable attenuators.

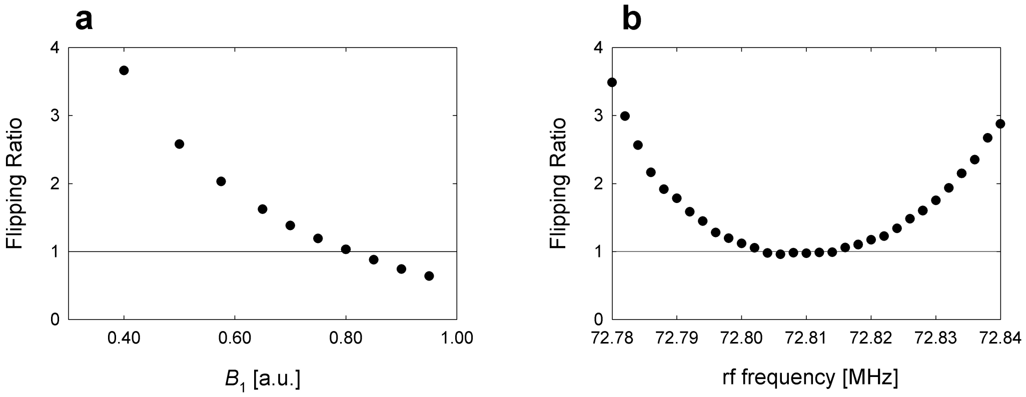

Figure 5.8: Neutron flipping ratio measurements to adjust the rf field of one solenoid $\pi/2$-spin flipper coil, with λ_0 = 5 Å. (a) A scan of the oscillating field amplitude B_1 at a steady frequency of 72.815 MHz. (b) A scan of the rf frequency for a fixed field amplitude B_1 =0.8 [a.u.]. The frequency where the flipping ratio has a minimum, here approximately 72.81 MHz, corresponds to the neutron Larmor frequency ω_0 in the steady magnetic field B_0 at the position of the rf coil.

5.1.6. Magnetic Field

A profile of the static magnetic field B_0 in the centre between the pole pieces along the neutron flight axis is presented in Fig. 5.9a. It was obtained using a vector field probe connected to a *LakeShore* 460 3-channel gaussmeter. The dips in the shape of the profile are caused by the specially shaped pole pieces of the magnet and help to fulfil the Ramsey condition given in Equ. (3.48). The spin flipper coils are located at $y \approx \pm 40$ mm and are separated by about 80 mm from each other.
Fig. 5.9b shows the deviation of the average field value as a function of the vertical position x. A deviation of only 10^{-4} Tesla (1 Gauss) on a flight length of 80 mm corresponds already to an additional phase shift of 100° for 5 Å neutrons. This obviously limits the size of the partial neutron beams in x-direction, as a too large beam causes that the phase coherence of the neutron spins is lost and the Ramsey signal smears out.
A similar field gradient is observed along the z-axis. In beam time seven, correction coils were used to correct for this linear magnetic field gradient (compare section 6.1.7). Fig. F.5 shows a photograph of correction coils mounted on the pole pieces of the magnet.

The magnetic field is continuously monitored by means of the proton resonance signal of a commercial NMR probe[7] operated at room temperature and placed in between the pole pieces of the magnet close to the sample position. Fig. 5.10a shows a typical histogram obtained during several hours of magnetic field stabilisation. The field of 2.5 Tesla can be kept constant within $\pm 1\ \mu$T using the monitored signal to regulate the current in the magnet. As visible from the simulated data in Fig. 3.4 signal oscillations have a period of $\Delta f \approx 8.5$ kHz. The field stability stated before corresponds to an uncertainty of the neutron Larmor frequency of ±30 Hz. Hence the phase stability due to the magnetic field is about $\pm 30\ \mathrm{Hz}/8.5\ \mathrm{kHz} \times 360° \approx \pm 1°$.

5.1.7. Neutron Analyser and Detector

To analyse the spins of the neutrons a remanent neutron bender is used.[8] A neutron bender consists of a stack of thin glass plates or wafers (substrate), which are sputtered on the front side with a magnetic coating and on the backside with an absorbing layer [Bön99, Kri04, Sen04]. The reflectivity of the magnetic coating is strongly spin-dependent, i.e. only neutrons with spin parallel to the magnetisation of the coating get reflected, while the others penetrate the substrate and get absorbed in the layer on the backside. The glass plates/wafers are slightly bent such that there is no direct sight through the bender and that any neutron which penetrates the bender has to get reflected at least once. The outgoing beam is typically bent by a few degrees with respect to the incoming neutron beam.
As detectors, we are employing two box shaped one inch high ^{3}He gas tubes, which were stacked onto each other and shielded from scattered neutrons by 5 cm thick plates of B_4C plastic. Each detector is directly coupled to a *Dextray* preamplifier ACHP96 and is supplied with a voltage of 950 V. Fig. F.6 shows a picture of the detector box.

---

[7] *http://www.drusch.com.*

[8] Swissneutronics: *http://www.swissneutronics.ch.*

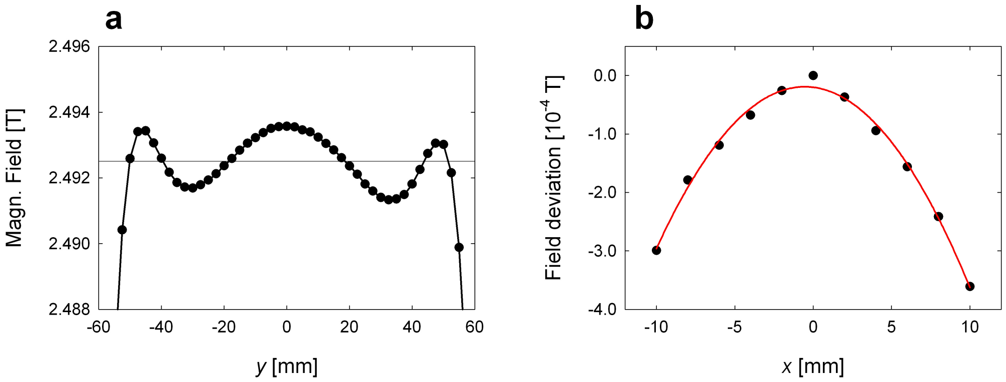

Figure 5.9: Magnetic field profile of the 2.5 Tesla magnet at 150 A. (a) Longitudinal field scan along the neutron flight path axis y (compare coordinate system in Fig. 5.2) in the centre between the pole pieces at $x = z = 0$ and average field value 2.4925 Tesla (horizontal line). (b) Reduction of the average field as a function of the vertical position x and parabolic fit.

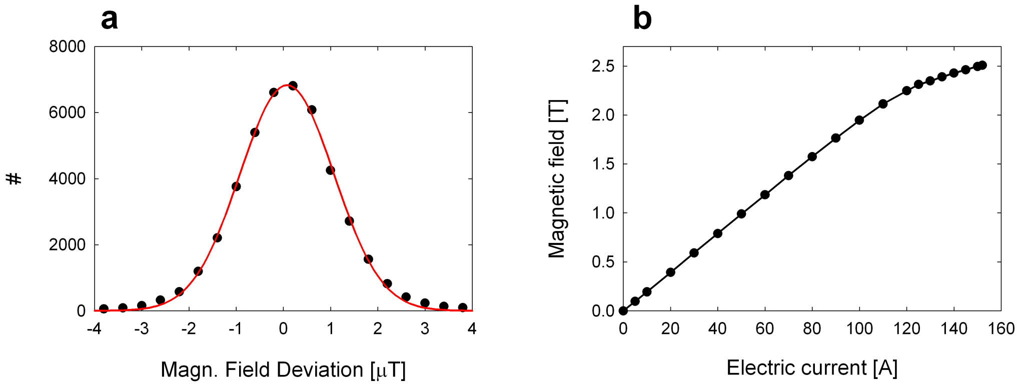

Figure 5.10: (a) Histogram of the deviation from the set value of the magnetic field and gaussian fit (red curve). (b) Magnetic field at the sample position as a function of the current provided by the magnet power supply.

5.1.8. Ramsey Frequency Scan

In Fig. 5.11a a typical Ramsey signal is shown, which was obtained with our setup by sweeping the frequency of the $\pi/2$-spin flippers in steps of 0.5 kHz from 72.75 to 72.87 MHz. Contrary to the simulated data shown in section 3.3, the neutron spin analyser in our setup absorbs the other spin component, which leads to an inversion of the Ramsey signal.

The quality of the measured Ramsey signals, with a signal-to-noise ratio of about 6 in the centre of the resonance, is very well suited to achieve a high precision in determining phase shifts. For that purpose it is more efficient to measure the centre part of the resonance rather than to sweep over the whole resonance. This saves measuring time without loss in precision. A scan of 21 data points with a frequency step size of 0.5 kHz samples more than one oscillation of the Ramsey signal and can be fitted using a simple sinusoidal fit, like presented in Fig. 5.11b. Instabilities have a minor influence on the accuracy of the phase extraction, because although the

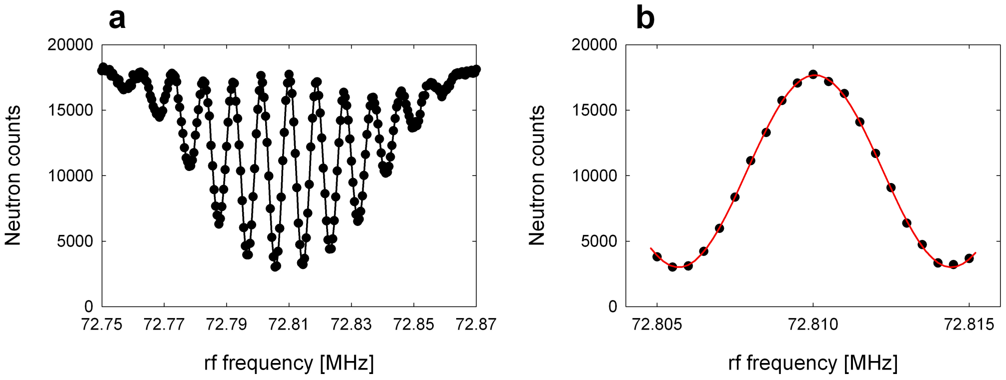

Figure 5.11: (a) Typical Ramsey resonance signal (frequency scan) measured with our setup without additional phase shift ($\varphi^* = 0°$) and with $\lambda_0 = 5$ Å. The measuring time for each data point was approximately 12 s. (b) Excerpt of the complete Ramsey signal shown in (a). The sinusoidal fit (red curve) on the 21 data points delivers a value of $\Delta f = (8.74 \pm 0.03)$ kHz for the period and of $\varphi = (-87.5 \pm 0.4)°$ for the phase with respect to 72.81 MHz.

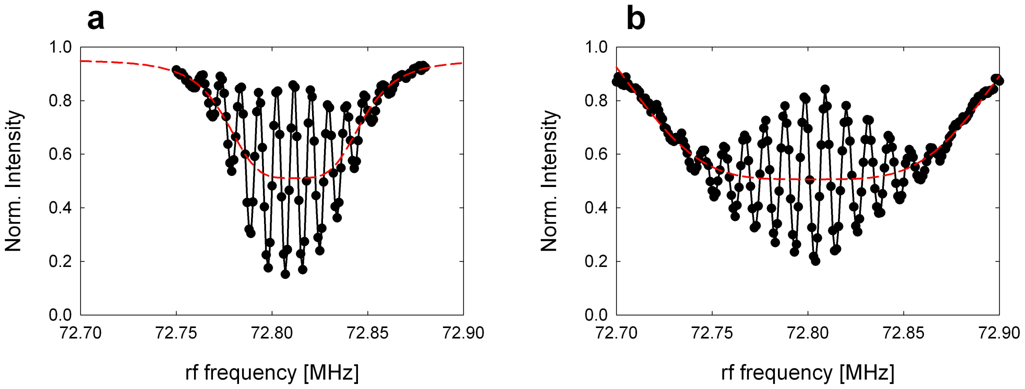

Figure 5.12: Effect of different spin flipper coils on the envelope of the Ramsey signals. The red dashed lines are fits to the background resonance curve using a heuristic fit function. (a) Solenoid coil with a length of 7 mm using 5 Å neutrons. FWHM of the background resonance is about 70 kHz. $\Delta f \approx 9.0$ kHz. (b) L-shaped flat box coils of the same length using 4.4 Å neutrons. FWHM of the background resonance is about 160 kHz. $\Delta f \approx 10.6$ kHz.

individual data point might scatter statistically with ±1°, for a whole set of 21 data points this reduces by a factor $\sqrt{21}$, i.e. to a statistical uncertainty of only ±0.2°.

Fig. 5.12 demonstrates the effect of the length of the spin flipper coils on the shape of the the Ramsey signal. The Ramsey signal obtained with the solenoid coil of length 7 mm is presented in Fig. 5.12a. A comparison with simulated data reveals that the period of the Ramsey oscillations of $\Delta f \approx 8.74$ kHz is close to the expected value of about 8.5 kHz, whereas the width of about 70 kHz of the background resonance curve is much narrower than the FWHM of about 128 kHz expected according to Equ. (3.46). This might be due to the fringe fields extending out of the coils along the beam path, resulting in an effective coil length l_{eff} of about 12 mm. Fig 5.12b presents a much broader Ramsey signal originating from beam time seven using the flat box coils with the same length of 7 mm. Here, the width of the background resonance of approximately 160 kHz corresponds to $l_{\text{eff}} = 6.3$ mm, which is close to the actual value.

As already mentioned in section 5.1.5, the necessary power per spin flipper is approximately 4 times larger for the flat box coils compared to the solenoid coils. This is in good agreement with the fact that its effective length is about half.

5.1.9. Two Beam Method and Phase Stability

The accuracy of the phase measurement can be strongly improved, if one analyses simultaneously two separate beams passing through the Ramsey apparatus. By subtraction of the phases measured for each of the beams, a common phase drift can be efficiently removed, as it might for instance be caused by day-night temperature changes in the experimental hall. Therefore, the already well collimated incident beam is split into two partial beams, which are detected behind the spin analysing bender by the two ^{3}He-gas detectors: an upper beam passes through the sample, whereas a lower beam serves as a reference passing by the sample. The splitting is achieved by exchangeable apertures, which are mounted on the entrance of the first and on the exit of the second spin flipper box. It turned out to be practicable to use 2 mm thick square cadmium plates (30×30 mm^2), which are slided in a frame mounted on the spin flippers, to achieve reproducible results. Additionally, another beam aperture made from sintered ^{6}Li powder is placed right in front of the sample inside the target cell of the cryostat. Three apertures with different shapes have been used, which are presented in Fig. 5.13. In the following the nomenclature introduced in the figure capture will be used (α, β and χ).

The mixing of the beams thus could be kept below 1%. Simulations show that in the worst case of a 90° phase difference between the two beams, this would lead to a phase shift of about 0.6° in the Ramsey signals of both partial beams, assuming they have the same intensity. The beam mixing was measured by comparing the background corrected count rate in the detector of one beam with and without covering its hole in the first beam splitting diaphragm.

Employing this two-beam method a long measurement was performed to test the stability. We repeatedly measured Ramsey signals during almost 24 hours, like the one shown in Fig. 5.11b. The individual phase of each beam and the phase difference was then determined. Fig. 5.14 shows that indeed the phases of the individual beams

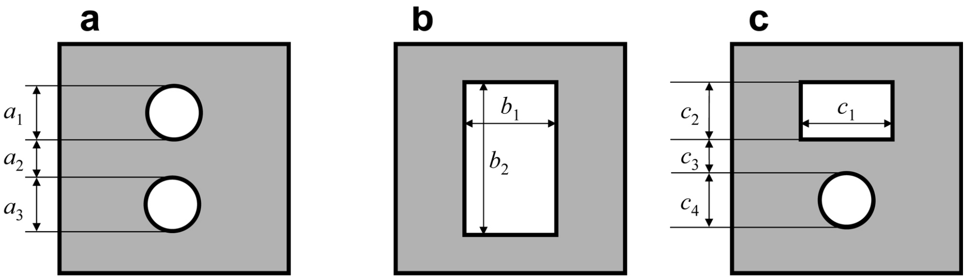

Figure 5.13: All three types of beam apertures used for beam shaping. (a) Double circular aperture with the following notation (lengths are given in millimeters): $\alpha_k(a_1, a_2, a_3)$. (b) Rectangular aperture: $\beta_k(b_1, b_2)$ and (c) rectangular and circular aperture: $\chi_k(c_1, c_2, c_3, c_4)$. The index $k \in \{1, 2, \mathrm{s}\}$ specifies whether the aperture is mounted on spin flipper 1, 2 or in front of the sample.

exhibit a common drift, leading to a constant phase difference, which scatters around the mean value by ±0.36°, while the average length of the error bars, occurring only from the sinusoidal fit, is 0.65°. The two jumps in the phase difference at the end of the whole run, each of about 2°, were caused by an intentional drastic increase of the oscillating field amplitude of the first spin flipper, first by 6% and then by 12%.

As expected, changes in the relative phase ϑ_{rf} of the spin flippers lead to jumps in the individual beam phases, but have no influence on the phase difference. This was tested, while during the time from the third to the fifth hour the set value of the DC voltage for the relative phase of the spin flippers was intentionally misadjusted three times from 0 V to +0.5 V, -0.5 V and +1.0 V and finally back to 0 V (output line 3 in Fig. 5.7). More extensive studies showed that a change of this set value delivers equal-sized phase shifts in both beams by $(8.1 \pm 0.1)°/\mathrm{V}$. Note that the measured stability of ±10 mV given in section 5.1.5 then corresponds to a stability of better than ±0.1°.

The absence of an effect in the phase difference plot demonstrates the power of the two-beam method, which was already successfully employed in a measurement of the incoherent scattering length of ^{3}He [Zim02].

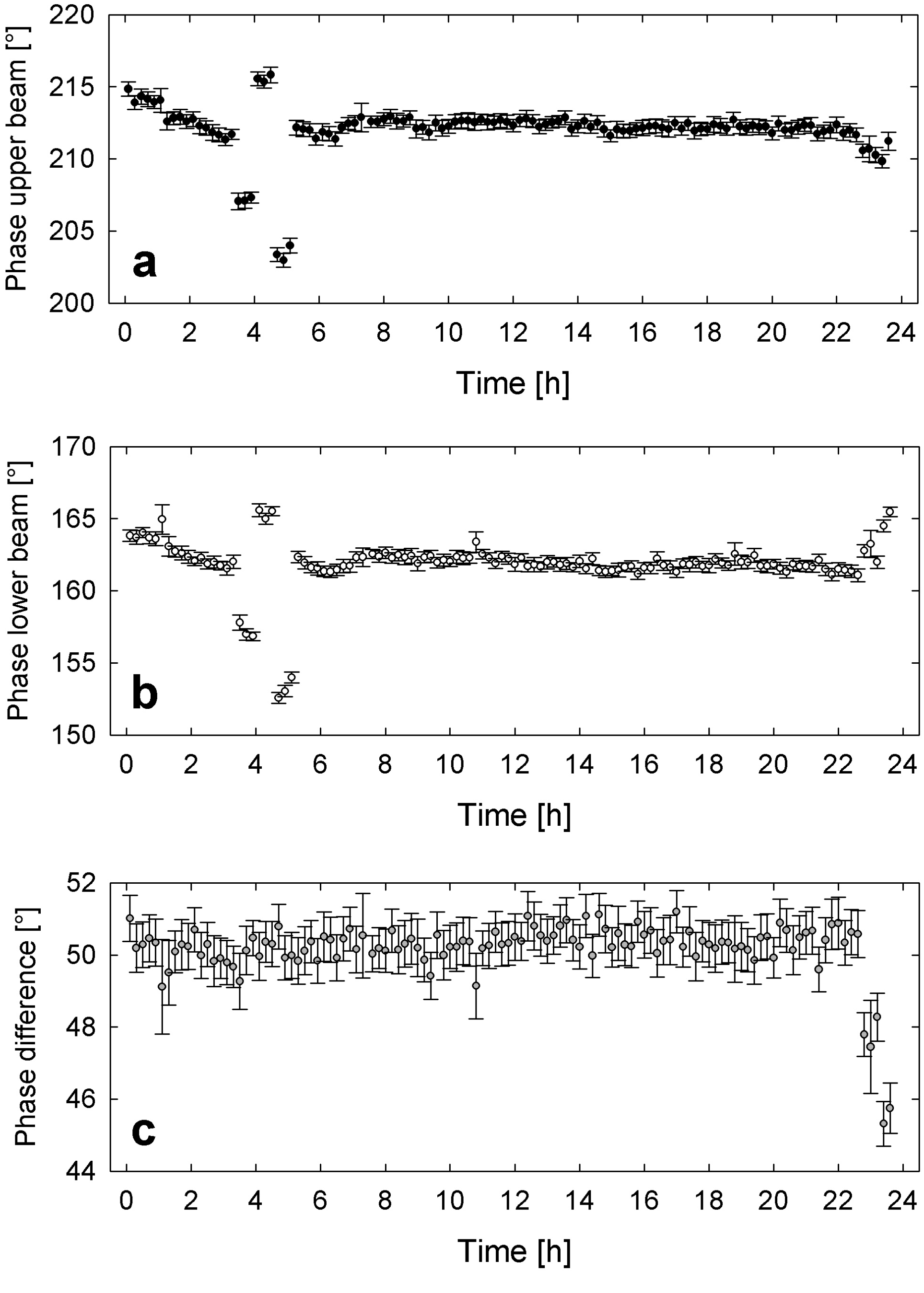

Figure 5.14: Demonstration of the phase stability of the Ramsey setup. Plot (a) and (b) show the individual phases of the upper and the lower neutron beam measured continuously over almost 24 hours. Plot (c) shows the phase difference of the two beams. The jumps in the individual beam phases and the phase difference from the third to the fifth hour and at the end of the measurement run are due to intentional misadjustments of the spin flippers. For the reason of visibility only every second measured point is plotted.

5.1.10. Phase Shift Retrieval

In this section an example is presented, which shows how the pseudomagnetic precession angle φ^* due to polarised nuclear spins is actually determined.

The considered sample consists of deuterated polystyrene with a thickness of 1.2 mm and a degree of deuteration of about 97% (sample #14, compare appendix E). Using the technique of dynamic nuclear polarisation[9] proton (deuteron) polarisations of about 40% (20%) are achieved. Inserting these polarisation values and sample properties in Equ. (3.38) yields a pseudomagnetic phase shift of approximately $\varphi^* = \varphi^*_\mathrm{p} + \varphi^*_\mathrm{d} \approx 550^\circ + 1650^\circ = 2200^\circ$ for 5 Å neutrons.

Fig. 5.15a shows the corresponding Ramsey signals for the unpolarised and dynamically polarised sample. The latter has a damped amplitude due to the large pseudomagnetic shift and possible polarisation inhomogeneities of the nuclei in the sample [Bra061]. Due to asymmetric signal envelopes of the Ramsey oscillations at such large phase shifts (compare simulations in Fig. 3.5), it can be advantageous not to apply a simple sinusoidal fit as previously used in section 5.1.8, but the following function:

$$\zeta(\omega) = \zeta_0 + \zeta_1 \cdot \sin\left(\frac{\omega}{\Delta f} - \varphi\right) \cdot (1 + \zeta_2 \cdot \omega + \mathcal{O}(\omega^2)) \ , \tag{5.3}$$

where ζ_2 is the first order coefficient of an expansion describing the signal deformation. Careful comparisons between the two fit functions (sinusoidal and $\zeta(\omega)$) show that the resulting value for the phase shift is equal within the errors of the fits, but that χ^2 is smaller for $\zeta(\omega)$ (here: $\chi^2_\zeta < 2$).

Using the fit function given in Equ. (5.3) to fit the two signals in Fig. 5.15a delivers two slightly different periods of the Ramsey oscillations: Δf_unpol = 8.82 kHz and Δf_pol = 8.89 kHz. In order to determine the phase shift, one therefore has to define the period to a common fixed value Δf_fixed prior to the fit of both signals. Fig. 5.15b demonstrates that the relative phase shift of the sample beam $\Delta\varphi_\mathrm{sample} = \varphi_\mathrm{sample,pol} - \varphi_\mathrm{sample,unpol}$ is almost unaffected by the choice of Δf_fixed and that the fit error becomes minimal around Δf_fixed = 8.85 kHz.

For the signals shown in Fig. 5.15a the relative phase shift is $\Delta\varphi_\mathrm{sample} = (-29.2 \pm 0.6)^\circ$ for the sample beam and $\Delta\varphi_\mathrm{ref} = (+10.7 \pm 0.3)^\circ$ for the reference beam (not shown), which passes by the sample. The total pseudomagnetic phase shift is given by

$$\Delta\varphi_\mathrm{total} = n \times 360^\circ + \Delta\varphi_\mathrm{sample} - \Delta\varphi_\mathrm{ref} \ , \tag{5.4}$$

where n can either be determined by successive destruction of the nuclear polarisation employing saturating radio frequency pulses or by nuclear polarisation decay (compare Fig. 5.16 and Fig. 6.3b in section 6.1). In this case $n = 6$, which leads to $\Delta\varphi_\mathrm{total} = (2120.1 \pm 0.7)^\circ$, where the relative accuracy of 4×10^{-4} is only due to the fit error.

Besides the fit, one has to take into account errors caused by the following sources:

- The phase stability of the Ramsey apparatus of ±0.36° (see section 5.1.9).
- The beam separation/mixing, leading in the worst case to be ±0.6° × 2 (also section 5.1.9), where the factor two takes into account that the beam mixing produces phase shifts in the sample and the reference beam.

---

[9] Compare later in section 5.4.

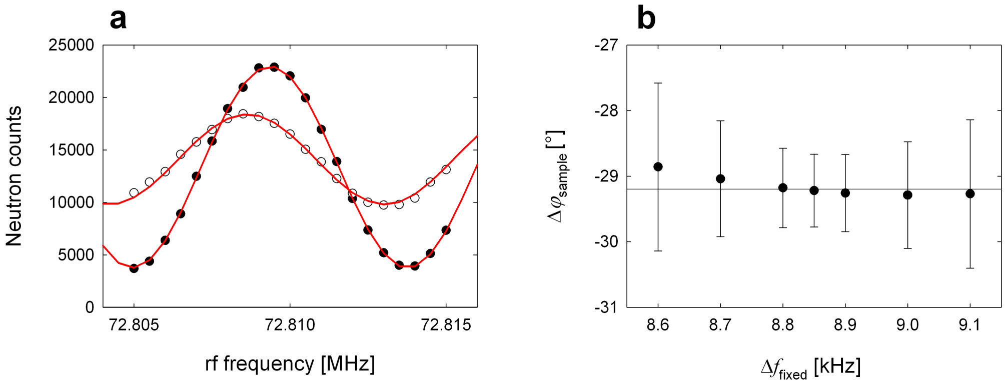

Figure 5.15: a) Ramsey signals for an unpolarised sample (●) and a polarised sample leading to a phase shifted and damped signal (○) with the corresponding fits using Equ. (5.3) (red curves). b) Dependence of the relative phase shift in the sample beam for different fixed values of the Ramsey oscillation period Δf_{fixed}. The horizontal line marks a relative phase shift of -29.2°.

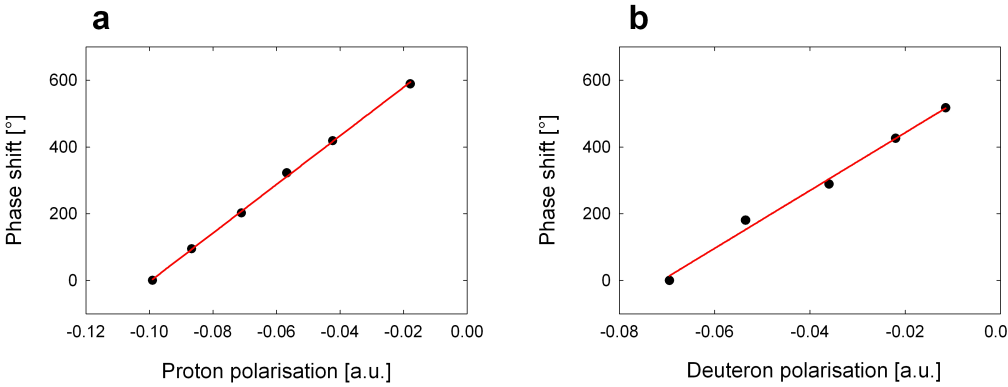

Figure 5.16: Example measurement to demonstrate the phase shift of the Ramsey oscillation signal caused by successive destruction of the negative nuclear spin polarisation. The points of zero phase shift have been set arbitrarily. (a) Phase shift as a function of the proton polarisation at constant deuteron polarisation ($J_{d,16} = -0.10$ [a.u.]) with linear fit (red line). (b) Phase shift as a function of the deuteron polarisation with totally destroyed proton polarisation.

- The nuclear polarisation relaxation during the measurement of the Ramsey signal, which in this case leads to a signal drift of about 18°/h (compare section 6.1.5 and 6.1.6). This yields an additional systematical error of about ±1.5°, for a measurement time of 10 minutes per Ramsey signal consisting of 21 points. This error can be entirely attributed to the sample and is independent of the Ramsey apparatus.

One thus obtains a total phase shift of $\Delta\varphi_{\text{total}} = (2120.1 \pm 0.7_{\text{ fit}} \pm 0.4_{\text{ stab}} \pm 1.2_{\text{ beam}})^{\circ}$, with three separate contributions to the error.[10] Hence, the relative accuracy of the phase shift retrieval is approximately 10^{-3}, which just corresponds to the aimed precision stated in section 3.4.

---

[10] At this point we are only interested in the accuracy of the Ramsey apparatus and therefore omit the signal drift error caused by the nuclear spin relaxation.

5.2. The Frozen Spin Polarised Target

To observe the spin-dependent interaction of the neutron with a nucleus, it is necessary that not only the neutron spins but also the nuclear spins are oriented. They are localised in a so-called *polarised target*. Polarised targets are common tools in high- and low-energy physics to investigate spin-dependent interactions with beams of particles or nuclei. Polarised targets can either be gaseous or solid. The manner of polarisation of the nuclear spins depends on the used target material.

In the nd-experiment we polarise the spins of the protons and deuterons in deuterated organic substances (e.g. frozen alcohols, polystyrene etc. - see section 5.2.4) with implemented *paramagnetic centres* by means of the so-called *dynamic nuclear polarisation* technique (DNP - see section 5.4). This technique utilises the fact that at low temperatures and high magnetic fields the electrons of the paramagnetic centres are polarised to almost 100%, due to their large gyromagnetic ratio. By irradiation of microwaves close to the electron paramagnetic resonance frequency (EPR) the electron spin polarisation can be transfered to the nuclear spins.

When the DNP process, i.e. the irradiation of microwaves, is stopped the nuclear polarisation relaxes again to its low thermal equilibrium value. The characteristic time T_1 of this relaxation depends strongly on the ratio of the external magnetic field and the sample temperature B_0/T. For large magnetic fields of about 2.5 Tesla and at dilution refrigerator temperatures, T_1 can exceed 100 hours [Bra00]. Hence, the nuclear polarisation can be considered constant or "frozen" on a time scale much shorter than T_1 – *frozen spin target*.

5.2.1. The Dilution Refrigerator

The dilution refrigerator for the nd-experiment has to fulfil the following necessary requirements:

- The sample/target has to be at temperatures of about 100 mK to obtain nuclear spin relaxation times long compared to the measuring time of a neutron Ramsey signal.
- The sample must not be located in the mixing chamber of the dilution refrigerator as neutrons are strongly absorbed in liquid ^{3}He.
- The cooling power must be large enough to allow to irradiate microwaves with several milliwatts of power on the sample.
- The outer dimensions of the cryostat must fit between the pole pieces of the magnet of the Ramsey setup, which are separated by a distance of about 48 mm.

A special refrigerator had to be designed and built, to meet these constraints. Its shape and features were optimised for the nd-experiment, whereas the design of the cryostat inserts follows previous dilution refrigerators developed and constructed by the *Sample Environment and Polarised Targets Group* of PSI [Bra90].

Cryostat

As already mentioned in Ref. [Bra90], the design of the presented cryostat and the dilution insert is essentially based on the ideas of Roubeau and co-workers [Rou76, Rou78]. A cutaway view of the cryostat for the nd-experiment ("*nd-cryostat*") is presented in Fig. 5.17. It consists of a specially shaped aluminium vacuum vessel with a cylindrical nose with a diameter of only 46 mm at the lower end. In its centre a thin walled stainless steel tube ("*centre tube*" - upper part: 50 × 49 mm, lower part: 43 × 42 mm) is situated, where the dilution insert firmly fits into. Its upper part is surrounded by an annular liquid ^{4}He bath and cold helium vapour. The bath is refilled automatically via a siphon in intervals of about 15-20 min. Thus, the liquid helium level of the bath is kept stable in a range of ±3 cm. By pumping through a needle valve just above the bottom of the bath, the temperature of the lower part of the bath is brought to 2.17 Kelvin, while the surface remains at 4.2 Kelvin.[11] This configuration allows to have a helium bath, which can be refilled from the top at about 1 bar from a liquid helium dewar and to maintain a low enough temperature to condense the ^{3}He/^{4}He mixture. In case of blocking of the needle valve, the 2 Kelvin pumping tube can be easily removed, cleaned and reinstalled during continued operation of the cryostat.

In the isolation vacuum of the cryostat, two vapour-cooled radiation shields are attached to the neck of the helium bath and a third radiation shield is thermally anchored to the centre tube at the height of the still. At the bottom of the tube a cylindrical heat exchanger transfers the heat/cold from the mixing chamber to the mounted target cell. ^{4}He is condensed into the cell via two capillaries[12], which are connected to a gas vessel at room temperature. The capillaries are introduced in the cryostat through the helium bath and are soldered to the lower part of the centre tube.

Also the cables for the NMR system pass through the helium bath. Connectors at the bottom of the bath and at the top of the target cell ("*spider*", see Fig. F.8) allow to feed the NMR signals through the isolation vacuum to the sample in the cell.

Another description of the target cell and the heat exchanger can be found in Ref. [Bra092].

Dilution and Microwave Insert

A drawing of the cryostat inserts is presented in Fig. 5.18. The *dilution insert* consists of a top flange with three o-rings, an upper gas-gas heat exchanger where the incoming helium condenses, a flow impedance (needle valve), a lower liquid-liquid heat exchanger with a secondary flow impedance and two step heat exchangers, and a mixing chamber. The upper and lower heat exchangers have axial openings for the microwave insert, which is described below.

The gas-gas heat exchanger is made out of three thin walled stainless steel tubes, which are axially aligned: a through-going tube (28.6 × 27.8 mm) to guide the microwave insert, the upper tube (43 × 42 mm) and a lower tube (38 × 37 mm). In between the upper and the through-going tube five copper baffles are inserted. On the outside of the upper tube a 10 m long capillary (3 × 2 mm) and on the outside

---

[11] This is due to the fact that the helium density has a maximum at 2.17 Kelvin (compare Fig. 4.3).

[12] 1.1×0.5 mm filled with a wire of 0.4 mm in diameter, reaching a ^{4}He gas flow of 6 ml/min each at 1 bar pressure difference and 300 Kelvin.

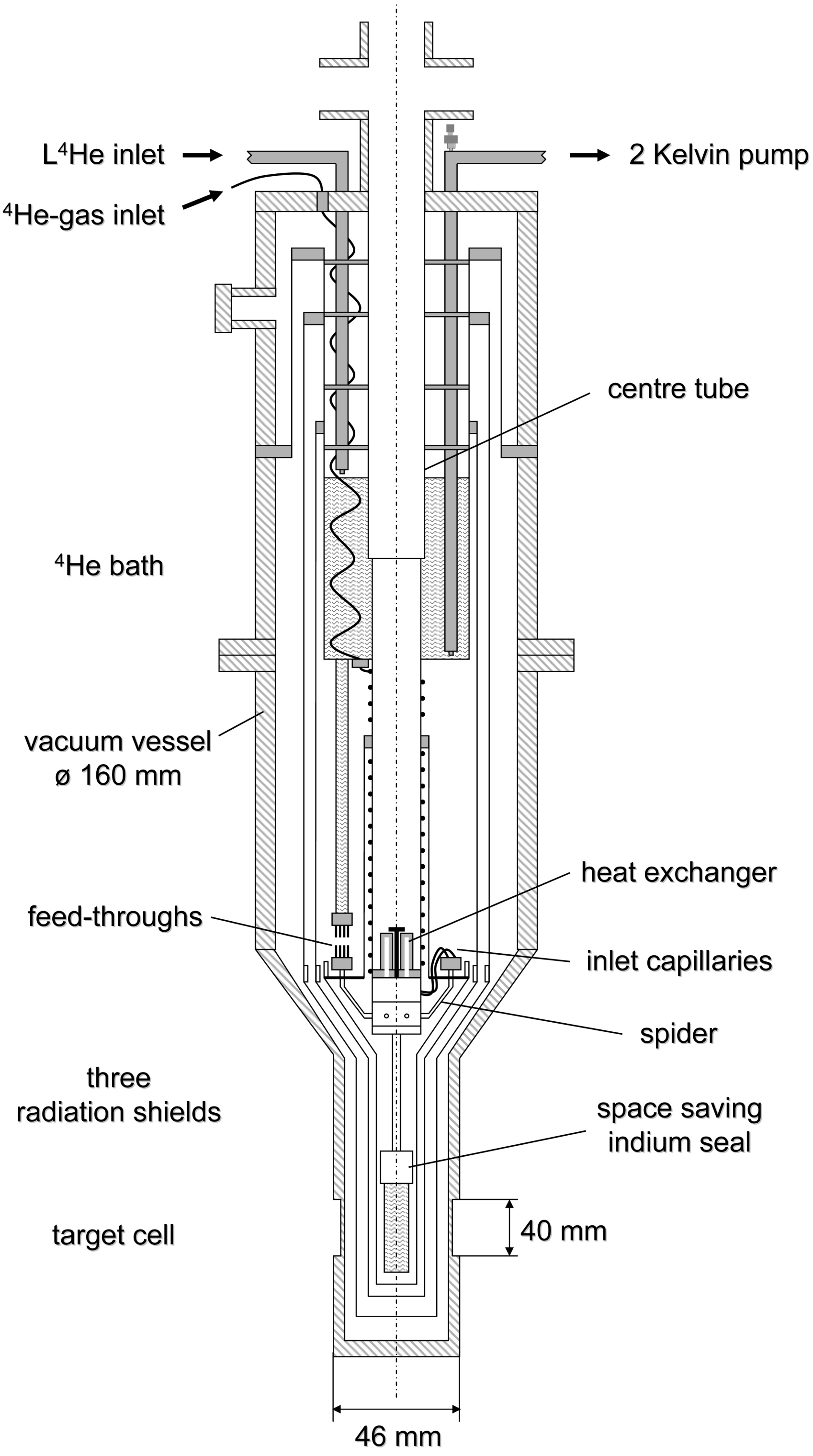

Figure 5.17: Scheme of the cryostat for the nd-experiment. See also Fig. F.7, F.8 and F.9 in the appendix. Illustration is not to scale.

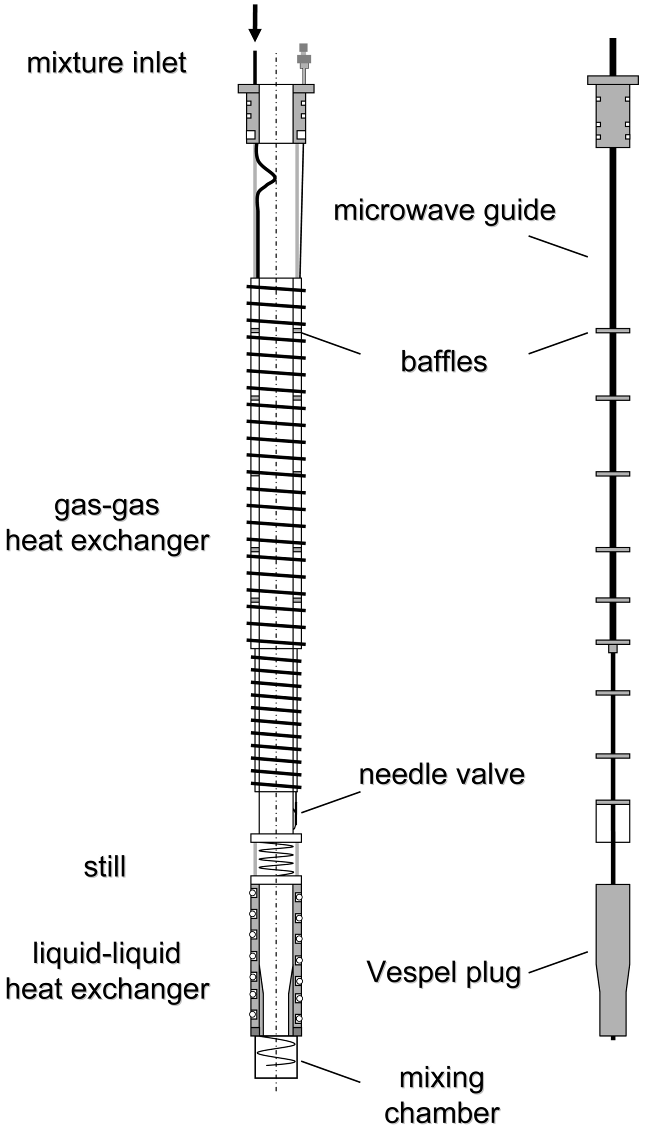

Figure 5.18: Cryostat inserts. Left: dilution insert, which fits in the centre tube of the cryostat. Right: microwave insert with several brass baffles and a conical Vespel plug. Compare Fig. F.10 and F.11 in the appendix. Illustration is not to scale.

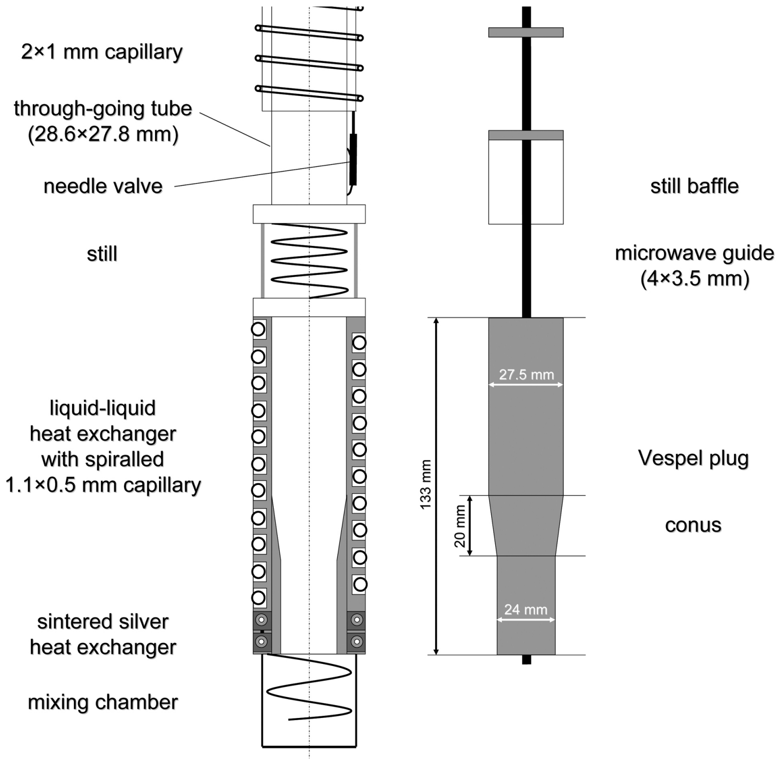

Figure 5.19: Detail of the lower part of the cryostat inserts. Compare Fig. F.11a. Illustration is not to scale.

of the lower tube a 5 m long capillary (2×1 mm) are soldered, through which the condensing gas is led downwards.

A detailed view of the liquid-liquid heat exchanger is shown in Fig. 5.19. It consists of a spiralled capillary (1.1×0.5 mm, about 15-20 m long) placed in a helically grooved Vespel bobbin with an outer diameter of 42 mm. Two sintered step heat exchangers are situated at the end of the capillary. They are made from silver plated stainless steel tubes, which were circularly bent. Silver powder has been sintered inside and outside the tubes [Bra90].

Hence, the liquid helium in the capillary flows downwards through the step heat exchangers into the mixing chamber and then upwards on the outside of the mixing chamber, passing the spiralled capillary. Note that the dilution insert is surrounded by the firmly fitting centre tube of the cryostat. The total amount of mixture is adjusted in such a way that the liquid level is located at the 40 cm^3 space above the Vespel plug, *the still*.[13]

The *microwave insert* depicted in Fig. 5.18 consists of a small top flange with three o-rings for hermetic sealing, which fits into the top flange of the dilution insert. Two stainless steel tubes (upper part: 6.3×6.0 mm and lower part: 4.0×3.5 mm) are used as a microwave guide and as a mechanical support for several brass baffles. The lowest baffle (still baffle) is preventing a helium film to flow up the through-going tube of the dilution insert. On the lower part of the insert a Vespel plug with a 5° conus seals the

---

[13] The flow rate of helium gas through the entire system of capillaries of the dilution insert with totally opened needle valve was measured to be 25 ml/min at room temperature and at a pressure difference of 1 bar between the gas inlet and outlet.

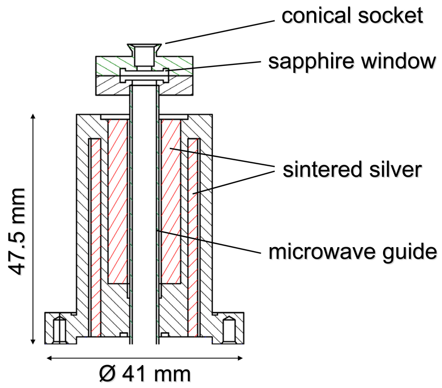

Figure 5.20: Cutaway view of the cylindrical heat exchanger between the mixing chamber and the target cell.

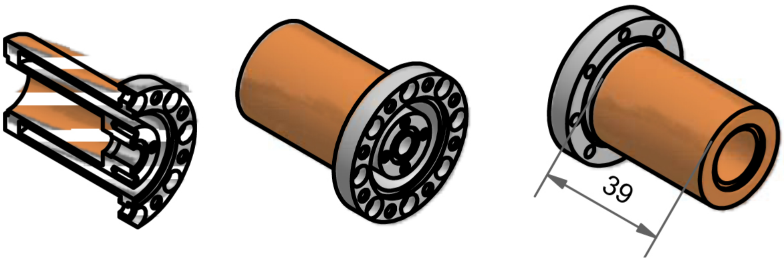

Figure 5.21: Drawings of the heat exchanger made from a copper-stainless steel friction-weld, without the sintered silver powder and the microwave guide.

axial hole in the liquid-liquid heat exchanger of the dilution insert.
The microwave guide is filled with a tightly fitting 30 cm long PTFE rod ("*Teflon spaghetti*") to suppress film flow, which can cause a considerable heat input. On the room temperature end of the insert the guide is sealed with a thin PTFE foil.

Heat Exchanger

The mixing chamber and the target cell are thermally connected by the already mentioned specially designed vertical, coaxial heat exchanger. It is made from a cylindrical friction-weld from stainless steel (the flange part) and copper (the thermal part) with silver powder sintered on both sides in annular, spark eroded groves: 20.6 g silver powder on the mixing chamber side and 27.7 g on the target cell side [Bra092].[14]
A conical socket is attached to the top of the heat exchanger, which serves to accommodate the lower part of the microwave guide of the microwave insert. Hence, the microwaves can be transfered from outside the refrigerator at room temperature directly into the target cell to the sample, only passing through a sapphire window, which separates the mixing chamber from the target cell.
Drawings of the heat exchanger are shown in Fig. 5.20 and 5.21, while a photograph is presented in Fig. F.11c in the appendix.

---

[14] XRP5 flakes, CLAL, 13, rue de Montmorency, 75139 Paris (France).

Cool Down Procedure

The following steps describe the cool down procedure of the nd-cryostat:

1. The dilution and the microwave inserts are inserted through the access at the top of the cryostat into the centre tube and the centre tube is evacuated using the pumping set described in section 5.2.3.

2. A turbo pump provides a sufficient isolation vacuum ($< 10^{-5}$ mbar).

3. The target cell is flushed with helium gas for 12 hours, to prevent blocking of the capillaries during the cool down.

4. A small amount of ^{4}He gas is admitted in the centre tube to provide thermal contact between the inserts and the rest of the cryostat.

5. The transfer of liquid ^{4}He into the helium bath can be started. It is filled for the first time after about one hour and after approximately 24 hours the whole system is thermalised to 4.2 Kelvin.

6. The contact gas in the centre tube is pumped out and the pumping on the helium bath can begin (2 Kelvin stage).

7. The condensation of the ^{3}He/^{4}He mixture and of the ^{4}He gas in the target cell is started (compare Fig. 5.24).

8. Circulation is started and the residual mixture is pumped into the system using a hermetic auxiliary pump.

9. The fraction of ^{3}He in the mixture is adjusted by distillation, until the phase boundary is at an optimal position in the mixing chamber.

10. Starting from room temperature, a base temperature of about 85 mK in the mixing chamber can be reached within 30 hours.

Target Cell and Sample Holder

In Fig. 5.22 the sample holder and the target cell are sketched. The sample holder is made from a PTFE cylinder with a diameter of 16 mm and a length of about 40 mm. A slit in its face side allows to place a 2 mm thick ^{6}Li aperture directly in front of the target ("*target aperture*"). The target is held by the sample frame, which also serves as a support for the NMR coils. It is inserted from the side into a central slit in the cylinder and is fixed to the sample holder by two tiny PFTE rods, such that it is located approximately in the centre of a volume enclosed by a saddle coil. This saddle coil consists of 2×2 windings and is used to destroy the nuclear polarisation in the target. The sample holder is mounted to an aluminium microwave horn, which itself is screwed to the end of the microwave guide.
The target cell, which encases the sample holder, is sealed with indium against the isolation vacuum and is specially designed to conserve the maximum radial space. It is made from an aluminium-stainless steel friction-weld with an inner (outer) diameter of 18 mm (19 mm).
To correctly adjust the position of the sample between the pole pieces of the magnet, the whole cryostat is mounted to a lifting apparatus (see Fig. F.9), which can be adjusted with a precision of 0.1 mm in height. This is necessary, as the inside of the cryostat is shrinking during the cool down by approximately 1.5 mm. This can be seen on the neutron radiography images presented in Fig. 5.23. They show that the position of the target aperture ($\chi_s(8,7,4,5)$ - compare Fig. 5.13) moves slightly up when the cryostat temperature drops from 300 Kelvin to 4 Kelvin. In the images the upper rectangular beam spot corresponds to the sample beam, while the lower circular beam spot is the reference beam (compare section 5.1.9).

Condensation of ^{4}He into the Target Cell

In Fig. 5.24 the process of helium gas condensation into the target cell is displayed in two time histograms. A 66 litre helium gas vessel is connected to the target cell via a liquid nitrogen cooled cold trap to prevent blocking of the capillaries. After admitting helium to condense the temperature in the cell immediately drops from 460 mK to about 390 mK. This is caused by the cooling by a superfluid film as described in Ref. [Bra96]. Afterwards the temperature gradually drops until after 5 hours the whole cell is filled with liquid helium. The total amount of condensed ^{4}He corresponds to 1.3 mol.
The remaining temperature difference between mixing chamber and cell is approximately 25 mK, with $T_{\mathrm{m}} \approx 85$ mK and $T_{\mathrm{c}} \approx 110$ mK. Note that firstly, the temperature difference depends on the temperature, due to the thermal conductivity of liquid helium[15] and secondly, the temperature in the mixing chamber is almost independent whether the target cell is filled with helium or not.
Throughout calibrated ruthenium oxide thermometers were used.[16]

---

[15] Compare section 4.3.1 and Fig. 4.7.

[16] *Scientific Instruments* RO-600 series.

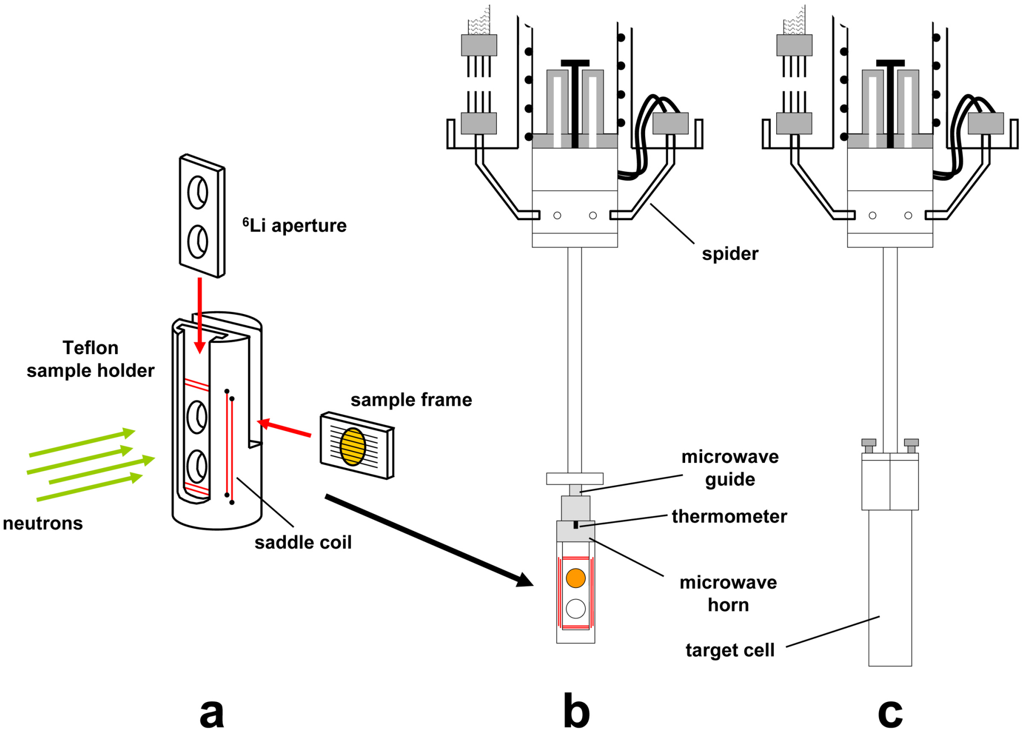

Figure 5.22: (a) Cylindrical sample holder with sample aperture, sample frame and a saddle coil. (b) Lower part of the nd-cryostat. The sample holder is mounted to the end of the microwave guide. (c) The sample volume is closed with the target cell (also microwave cavity). Compare Fig. F.13 in the appendix. Illustration is not to scale.

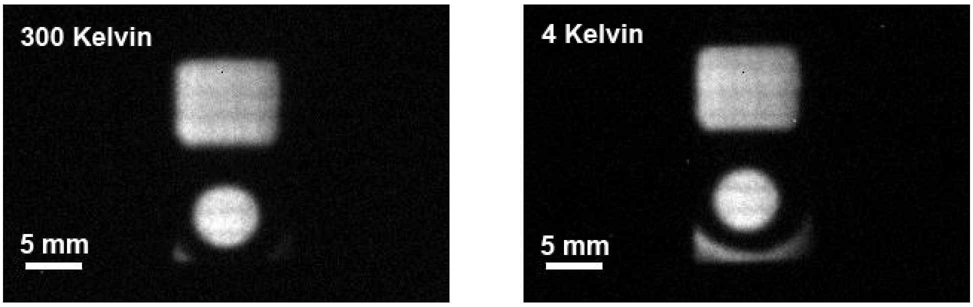

Figure 5.23: Neutron radiography of the target cell before and after the cool down of the refrigerator taken in the seventh beam time. A neutron CCD-camera [Müh05] was placed approximately 30 cm behind the nose of the cryostat. The exposure time was about 2 min using 4.4 Å neutrons. The vaguely visible horizontal lines are caused by the coil windings of the spin flipper.

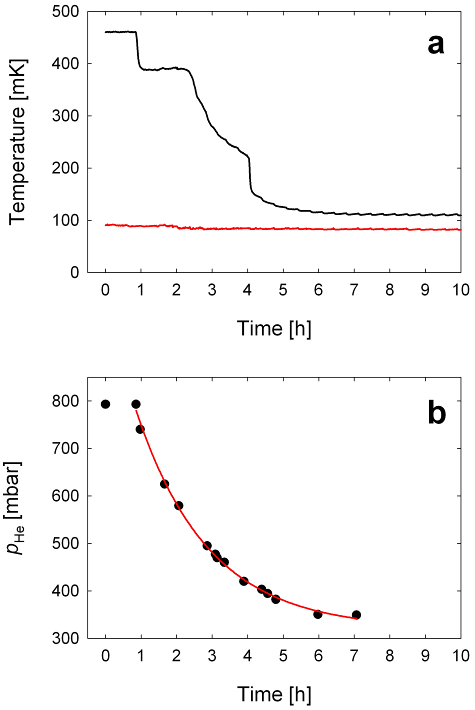

Figure 5.24: (a) Time histogram of the temperature in the mixing chamber (red curve) and in the target cell (black curve). After one our ^{4}He gas was admitted to the cell. The ripples in the curves are caused by the refill cycle of the helium bath. (b) Corresponding time histogram of the pressure in the helium gas vessel connected to the cell and exponential fit (red curve) - decay time: (128 ± 7) min.

Cooling Power and Performance

The cooling power of the dilution refrigerator is given in Fig. 5.25a. The dilution insert was tested with two different cryostats: the nd-cryostat presented in Fig. 5.17 and a laboratory cryostat without a target cell attached to the mixing chamber. In the latter case the volume occupied by the heat exchanger was filled with a cylindrical dummy made from PTFE. The reached base temperature for the laboratory cryostat is 60 mK, whereas for the nd-cryostat it is about 85 mK. Both heating curves have been taken for the same still power $\dot{Q}_{\text{still}}$ of 40 mW and approximately the same gas flow of about 1.3 mmol/s (compare Fig. 5.26a). As a result, the temperature dependent cooling powers $\dot{Q}_{\text{c}}(T)$ are almost identical in both cases. This can be seen by fitting the data points using Equ. (4.6) and assuming that $\dot{Q}_{\text{c}}(T)$ is proportional to the mixing chamber temperature squared[17]:

$$\begin{aligned} \text{lab-cryostat:} \quad \dot{Q}_{\text{c}}(T) &= (89 \pm 5)\ \text{mW/K}^2 \cdot T_{\text{m}}^2 \\ \text{nd-cryostat:} \quad \dot{Q}_{\text{c}}(T) &= (97 \pm 5)\ \text{mW/K}^2 \cdot T_{\text{m}}^2 \end{aligned}$$

The heat leak $\dot{Q}_{\text{hl}}$ on the other hand is twice as large for the nd-cryostat as for the laboratory cryostat, most probably due to the attached target cell:

$$\begin{aligned} \text{lab-cryostat:} \quad \dot{Q}_{\text{hl}} &= (0.38 \pm 0.05)\ \text{mW} \\ \text{nd-cryostat:} \quad \dot{Q}_{\text{hl}} &= (0.76 \pm 0.06)\ \text{mW} \end{aligned}$$

---

[17] The mixing chamber heater power $\dot{Q}_{\text{mix}}$ corresponds to the externally applied heating power.

Hence, at a mixing chamber temperature $T_{\rm m}$ of 100 mK (135 mK) the cooling power of the dilution insert using the nd-cryostat is 0.2 mW (1 mW). The corresponding target cell temperatures $T_{\rm c}$ are plotted in Fig. 5.25b.
In Fig. 5.26b the temperatures $T_{\rm m}$ and $T_{\rm c}$ are presented as a function of the still power for $\dot{Q}_{\rm mix}$ = 0 mW and 1 mW. It shows that without additional heating in the mixing chamber the temperatures do not depend on the still power, whereas the cooling power rises with increasing $\dot{Q}_{\rm still}$, i.e. increasing flow.

During the nd-experiment the target cell experiences heat inputs, e.g. rf heating by the spin flippers situated close to the nose of the cryostat, rf heating by the NMR coils in the cell and eddy current heating by ramping of the magnetic field during the NMR cross-calibration (compare section 5.3).
To study the effect of these heat inputs on the achievable base temperatures a separate heater is implemented in the cell. In Fig. 5.27 the mixing chamber and the target cell temperatures are plotted as a function of the heater power $\dot{Q}_{\rm cell}$. It shows that $T_{\rm m}$ almost stays constant over a large heating range, while $T_{\rm c}$ immediately starts rising to higher temperatures and reaches already 150 mK at a heater power of approximately 30 μW. This is clearly caused by the low thermal conductivity of the superfluid helium in the target cell (see section 4.3).[18]
Ultimately, this limits of course the final accuracy of the determination of the incoherent scattering length $b_{\rm i,d}$, as the heating by the above stated sources reduces the nuclear spin relaxation time T_1.

---

[18] Also the Kapitza resistance at these low temperatures contributes to the overall thermal resistance.

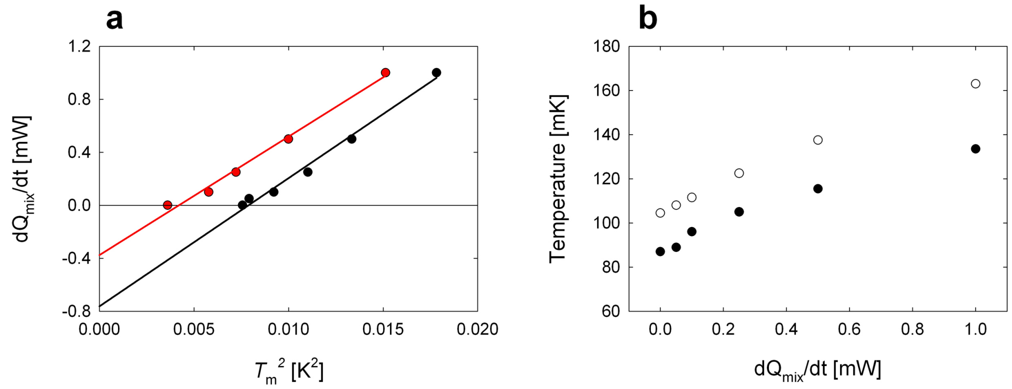

Figure 5.25: Cooling power of the dilution refrigerator. (a) Mixing chamber heater power $\dot{Q}_{\mathrm{mix}}$ as a function of the squared mixing chamber temperature using the nd-cryostat with attached target cell (black dots) and using a laboratory cryostat without target cell (red dots). The lines are linear fits to the data points. (b) Temperature in the mixing chamber T_{m} (●) and in the target cell T_{c} (○) as a function of $\dot{Q}_{\mathrm{mix}}$.

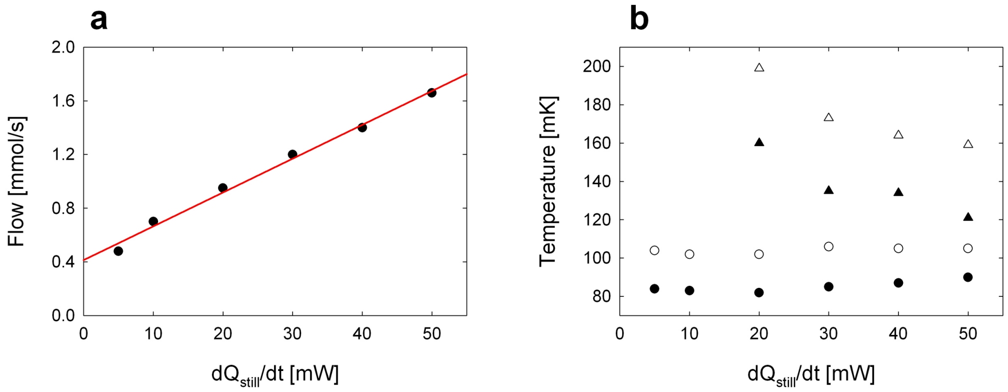

Figure 5.26: (a) Flow rate in the dilution insert as a function of the still power $\dot{Q}_{\mathrm{still}}$ and linear fit (red line). (b) Temperature in the mixing chamber (●, ▲) and in the target cell (○, △) as function of the still power $\dot{Q}_{\mathrm{still}}$ for $\dot{Q}_{\mathrm{mix}}$ = 0 mW (circles) and 1 mW (triangles). All the data in (a) and (b) was obtained using the nd-cryostat.

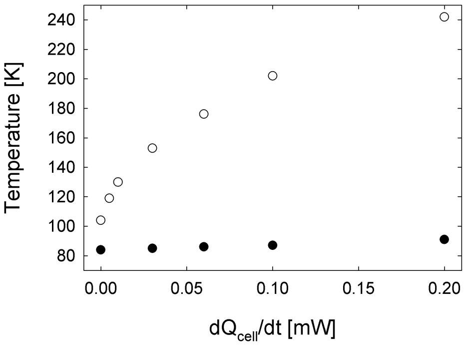

Figure 5.27: Mixing chamber (●) and target cell temperatures (○) as a function of the target cell heater power $\dot{Q}_{\mathrm{cell}}$. Note, this plot was actually measured using a previous version of the above described dilution insert. However, the nd-cryostat with the same target cell filled with liquid helium has been employed.

5.2.2. The ^{4}He Evaporation Refrigerator used in the 3$^{\text{rd}}$ Beam Time

In section 5.2.1 the dilution refrigerator for the nd-experiment was described, which reaches base temperatures of the target of about 100 mK providing long relaxation times of the nuclear polarisation. However, its drawback is that a sample exchange is rather troublesome and may take several days, due to its complicated target cell design. Therefore, a modified version of the cryostat was built including a ^{4}He evaporation insert, which allow to perform a sample exchange within about two hours, i.e. take out the old sample, load a new sample and after two hours the refrigerator reaches again its working temperature of about 1.1 Kelvin (see below).
This temperature is not suitable for the actual measurement of the incoherent scattering length (fast spin relaxation time), but allows to systematically examine whether or not a certain sample material is promising in terms of polarisation homogeneity, spin relaxation time and maximum achievable polarisation.
This refrigerator was used in the third beam time for the investigation of sample materials (see section 6.1.3).

One Kelvin Cryostat

In Fig. 5.28 a slightly modified version of the nd-cryostat is presented. The main difference to the cryostat shown in Fig. 5.17, lies in the removed heat exchanger, spider and target cell, which was mounted to the lower end of the centre tube. Instead the tube is elongated with an aluminium-stainless steel friction-weld extension, which is presented in Fig. F.14 in the appendix. This permits that one can directly insert a target through the central access at the top of the cryostat using a sample insert.
Further, the innermost radiation shield has to be removed because of the space occupied by the extension tube. This does not harm the performance of the refrigerator as it is not required for the operation at 1 Kelvin.
The helium bath works identically as already described above for the dilution cryostat and provides a temperature of about 2 Kelvin to condense the incoming ^{4}He gas.

Evaporation and Sample Insert

Fig. 5.29 shows a drawing of the inserts of the one Kelvin cryostat. The *evaporation insert* is designed similarly to the dilution insert presented in Fig. 5.18, except that the capillaries used for the upper gas-gas heat exchanger are shortened (5 m long 3×2 mm capillary and 2.5 m long 2×1 mm capillary) and the lower liquid-liquid heat exchanger is omitted. The latter is replaced by a prolongation of the capillary, which leads to a Vespel ring.
The *sample insert* or *sample stick* consists of a top flange with an attached long stainless steel microwave guide with several baffles and a microwave horn and a sample cavity mounted to its lower end. A conical Vespel plug fits in the Vespel ring of the evaporation insert. This connection allows to transfer the condensed helium from the evaporation insert to the sample insert and down to the cavity via two capillaries (compare Fig. F.16). The Vespel plug has two holes of 4 mm in diameter, such that pumping on the liquid helium in the extension tube of the cryostat is

possible. Moreover, coaxial NMR cables and thermometer cables are fixed to the sample insert and lead to the sample cavity to measure the sample polarisation and temperature.

Sample Loading

To load a new sample the condensed helium is completely evaporated and pumped back into the storage vessel (compare section 5.2.3). Then the sample insert can be removed and the axial opening in the top flange of the evaporation insert is sealed with a dummy plug. After placing the new sample in the cavity the plug can be removed and the sample stick is inserted again. During these operations, helium gas is flushed into the centre tube via a separate inlet, to avoid that air condenses in the cold cryostat.

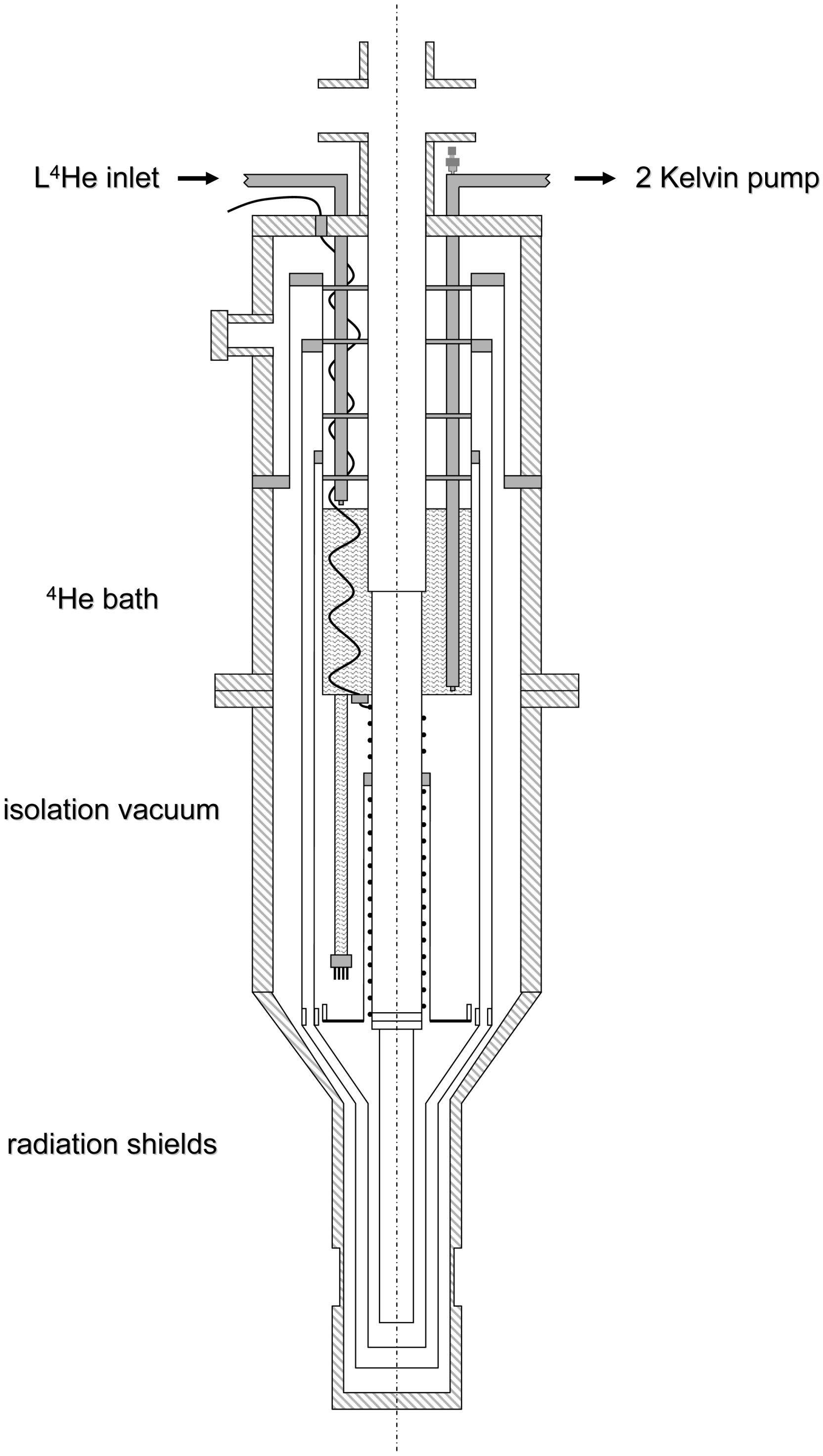

Figure 5.28: Scheme of the modified nd-cryostat, which can be operated with the evaporation insert in Fig. 5.29. Illustration is not to scale.

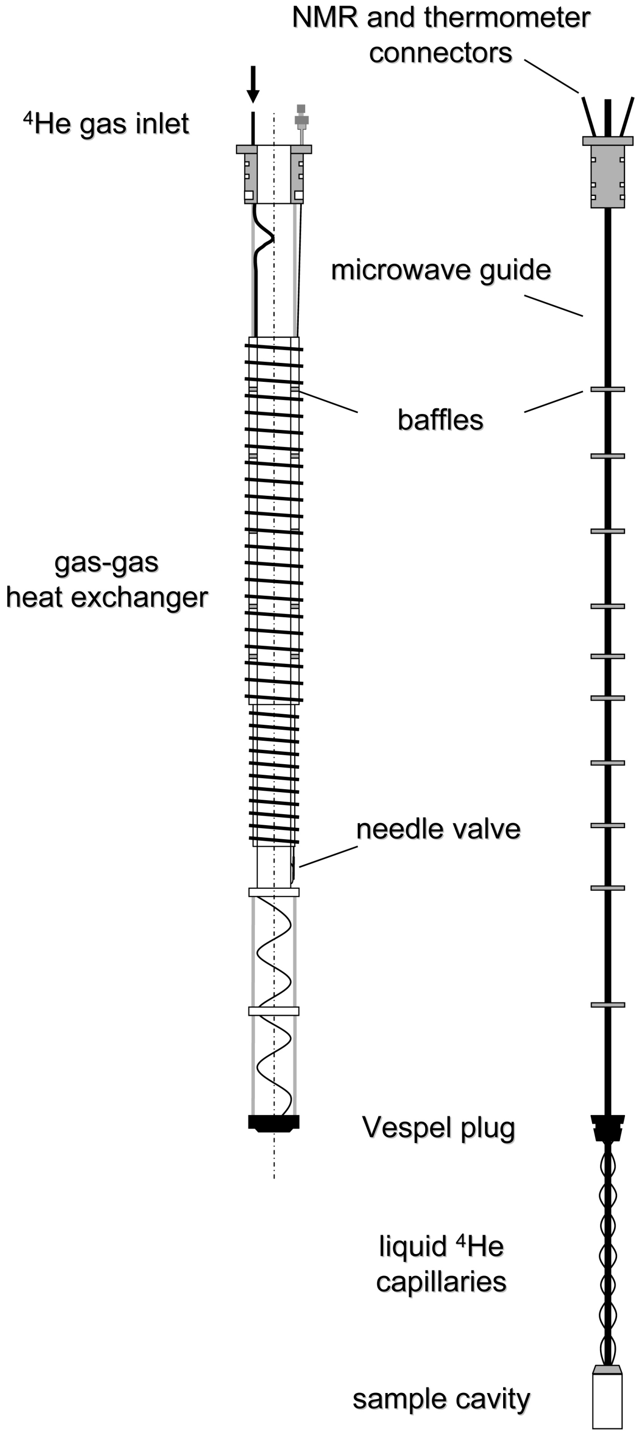

Figure 5.29: One Kelvin cryostat inserts. Left: evaporation insert. Right: sample insert with microwave cavity for the sample/target. Compare Fig. F.15 and F.16. Illustration is not to scale.

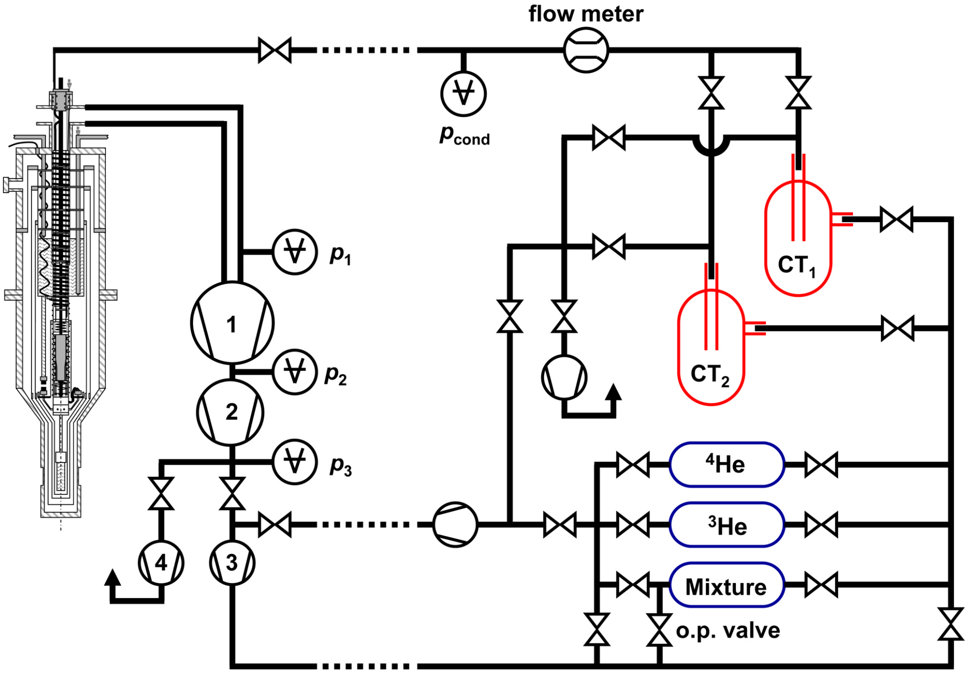

Figure 5.30: Scheme of the gas handling system with the dilution refrigerator. The pump system consists of: 1. *Alcatel* MIV 1000, 2. *Leybold* WS 252 and 3. *Alcatel* ADP 31. Pump 4 is a service pump to evacuate the pumping line and the cryostat (*Alcatel* LS90S1). For the 2 Kelvin stage of the cryostat a *Leybold* S100F pump with a nominal pumping speed of 110 m^3/h is used. The pressures are measured using *Pfeiffer* pirani gauges.

5.2.3. Gashandling System and Pumping Set

A scheme of the gas handling system of the dilution refrigerator is presented in Fig. 5.30. It includes three gas tanks for pure ^{3}He, pure ^{4}He and a ^{3}He/^{4}He mixture. Once the correct ratio between ^{3}He and ^{4}He and the right amount of total mixture is established one only uses the mixture tank for condensation and distillation. For our dilution refrigerator the total amount of mixture was about 100 litre (gas) at 920 mbar, which corresponds to about 4 mol of helium, with a ^{3}He/^{4}He ratio of about 0.3, i.e. 1 mol of ^{3}He and 3 mol of ^{4}He.

After the mixture has been completely condensed into the cryostat, ^{3}He is circulated by means of a pump system. It consists of two roots blowers in series with nominal pumping speed of 1000 m^3/h and 250 m^3/h backed up by a 40 m^3/h hermetically sealed dry pump. This pump system permits a flow of 1 mmol/s at a pumping pressure of 0.1 mbar. The exhaust gas of the pumps is forced through one of the parallel cold traps (CT$_1$ or CT$_2$ - containers filled with zeolite and cooled to liquid nitrogen temperature), before it recondenses at a typical condensation pressure p_{cond} of 300-500 mbar.

The same gas handling system has also been used in combination with the ^{4}He evaporation refrigerator (see section 5.2.2).

5.2.4. Sample Preparation

The samples for the frozen spin target are deuterated organic substances with implemented paramagnetic centres (radicals). Their properties have been systematically investigated using laboratory cryostats (polarisation, relaxation time etc.) and during the third neutron beam time (homogeneity, Ramsey signal phase shift etc.). The studied sample materials can be divided into two groups: *polystyrene samples*, which are solid at room temperature and *frozen alcohol samples*, which have to be kept under liquid nitrogen temperatures. They are prepared in the following ways.

Deuterated Polystyrene Samples

The deuterated polystyrene samples are made from a mixture of normal non-deuterated polystyrene (n-PS) and deuterated polystyrene (d-PS).[19] The degree of deuteration of the d-PS is typically about 99%. As paramagnetic centres deuterated TEMPO[20] with a degree of deuteration of approximately 95% is used (see Fig. 5.31 for the chemical structures):

1. 5 wt.% of the desired amount of d-PS and n-PS is dissolved in deuterated toluene. To speed up the dissolution process the mixture is heated to about 120°C on a hotplate.

2. When the polystyrene is fully dissolved - this can take several hours - the glass beaker with the mixture is taken away from the hotplate and TEMPO is added to the liquid.

3. The liquid is poured onto flat glass surfaces and one waits until the toluene is completely evaporated in a flue (about 12 hours).

4. One obtains thin plastic foils.

5. The foils are cut into small square pieces of about 14×14 mm^2, which are stacked and then warm pressed in a stainless steel press. The press is heated up to about 95°C in an oven (*glass transition temperature* of polystyrene) and is then taken out of the oven and allowed to cool down naturally to room temperature. The exact procedure and the necessary temperatures have been optimised by trial and error.

6. Finally, a plastic platelet is obtained, which can be further processed, i.e. machined to the desired size and thickness (compare Fig. F.12a).

A description of the production process is also given in Ref. [Bra00]

---

[19] Polymerised using UV-light by ARMAR AG (Döttigen): *http://www.armar.ch.*

[20] 2,2,6,6-Tetramethylpiperidine-1-oxyl.

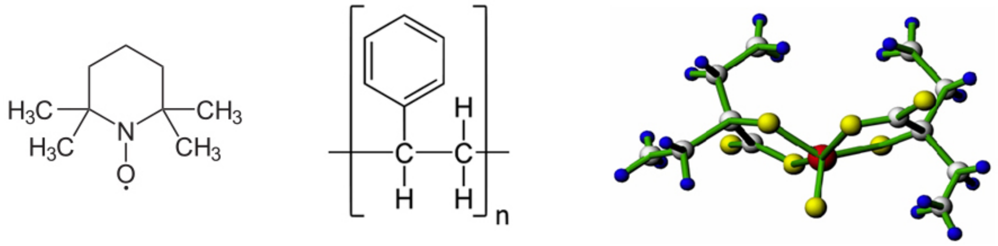

Figure 5.31: Left: chemical structure of TEMPO. Middle: polystyrene. Right: EHBA-Cr(V).

Frozen Alcohol Samples

We were using frozen alcohol samples made from a mixtures of H_2O and glycerol and D_2O and d-glycerol, respectively. As paramagnetic centres TEMPO and EHBA-Cr(V) have been employed.[21] To cast frozen platelets, the water/alcohol mixture is injected in a copper mould, which is cooled with liquid nitrogen (compare Fig. F.12b). A brief description of the procedure is given in Ref. [Bra062].

The obvious drawback of the frozen alcohol samples is that they cannot be used as targets when employing the dilution refrigerator described in section 5.2.1, due to the fact that the sample loading in the target cell has to be done at room temperature. Therefore, these samples have only been used during the third beam time with the one Kelvin evaporation cryostat, which allows quick sample loading directly into the cold cryostat.

---

[21] EHBA-Cr(V) is a complex of chromium (V) with 2-ethyl-2-hydroxybutanoic acid.

5.3. Nuclear Magnetic Resonance

As already mentioned in section 3.4, the necessary accuracy for the relative measurement of the nuclear spin polarisation should be in the order of 10^{-3} to determine the incoherent scattering length $b_{\mathrm{i,d}}$ with the aimed precision. The nuclear spin polarisation of a polarised target is most accurately measured using continuous wave nuclear magnetic resonance (cw-NMR) employing a so-called *Q-meter* setup [Cou93, Cou04].[22] In this section the principles of cw-NMR using a resonant and a non-resonant cable circuit are explained. Also the NMR coil geometry of the frozen spin target, the data treatment of the obtained NMR signals as well as the NMR cross-calibration are presented. Furthermore, tests are described with the goal to increase the signal-to-noise ratio of the NMR signals using a commercially available rf preamplifier operated at liquid helium temperatures.

5.3.1. CW-NMR using a Resonant Cable Circuit

A good description of how to determine the nuclear polarisation with cw-NMR is given in Ref. [Hau04] and references therein. The technique is based on the relationship between the complex nuclear spin susceptibility $\chi(\omega) = \chi'(\omega) - i\chi''(\omega)$ and the nuclear polarisation P:

$$P = \left(\frac{2\hbar I}{g^2 \mu_{\mathrm{N}}^2 \pi N}\right) \int_0^\infty \frac{\omega_0}{\omega} \chi''(\omega) d\omega \ , \tag{5.5}$$

where ω is the angular frequency of the applied rf field, g is the g-factor of the nucleus with spin I and μ_{N} is the nuclear magneton and N is the number of spins. In table 5.1 the g-factors and the gyromagnetic ratios γ of several nuclear species and of the neutron and the electron are summarised.
The absorptive part $\chi''(\omega)$ of the susceptibility, which is non-zero only in a small frequency band around the nuclear Larmor frequency $\omega_0 = -\gamma B_0$, is measured by inductive coupling between the nuclear spins of a sample and a surrounding coil, resulting in a complex impedance

$$Z_{\mathrm{L}}(\omega) = i\omega L_{\mathrm{Q}}(1 + 4\pi\eta\chi(\omega)) \ , \tag{5.6}$$

where L_{Q} is the inductance and η is the filling factor of the coil [Abr831]. From Equ. (5.6) it follows that $\chi''(\omega)$ causes a frequency dependent additional real resistance, which is best detected by using a constant current series LCR circuit connected to a phase sensitive detector.

The conventional resonant cable circuit is presented in Fig. 5.32: a rf signal feeds a series LCR resonant circuit via a constant current resistor $R_{\mathrm{cc}} \approx 1$ kΩ. All passive elements, i.e. the damping resistor $R_{\mathrm{Q}} \approx 10$ Ω and the tuning capacitor C_{Q}, of the LCR circuit are at room temperature and connected to the sample coil via a coaxial cable with a length $n \cdot \lambda_{\mathrm{rf}}/2$ ($n \in \{1, 2, 3, ...\}$), where λ_{rf} is the wavelength of the rf

---

[22] Pulse NMR cannot be applied due to the necessity to excite broad deuteron signals.

Particle or nucleus	Natural abundance	Spin	$\gamma/2\pi$ [MHz/T]	μ/μ_N
Electron e$^-$		1/2	-28024.95	-1838.28
Neutron n		1/2	-29.1639	-1.91304
Proton ^{1}H	99.985 %	1/2	+42.5764	+2.79285
Deuteron ^{2}H	0.015 %	1	+6.5357	+0.85744
Helium ^{3}He	0.013 %	1/2	-32.4351	-2.12762
Lithium ^{6}Li	7.5 %	1	+6.2660	+0.82205
Carbon ^{13}C	1.10 %	1/2	+10.7081	+0.70241
Fluor ^{19}F	100 %	1/2	+40.0765	+2.62887

Table 5.1: Magnetic resonance properties of the electron and important nuclei, taken from Ref. [Lid98]. μ is the magnetic moment and the nuclear magneton is given by μ_N=0.505078×10^{-26} Am^2. The ratio μ/μ_N is also known as the g-factor.

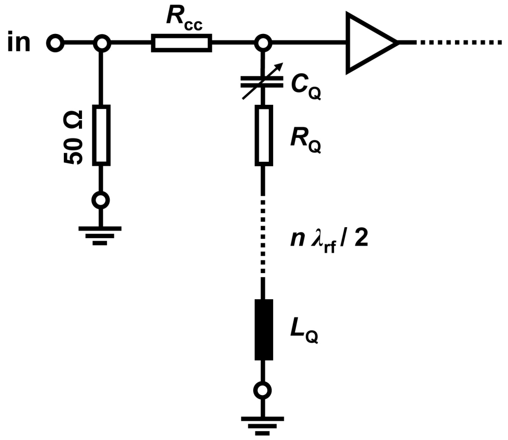

Figure 5.32: Resonant cable circuit for cw-NMR. A typical rf signal input power for the Q-meter resonant cable circuit is about -7 dBm.

signal in the cable.[23] By modulating the rf frequency around the Larmor frequency ω_0 of the investigated nuclear spin species and measuring the real part of the voltage over the LCR circuit, one obtains a so-called *Q-curve*.[24]

An example of such a Q-curve of a sample with polarised protons is given in Fig. 5.33a. The black *foreground* curve taken at a field of about 2.5 Tesla has a prominent proton absorption peak at 106.34 MHz with a FWHM of about 35 kHz (proton *NMR signal*). The red *background* curve (*baseline*) is taken at a slightly lower magnetic field. Hence, the proton absorption peak is shifted to lower frequencies and is no longer visible in the parabolic Q-curve.

The shape of the Q-curve (voltage offset, depth) depends on the properties of the LCR circuit, on the constant current resistor R_{cc} and on the length of the coaxial cable:

- With increasing R_{cc} the current in the LCR circuit decreases and thus the voltage offset and the size of the NMR signal reduces.

- With increasing R_Q the voltage offset increases, while the size of the NMR signal reduces. The voltage offset and the signal size should not be too large, to avoid saturation of the rf amplifiers and non-linear amplification of the NMR signal.

- A shorter coaxial cable, i.e. small n, causes a shallower Q-curve [Hau04]. A flat baseline improves the accuracy of the NMR signal integral determination (see below), especially when dealing with small signal sizes.

To avoid fluctuations of the shape of the Q-curve and thus of the NMR signal, one has to ensure that the used resistors, capacitors and coaxial cables are not sensitive to changes of the temperature (e.g. by refill of the helium bath) and the magnetic field.[25] As this is only achievable to a certain extent, one has to perform NMR measurements under the same conditions if possible.

In Fig. 5.33b and 5.33c the further data treatment of the Q-curves is shown: subtraction of the background curve from the foreground, polynomial fit of the residual background (linear, parabolic or cubic) and determination of the area under the proton peak (*NMR signal integral*).

Note, the cw-NMR technique allows to determine absolute values of nuclear polarisation by calibrating the obtained NMR signal integral with a known thermal equilibrium polarisation signal (*thermal equilibrium calibration* – compare section 5.4.1), although this is not necessary for the relative measurement of the incoherent neutron-deuteron scattering length (see section 3.4).

---

[23] For a typical signal velocity in a coaxial cable of 2×10^8 m/s, we obtain a wavelength λ_{rf} of 12.5 m (1.9 m) for a rf frequency of 16 MHz (106 MHz).

[24] Actually it would be advantageous to perform a magnetic field sweep instead of a rf frequency modulation. Firstly, because complications due to frequency dependent behaviour of rf components, e.g. frequency dependent gain of amplifiers etc., would cancel. And secondly, instead of a Q-curve one would obtain a perfectly flat baseline (constant tuning).

[25] We used special low temperature resistors and capacitors: *http://www.atceramics.com.* Coaxial cables: *http://www.microtech.com* (LN-3-30). Semi rigid cables: *http://www.hubersuhner.ch* and *http://www.micro-coax.com.*

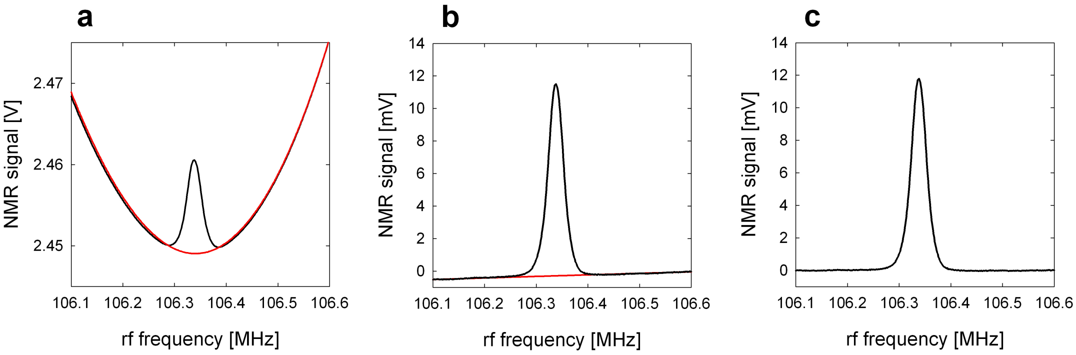

Figure 5.33: Proton NMR of a 110 mg d-PS sample with a degree of deuteration of nominal 97% (sample #15, see appendix E). Number of coil windings: N_{106} = 4 (compare section 5.3.3). (a) Foreground Q-curve with proton absorption NMR signal taken at 2.5 Tesla (black) and background Q-curve (red). Each curve is an average over 1000 sweeps with a width of 600 kHz and 512 data points. (b) Background subtracted foreground curve (black) and parabolic fit using the data points besides the peak (red). (c) NMR signal after subtracting the parabolic fit. The integral value, i.e. the area under the peak, is $J_{\mathrm{p},106}$ = +0.39 [a.u.], which corresponds to proton polarisation of about 50% (TE calibration).

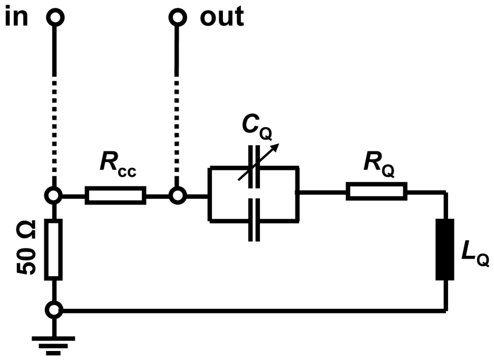

Figure 5.34: Non-resonant cable circuit. All passive components are at low temperature inside the cryostat. In this configuration two coaxial cables are needed. A typical rf signal input power is about -1 dBm.

5.3.2. Low Temperature NMR or Non-Resonant Cable Circuit

A resonant cable circuit as described in the previous section has the drawback that the coaxial cable belongs to the resonant circuit and thus the imaging of the modulated coil impedance is not perfect, due to unwanted dispersion contributions. This problem can be avoided by using the so-called non-resonant cable circuit presented in Fig. 5.34, where all passive components are located inside the cryostat at low temperatures in the vicinity of the sample coil (*Low Temperature NMR* – LT NMR). From this configuration one can expect a better signal-to-noise ratio, a shallower baseline and minimises the dispersion effects.

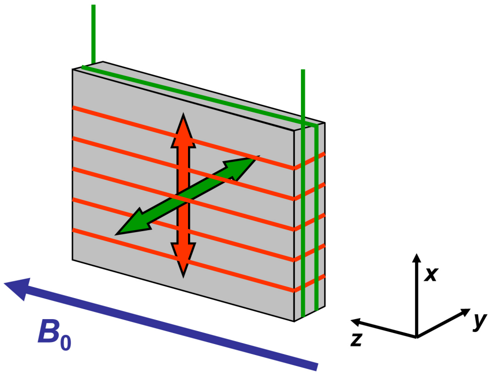

Figure 5.35: Two NMR coils wound on the polarised sample/target (compare Fig. 6.5). The direction of the rf fields generated by the 16 MHz LT NMR coil (red coil) and the 106 MHz coil (resonant cable circuit, green coil) are indicated by the arrows and are both perpendicular to the external magnetic field B_0 in z-direction.

5.3.3. NMR Coil Geometry of the Frozen Spin Target

For the nd-experiment we used two separate NMR systems integrated into the nd-cryostat:

1. A resonant cable circuit system tuned to about 106 MHz, which is used to monitor the proton polarisation at a field of 2.5 Tesla.

2. A LT NMR system tuned to about 16 MHz to measure the deuterons at 2.5 Tesla and the protons at about 0.38 Tesla.

The latter allows to measure both nuclear spin species at the same rf frequency like demanded in section 3.4. Hence, the obtained proton and deuteron NMR signal integrals correspond to the ones in Equ. (3.54). To avoid ramping of the magnetic field during a Ramsey neutron measurement, the two proton NMR signals (16 MHz and 106 MHz) are calibrated to each other off-line (see *cross-calibration* in section 5.3.5).

A scheme of how the NMR coils are wound on the sample is shown in Fig. 5.35. The number of windings and the exact coil geometry varied between the different beam times, but the field directions were always chosen identical. The coil belonging to the LT NMR system has N_{16} windings and produces a rf field in x-direction. The coil belonging to the resonant cable circuit has N_{106} windings and produces a rf field in y-direction, i.e. both rf fields are perpendicular to the external magnetic field.

Note, in Fig. 5.22 a third coil was presented (saddle coil). This coil also generates a rf field in y-direction, which serves to depolarise the nuclear spins by irradiation of rf pulses. The inductive coupling between this coil and the resonant cable coil can be neglected, as the distance between each other is rather large.

A picture of the circuit board of the LT NMR system is depicted in Fig. F.17. It is thermally anchored to the helium bath or the still radiation shield. The resonance frequency of the LT NMR is adjusted by means of a tunable capacitor, which is in parallel to a fixed special low temperature capacitor of about 100 pF. The tunable capacitor is placed in the helium bath and can be remotely manipulated from outside the cryostat using a long "screw driver". The tuning range is about ±0.5 MHz.

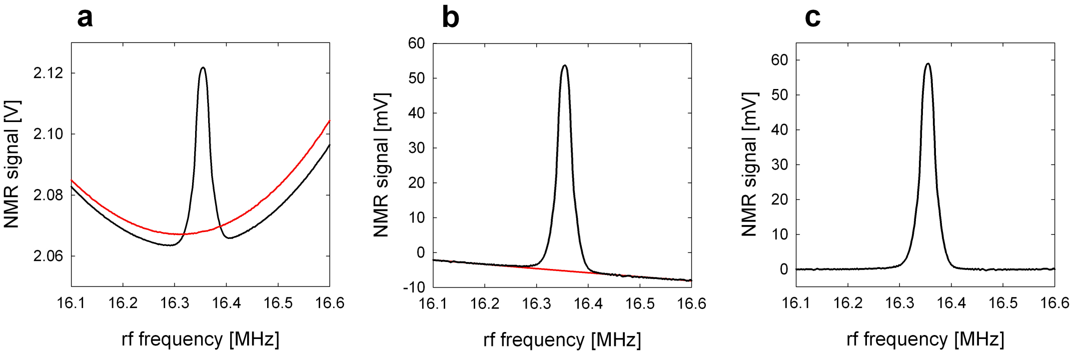

Figure 5.36: Proton NMR at about 0.38 Tesla. The Q-curve represents an average over 400 sweeps (width 600 kHz, 512 data points). The signal integral of the proton peak is $J_{\mathrm{p},16}$ = +1.90 [a.u.], which corresponds to a nuclear polarisation of about 49% (TE calibration).

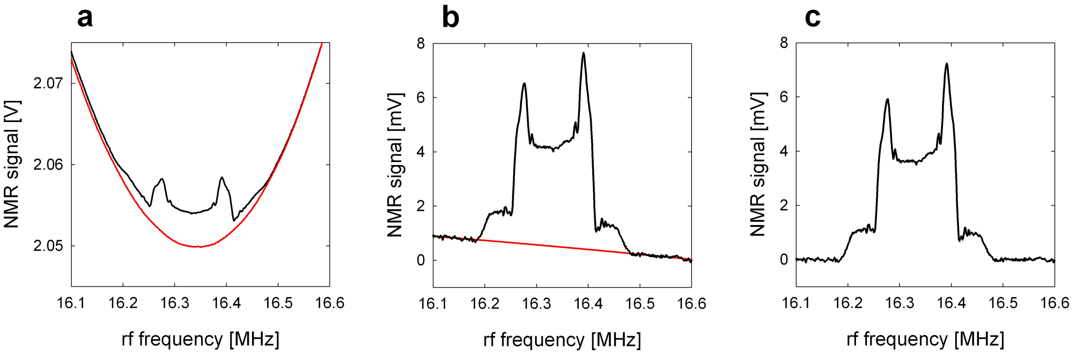

Figure 5.37: Deuteron NMR at 2.5 Tesla. The Q-curve represents an average over 400 sweeps. The signal integral of the deuteron signal is $J_{\mathrm{d},16}$ = +0.67 [a.u.], which corresponds to a nuclear polarisation of about 17% (peak ratio method).

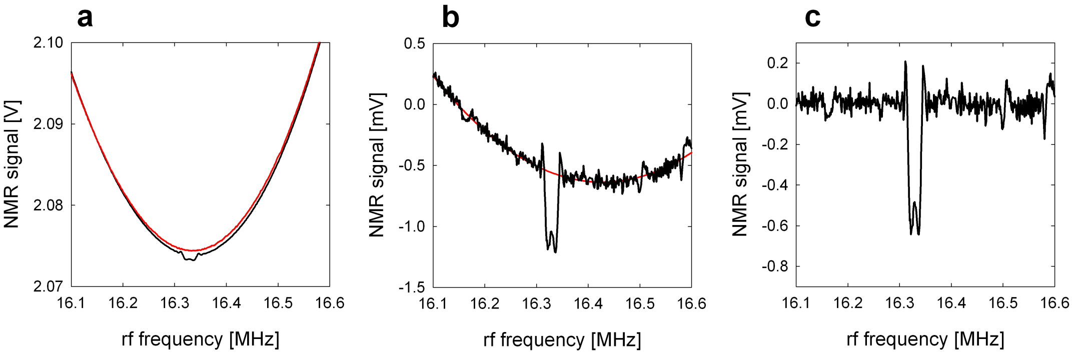

Figure 5.38: ^{13}C NMR at 1.5 Tesla. The Q-curve represents an average over 4000 sweeps. The signal integral of the ^{13}C peak is $J_{\mathrm{C},16}$ = −0.01 [a.u.], with $J_{\mathrm{p},106}$ = −0.43 [a.u.] (-55%) and $J_{\mathrm{d},16}$ = −0.91 [a.u.] (-24%). Assuming equal spin temperatures of the protons and ^{13}C yields a polarisation of about -14% (compare section 5.4.4).

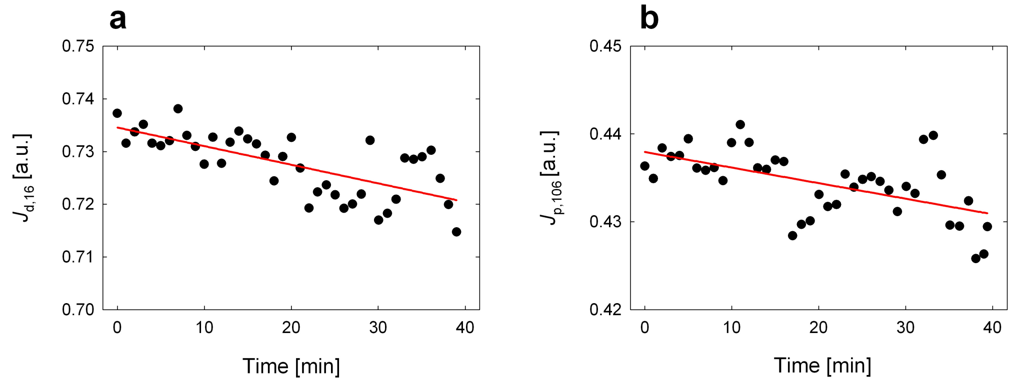

Figure 5.39: Series of NMR signal integral measurements at 2.5 Tesla with linear fits (red lines) using sample #15. (a) Deuterons. (b) Protons.

Fig. 5.36, 5.37 and 5.38 show Q-curves and NMR signals of protons, deuterons and ^{13}C obtained with the 16 MHz LT NMR system. The used sample (sample #15 with N_{16} = 10 and N_{106} = 4, see appendix E) was polarised positively in the case of the protons and the deuterons and negatively for carbon. The data treatment is identical to the one stated in section 5.3.1 for the resonant cable circuit.

The shape of the deuteron NMR signal deviates strongly from the peak shaped proton signal. This is caused by the interaction of molecular electric gradient fields with the quadrupole moment of the spin 1 of the deuteron, which causes an asymmetric splitting of the three Zeeman energy levels. From the height of the two peaks of the deuteron NMR signal one can roughly estimate the deuteron spin polarisation using the following formula (*peak ratio method*):

$$P = \frac{r^2 - 1}{r^2 + r + 1} \,, \tag{5.7}$$

where r is the ratio of the peak heights [Ada99].

5.3.4. Accuracy of the NMR measurement

Important for the accurate measurement of the incoherent neutron scattering length of the deuteron is to know, how precise one can determine the NMR signal integrals and how much nuclear polarisation is lost due to the NMR measurement itself (*signal saturation*).

Therefore a series of NMR signals of the protons and the deuterons were taken at 2.5 Tesla in intervals of 60 sec.[26] The result is presented in Fig. 5.39, showing that the signal integrals decay slowly with the number of measurements. Nevertheless, the decay is considerably faster than if it would be caused only by the nuclear spin relaxation ($T_1 \geq 100$ h, see section 5.4.2). Here, the loss per NMR measurement was determined to be below 0.05% for both spin species, which is still tolerable for the aimed measurement accuracy of $b_{\mathrm{i,d}}$.[27]

---

[26] In this case the NMR foreground signals were directly fitted with a polynomial function, without subtracting a baseline signal.

[27] Each measurement takes about 20 sec and consists of 2000 sweeps over the absorption signal with input rf powers of -1 dBm (-7 dBm) for the 16 MHz (106 MHz) NMR system. These rf powers are standard values for our Q-meter setups. Of course the loss per NMR measurement depends on the number of sweeps, the rf power and the NMR coil design.

The precision of the NMR measurement is given by the standard deviation of the fit residuals, which are defined as the deviations of the individual data points from the fit. In the presented case, one obtains an absolute accuracy for the proton signal integrals of about 3×10^{-3} and for the deuterons of about 4.5×10^{-3}, which yields a relative statistical accuracy of better than 1%, assuming reasonable NMR signal integrals.[28] This is almost one order of magnitude larger than it is necessary for the aimed precision measurement of $b_{\mathrm{i,d}}$. An improvement of the precision of the NMR measurement is difficult to accomplish, as the signal size is limited by the sample mass/size and the rf power, which both cannot be further increased. The first one because of the magnetic field inhomogeneity at larger neutron beam cross-sections (compare section 6.1.7) and the latter due to signal saturation.

5.3.5. NMR Cross-Calibration

Procedure

It was already mentioned before that the proton NMR signal integrals of the two NMR systems (16 MHz and 106 MHz) are correlated and can be "cross-calibrated" to each other, as both are measuring the same protons. The procedure, which can be performed without the neutron beam, allows to avoid ramping of the magnetic field during the neutron Ramsey measurement. It is divided into the following steps:

1. At 2.5 Tesla a foreground proton NMR signal is taken with the 106 MHz system.

2. The field is ramped down to 0.38 Tesla. The ramping speed of the magnet power supply can be adjusted to prevent large eddy current heating of the target cell, but should be fast enough to avoid unnecessary nuclear relaxation.[29]

3. During the ramping, Q-meter baseline curves are taken for both NMR systems.

4. When the power supply reached its preset current value, one waits for a certain time τ_{x} for the magnetic field to stabilise (typically about 15-30 sec).

5. Then the foreground proton NMR signal is taken with the 16 MHz system.

6. Wait another time τ_{x}, to provide a symmetric measurement scheme.

7. Ramp up the magnetic field to 2.5 Tesla and start again with step number 1. Usually the whole sequence takes about 10 minutes and is synchronised with the helium refill cycle.

The total NMR cross-calibration procedure is fully automated, such that one can perform systematic studies in terms of ramping speeds, temperature, waiting time τ_{x}, number of taken NMR signals etc. (see below).

---

[28] In absolute values this corresponds to a polarisation of 0.35% of the protons and 0.1% of the deuterons for this sample (#15).

[29] We chose a ramping speed, such that the ramping took about 4 min, i.e. between 0-120 A with 0.5 A/s and above 120 A with 1 A/s (compare Fig. 5.10b).

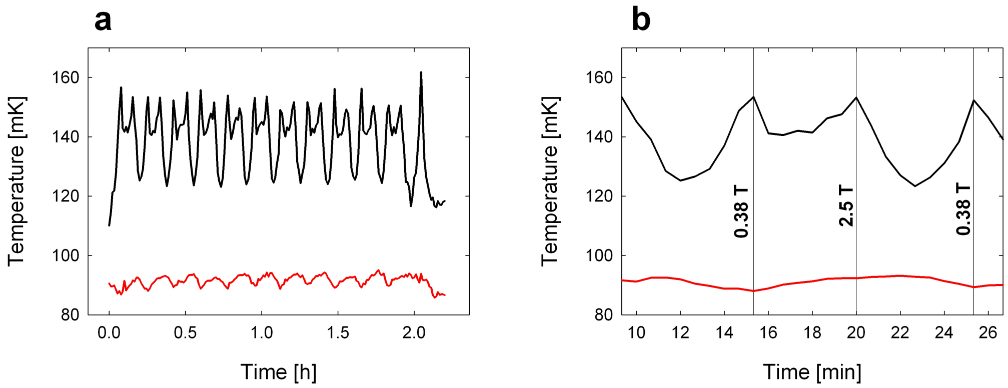

Figure 5.40: Temperature time histograms during a NMR cross-calibration with $\tau_\mathrm{x} = 30$ sec. (a) The magnetic field is swept 11 times from 2.5 Tesla to 0.38 Tesla and back. The mixing chamber temperature is almost unaffected (red curve, $T_\mathrm{m} = 88 - 94$ mK), while the temperature in the target cell changes drastically as a result of the induced eddy currents (black curve, $T_\mathrm{c} = 122 - 155$ mK). (b) Detail from the time histogram. The horizontal lines mark the moments, when the magnetic field reaches 0.38 Tesla and 2.5 Tesla, respectively. A whole cycle takes about 10 minutes. At low field T_c stays approximately 140 mK, due to rf heating from the 16 MHz LT NMR.

Example Measurement

As an example, we want to consider a cross-calibration performed on a positively polarised d-PS sample (sample #15, see Fig. F.13a).

Fig. 5.40 shows the time histogram of the mixing chamber temperature T_m and the target cell temperature T_c during 11 cross-calibration sequences. The ramping of the magnetic field obviously heats the target cell and causes T_c to rise from about 110 mK to above 150 mK, while T_m is almost unaffected. This is a result of the low thermal conductivity of the superfluid helium in the target cell (compare Fig. 5.27). Ideally the polarisation stays frozen during the cross-calibration sequence, however at the lower magnetic field of 0.38 Tesla and at the induced higher sample temperature the nuclear spin relaxation time reduces drastically from more than 100 hours to only a few tens of minutes. Hence, the NMR signal integrals before and after the ramping sequence are not identical, but a loss of nuclear polarisation is observed.

In Fig. 5.41 the NMR signal integrals of the protons and deuterons at low and high magnetic field are plotted. They show that the signal sizes decrease exponentially with the number of cross-calibration sequences (here: $\tau_\mathrm{x} = 30$ sec):

Protons:	$J_{p,16}$	→	loss per sequence:	(8.8 ± 0.1) %
	$J_{p,106}$	→	loss per sequence:	(8.7 ± 0.1) %
Deuterons:	$J_{d,16}$	→	loss per sequence:	(10.8 ± 0.2) %

As expected the loss per sequence of the protons is the same for both NMR systems within the error of the fit. The loss of the deuterons is slightly larger as a result of the shorter relaxation time T_1.

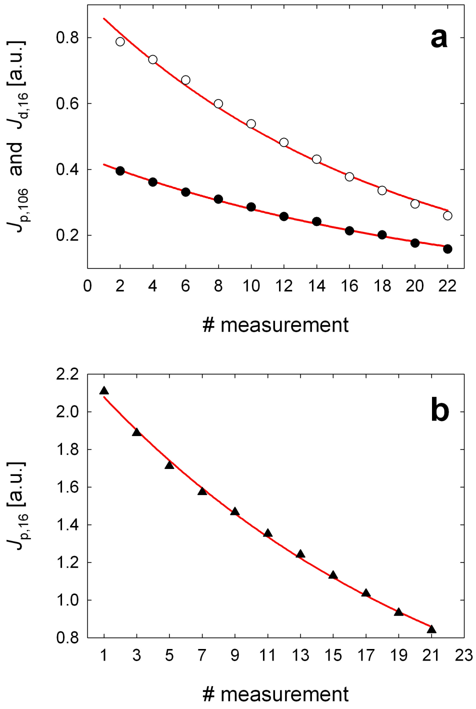

Figure 5.41: Example of a cross-calibration measurement with exponential decay fits (red curves). The 16 MHz NMR signals are averaged over 3×400 sweeps and the 106 MHz NMR signals over 1000 sweeps. (a) NMR signal integrals taken at 2.5 Tesla: protons $J_{\mathrm{p},106}$ (●) and deuterons $J_{\mathrm{d},16}$ (○). (b) Proton NMR signal integrals $J_{\mathrm{p},16}$ taken at 0.38 Tesla (▲).

In Fig. 5.42 the proton signal integrals $J_{\mathrm{p},16}$ at 0.38 Tesla are plotted as a function of the signal integrals $J_{\mathrm{p},106}$ at 2.5 Tesla. The slope of the linear fit yields the so-called *cross-calibration coefficient* c_{x}, which is defined as:

$$c_{\mathrm{x}} = \frac{J_{\mathrm{p},16}}{J_{\mathrm{p},106}} \tag{5.8}$$

Obviously c_{x} turns out different if the high field signal integral is combined with the low field signal integral before or after the magnetic field ramp. We thus obtain two values for the cross-calibration coefficient. In the presented example: $c_{\mathrm{x},1} = 5.2 \pm 0.1$ (before) and $c_{\mathrm{x},2} = 4.8 \pm 0.1$ (after). This leads to an average of $c_{\mathrm{x}} = (5.0 \pm 0.2 \pm 0.1)$, with a relative error of ±4% (syst.) and ±2% (stat.), due to the nuclear polarisation loss and the linear fits.

Of course these errors indicate the worst case and could be taken as a measure for the maximum uncertainty of the NMR cross-calibration procedure. Nevertheless, the exact systematic error of the method is hard to quantify without assumptions about the rate of polarisation loss as a function of time. Also the loss is difficult to decrease as the effective cooling power of the cryostat in the target cell is limited.

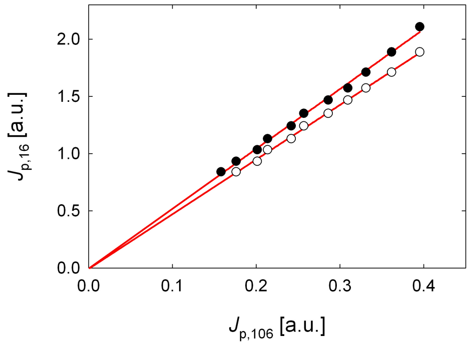

Figure 5.42: Example of a cross-calibration of the two proton NMR systems (16 MHz and 106 MHz). $J_{\mathrm{p},16}$ before (●) and after (○) the corresponding high field signal plotted against $J_{\mathrm{p},106}$. The linear fits (red lines) through the data points cross very precisely the origin, as should be the case.

Systematic Tests of the NMR Cross-Calibration

Systematic studies of the NMR cross-calibration have been performed. As the temperature could not be further decreased, the focus was directed on the waiting time τ_{x}.[30] A plot of the loss per sequence as a function of the total time at low field is given in Fig. 5.43. The total time at low field corresponds to twice the waiting time plus the time τ_{nmr}, which it takes to measure the actual NMR signal. Note, the loss caused by the NMR measurement itself can still be neglected compared to the waiting and measuring time losses (see section 5.3.4). From the linear fit to the data points one can determine the loss, which can be attributed to the ramping process itself. In this case it yields $(1.1 \pm 0.4)\%$.

An exponential fit to the same data leads to a decay time of the NMR signal at 0.38 Tesla of about 20 min ($T_{\mathrm{c}} \approx 140$ mK, compare Fig. 5.40). This is in good agreement with separately performed relaxation time measurements taken at two different temperatures presented in Fig. 5.44a. The loss due to the ramping can thus be expressed as an additional waiting time of about 15 sec at low field. This yields an effective time at low field of about 60 sec for a reasonable cross-calibration measurement, with $\tau_{\mathrm{x}} \geq 20$ sec and $\tau_{\mathrm{nmr}} \approx 5$ sec.

Using these values, one can estimate the loss per sequence, assuming a certain target cell temperature and a relaxation time T_1 at 0.38 Tesla, respectively:

$$T_{\mathrm{c}} \approx 90 - 100\ \mathrm{mK} \quad \rightarrow \quad T_1 \approx 120\ \mathrm{min} \quad \rightarrow \quad \text{Expected loss: } 1\%$$

$$T_{\mathrm{c}} = 110\ \mathrm{mK} \quad \rightarrow \quad T_1 = 65\ \mathrm{min} \quad \rightarrow \quad \text{Expected loss: } 2\%$$

$$T_{\mathrm{c}} = 135\ \mathrm{mK} \quad \rightarrow \quad T_1 = 29\ \mathrm{min} \quad \rightarrow \quad \text{Expected loss: } 4\%$$

These estimations show that even if the cell temperature could be kept at low temperatures of about 100 mK during the cross-calibration, one would still have to expect losses of about 1-2%. Hence, the systematic error due to the NMR cross-calibration would be still almost one order of magnitude larger than necessary for the aimed accuracy improvement of the incoherent scattering length $b_{\mathrm{i,d}}$.

---

[30] Actually also studies on the ramping speed have been made, but did not lead to improved results of the cell temperature.

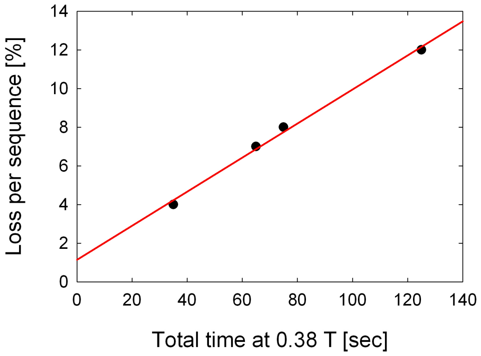

Figure 5.43: Loss of proton NMR signal integral per cross-calibration sequence as a function of total waiting and measuring time at low field. The red line is the linear fit to the data points, which intercepts the vertical axis at a loss of about 1%.

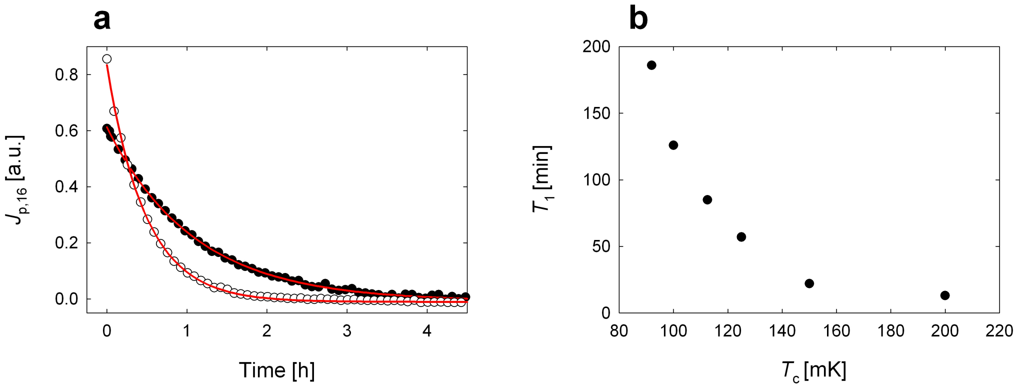

Figure 5.44: (a) Proton spin relaxation at 0.38 Tesla and 110 mK (•) and 135 mK (○). The exponential decay fits (red curves) yield relaxation times of $T_1 = (65 \pm 1)$ min at 110 mK and $T_1 = (29 \pm 1)$ min at 135 mK (sample #15). (b) Proton spin relaxation time T_1 at 0.38 Tesla as a function of the sample temperature. Note, a different sample was used than in (a): fully protonated PS with a nominal TEMPO concentration of 2.5×10^{19} cm^{-3} (sample #0a).

In order to reach at least the same accuracy as the present value of $b_{\mathrm{i,d}}$ of about 0.8% [Dil71], a loss per sequence of less than 2% needs to be achieved, i.e. T_{c} should be about 110 mK during the cross-calibration. This would require a much better thermal contact between the mixing chamber and the target cell, which is hardly realisable within the constraints of the present magnet setup.

Hence, the accuracy of the NMR cross-calibration and moreover the precise determination of the NMR signal integrals are presently limiting the total accuracy of the measurement of the incoherent scattering length of the deuteron $b_{\mathrm{i,d}}$ (see section 7.1).

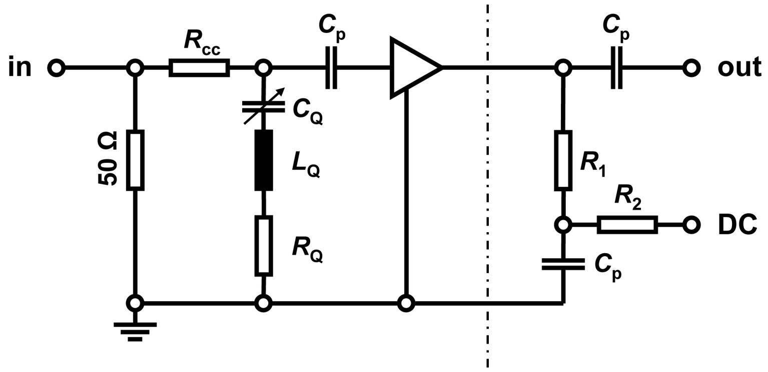

Figure 5.45: Preamplifier test circuit for the LT NMR system. The part on the right side of the dashed line could be kept outside of the cryostat at room temperature. This would also decrease the number of necessary coaxial cables.

5.3.6. Tests with a RF Preamplifier at 4 Kelvin

In section 5.3.3 the deuteron NMR signals have been presented, which possess a rather complicated shape. Moreover, their signal integral is at least two times smaller than the corresponding proton signal at low field, despite almost full deuteration of the polarised sample. Therefore, tests with a commercially available rf preamplifier have been carried out at liquid helium temperatures, to test whether it is possible to amplify the NMR signal already inside the cryostat to potentially increase the signal-to-noise ratio.

In Fig. 5.45 the preamplifier circuit including the LT NMR circuit is drawn. A InGaP amplifier (ERA-1+, DC-8 GHz, *Minicircuits*®) with a nominal amplification of +12 dB and a nominal operating temperature from -45°C to +85°C was used. The amplifier is internally matched to 50 Ω and represents together with the capacitor C_p a high-pass rf filter with a cut-off frequency of $f_\mathrm{c} = (2\pi \cdot C_\mathrm{p} \cdot 50\ \Omega)^{-1}$. The resistor R_1 and R_2 help to provide the amplifier with the necessary DC voltage of about 2-3 V and R_2 and C_p represent a low-pass rf filter.

For the 16 MHz NMR system, C_p was chosen to be 680 pF and R_1 = 470 Ω and R_2 = 150 Ω, with a DC voltage of about 15 V. This yields cut-off frequencies of 5 MHz for the high-pass and 1.5 MHz for the low-pass. A picture of the preamplifier circuit board is shown in Fig. F.18 in the appendix.

The preamplifier circuit was successfully operated at 4 Kelvin, although with slightly less amplification of about 1 dB and a higher DC voltage input of 16 V compared to room temperature operation. It also withstood several successive cool downs and warm ups.[31] However, it was decided not to implement the preamplifier circuit board in the cryostat, firstly because there was no visible improvement of the rf noise level and secondly to avoid possible complications using the amplifier at high magnetic fields.

---

[31] Moreover, a low noise amplifier ZFL-500 (+24 dB) by *Minicircuits*® has been tested, which also worked almost perfectly at these low temperatures.

5.4. Dynamic Nuclear Polarisation and Spin Relaxation

The technique of dynamic nuclear polarisation (DNP) is well explained in the book of Abragam and Goldman [Abr82]. Further descriptions of the method are given by Abragam [Abr78, Abr832], Borghini [Bor68, Bor71], Wenckebach [Wen74, Wen95] and others. Recently DNP has become of immediate interest in biomedical magnetic resonance, resulting in the first dedicated dynamic nuclear polarisation symposium held in Nottingham (UK) in 2007 [Pro08].
In the following section, we thus want to repeat just briefly the main ideas of the DNP technique.

5.4.1. Thermal Equilibrium Polarisation

The interaction of a spin $\vec{I}$, i.e. its associated magnetic moment $\vec{\mu} = \gamma\hbar\vec{I}$, with a magnetic field $\vec{B_0}$ yields $2I + 1$ Zeeman levels with the corresponding energies:

$$E_m = -m\gamma\hbar B_0 \ , \tag{5.9}$$

characterised by their magnetic quantum number m. In *thermal equilibrium* (TE) each of these levels is populated with a probability, which is proportional to the Boltzmann factor:

$$\exp\left(-\frac{E_m}{k_\mathrm{B}T_\mathrm{Z}}\right) \ , \tag{5.10}$$

where k_B is Boltzmann's constant 1.3806×10^{-23} J/K and T_Z is the temperature of an ensemble of identical spins (*spin temperature*). The polarisation P of this spin ensemble is defined as:

$$P = \frac{\sum\limits_m m \exp\left(-\frac{E_m}{k_\mathrm{B}T_\mathrm{Z}}\right)}{I \cdot \sum\limits_m \exp\left(-\frac{E_m}{k_\mathrm{B}T_\mathrm{Z}}\right)} \tag{5.11}$$

This leads in the case of $I = 1/2$ and $I = 1$ to:[32]

$$\text{Spin } 1/2\text{:} \qquad P_{1/2} = \tanh\left(\frac{\gamma\hbar B_0}{2k_\mathrm{B}T_\mathrm{Z}}\right) \tag{5.12}$$

$$\text{Spin } 1\text{:} \qquad P_1 = \frac{\sinh\left(\frac{\gamma\hbar B_0}{k_\mathrm{B}T_\mathrm{Z}}\right)}{1 + \cosh\left(\frac{\gamma\hbar B_0}{k_\mathrm{B}T_\mathrm{Z}}\right)} \tag{5.13}$$

As the magnetic moment of a nucleus is typically three orders of magnitude smaller than the Bohr magneton μ_B, *brute force* polarisation of nuclear spins requires temperatures in the millikelvin range and large magnetic fields of several Tesla (compare Fig. 5.46). Moreover, the nuclear spin relaxation time may under these conditions be excessively long, such that the spins do not relax in the energetically favoured orientation on a reasonable time scale.

---

[32] Ref. [Gre87] gives a derivation of the entropy, magnetisation and heat capacity C_B from the partition function and free energy of a system of non-interacting spins, respectively.

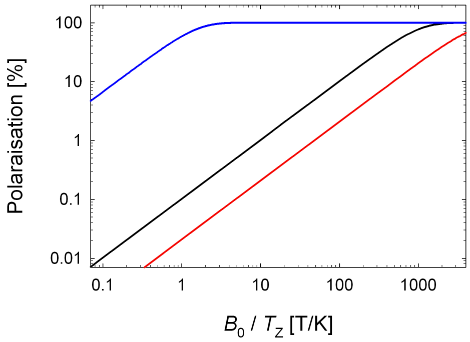

Figure 5.46: Thermal equilibrium spin polarisation of protons (black), deuterons (red) and electrons (blue) as a function of B_0/T_Z.

DNP is a technique, which allows to polarise nuclear spins in a solid under less restricted conditions [Wen08]. Therefore the solid needs to contain a certain amount of unpaired electron spins (paramagnetic centres or radicals). As the electron spins have a much larger magnetic moment and a very short spin-lattice relaxation time they easily reach polarisations of almost 100% at moderate temperatures of 1 Kelvin and typical magnetic fieds of 2.5 or 3.5 Tesla. Exploiting the dipolar interaction between the nuclear and electron spins, the electron polarisation/spin entropy can be transfered to the nuclear spin by irradiation of microwaves close to the electron paramagnetic resonance (EPR) frequency.

In insulators, the main mechanism responsible for the polarisation transfer is either the so-called (well-resolved) *solid effect* or *thermal mixing*, depending on whether the concentration of unpaired electrons is low or high, i.e. the mutual interaction between neighbouring electron spins can be neglected or not.

5.4.2. Spin Relaxation of Nuclear and Electron Spins

Before we consider the DNP mechanism, it is important to understand the relaxation processes of the nuclear and electron spins in a diamagnetic solid.

At temperatures and fields used for DNP (below 1 Kelvin and above 1 Tesla) the electron spin relaxation is causes by the so-called *direct process*, i.e. absorption or emission of a single phonon of energy $\hbar\omega_\mathrm{s}$, where ω_s is the electron Larmor frequency of the spin in the magnetic field. In Ref. [Abr82] it is shown that the resulting (longitudinal) electron spin-lattice relaxation time $T_{1,\mathrm{e}}$ is proportional to:

$$\frac{1}{T_{1,\mathrm{e}}} \propto \omega_\mathrm{s}^5 \cdot \coth\left(\frac{\hbar\omega_\mathrm{s}}{2k_\mathrm{B}T}\right) \tag{5.14}$$

Hence, $T_{1,\mathrm{e}}$ mainly depends on the shape of the phonon spectrum and the number of phonons of energy $\hbar\omega_\mathrm{s}$ per mode and is typically of the order 10^{-1} s.

In Equ. (5.14) it is assumed that the phonons are in thermal equilibrium with the surrounding thermal bath. Often this is not the case and a so-called *phonon bottleneck* occurs, which increases $T_{1,\mathrm{e}}$ and thus limits the nuclear spin polarisation achievable with DNP. Then the spin relaxation process can be described as follows: first the electron spins and the phonons reach a common temperature, while in a second step the whole system relaxes towards the temperature of the bath.

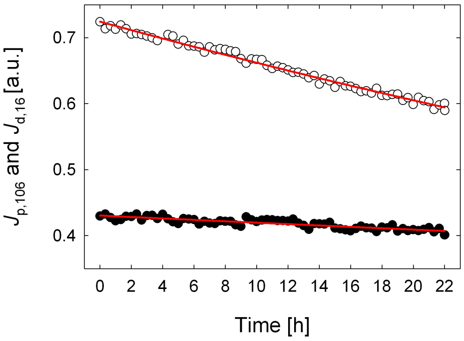

Figure 5.47: Nuclear spin relaxation at 2.5 Tesla and 110 mK. The NMR signal integrals of the negatively polarised protons (●) and deuterons (○) have been measured in intervals of 20 minutes. The exponential fits (red curves) yield $T_{1,\mathrm{p}} = (395 \pm 30)$ h and $T_{1,\mathrm{d}} = (111 \pm 1)$ h (sample #15).

In general, the nuclear spin relaxation time is several orders of magnitude longer than the one of the electrons, as the direct process is suppressed due to the low density of phonon states at the Zeeman energy $\hbar\omega_\mathrm{I}$ of the nuclear spins. Instead the nuclear spins relax via the dipolar interaction of a nuclear spin $\vec{I}$ with a neighbouring electron spin $\vec{s}$ (paramagnetic impurities), which allows mutual spin flips and the associated absorption or emission of a single phonon of energy $\hbar(\omega_\mathrm{s} \pm \omega_\mathrm{I})$.[33]
As the dipolar interaction depends on the direction, we also obtain a nuclear spin relaxation time $T_{1,\mathrm{N}}(\vec{r})$, which depends on the relative coordinate $\vec{r}$ between the electron and the nucleus:

$$\frac{1}{T_{1,\mathrm{N}}(\vec{r})} = \left(\frac{3\mu_0\hbar\gamma_\mathrm{e}}{4\pi}\right)^2 \cdot \frac{\sin^2\theta\cos^2\theta}{r^6} \cdot \frac{\left(1-P_\mathrm{e}^2\right)}{B_0^2} \cdot \frac{1}{T_{1,\mathrm{e}}} , \tag{5.15}$$

where P_e is the thermal equilibrium polarisation of the electron spins. Hence, the factor $(1 - P_\mathrm{e}^2)$ in Equ. (5.15) expresses, that the number of flipping electron spins decreases with increasing electron polarisation, which results in a strong temperature and field dependence of the nuclear spin relaxation time.
So far we neglected the so-called *transverse relaxation times* $T_{2,\mathrm{e}}$ and $T_{2,\mathrm{N}}$, which describe mutual flips among electrons spins and among nuclear spins, respectively. This spin-spin interaction of the nuclear spins equalises nuclear polarisation gradients very fast, as $T_{1,\mathrm{N}} \gg T_{2,\mathrm{N}}$. Therefore $T_{1,\mathrm{N}}(\vec{r})$ can be spatially averaged yielding a mean nuclear relaxation time of $T_{1,\mathrm{N}}$ ranging from 10^3 to 10^6 s (compare also *spindiffusion* and *diffusion barrier* in Ref. [Abr82]).

Fig. 5.47 presents the measurement of the nuclear spin relaxation of protons and deuterons at 110 mK and 2.5 Tesla in one of our samples using cw-NMR. The relaxation times $T_{1,\mathrm{p}}$ and $T_{1,\mathrm{d}}$ exceed 100 hours.[34]

---

[33] These spin flips, often called flip-flip and flip-flop transitions, are only allowed by first order perturbation theory (compare *scrambled state approach* and section 5.4.3).

[34] The faster spin relaxation time of the deuterons compared to the protons is a result of their quadrupole interaction.

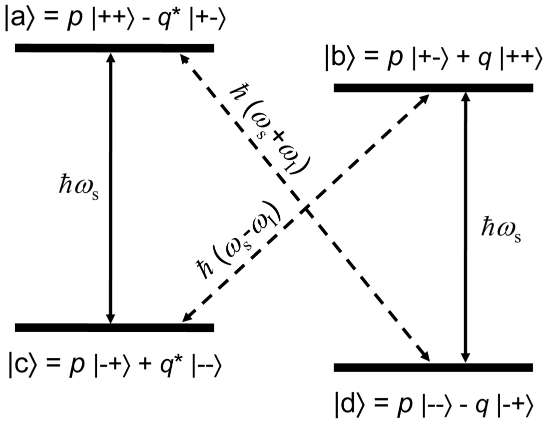

Figure 5.48: Eigenvalues of a nucleus-electron pair of spins 1/2 coupled by the dipolar interaction (compare Fig. 6.2 in [Abr82]). The states $|a\rangle$, $|b\rangle$, $|c\rangle$ and $|d\rangle$ are linear combinations of the unperturbed states $|{+}{+}\rangle$, $|{+}{-}\rangle$, $|{-}{+}\rangle$ and $|{-}{-}\rangle$, where the first sign ($+$ or -) denotes the spin of the electron and the second sign the spin of the nucleus, with $p = \sqrt{1 - qq^*} \approx 1$ and $q \ll 1$. The dashed arrows represent the flip-flip and flip-flop transitions, which are forbidden without the dipolar interaction.

5.4.3. The Well-Resolved Solid Effect

In the polarised target of the nd-experiment the well-resolved solid effect (SE) is not responsible for the dynamic nuclear polarisation. Nevertheless, it is worth discussing the SE, as it intuitively illustrates the general mechanisms of DNP.
Let us first consider an assembly of nuclear spins $I = 1/2$ with the nuclear Larmor frequency ω_I embedded in a solid that contains a low concentration of paramagnetic centres with spin $s = 1/2$ and the Larmor frequency ω_S. As the concentration of the centres is low, the mutual interaction between the electron spins (electron spin-spin interaction) can be neglected and we can assume for simplicity an isolated electron-nucleus pair with the energy eigenvalues depicted in Fig. 5.48. Due to the dipolar interaction between the two spins, new states are generated, which are linear combinations of the unperturbed states. Moreover, former forbidden transitions become allowed by first order perturbation theory (flip-flop transition: $|b\rangle \leftrightarrow |c\rangle$ and flip-flip transition: $|a\rangle \leftrightarrow |d\rangle$).[35] Further, it is assumed that the electronic linewidth $\Delta\omega_\mathrm{S}$ is much smaller than the nuclear Larmor frequency and the transitions of frequencies $\omega_\mathrm{S} \pm \omega_\mathrm{I}$ and ω_S do not overlap and that a microwave field tuned to any of them cannot drive either of the other two.[36]

At low temperatures and large magnetic fields the population probability for the states $|c\rangle$ and $|d\rangle$ is much larger than for $|a\rangle$ and $|b\rangle$, since $\hbar\omega_\mathrm{S} \gg k_\mathrm{B}T$. Assume now that we force flip-flop transitions by irradiating microwaves with the frequency $\omega_\mathrm{S} - \omega_\mathrm{I}$ and that the strength of the source is such that the rate at which the transitions occur is much greater than the nuclear spin relaxation rate $T_{1,\mathrm{N}}^{-1}$. Hence, the state $|b\rangle$ gets populated, but due to the fast electron spin-lattice relaxation the electron

---

[35] For a detailed calculation of the states and the transition probabilities see also Ref. [Pie04].

[36] Actually, this condition is violated in most substances where DNP is observed due to inhomogeneous broadening of the linewidth caused by: the anisotropy of the electron g-factor, the hyperfine coupling with neighbouring nuclei and the spin-spin interaction between electrons.

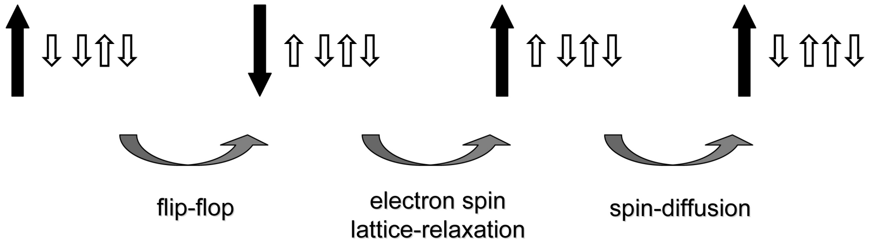

Figure 5.49: Scheme of the spin diffusion process. A microwave induced flip-flop process causes the simultaneous transition of a electron and a neighbouring nuclear spin. The electron relaxes very fast in its initial direction and mutual spin flips between nuclear spins transfer the polarisation into the sample.

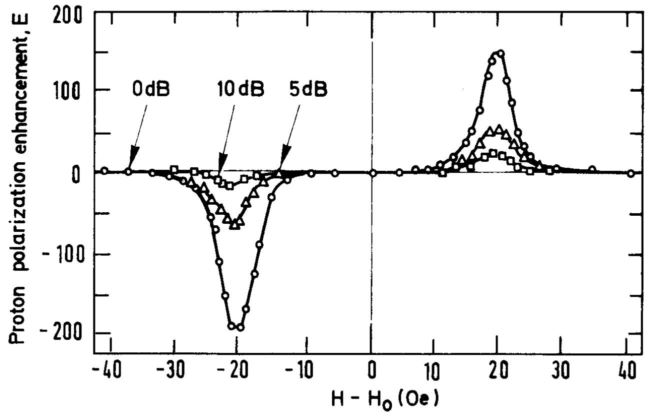

Figure 5.50: Enhancement of the proton polarisation by the solid effect in LMN:Nd for three different microwave powers by Schmugge and Jeffries. Instead of changing the microwave frequency the external magnetic field was shifted to cause either positive or negative polarisation. Taken from Ref. [Abr82].

spin almost immediately flips back into its initial direction and we arrive at state $|d\rangle$. This process thus corresponds to a pumping of the population probability from state $|c\rangle$ to $|d\rangle$, which causes nuclear spins close to an electron spin to polarise.[37] Next the polarisation is transported further away by means of flip-flop transitions of neighbouring nuclear spins. The process, which is called spin-diffusion, is depicted in Fig. 5.49.

It is clearly seen that for DNP only a low concentration of paramagnetic centres is necessary, as $T_{1,\mathrm{e}} \ll T_{1,\mathrm{N}}$ and therefore one electron spin can serve to polarise thousands of nuclear spins.

In Fig. 5.50 a classical example of the well-resolved solid effect is presented by the observation of DNP in LMN:Nd [Sch65].[38] The two peaks of the proton polarisation enhancement are well-separated.

---

[37] Of course, the same holds for the irradiation of microwaves with the frequency $\omega_\mathrm{S} + \omega_\mathrm{I}$ and forced flip-flip transitions.

[38] Lanthanum magnesium nitrate doped with neodymium Nd^{3+}.

5.4.4. Thermal Mixing

A necessary condition for the validity of the theory of DNP by the solid effect, is a low concentration of paramagnetic centres. If this condition is not fulfilled, the electron spin-spin interaction is not negligible and electron flip-flops occur at a rate of $T_{2,\mathrm{e}}^{-1}$ much faster than $T_{1,\mathrm{e}}^{-1}$. Hence, the picture of the isolated electron-nucleus pair breaks down. Instead, we can consider the electron spins acting as a whole.
Thermal mixing now means that this system of interacing electron spins (also called *electron non-Zeeman reservoir* or *electron spin-spin system*) is in good thermal contact with the nuclear Zeeman system and both reach rapidly a common spin temperature T_{ss}, which can differ from the electron Zeeman spin temperature T_{Z}.[39] This relaxation process is possible because of the broad EPR linewidth[40], which allows that two electron spins are able to perform a flip-flop transition, while at the same time a nuclear spin is flipped (three spin process). Note, thermal mixing thus even exists in the absence of microwave irradiation.
The gist of the DNP mechanism is now to cool the electron spin-spin system by irradiation of microwaves close to the electron Larmor frequency ω_{s}, which is then transfered via thermal mixing to the nuclear Zeeman system and thus induce nuclear polarisation (compare Fig. 5.51 and Ref. [Gol08]).

The first experimental proof of the strong thermal coupling between the nuclear Zeeman and the electron non-Zeeman reservoirs was given by Wenckebach and co-workers in 1969 using a paramagnetic crystal of LMN:Nd [Wen69].
This was confirmed in 1974 by DeBoer and co-workers, who compared the Zeeman spin temperatures of several nuclear species present in a deuterated ethandiol sample throughout the whole duration of the DNP process (^{1}H, ^{2}H and ^{13}C) [DeB74]. They found that the spin temperatures deduced for each nuclear species turned out to be equal at all time, while the ratios of the spin polarisations did not remain constant. This is a natural consequence of the existance of a strong coupling between the nuclear spin species mediated by the electron spin-spin system.

An example of a thermal equilibrium NMR signal and a polarised NMR signal of a sample used for the nd-experiment is presented in Fig. 5.52.

---

[39] Rapidly means here on a time scale shorter than any other process affecting the two spin systems.
[40] The broadening of the EPR line, i.e. $\Delta\omega_{\mathrm{s}} \gg \omega_{\mathrm{I}}$, is mainly caused by the g-factor anisotropy.

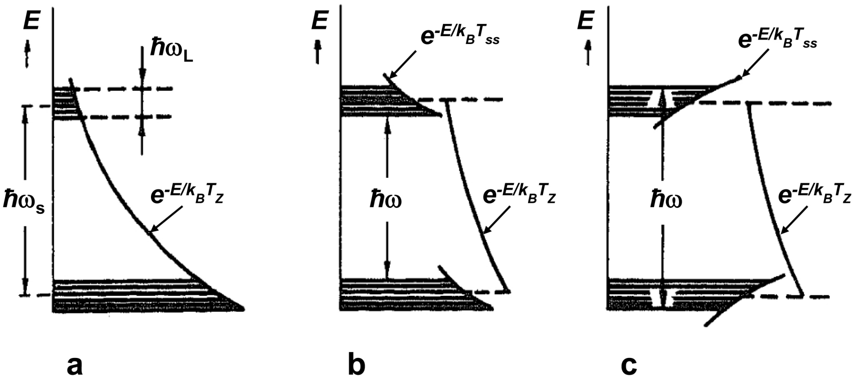

Figure 5.51: The distribution of the population as a function of the energy. Due to the electron spin-spin interactions, the Zeeman levels have a certain width $\hbar\omega_{\rm L}$. (a) In thermal equilibrium with the lattice the distribution can be described by one spin temerpature, i.e. $T_{\rm Z}$ = $T_{\rm ss}$. (b) During microwave irradiation at a frequency ω the spin system may be described by two spin temperatures, $T_{\rm Z}$ and $T_{\rm ss}$. If ω < $\omega_{\rm s}$ the populations become such that $T_{\rm Z}$ > $T_{\rm ss}$ > 0. (c) As in (b) but for ω > $\omega_{\rm s}$. Then $T_{\rm ss}$ may become negative. Compare also Ref. [DeB76].

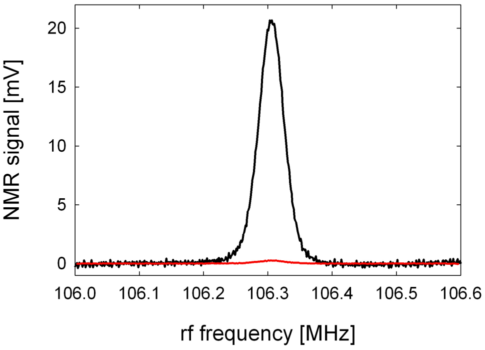

Figure 5.52: Comparison of the NMR signals from a sample with dynamically polarised protons (black curve: $J_{\rm p,106} = 0.90$ [a.u.], $P_{\rm p}$ = 17%) and from the same sample with TE proton polarisation at 1.1 Kelvin and 2.5 Tesla (red curve, average of 30 signals: $J_{\rm p,106} = 0.012$ [a.u.], $P_{\rm p,TE}$ = 0.23%). Using sample #10 (see appendix E).

6. Beam Times and Measurements

In this chapter the seven beam times of the nd-experiment will be summarised. They have been carried out at the fundamental cold neutron physics beam line FUNSPIN at the spallation source SINQ at the Paul Scherrer Institute. Firstly, each individual beam time will be described with their most important measurements, while afterwards two measurements of $b_{\mathrm{i,d}}$ from the beam times four and six will be presented.

6.1. Summaries of the Beam Times

6.1.1. First Beam Time (Summer 2004)

During the first beam time (June, 1^{st} 2004 – July, 5^{th} 2004) the neutron Ramsey apparatus was successfully commissioned and first Ramsey test measurements could be performed: first measurements of a Ramsey pattern, stabilisation measurements, test of the two beam method etc. The apparatus consisted entirely of components used previously in Saclay in the 1970's [Abr733]. Instead of a polarised nuclear spin target, a small auxiliary coil was used to simulate the pseudomagnetic effect.
A detailed description of the first beam time and its results are given in Ref. [Pie04].

6.1.2. Second Beam Time (Summer 2005)

In the second beam time (June, 1^{st} 2005 – September, 7^{th} 2005) the neutron setup was refined, resulting in improved Ramsey signals presented in Fig. 6.1. For comparison also a typical Ramsey signal from the first beam time is shown. The frequency scans exhibit now more wiggles, also their amplitude could be slightly increased and the background resonance curve became broader. This allows to measure pseudomagnetic phase shifts well beyond 1000°, which is necessary to reach the aimed phase measurement accuracy.
These improvements are caused by the replacement of the previous neutron monochromator mirror ($\Delta\lambda/\lambda = 15\%$) by one of the specially designed mirrors presented in section 5.1.4 ($\Delta\lambda/\lambda = 6\%$). Also the original $\pi/2$-spin flippers were substituted by two new ones, which are now placed on a platform to adjust their position in all three dimensions. Moreover, their solenoid rf coils have a larger diameter to accommodate two neutron beams (implementation of the two beam method). More details on these and other improvements (better collimation system, detector box with two ^{3}He gas tube detectors etc.) can be found in the diploma thesis by B.S. Schlimme [Sch05].

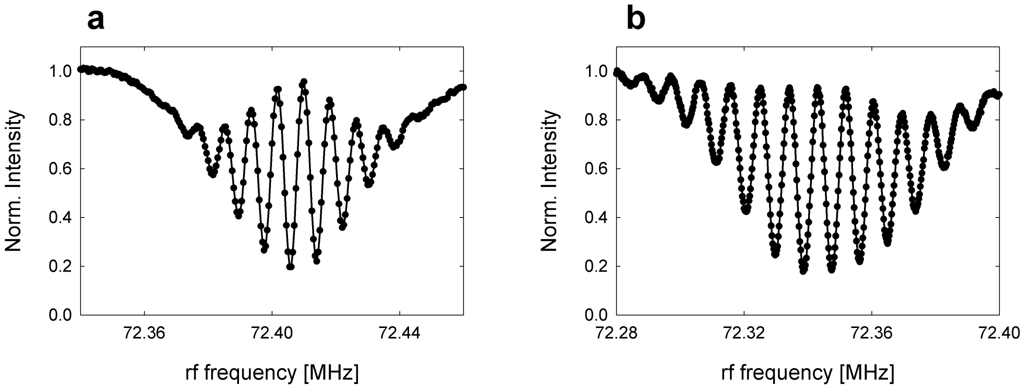

Figure 6.1: Comparison of typical Ramsey frequency scans taken during the beam times in (a) summer 2004 and in (b) summer 2005.

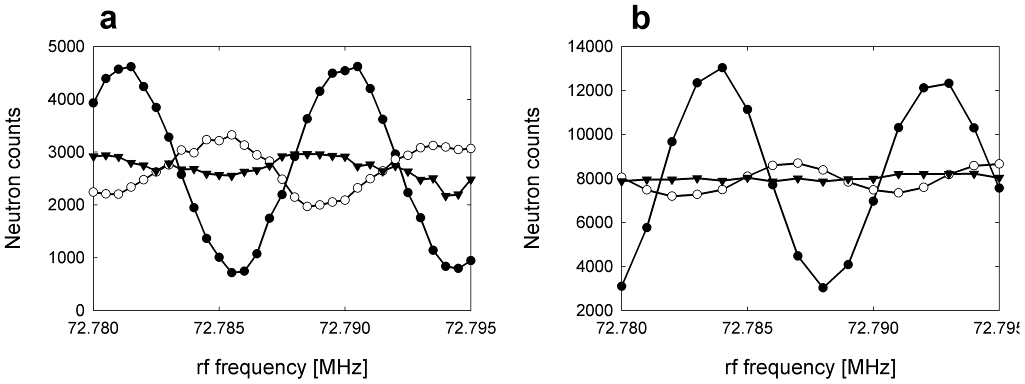

Figure 6.2: First results obtained with polarised nuclear targets. The plots show the centre of a complete Ramsey signal (see Fig. 6.1). The pseudomagnetic phase shifts are accompanied by a strong damping of the signal amplitudes already for small pseudomagnetic phase shifts, i.e. degrees of nuclear spin polarisation. (a) d-polystyrene (sample #0b, see appendix E). (b) d-PS mixed with 10 wt.% p-terphenyl (sample #0c). Thermal equilibrium polarisation (●), $P_\mathrm{p} \approx 2.5\%$ (○) and $P_\mathrm{p} \approx 10\%$ (▼).

In this beam time, the polarised frozen spin target was employed for the first time. As shown in Fig. 6.2, a phase shift of the Ramsey signal was observed due to the pseudomagnetic neutron precession in the polarised nuclear target. Unfortunately, the phase shift was accompanied by a severe damping of the signal. Both investigated targets (d-PS and d-PS mixed with p-terphenyl) showed similar damping already at a low degree of nuclear polarisation. An obvious reason for the origin of this effect are inhomogeneities of the sample density and/or of the nuclear polarisation [Bra061]. Due to the utilisation of the dilution refrigerator described in section 5.2.1, it was not possible to test more than two target materials during several weeks of beam time. Hence, for the following beam time it was decided to modify the nd-cryostat and to employ the ^{4}He evaporation inserts introduced in section 5.2.2, which allow for a quick change of the samples.

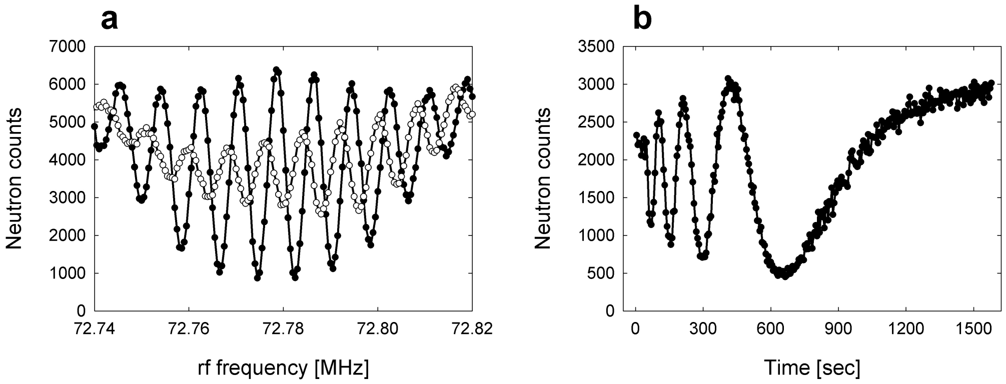

Figure 6.3: Pseudomagnetic phase shift and relaxation measurement using a 1.6 mm thick d-PS sample (sample #9). (a) Ramsey signal at thermal equilibrium polarisation (●) and at $P_\mathrm{p} \approx 20\%$ (○). The measuring time per data point is about 10 sec. (b) Demonstration, that the observed phase shift is indeed about 1350°: measurements of the neutron intensity at a fixed rf frequency, during the relaxation of the nuclear spin polarisation at 1.1 Kelvin.

6.1.3. Third Beam Time (Winter 2005)

The third beam time (November, 14th 2005 – December, 22nd 2005) was dedicated to conduct a systematic investigation of target materials and polarisation methods (frequency modulated microwaves etc.) using a ^{4}He bath cryostat.[1] A series of 12 different samples (frozen alcohols and polystyrene – samples #1-#12, see appendix E) has been tested. The best results in terms of nuclear polarisation homogeneity, i.e. visibility of the Ramsey oscillations, and spin relaxation time were obtained with a sample of the same material as used in the previous beam time, prepared by a slightly modified procedure (longer baking of the d-PS foils at higher temperatures – compare section 5.2.4). The Ramsey signals are now well visible even for a large pseudomagnetic phase shift of about 1350° (see Fig. 6.3).

One of the investigated samples was a $14 \times 14 \times 3$ mm^3 n-polystyrene slab with a weight of 606 mg (sample #1). It was placed in the beam of the Ramsey apparatus such that the neutrons see a target thickness of 3 mm. Fig. 6.4a shows several Ramsey signals taken at different temperatures of the sample, i.e. different thermal equilibrium polarisations (compare section 5.4.1). A temperature decrease causes an increase of the proton spin polarisation, which shifts the Ramsey oscillations to higher frequencies. The phase shifts of these oscillations could be determined with an accuracy of ±0.9°. In Fig. 6.4b these are plotted against the inverse temperature, showing the expected linear behaviour with a slope of $(115 \pm 3_{\,\mathrm{stat}} \pm 8_{\,\mathrm{syst}})^\circ$ K/mm, which is close to the estimated value of 102° K/mm, which results from Equ. (3.38) and (5.12). The systematical error is due to uncertainties of the neutron wavelength[2] and of the nuclear number density at 1 Kelvin and is estimated to be about 7% in total [Pie082].

---

[1] Please note, that the ^{4}He bath cryostat cannot provide the low temperature required to keep the nuclear spin relaxation at an acceptable level for the actual measurement of $b_{\mathrm{i,d}}$.

[2] The neutron wavelength was not measured, but just calculated from the reflectivity curve of the monochromator mirror.

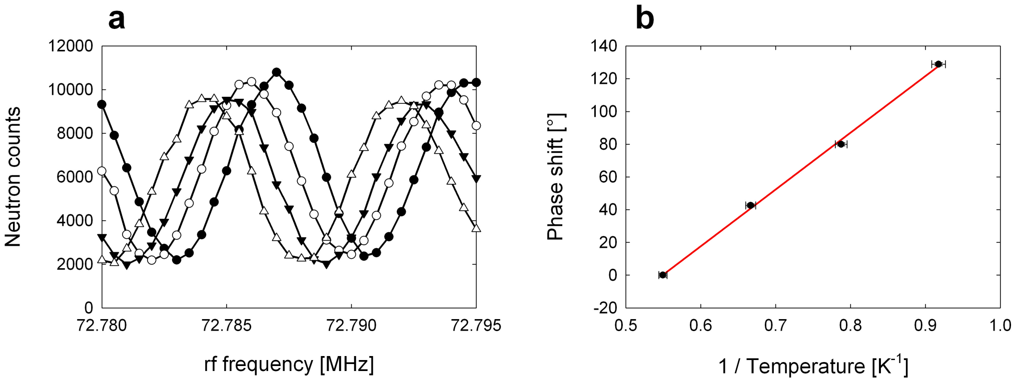

Figure 6.4: (a) Ramsey signals measured with a 3 mm thick n-polystyrene sample at four temperatures: $T_s = 1.82$ K (△), $T_s = 1.50$ K (▼), $T_s = 1.27$ K (○) and $T_s = 1.09$ K (●). With decreasing temperature the proton polarisation increases, which leads to a shift of the Ramsey oscillations to higher frequencies. (b) Phase shift due to the decrease of the sample temperature and linear fit (red line). The phase shift of the data point measured at $T_s = 1.82$ K has been arbitrarily set to 0°. Error bars: temperature ±1% and phase shift ±0.9°.

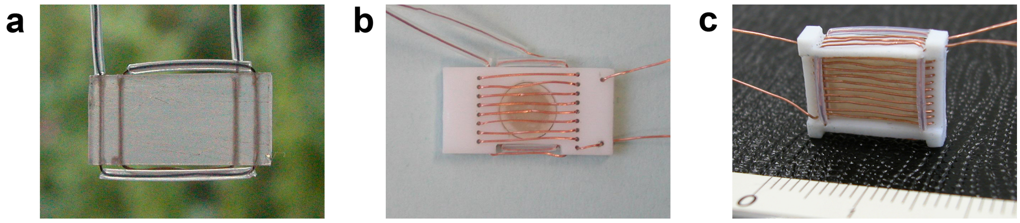

Figure 6.5: Changes of the geometry of the polarised targets over the beam times. (a) Sample from the fourth beam time with a size of about $14 \times 7 \times 1.2$ mm^3 (sample #13). The 16 MHz NMR coil is not yet wound on the sample. NMR coil windings: $N_{16} = 6$ and $N_{106} = 2$. (b) Sample from beam times five and six with a diameter of 5 mm and a thickness of 1.2 mm (sample #14). The 25 mg sample disc is made from the sample platelet used in 2006. The NMR coils are now wound on a PTFE support frame: $N_{16} = 8$ and $N_{106} = 2$. (c) Sample from the last beam time with a size of $10 \times 8 \times 1.3$ mm^3 and a weight of 110 mg (sample #15). NMR coil windings: $N_{16} = 10$ and $N_{106} = 4$.

6.1.4. Fourth Beam Time (Summer 2006)

During the fourth beam time (August, 21th 2006 – September, 5th 2006) a first complete run with measurements of Ramsey and NMR signals could be performed using sample #13 presented in Fig. 6.5a. From these data we could determine first values for the incoherent scattering length $b_{i,d}$. The results are presented in section 6.2 showing large systematic errors, which are caused by polarisation inhomogeneities, depolarisation of the nuclear spins[3], the LT NMR system and the fact that the sample was much larger than the employed neutron beam with a diameter of about 3 mm [Bra07].[4]

---

[3] The 106 MHz coil was used to destroy and measure the proton polarisation. Hence, it probably occurred that we only depolarised the nuclei close to the windings and not the entire sample.

[4] Further, in this beam time the old Saclay magnet power supply broke down and had to be replaced.

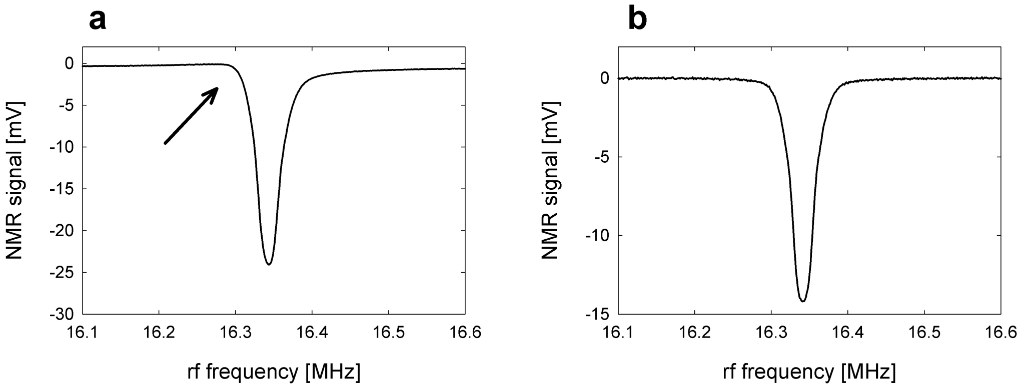

Figure 6.6: (a) In summer 2006 the 16 MHz NMR system showed large dispersion contributions to the absorption signal (asymmetry, red arrow). Sample #13: $J_{\mathrm{p},16} = -0.80$ [a.u.], which corresponds to $P_{\mathrm{p}} \approx -23\%$. (b) In winter 2006 the coaxial cables have been exchanged (with 50 Ω impedance cables instead of the accidentally used 40 Ω cables). Sample #14: $J_{\mathrm{p},16} = -0.48$ [a.u.], which corresponds to $P_{\mathrm{p}} \approx -32\%$.

6.1.5. Fifth Beam Time (Winter 2006)

In the fifth beam time (November, 22$^{\mathrm{nd}}$ 2006 – December, 22$^{\mathrm{nd}}$ 2006), we thus concentrated on the suppression of these systematic errors, by guaranteeing that the measurements of the pseudomagnetic precession angle and the NMR signals are performed as exactly as possible for the same sample of polarised nuclei. Firstly, we changed the sample geometry, i.e. we used a sample with approximately the same size as the neutron beam and redesigned the NMR coils to provide homogeneous sampling of the nuclear polarisation (see Fig. 6.5b). The result of using such a small sample is that the obtained NMR signals have a worse signal-to-noise ratio. Secondly, we implemented a separate coil to homogeneously destroy the nuclear polarisation (saddle coil with a volume of $20 \times 11 \times 7$ mm^3). And thirdly, a problem with the 16 MHz LT NMR system leading to a strong dispersion contribution in the NMR absorption signal was cured by using a different type of low temperature coaxial cable (compare Fig. 6.6).
With the dilution refrigerator a higher nuclear polarisation was achievable resulting in pseudomagnetic precession angles of more than 2000°. As shown in Fig. 6.7, the Ramsey wiggles are still well visible and allow for a precise extraction of the phase shift. A maximum visibility of the oscillations was obtained using maximum microwave power and wide frequency modulation of ±0.5% at a centre frequency of about 70 GHz with a modulation frequency of typically 1 kHz.

Nevertheless, a scan of the sample with a beam of only 1.5 mm diameter showed that the phase shift acquired by the neutrons passing through the sample was still not perfectly homogeneous. As presented in Fig. 6.8, phase shifts differed by several tens of degrees at three different sample positions (upper, middle and lower part of the sample), when the sample was almost fully polarised. However, the situation was much better compared with the second beam time, when the inhomogeneities had been so large that the Ramsey signals had became invisible already at small nuclear polarisations.

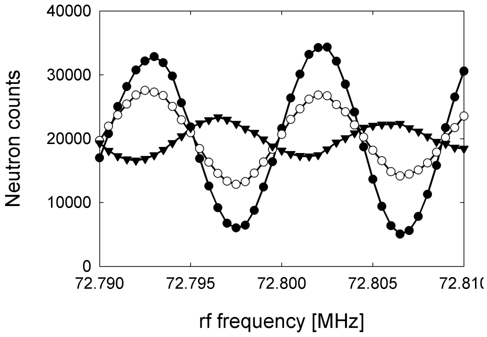

Figure 6.7: Ramsey frequency scans, performed for three different degrees of nuclear polarisation: unpolarised sample (●), $P_\mathrm{p} \approx -30\%$ and $P_\mathrm{d} \approx -5\%$ corresponding to a phase shift of about -1080° (○) and $P_\mathrm{p} \approx -55\%$ and $P_\mathrm{d} \approx -15\%$ corresponding to a phase shift of about -2400° (▼).

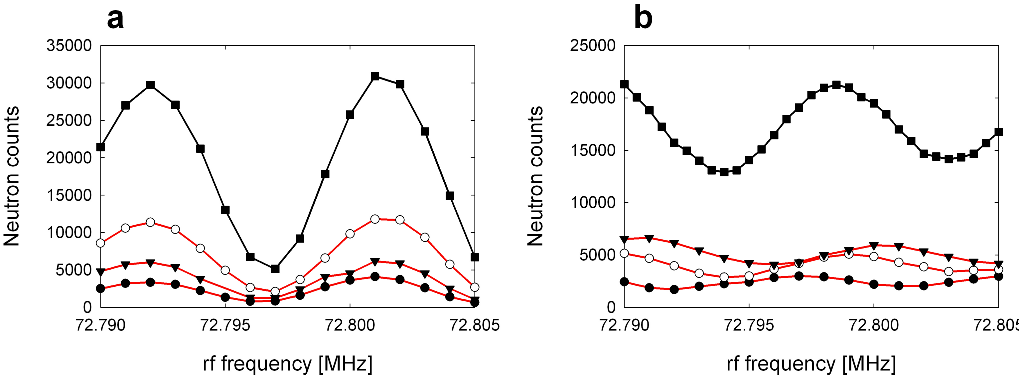

Figure 6.8: Ramsey scan on sample #14 using a neutron beam with a diameter of about 3 mm (black curves). Ramsey frequency scan performed with a neutron beam with a diameter of only 1.5 mm at three different positions through the sample (red curves: upper (●), middle (▼) and lower part of the sample (○)) (a) With the unpolarised sample, there is no visible phase shift spread between the three sample positions. (b) Polarised sample with $P_\mathrm{p} \approx -45\%$ and $P_\mathrm{d} \approx -11\%$ corresponding to a phase shift of about -1900°. The relative phase shift spread stays approximately within ±4%, which is of the same order as the width of the neutron wavelength distribution $\Delta\lambda/\lambda_0$.

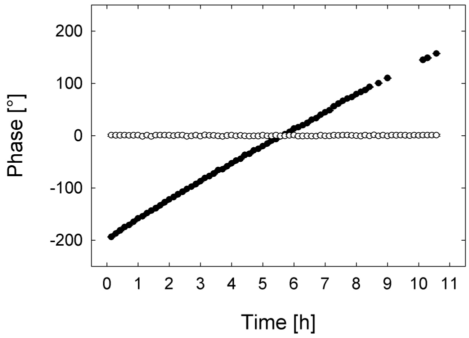

Figure 6.9: Phase shift of the Ramsey signal during the relaxation of the nuclear polarisation at T_c = 170 mK and 2.5 Tesla (sample beam (•) and reference beam (○)). The total phase shift at the beginning of the measurement was about 2000° decaying with approximately 35°/h. The nuclear relaxation times have been measured with NMR: $T_{1,p} \approx 90$ h and $T_{1,d} \approx 40$ h.

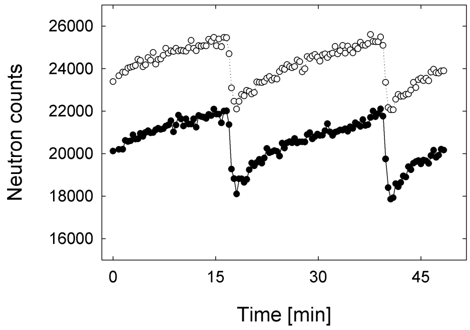

Figure 6.10: Drifts in the neutron count rates of up to ±10% in the sample beam (•) and reference beam (○), caused by the refill cycle of the helium bath.

The main limitation in this beam time was a high base temperature of about 150-170 mK in the target cell, which was probably caused by a leak in the condensation line of the dilution insert. As a result the nuclear spin relaxation was too fast for a reasonable measurement of the pseudomagnetic phase shift, i.e. the nuclear polarisation could not be considered frozen during a Ramsey measurement of 10-15 min. This is demonstrated in Fig. 6.9, where the change of the pseudomagnetic phase shift was measured as a function of time. Moreover, the loss per sequence was as large as 20% during the field sweep of the NMR cross-calibration.

A second problem was due to the restricted sample size. The precise beam collimation made the system more susceptible to shifts of the sample aperture with respect to the neutron beam, e.g. caused by the refill cycle of the helium bath and associated thermal contraction and expansion of the cryostat (see Fig. 6.10).

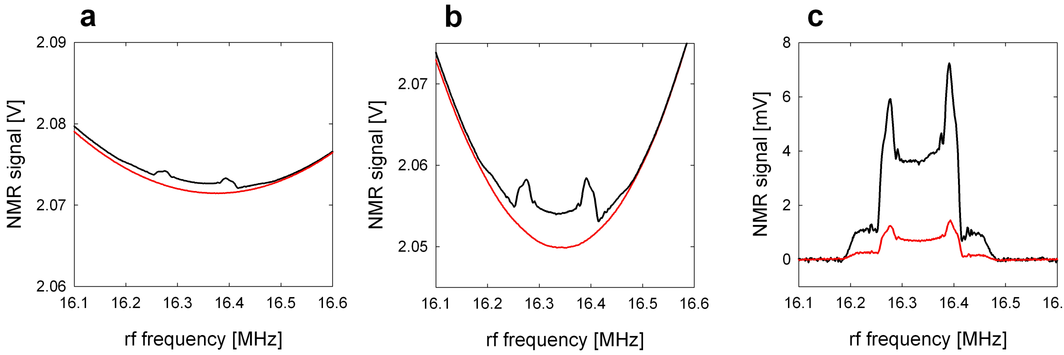

Figure 6.11: Comparison of the deuteron NMR signals obtained in 2007 with sample #14 and in 2008 with sample #15. (a) NMR foreground (black) and background (red) in 2007. (b) The same measurement in 2008. The nuclear polarisation was approximately the same in both years. (c) Direct comparison of the deuteron signals: $J_{\mathrm{d},16} = 0.13$ [a.u.] (2007, red) and $J_{\mathrm{d},16} = 0.67$ [a.u.] (2008, black).

6.1.6. Sixth Beam Time (Summer 2007)

In the following beam time (April, 19th 2007 – June, 23rd 2007) the problem with the dilution insert could be solved, allowing us to achieve again sample temperatures of 110 mK. This increased the nuclear spin relaxation time and reduced the phase shift during the Ramsey frequency scans from previously 35°/h down to about 18°/h at a similar degree of nuclear spin polarisation.[5] Moreover, as a result of a more careful alignment and fixation of the cryostat with holding clamps, the drifts due to the helium refill cycle could be completely suppressed.[6]

Using the same sample as in the previous beam time (sample #14), an improved measurement of the incoherent neutron-deuteron scattering length compared to the fourth beam time could be performed. The accuracy of the measurement of $b_{\mathrm{i,d}}$ was directly limited by the size of the proton and deuteron NMR signals (see section 6.1.7). Further details of this beam time and its results are presented in section 6.3.

6.1.7. Seventh Beam Time (Summer 2008)

The only way to improve the NMR signal size, as we are already using state of the art cw-NMR techniques, is to increase the sample mass. This was the basic idea for the last beam time (July, 25th 2008 – September, 1st 2008). In order to still fully illuminate the target by the neutron beam, the Ramsey setup had to be modified to accommodate a large neutron beam (collimation, new spin flippers etc.). The larger beam allowed us to use a correspondingly larger sample (compare Fig. 6.5c), which increased the number of nuclei sampled by the NMR coils by more than a factor 4. Also the filling factor and the number of coil windings could be increased, where the latter leads to a higher Q-value of the resonance [Bra091]. In Fig. 6.11 the deuteron NMR signals from 2007 and 2008 are compared showing a signal integral improvement of more than a factor 5.

---

[5] The deuteron spin relaxation time during this measurement was $T_{1,\mathrm{d}} \approx 130$ h. The proton relaxation time could not be determined due to problems with the 106 MHz NMR system.

[6] Attempts to keep the helium level constant by employing an additional pump on the helium exhaust of the cryostat were not successful.

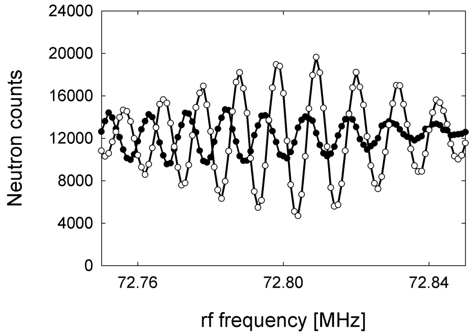

Figure 6.12: Comparison of the Ramsey oscillations employing a rectangular neutron beam (λ_0 = 4.4 Å) with a cross-section of 8 × 7 mm^2: without correction coils (●) and with correction coils using a current of 5 A (○). The complete Ramsey frequency scan was already presented in Fig. 5.12b.

For this beam time a batch of target samples, slabs of 97% deuterated polystyrene doped with d-TEMPO ranging in concentration between 1.5 and 2.5 × 10^{19} cm^{-3} (samples #15-#18 in appendix E), has been prepared and DNP tests performed in the laboratory cryostat (1 Kelvin, 3.5 Tesla). Sample #15 with 2 × 10^{19} cm^{-3} d-TEMPO was found to be the optimum with respect to maximum polarisation and slow spin relaxation.

During the beam time it turned out that the field produced by the 2.5 Tesla magnet was not homogeneous enough to employ a neutron beam with a cross-section of up to 1 cm^2, as the smearing of the Ramsey signals became too severe. However, we obtained promising results using a pair of gradient correction coils[7] mounted on the pole pieces of the magnet, which considerably improved the visibility of the Ramsey oscillations (see Fig. 6.12).

Using a CCD-camera instead of the ^{3}He detectors allows to perform the newly developed neutron spin phase imaging technique [Pie081] and to measure a phase map over the whole beam cross-section. Fig. 6.13 presents the phase maps obtained with and without the correction coils, which clearly demonstrate the improvement in homogeneity when using the coils. The corresponding horizontal cuts through the phase maps are given in Fig. 6.14a and exhibit a linear gradient, which becomes smaller with increasing current.[8] At a current of approximately 7 A the gradient cancels completely (extrapolation), but would require additional cooling of the coil windings. Each coil has an ohmic resistance of 2 Ω, which yields a total power of 2 × 50 W at 5 A. At this current the coils can still be operated without providing further cooling.

Moreover, the additional magnetic field by the correction coils does not harm the phase stability of the Ramsey apparatus. This was tested in a 17 hours measurement (compare Fig. 6.15), which demonstrated a stability between the phases of the two partial beams of ±0.75°, i.e. still better than the necessary absolute accuracy of about one degree (compare section 5.1).

---

[7] A set of split pair coils was used with opposite direction of the electric currents. Compare Fig. F.5 in the appendix.

[8] Note, the vertical cut through the spin phase map depicted in Fig. 6.14b shows the same parabolic shape as the magnetic field in Fig. 5.9b.

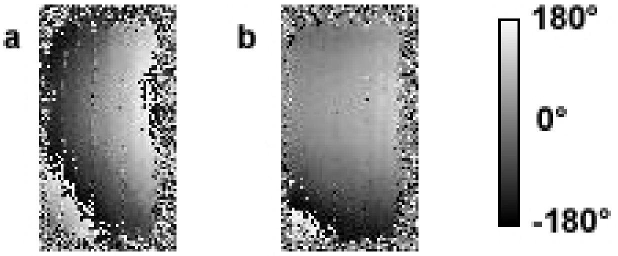

Figure 6.13: Neutron spin phase maps/images over the beam cross-section measured with a CCD-camera using a binning of 2×2 pixels [Müh05]. The distance between the centre of the magnet and the camera was approximately 80 cm. (a) Without correction coils. (b) With correction coils and a current of 5 A in each coil. The images have a size of 50×90 pixels, which corresponds to about 13×23.5 mm^2.

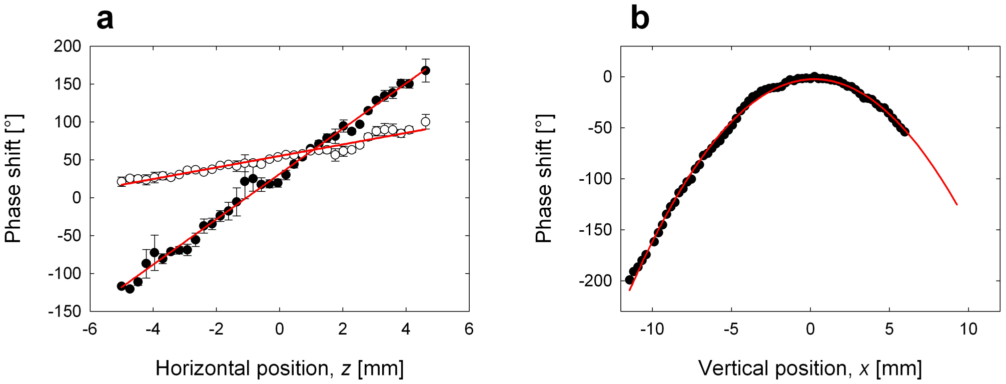

Figure 6.14: (a) Horizontal cuts (along the magnetic field axis z) through the neutron spin phase maps presented in Fig. 6.13 and linear fits (red lines): no correction coils (•, gradient: 30°/mm) and with correction coils using a current of 5 A (∘, gradient: 7.6°/mm). (b) Vertical cut (along the x-direction) through the phase map with a correction coil current of 5 A and parabolic fit. The lower reference beam (upper sample beam) is approximately situated at $x = -10 \ldots -5$ mm ($x = -1 \ldots 6$ mm).

Hence, with the refined Ramsey apparatus we are now able to measure phase shifts employing large neutron beam cross-sections. Nevertheless, a measurement of $b_{\mathrm{i,d}}$ could not be performed, as we were again suffering from problems concerning the homogeneity of the nuclear spin polarisation of the sample. The disappearance of the Ramsey oscillations might by caused by the following reasons:

- Probably the sample preparation/baking was again not perfect.
- The size of the sample is now larger than the wavelength of the microwaves. Therefore the irradiated microwave power is probably not equally distributed over the sample, which could generate a spatial variation of the polarisation.
- The sample has been chosen because of its long nuclear spin relaxation time, which might be a reason for the polarisation inhomogeneity.

Due to lack of beam time, it was not possible to test another sample and with the knowledge that the NMR cross-calibration will ultimately limit the achievable accuracy of $b_{\mathrm{i,d}}$, no further measurement request was justified under the present conditions.

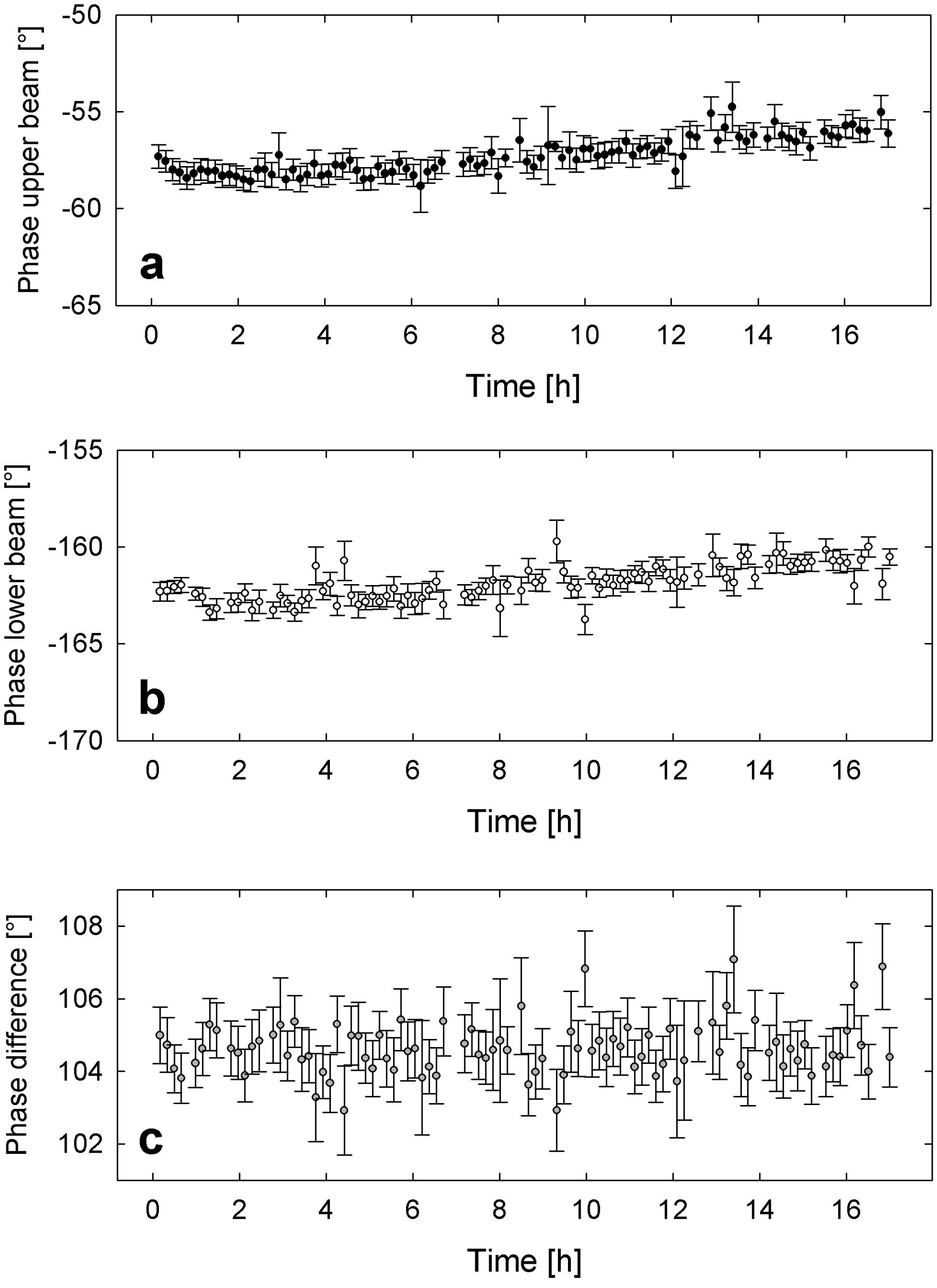

Figure 6.15: Demonstration of the phase stability of the Ramsey setup employing the gradient correction coils with a current of 5 A. Plot (a) and (b) show the individual phases of the upper (8×7 mm^2) and the lower neutron beam (5 mm in diameter) measured continuously over about 17 hours. Plot (c) shows the phase difference of the two beams. The phase stability is about a factor two worse than reported without the correction coils in section 5.1.9, but here the individual phase measurements have also a lower precision of only ±0.9° (before ±0.65°).

6.2. Measurement of $b_{\mathrm{i,d}}$ in Summer 2006

As stated in section 6.1.4, in the beam time of summer 2006 the first direct measurement of the incoherent neutron-deuteron scattering length $b_{\mathrm{i,d}}$ was performed.
In section 3.4 the principle of the measurement was already briefly described. It consists of three Ramsey frequency scans and the corresponding NMR signal measurements with the nuclear spin sample in three different states:

1. the sample is unpolarised, measuring the so-called *zero phase*: ϕ_0
2. both spin species (protons and deuterons) in the sample are polarised, measuring ϕ_1 and
3. only the deuteron spins are polarised, i.e. the proton polarisation has been completely destroyed by irradiation of rf fields, measuring ϕ_2.[9]

The measuring scheme corresponds to the one described in Ref. [Bra04] and yields the ratio $R_\phi = (\phi_1 - \phi_0)/(\phi_2 - \phi_0)$, which was previously defined in Equ. (3.51).
The relative accuracy of this ratio depends on the precision of the phase retrieval of the individual Ramsey signals. For the fit of the Ramsey oscillations the function given in Equ. (5.3) was used, resulting in an accuracy of about $\pm 2°$, which already includes the fit of the reference beam signal. Together with the stability of the Ramsey apparatus ($\pm 0.5°$), the error due to the mixing of the two partial beams (maximum $\pm 1°$) and the phase shift caused by the nuclear spin relaxation during a 15 min measurement (about $\pm 2°$), one obtains an absolute accuracy of the phase determination for ϕ_1 and ϕ_2 of $\pm 5.5°$ each (compare section 5.1.10). On the other hand, the accuracy of the determination of the zero phase ϕ_0 is mainly limited by the uncertainty of how precisely the nuclear polarisation is actually zero, which is limited by the accuracy of the NMR measurement. As an upper limit we get $\delta\phi_0 \approx \pm 5°$, which is estimated by employing the NMR signal integral accuracy (see below) and Equ. (3.38).[10] Using standard error propagation and average phase shifts of $\phi_1 \approx 700°$ and $\phi_2 \approx 350°$, one thus obtains a total relative accuracy of $\delta R_\phi / R_\phi = \pm 2\%$.
Further, the absolute NMR signal integral accuracy of 3×10^{-3} combined with the average values for the NMR signals at 2.5 Tesla of $J_{\mathrm{p},106} \approx 0.4$ [a.u.] and $J_{\mathrm{d},16} \approx 0.3$ [a.u.], yields relative NMR accuracies of 0.8% and 1.0% for the protons and deuterons, respectively. Due to large dispersion contributions in the 16 MHz LT NMR system, especially for the deuteron signals (compare Fig. 6.16), an error of approximately ±5% is added to the uncertainty of the deuteron NMR. This error takes the strong variation of the signal integral into account, obtained for different polynomial fits and fit boundaries. It does not include the frequency dependent amplification, which can lead to an additional error due to the distinctive shape of the deuteron NMR signal.
A summary of all the individual contributions to the error of $b_{\mathrm{i,d}}$ is presented in table 6.1, including the values for the cross-calibration of the proton NMR (see Fig. 6.17).

---

[9] This state is preferred compared to the one where the proton spins are kept polarised, as it is more difficult to saturate the broad deuteron NMR signal.

[10] The signal integral accuracy of the NMR measurements is determined as explained in section 5.3.4.

Neutron spin precession - phase retrieval		
Fit accuracy	±2°	
Ramsey apparatus stability	±0.5°	
Phase shift (relaxation at $T_\mathrm{c} \approx 125$ mK)	±2°	
Beam separation/mixture	±1°	
Sub-total: $\delta\phi_1/\phi_1$	±5.5° / 700°	±0.8%
Sub-total: $\delta\phi_2/\phi_2$	±5.5° / 350°	±1.5%
Zero phase determination: $\delta\phi_0$	±5°	
Total: $\delta R_\phi/R_\phi$		±2%
NMR-Accuracy		
Proton (stat., 2000 sweeps)	$\pm 3 \times 10^{-3}$ / 0.4	±0.8%
Deuteron (stat., 2000 sweeps)	$\pm 3 \times 10^{-3}$ / 0.3	±1.0%
Deuteron (dispersion - fit)		±5%
Proton NMR cross-calibration		
Statistical (linear fit)		±0.6%
Systematical (polarisation loss)		±11%
Total Error: $\delta b_{\mathbf{i,d}}/b_{\mathbf{i,d}}$		
without syst. error of cross-calibration		±7.5%
with syst. error of cross-calibration		±14%

Table 6.1: Error budget in summer 2006 for typical pseudomagnetic phase shifts and NMR signal integral values.

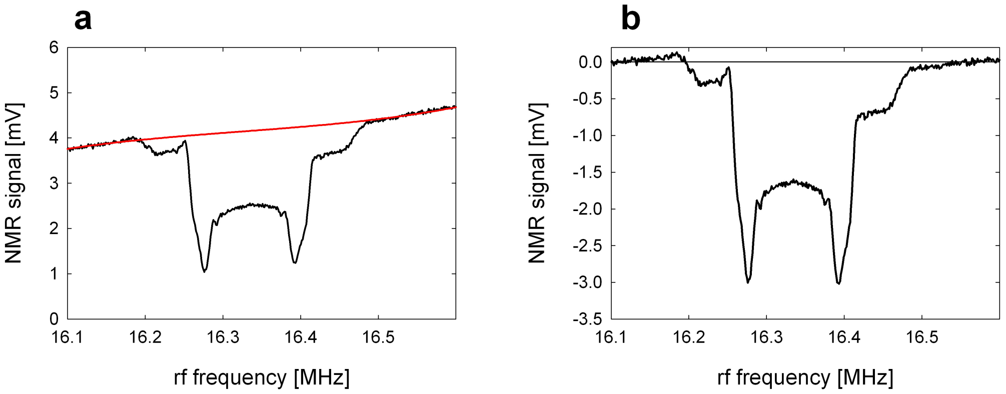

Figure 6.16: The deuteron NMR signal shows a large dispersion contribution in the beam time of summer 2006 (compare also Fig. 6.6). (a) Baseline subtracted NMR signal (black, 2000 sweeps) and cubic fit (red). (b) Strongly deformed deuteron NMR signal ($J_{\mathrm{d},16}$ = −0.31 [a.u.]). Actually, at a negative spin polarisation, as presented here, the low-frequency peak should be larger than the high-frequency peak and not opposite. Further, below 16.18 MHz and above 16.48 MHz the signal should be zero.

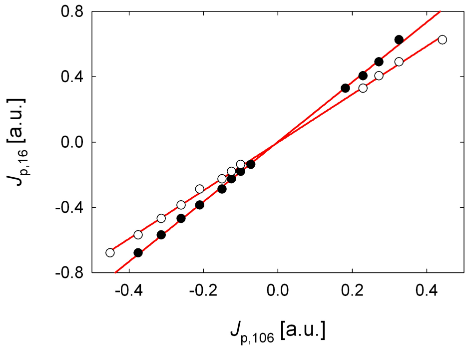

Figure 6.17: Data from the cross-calibration of the proton NMR: c_x = $(1.65 \pm 0.01_{\mathrm{stat}} \pm 0.18_{\mathrm{syst}})$. The linear fits (red lines) through the data points cross very precisely the origin.

As the error of the deuteron NMR measurement is rather large, it is justified to approximate that the deuteron polarisation is the same before and after the destruction of the proton polarisation. Further, we assume that the proton polarisation is completely zero after the rf saturation, as we cannot detect a remaining proton signal. Hence, for the data analysis one can employ the simplified Equ. (3.56) in section 3.4. The incoherent scattering length was determined for several different initial degrees of nuclear polarisation (positive and negative DNP). The results for $b_{\mathrm{i,d}}$ are depicted in Fig. 6.18, presenting two plots with the same data points but with different lengths of the error bars, i.e. either neglecting or including the large systematic error of 11% from the NMR cross-calibration. Nevertheless, this large uncertainty still cannot explain the outliers at low degrees of nuclear polarisation, which deviate from the literature value by almost a factor two.

As the most likely reason for these outliers, we suspect polarisation inhomogeneities, mainly because the sample was much larger than the neutron beam (sample size: 14×7 mm^2, neutron beam diameter: about 3 mm). And secondly, imperfect saturation because the proton polarisation was measured and destroyed with the same coil, as no

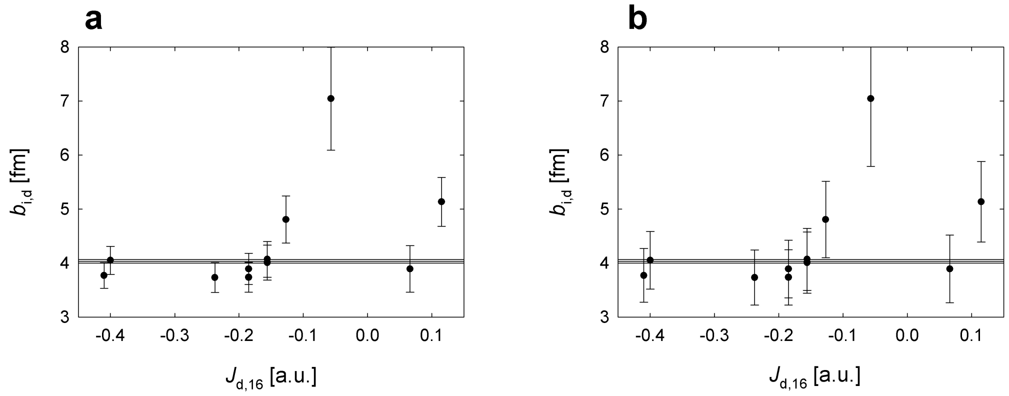

Figure 6.18: Results from the measurement of the incoherent neutron-deuteron scattering length in summer 2006 as a function of the initial deuteron polarisation $J_{\mathrm{d,16}}$. The three horizontal lines give the literature value with error bars of $b_{\mathrm{i,d}} = (4.033 \pm 0.032)$ fm, for comparison [Dil71]. (a) Data points – neglecting the systematical error of the NMR cross-calibration. (b) Data points – including the systematical error of 11%.

additional saturation coil was implemented in the setup yet. This could result in a wrong measurement of the proton NMR signal integral, as the applied rf pulses might only saturate the proton spins in the vicinity of the wire of the coil, but not entirely over the whole sample (compare Fig. 6.5a).

6.3. Measurement of $b_{\mathrm{i,d}}$ in Summer 2007

The obvious solution to reduce the systematic error of the measurement, is to adjust the size of the polarised sample to the size of the neutron beam. Therefore a disc shaped sample with a diameter of 5 mm was employed in summer 2007 as presented in section 6.1.5. This means that a 3 mm neutron beam illuminates about 40% of the sample cross-section – in 2006 it was less than 10%. The consequence is of course that the NMR signal integrals become much smaller, which reduces the signal-to-noise ratio (compare Fig. 6.19) and increases the statistical error of the cross-calibration (compare Fig. 6.20). On the other hand, the dispersion contribution to the absorption signal is now negligible.

Moreover, the newly included separate saturation coil with a volume much larger than the polarised target sample, provides a homogeneous destruction of the nuclear spin polarisation over the whole sample and thus largely suppresses systematic effects.[11]

Further, in this beam time the zero phase was directly determined by measuring Ramsey oscillations at different thermal equilibrium polarisations above one Kelvin, analogue to the measurement presented in Fig. 6.4a. By extrapolating to infinite temperatures, the zero phase shift is obtained by a linear fit with an accuracy of ±0.5° (compare Fig. 6.21). In principle this zero phase needs to be further corrected for the ^{13}C polarisation and the magnetic field produced by the paramagnetic electron spins (compare appendix C). Instead an additional error is added, leading to a total uncertainty of the zero phase of $\delta\phi_0 = \pm 2°$.

---

[11] Target volume: 25 mm^3. Saturation coil volume: 1500 mm^3 (compare section 6.1.5).

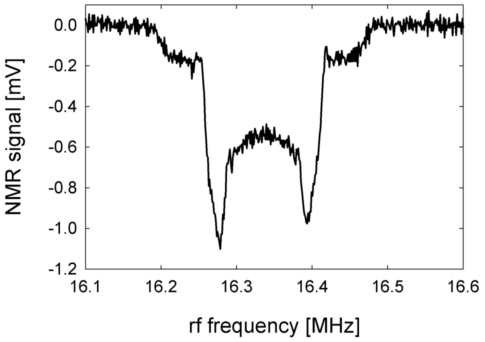

Figure 6.19: Example of a deuteron NMR signal with 2000 sweeps, showing the worsened signal-to-noise ratio compared to 2006 (compare Fig. 6.16) due to the smaller sample size ($J_{\mathrm{d},16} = -0.11$ [a.u.]).

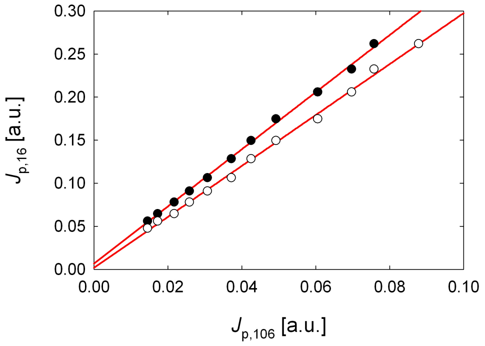

Figure 6.20: Data from the cross-calibration of the proton NMR: $c_\mathrm{x} = (3.14 \pm 0.05_\mathrm{stat} \pm 0.18_\mathrm{syst})$.

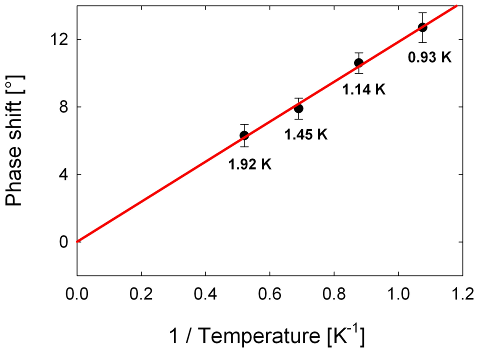

Figure 6.21: Zero phase determination by measuring the phase of the Ramsey oscillation as a function of the inverse temperature. The linear fit (red line) yields the zero phase for $T \to \infty$ with a precision of ±0.5°.

Neutron spin precession - phase retrieval		
Fit accuracy	±1.5°	
Ramsey apparatus stability	±0.5°	
Phase shift (relaxation at $T_{\mathrm{c}} \approx 115$ mK)	±2°	
Beam separation/mixture	±1°	
Sub-total: $\delta\phi_1/\phi_1$	±5° / 1600°	±0.3%
Sub-total: $\delta\phi_2/\phi_2$	±5° / 800°	±0.6%
Zero phase determination: $\delta\phi_0$	±2°	
Total: $\delta R_\phi/R_\phi$		±0.7%
NMR-Accuracy		
Proton (stat., 1000 sweeps)	$\pm 1.5 \times 10^{-3}$ / 0.1	±1.5%
Deuteron (stat., 2000 sweeps)	$\pm 3 \times 10^{-3}$ / 0.1	±3%
Proton NMR cross-calibration		
Statistical (linear fit)		±1.5%
Systematical (polarisation loss)		±6%
Total Error: $\delta b_{\mathbf{i,d}}/b_{\mathbf{i,d}}$		
without syst. error of cross-calibration		±4%
with syst. error of cross-calibration		±8.5%

Table 6.2: Error budget in summer 2007 for typical pseudomagnetic phase shifts and NMR signal integral values.

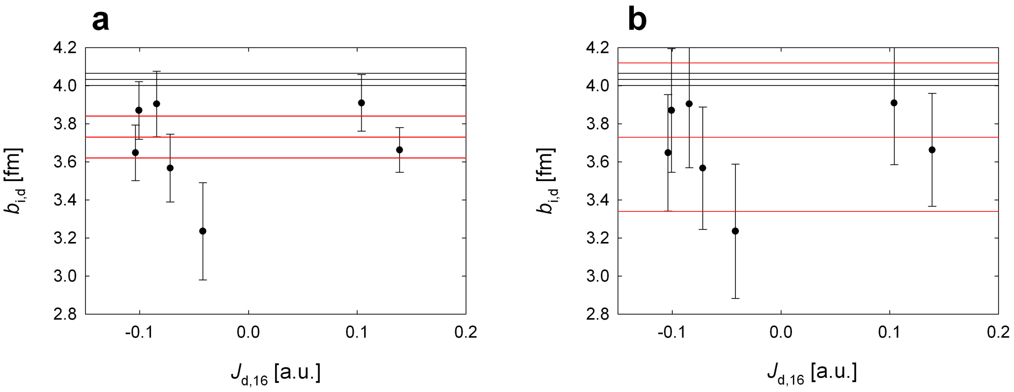

Figure 6.22: Results from the measurement of the incoherent neutron-deuteron scattering length in summer 2007 as a function of the initial deuteron polarisation $J_{d,16}$. The three horizontal black lines give the literature value with error bars for comparison [Dil71]. The three horizontal red lines indicate the corresponding result from Equ. (6.1). (a) Data points – neglecting the systematical error of the NMR cross-calibration. (b) Data points – including the systematical error of 6%.

Table 6.2 gives a summary of the resulting individual contributions to the error of $b_{\mathrm{i,d}}$ for typical pseudomagnetic phase shifts and NMR signal integrals. The total error could be reduced by about a factor two compared to the previous measurement in 2006. However, the accuracy is still on an unsatisfactory level.

Fig. 6.22 presents the obtained values for the incoherent scattering length, again neglecting and including the systematical error due to the cross-calibration, respectively. Combining all seven data points yields (weighted mean):

$$b_{\mathrm{i,d}} = (3.73 \pm 0.05 \pm 0.06 \pm 0.28)\ \mathrm{fm}\ , \tag{6.1}$$

where the uncertainties are due to:

- the statistical error of the phase shift retrieval and the NMR signal integral measurements ($\pm 3.5\%/\sqrt{7} = \pm 1.3\%$)
- the statistical error of the NMR cross-calibration (±1.5%) and
- the systematical error of the cross-calibration (±6%).

This result deviates by approximately 8% from the literature value given by Dilg et al., but due to the large total error it is still in agreement with (4.033 ± 0.032) fm. However, the systematic uncertainty caused by the NMR cross-calibration describes the upper limit and the real error might well be much smaller (compare section 5.3.5). However, only 40% of the sample cross-section was illuminated by the neutron beam, i.e. the neutrons see only a fraction of the polarised target, which is sampled by NMR. To account for the discrepancy to the literature value, the NMR measurements (protons or deuterons) would need to be sytematically off by 8% or the R_ϕ ratio determination by 4%.

7. Conclusion and Outlook

7.1. Conclusion

In the first part of the present thesis an experiment was described, which aims to measure directly the incoherent neutron-deuteron scattering length $b_{\mathrm{i,d}}$ for the first time. A linear combination of $b_{\mathrm{i,d}}$ with the well-known coherent neutron-deuteron scattering length $b_{\mathrm{c,d}}$ can provide a new value of the doublet neutron-deuteron scattering length $b_{2,\mathrm{d}}$, which is a crucial input parameter for modern effective field theories. The goal of the experiment is to reduce the accuracy of $b_{2,\mathrm{d}}$ from presently 5% below 1%, which requires an improvement of the accuracy of $b_{\mathrm{i,d}}$ from 0.8% to better than 0.13%.
The experiment utilises the effect of pseudomagnetic precession of neutron spins in a target containing polarised nuclear spins. The neutron spin precession angle is proportional to the incoherent scattering length and is determined using Ramsey's method of separated oscillating fields adapted for cold neutrons.
A neutron Ramsey apparatus working at 2.5 Tesla, a specially designed dilution refrigerator and a sensitive NMR system have been developed and set up:

- The steady magnetic field and the rf fields of the $\pi/2$-spin flippers of the neutron Ramsey apparatus are stabilised by feedback loops. Further, the so-called two beam method is employed, such that one can routinely achieve a phase shift retrieval of the Ramsey oscillation patterns with an accuracy of $\pm 1^\circ$ within about 10-15 minutes of measuring time. The maximum observable phase shift is limited by the monochromacy of the neutron beam. With $\Delta\lambda/\lambda_0 = 6\%$ it is possible to measure phase shifts of more than 2000°. This yields a relative accuracy of better than 10^{-3}, which is sufficient for the aimed accuracy goal of $b_{\mathrm{i,d}}$.
  Moreover, the use of correction coils allows for a beam cross-section of up to almost 1 cm^2.

- The dilution refrigerator is designed to fit between the pole pieces of the 2.5 Tesla magnet (distance: about 48 mm). The deuterated polystyrene sample is situated in a separate target cell, which is filled with liquid ^{4}He and thermally anchored to the mixing chamber. With the cryostat a base temperature of about 85 mK (105-110 mK) is reached in the mixing chamber (target cell).
  The large cooling power of the cryostat (1 mW at about 135 mK) and an unique heat exchanger configuration allows to irradiate microwaves directly into the target cell. This is necessary to polarise the nuclear spins in the sample with the dynamically nuclear polarisation process. At these low temperatures and large magnetic fields, the relaxation time of the nuclear spin polarisation exceeds 100 hours, which is much longer than the measuring time of a neutron Ramsey signal (frozen spin target).

- The NMR system is used to measure the nuclear polarisation in the sample and consists of two Q-meter setups: a non-resonant cable configuration at 16 MHz and a resonant cable setup at 106 MHz. The first one is used to measure the NMR signal integrals of the protons and the deuterons at a field of 0.38 Tesla and 2.5 Tesla, respectively, while the second setup serves to monitor the proton polarisation at high field. The absolute accuracy of the NMR signal integral measurement is approximately of the order 3×10^{-3}, which yields a relative precision of better than 1% for typical signal integrals.
  For the determination of the incoherent scattering length $b_{\mathrm{i,d}}$, it is necessary to perform a so-called cross-calibration of the two proton NMR systems. The procedure involves ramping of the external magnetic field to about 0.38 Tesla, which causes an increase of the sample temperature (eddy current heating) and further drastically decreases the already short nuclear spin relaxation time at this low field. Hence, the resulting systematic error presently limits the accuracy of the determination of $b_{\mathrm{i,d}}$.

Seven beam times of the nd-experiment have been carried out at the fundamental cold neutron physics beam line FUNSPIN at the spallation source SINQ at the Paul Scherrer Institute. For the first time, a direct measurement of $b_{\mathrm{i,d}}$ has been performed (compare Equ. (6.1)), leading to a value for the doublet neutron-deuteron scattering length of

$$b_{2,\mathrm{d}} = (1.39 \pm 0.07 \pm 0.08 \pm 0.40)\ \mathrm{fm}\ , \tag{7.1}$$

where the errors are caused firstly, by the phase retrieval of the Ramsey frequency scans and the NMR signal integral measurements, secondly, by the statistic error of the NMR cross-calibration and lastly, by the systematic uncertainty of the cross-calibration (upper limit). The fact that the sample is not fully illuminated by the neutron beam can produce a further systematic uncertainty, which is not yet included in these errors.

The result is in agreement with the value given by Dilg et al. [Dil71] but is considerably less accurate (compare section 3.2.7). The main limitation is due to the NMR accuracy and the NMR cross-calibration, which itself is limited by the relatively fast nuclear spin relaxation at low fields.

An increase of the sample size by a factor five in the last beam time in 2008 improved the NMR accuracy significantly. Unfortunately, the improvement was accompanied by polarisation inhomogeneities, which caused the Ramsey signals to smear out already at a low degree of nuclear polarisation. Hence, under the present conditions the result given in Equ. (7.1) remains our best value attained for the doublet neutron-deuteron scattering length $b_{2,\mathrm{d}}$.

7.2. Outlook

The ultimate goal of the nd-experiment, to determine $b_{2,\mathrm{d}}$ with an accuracy of better than 1%, could not be reached during the work of the present thesis. Hence, the following various ideas summarise possible future improvements of the experimental setup.
Firstly, we want to consider the current accuracy limits of the method estimated for a large sample (sample #15) and a large neutron beam cross-section, as it was used in the last beam time:
The statistical errors (NMR, phase shift retrieval and cross-calibration) can all be kept on a level of about 0.5% with the present setup. As presented in table 7.1, this leads to a total statistical precision of about 1.3% for each individual measurement of $b_{\mathrm{i,d}}$, which reduces further with the square root of the number of measurements performed.

Neutron spin precession - phase retrieval		
Fit accuracy	±1.5°	
Ramsey apparatus stability	±0.5°	
Phase shift (relaxation)	±1.5°	
Beam separation/mixture	±0.5°	
Sub-total: $\delta\phi_1/\phi_1$	±4° / 2000°	±0.2%
Sub-total: $\delta\phi_2/\phi_2$	±4° / 1000°	±0.4%
Zero phase determination: $\delta\phi_0$	±2°	
Total: $\delta R_\phi/R_\phi$		±0.5%
NMR-Accuracy		
Proton (stat.)	$\pm 2 \times 10^{-3}$ / 0.4	±0.5%
Deuteron (stat.)	$\pm 3 \times 10^{-3}$ / 0.6	±0.5%
Proton NMR cross-calibration		
Statistical (linear fit)		±0.5%
Total Error: $\delta b_{\mathbf{i,d}}/b_{\mathbf{i,d}}$		
without syst. error of cross-calibration		±1.3%

Table 7.1: Estimated attainable error budget using the present Ramsey setup and sample #15. The systematical error due to the NMR cross-calibration is neglected. Further, it is assumed that the neutron beam illuminates the entire sample cross-section.

How could these errors be further reduced?

- A reduction of the neutron wavelength spread $\Delta\lambda/\lambda_0$ is advantageous to be able to measure even larger phase shifts than 2000°, which will increase the accuracy of the phase shift determination. Of course this will be accompanied by longer measurement times due to a lower neutron flux.

- A higher neutron flux allows faster scanning of the Ramsey signals and thus reduces the error caused by the relaxation of the nuclear spins during a frequency scan.

- An improvement of the stability of the magnetic field and the rf spin flippers of the Ramsey apparatus is very challenging, since the present phase stability is already better than 0.5°. An option would be to decrease the distance between the $\pi/2$-spin flippers, which yields an increase of Δf (see section 3.3). But this is not possible with our apparatus, due to the size of the cryostat situated between the spin flippers.

- Reducing the neutron wavelength λ_0 actually has the same effect, but requires to increase the power of the rf fields, which can cause further rf heating of the cryostat (compare section 5.1.5).
  On the other hand, a shorter neutron wavelength provides that one can employ thicker samples, which increases the NMR signal integrals. However, it is hard to predict how homogeneously such thick samples would polarise.

- A further increase of the sample cross-section is not promising, as the size of the neutron beam already reached its limit in terms of coherence of the neutron spin precession. Moreover, a larger sample also implies the use of a huge saturation coil to provide homogeneous destruction of the nuclear spin polarisation, but the present coil already uses the maximum available space.

- The use of a position sensitive detector probably cannot help to overcome problems related to the polarisation inhomogeneities, as firstly the inhomogeneities might well be oriented along the neutron flight path and not in the plane of the sample. And secondly, the sample-detector distance is too long to provide a reasonable geometric resolution. Moreover, the sensitivity of a CCD-camera is too low, which yields very long measuring/exposure times compared to a ^{3}He-gas detector.

- As a normal conducting magnet is used in the present setup the steady magnetic field is limited to 2.5 Tesla. In principle, it is possible to employ higher magnetic fields employing a superconducting magnet system, e.g. 3.5 Tesla. This totally new approach would require a redesign of the entire Ramsey apparatus, but would increase the spin relaxation times especially during the cross-calibration. However, initially one has to consider the possible problem of a slow ramping speed, which might appear with superconducting coils.

Each one of the above ideas and suggestions provides an improvement of the statistical uncertainty of the determination of $b_{\mathrm{i,d}}$ and needs to be considered in future beam times of the nd-experiment.

On the other hand, the main problem remains the systematical error of the cross-calibration, which still dominates the total accuracy. The most obvious remedy would be to decrease the base temperature of the dilution refrigerator. However, the temperature limitation is not caused by the employed Roubeau type cryostat, which can provide mixing chamber temperature of below 70 mK, but by the the thermal conductivity of the superfluid ^{4}He in the target cell at these low temperatures. Hence, the distance between the mixing chamber and the sample should be kept as short as possible in a future cryostat design, to provide maximum thermal conductivity. In the present setup such a design is hardly realisable due to the distance between the pole pieces, which limits the available space.
A completely new approach would be to use a so-called polarised MIONP target.[1] These targets reach a high degree of nuclear polarisation already at low magnetic fields and modest temperatures (see for instance Ref. [Hen90, Iin00, Tak04, Ver90, Wak05]). Moreover, they have the advantage of long nuclear spin relaxation times even at low magnetic fields, as the paramagnetic centres are short-lived and created by laser pulses. Unfortunately, so far there has been no MIONP target realised using a deuterated sample.

As long as this problem is not solved, a new attempt with the present nd-apparatus would not deliver a more accurate result of the doublet neutron-deuteron scattering length $b_{2,\mathrm{d}}$.

---

[1] Microwave induced optical nuclear polarisation.

Part II.

Neutron Spin Phase Imaging (NSPI)

The second part of the thesis presents a "spin-off" project of the nd-experiment: *Neutron spin phase imaging* (NSPI) [Pie081, Pie092]. This novel imaging technique also uses the Ramsey principle. For the first time, quantitative imaging measurements of magnetic objects and fields could be performed. The strength of the spin-dependent interaction is detected by a change in the Larmor precession frequency of the neutron spins. Hence, one obtains in addition to the normal attenuation radiography image a so-called neutron spin phase image, which provides a two dimensional projection of the magnetic field integrated over the neutron flight path.
Chapters 8 and 9 give an overview about the motivation and the experimental setup. In chapter 10, first results obtained with the NSPI technique are presented.

Some of the following sections have been taken and modified from references written and published by the thesis author and co-workers:

Section 9.1 has been taken from Ref. [Pie091].
Section 9.2 has been taken from Ref. [Pie083].
Sections 10.1 and 10.2 have been taken from Ref. [Pie092].

8. Neutron Radiography of Magnetic Fields and Samples

Radiography and tomography with neutrons have become well established techniques to image macroscopic objects of interest in various research disciplines [Ari08, Bar82]. Neutrons interact with the nuclei in matter via the strong interaction and therefore deliver complementary information to X-rays, which are sensitive to the electron density distribution. Spatial resolutions of down to a few tens of micrometers can be reached using state of the art techniques [Leh07, Tre08, Grü07]. So far in the history of these techniques the property of the spin of the neutron and the associated magnetic momentum μ_n has been completely neglected.

As neutrons do not possess an electric charge, but a magnetic moment, they are the ideal probes to investigate magnetic interactions. This is the basis of solid state research of magnetic samples with polarised neutrons, e.g. examining transitions between different magnetic phases or magnetic excitations. These scattering techniques are complementary to neutron radiography as they are probing the momentum space and the energy transfer instead of the real space. The here presented radiography technique combines a method well-known in neutron scattering [Gol94, Rek02] with a typical imaging setup.

8.1. Introduction to Neutron Spin Phase Imaging

Ramsey's technique of separated oscillating fields is a method sensitive to spin-dependent interactions of particles with external fields, detected as a spin precession angle [Ram50, Ram56] and is therefore similar to spin-echo techniques, e.g. pulsed nuclear magnetic resonance [Sli96] or neutron spin-echo [Mez72].

It was already shown in the first main part of this thesis that Ramsey's technique adapted to neutrons can be employed to observe interactions between neutron spins and magnetic or pseudomagnetic fields [Glä87, Pie082]. The neutron spin precession angle φ_m due to magnetic interaction is given by

$$\varphi_\mathrm{m} = \frac{m_\mathrm{n}\gamma_\mathrm{n}B}{h} \cdot \lambda\ s = 46.32\ \mathrm{rad} \cdot B\ [\mathrm{T}] \cdot \lambda\ [\text{Å}] \cdot s\ [\mathrm{mm}]\ , \tag{8.1}$$

where λ and m_n are the neutron de Broglie wavelength and mass, s is the length of the flight path in which the neutron spins sense a magnetic field B and h is Planck's constant.

The Ramsey apparatus presented in section 5.1 uses a ^{3}He gas tube to detect the neutrons. Employing a position sensitive detector instead allows to locally determine the spin precession angle, from which one obtains a two dimensional spin precession map or neutron spin phase image (compare Fig. 8.1). This leads to a novel radiography

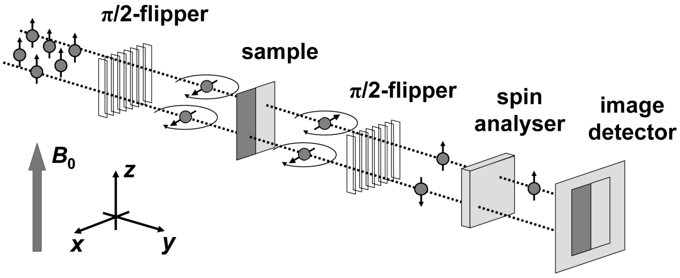

Figure 8.1: Scheme of a NSPI setup. The spins of the incoming polarised neutron beam are primarily oriented in z-direction along the steady magnetic field $\vec{B}_0$. They pass two phase-locked $\pi/2$-spin flipper coils, which produce a linear oscillating field in x-direction with an angular frequency ω. A sample with a spin-dependent potential produces additional neutron spin precession, causing dephasing of the neutron spins. The spin analyser lets only pass neutrons of one spin state, which get detected by the two dimensional image detector.

technique, which was originally proposed and explained in Ref. [Pie081] – neutron spin phase imaging. It can be used to quantitatively image macroscopic magnetic objects, i.e. ferromagnetic samples or magnetic fields, with a sub-millimeter resolution. Thereby, its measurement principle is equivalent to the one described in sections 3.3 and 5.1.8.
A prototype of a NSPI Ramsey apparatus has been built and is presented in chapter 9. First test measurements have been performed at the small angle scattering instrument SANS-I at PSI to demonstrate the possibilities of the technique (compare chapter 10).

8.2. Other Approaches

Lately, a few groups came up with other approaches to perform neutron radiography of magnetic fields and samples. Most of them do not use polarised neutrons, but utilise the effect that neutrons experience a spin-dependent refractive index, when passing through a magnetic field region. This causes phase shifts in the neutron wave packet, which can be measured using a grating-based shearing interferometer [Pfe06] or a double crystal diffractometer [Str07]. Both methods have in common that they measure the induced refractive angle (USANS or Fresnel near field) and are therefore only sensitive to phase-shift gradients and to magnetic field gradients, respectively. Grünzweig et al. succeeded in imaging the magnetic domains in a ferromagnetic FeSi sample employing a grating interferometer with a modified measuring method (*neutron dark field radiography*) [Grü08].
Kardjilov et al. presented an approach, which uses polarised neutrons but determines simply the change in the neutron spin projection caused by a magnetic sample and thus needs further assumptions and input information to perform an image reconstruction [Kar08].

In contrast, the neutron spin phase imaging technique is also sensitive to homogeneous magnetic fields and does not need further input or simulations, as it uses the full information encoded in the neutron spin precession.

9. Instrumental Setup

9.1. The NSPI Setup

In this section the properties of the compact Ramsey apparatus used for the neutron spin phase imaging technique will be described in detail.
A scheme of the 480 mm long apparatus is presented in Fig. 9.1. Despite its shortness, the magnetic field homogeneity allows for large beam cross-sections of up to 20×20 mm^2. The applied magnetic field at the sample position is variable and can be tuned from about 4 to almost 32 mT without violating the Ramsey resonance condition. The performance of the apparatus is demonstrated in systematic tests, which show a phase stability of $\pm 1^\circ$ and a sensitivity of about $\pm 7.5 \times 10^{-8}$ Tm.

9.1.1. The NSPI Ramsey Apparatus

The NSPI Ramsey apparatus consists of two 4 mm thick ferromagnetic steel plates (a), which are connected at every corner by four blocks, each assembled from two NdFeB/N35 permanent magnets[1] (b) and a sandwiched ferromagnetic steel block (c). Each steel block is wound with a coil of 3×50 windings of 0.7 mm diameter copper wire, which can be used to trim the magnetic field produced by the permanent magnets. This yields a mean magnetic field of about 18 mT, corresponding to a neutron Larmor frequency of about 530 kHz, in the centre of the $100 \times 480 \times 65$ mm^3 volume. The magnetic field strength in z-direction along the neutron flight path has been measured and is plotted in Fig. 9.2. It shows a plateau of $B_0 = (17.94 \pm 0.04)$ mT from $y = 180$ mm to 300 mm, where the neutron spin precession takes place. Due to the trimming, the field at both ends of the apparatus diverges from the field in the plateau region. But this does not harm the functionality of the Ramsey apparatus, as there the field only serves as a holding field for the neutron polarisation and the magnetisation of the remanent transmission spin analysing device[2] (d), respectively.
The two radio frequency $\pi/2$-spin flippers (e) are $24 \times 10 \times 23$ mm^3 box-shaped coils, which are wound on a PFTE body with a 20×20 mm^2 window for neutrons. Each coil consists of 9 turns of a 0.3 mm diameter bare copper wire with a pitch of 3 mm and produces a linear oscillating field along the x-axis. They are connected in series and form the inductance of a matched resonant circuit for frequencies around 790 kHz. The circuit is driven far off resonance by a signal generator and a 250 W power amplifier at about 550 kHz to profit from the almost flat power absorption spectra of the circuit in the operating frequency range.[3] The distance between the $\pi/2$-spin flippers can be

---

[1] *http://www.maurermagnetic.ch*

[2] For a detailed description of the device see section 9.2.

[3] The forward and reflected power of the amplifier are 125 W and 113 W, respectively, which yields an absorbed rf-power of about 12 W for both $\pi/2$-spin flippers.

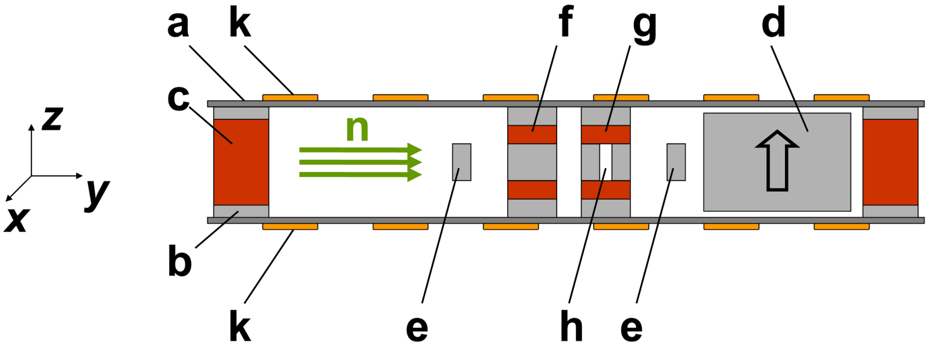

Figure 9.1: Scheme of the Ramsey apparatus with the monochromatic polarised neutron beam (n) coming from the left. (a) ferromagnetic steel plates (100 × 480 × 4 mm^3), (b) permanent magnet blocks (15 × 40 × 8 mm^3), (c) ferromagnetic steel blocks (12×40×49 mm^3) wound with copper wire serving as trim coils, (d) neutron polarisation analyser, (e) radio frequency $\pi/2$-spin flippers, (f) split pair coil (compensation coil), (g) split split pair coil (sample coil), (h) 4×20 mm^2 slit for sample positioning and (k) copper tubes with cooling water soldered on copper plates, which are thermally anchored to the steel plates. Drawing is not to scale.

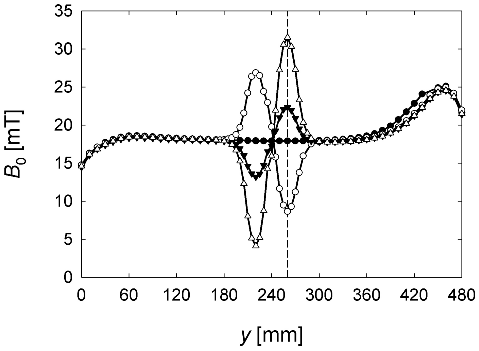

Figure 9.2: Plot of the magnetic field strength in z-direction along the neutron flight path in the centre of the volume enclosed by the steel plates. The field was determined for different currents in the sample coil and the compensation coil: $I_s = I_c = 0$ A (filled circles), $I_s = -I_c = -2$ A (white circles), $I_s = -I_c = +1$ A (filled triangles) and $I_s = -I_c = +3$ A (white triangles). The vertical dashed line at $y = 260$ mm marks the sample site. The two 10 mm thick $\pi/2$-spin flippers can be freely positioned at $y = 180...190$ mm and $y = 290...300$ mm, respectively.

adjusted between 100 and 120 mm to optimise for the Ramsey resonance condition.

To apply magnetic fields on a sample, which differ from the field provided by the permanent magnets, it is necessary to compensate the additional field integral along the neutron flight path by a compensation coil to fulfill the Ramsey condition. The compensation coil (f) and the sample coil (g) are two identical rectangular split pair coils consisting each of 2×150 windings of 0.7 mm diameter copper wire wound on an aluminium body. The cross-sections of the windings have a size of 15×7.5 mm^2 and are vertically separated by a 20 mm distance, which allows for a 20×20 mm^2 neutron beam window. Each coil produces a magnetic field with a strength of about 4.4 mT/A along the z-axis.[4] In the following the convention is used, that a positive (negative) current in the coil strengthens (weakens) the steady field produced by the permanent magnets. During the normal operation of the Ramsey apparatus the polarities of the applied voltages are chosen such that the fields are pointing anti-parallel to each other, as presented in Fig. 9.2. Furthermore, the plot shows that the magnetic field at the position of the $\pi/2$-spin flippers stays almost constant, while the sample field can be chosen freely over a large range. Hence, the field at the sample position (h) can be varied from about 4 up to 32 mT. In principle lower or higher fields can be achieved but produce depolarisation at the edges of the neutron beam, as the magnetic field direction inverts due to the stronger field close to the coil windings. On the other hand, a short-time inversion of the magnetic field above the coercivity over the whole sample size can be used to demagnetise ferromagnetic samples.

A picture of the Ramsey apparatus is given in Fig. G.1 in the appendix, showing the meandering water cooling tubes (k) soldered on copper plates. They stabilise the temperature of the setup to 20°C and avoid unwanted phase drifts of the neutron spins and the Ramsey patterns due to thermal expansions.

9.1.2. Systematic Performance Tests of the Apparatus

The performance of the Ramsey apparatus has been tested with the cold polarised neutron reflectometer Narziss at the spallation neutron source SINQ at the Paul Scherrer Institute (see Fig. G.3 in the appendix). The monochromator of the reflectometer provides a neutron beam with a wavelength spectrum which peaks at $\lambda_0 = 5$ Å and has a width $\Delta\lambda/\lambda_0$ of 1.5%. The beam size is restricted by two cadmium diaphragms in front of the apparatus, with rectangular holes of 1 mm width, 5 mm height and a distance of 725 mm between each other. The collimation behind the sample only restricts the height of the neutron beam (also 5 mm), but not its width.

Fig. 9.3 shows a typical Ramsey pattern obtained with the setup, by successively scanning the $\pi/2$-spin-flipper frequency in steps of 1 kHz. Its period Δf of about 7 kHz is in agreement with the theoretically expected value [Pie082]. The dip of the envelope of the resonance signal at about 540 kHz is caused by the fringe fields of the $\pi/2$-spin flipper coils.[5] To reduce measurement time and to achieve a good signal-to-noise ratio the frequency scans are typically restricted to the region close to 560 kHz and to only 11 points (from 555 to 565 kHz). These excerpts of the complete Ramsey pattern are then fitted with a sinusoidal function, from which a phase angle is obtained (*neutron spin phase angle*).

---

[4] This field strength was measured in the centre of the neutron beam window, with the coils placed between the ferromagnetic steel plates.

[5] This can be confirmed by quantum mechanical simulations of the Ramsey apparatus using time-evolution operators (compare appendix B).

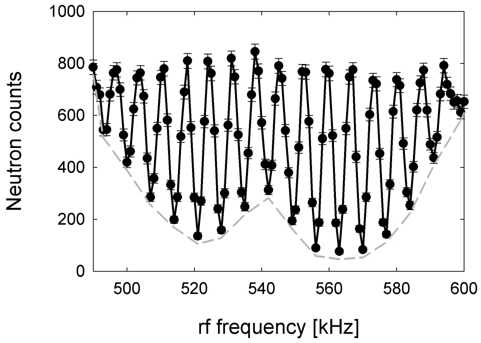

Figure 9.3: Scan of the neutron count rate as a function of the $\pi/2$-spin flipper frequency, with $I_s = I_c = 0$ A. The envelope of the resonance is plotted as a dashed curve.

To test the stability of the apparatus we repeatedly performed such Ramsey frequency scans and determined the phase angle, while keeping the magnetic field constant (see section 5.1.9). The result of a long term measurement over 3.5 hours, which is much longer than typical exposure times in neutron imaging, is shown in Fig. 9.4. This delivers a phase stability of about ±1.0° for 5 Å neutrons. The sensitivity of a Ramsey apparatus can be described as the minimal magnetic field path integral, which is still detectable due to the limited phase stability. In our case this yields a sensitivity of $\pm 7.5 \times 10^{-8}$ Tm.

Another important property of the apparatus is demonstrated in Fig. 9.5, which describes how well the initial value of the neutron spin phase angle is reproduced, after the magnetic field at the sample position has been varied. It is checked by periodically changing the current through the sample and the compensation coil, while Ramsey frequency scans are taken continuously. The changes in the coil currents ($I_s = -I_c =$ -3.5 A, -1.5 A, 0 A, +1.5 A and +3.5 A) are clearly visible as jumps in the phase angle. This is due to the fact that the two coils are not perfectly identical and therefore deliver slightly different magnetic fields at equal currents. The effect can in principle be canceled by a corresponding correction of the compensation coil current.[6] The reproducibility over 8 hours was in average ±3° and is therefore slightly larger than the stability. This is caused by the hysteresis of the two steel plates, which enclose the apparatus at the bottom and the top. Hence, the use of ferromagnetic materials should be reduced as much as possible in future setups.

As a test of the functionality the neutron count rate at a fixed $\pi/2$-spin flipper frequency is measured for different currents in the sample coil (see Fig. 9.6). As expected the number of detected neutrons oscillates with the accumulated neutron spin precession due to the additional magnetic field. A broader wavelength spectrum causes a smearing of the Ramsey pattern and therefore leads to a decrease in the signal-to-noise ratio. Therefore the relative width of the wavelength distribution restricts the precession angle to a practical limit of approximately $180° \cdot \lambda_0/\Delta\lambda$. Hence, the wavelength λ_0 and the width of the spectrum have to be chosen correctly in relation to the sample thickness and the expected additional spin precession.

---

[6] Here the correction would have been on the level of about 2%.

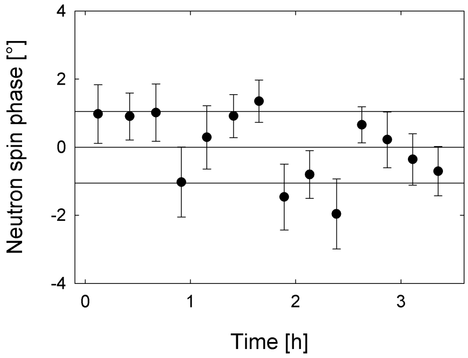

Figure 9.4: Demonstration of the phase stability of the Ramsey apparatus with $I_s = -I_c = +2$ A, which corresponds to a field at the sample position of about 27.5 mT. The mean value of the neutron spin phase angle has been arbitrarily set to 0°. The standard deviation (thin horizontal lines) is ±1.0°, with a mean length of the statistical error bars of the individual measurements of ±0.8°.

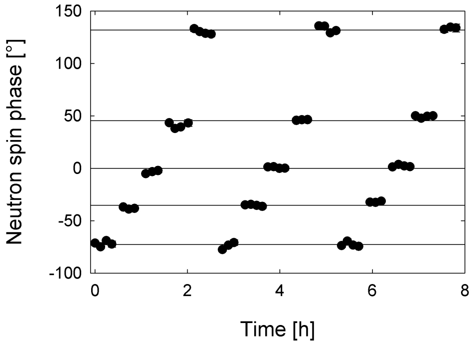

Figure 9.5: Test of reproducibility of the neutron spin phase by simultaneously changing the currents in the sample and the compensation coil every 30 min. One cycle consists of five magnetic field changes at the sample position: 2.5 mT, 11.5 mT, 18.5 mT, 25.5 mT and 34.5 mT, which correspond to the following mean neutron spin phase angles: -73°, -35°, 0°, 45° and 132°. The mean length of the error bars is approximately ±2°.

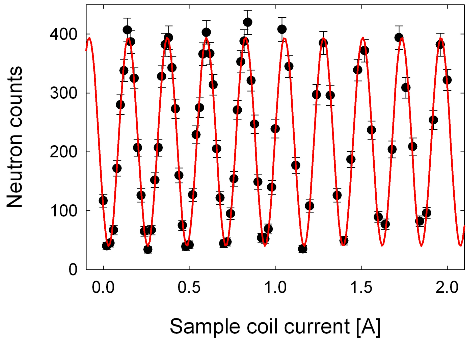

Figure 9.6: Neutron counts at a fixed $\pi/2$-spin flipper frequency of 560 kHz as a function of the sample coil current. The plotted line describes a sinusoidal fit through the measured points with a period of (227.3 ± 0.2) mA, which corresponds to an additional neutron spin precession of $(1583.8 \pm 1.4)°/\text{A}$.

9.2. A short-length Neutron Transmission Polariser

Now a polarisation device for cold neutrons is presented, which was especially developed for polarised neutron radiography, e.g. neutron spin phase imaging. It combines the shortness and the large beam cross-section acceptance of a bender with the advantages of a transmission polarising cavity. Characterisations show a polarisation efficiency of about 78% and a transmission of 44% for neutrons with a wavelength of 5 Å (compare section 9.2.3). Its compact design with a length of only 160 mm makes the device versatile and easily implementable for many purposes in neutron physics. Some further details about the device can be found in Ref. [Pie083].

9.2.1. Standard Neutron Polarisers

Most neutron spin polarisation devices, except polarised solid proton targets [Asw08, Zim99] and polarised ^{3}He gas [Hei99], use the principle of spin-dependent reflection of neutrons on a surface of ferromagnetic multilayers sputtered on float glass or silicon wafers [Bön97, Kri04]. The obtainable critical momentum transfer q_c for total reflection of the preferred spin state can routinely reach up to 0.065 Å^{-1} ($m = 3$, where m denotes the ratio of q_c of the multilayer and the critical momentum transfer of natural Nickel). This leads for a single polarising mirror with a typical length of 500 mm to a maximum neutron beam width of about 10 mm for 5 Å neutrons. One either uses the reflected or transmitted beam for the further application, while the other is stopped in an absorbing diaphragm behind the mirror.

Larger beam cross-sections can be polarised with neutron benders, which usually absorb the transmitted beam already inside the device, in an absorbing coating on the back side of each stacked polarising silicon wafer [Sch89, Bön99]. Their drawback is that they can deform the beam spot and produce a striped reflected beam profile. The reflected beam is typically bent by a few degrees with respect to the incoming neutron beam.

Another polarisation device is the so-called polarising cavity, which uses coated silicon wafers placed at a slightly tilted angle to the neutron beam direction (see for instance Ref. [Kri92]). Hence one spin component is transmitted through the wafers, while the other gets reflected and afterwards absorbed in the walls of the surrounding neutron guide. This geometry has the advantage that it operates in transmission, which makes it easier to implement in an already existing instrument. However, the length of such a device is typically several meters, which prevents easy handling and construction.

In the case of neutron radiography, it is preferable to have a very short sample-detector distance to reach a high spatial resolution [Bar82]. This makes it necessary to have a short spin-analyser capable of analysing large neutron beam cross-sections, without bending the neutron beam and without producing a heavily striped image. As already mentioned, polarised ^{3}He gas can in principle be used to polarise relatively large neutron beam cross-sections on a short distance. However, its nuclear spin relaxation time is highly sensitive to magnetic field gradients, which makes it difficult to use it in a magnetic environment [Hei95].

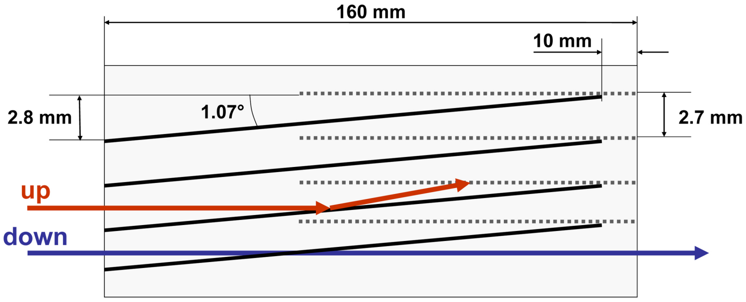

Figure 9.7: Schematic top view of the multi N-shaped arrangement of the coated silicon wafers with a distance of 2.7 mm. The 100 mm long absorbing wafers (grey dotted lines) are aligned parallel, while the 150 mm long polarising wafers (thick black lines) are tilted with an angle of 1.07° with respect to the neutron beam axis. This arrangement causes that only one neutron spin state (down) can penetrate the device, while the other (up) gets reflected on the polarising wafers and absorbed. Illustration is not to scale.

9.2.2. Geometrical Arrangement of the Transmission Polariser

The here presented polarisation device consists of an arrangement of two kinds of coated 0.3 mm thin silicon wafers. The first type has a rectangular shape of 150 × 40 mm^2 and is coated on both sides with a remanent $m = 3$ polarising multilayer structure of FeCoV/TiN_x [Bön99, Sen04]. The second type with a size of 100 × 40 mm^2 serves as an absorber for neutrons with the wrong spin state. This type is coated on one side with an approximately 2.5 μm thick TiGd absorption layer and on the back side with a thin TiGd anti-reflecting layer of about 0.15 μm. All coatings have been made at the DC magnetron sputtering facility of the Paul Scherrer Institute. These two types of wafers are arranged in a multi N-shaped geometry shown in Fig. 9.7, allowing only the neutrons of one spin state to pass the device, whereas the neutrons of the other spin state are reflected and absorbed. In order to arrange and to align the wafers, 0.3 mm wide and 6 mm deep slits were eroded in a 20 mm thick aluminium base-plate, in which one can firmly slide the silicon wafers. A picture of the device is shown in Fig. G.2 in the appendix. A similar polarising device has been realised by another group for a radial geometry, but is about a factor 3 longer [Fal06].

Both types of wafers have been tested separately at the neutron reflectometer Narziss at the Paul Scherrer Institute. The monochromator of the reflectometer provides a 5 Å neutron beam with $\Delta\lambda/\lambda_0 = 1.5\%$. The two collimating slits in front of the sample were set to a height of 30 mm and to a width of 0.35 mm such that a horizontal beam divergence of about 0.05° was achieved.[7] The collimation behind the sample only restricts the height of the neutron beam (also 30 mm), but not its width.
The polarising wafers were placed in a vertical magnetic field of approximately 450 G provided by the sample magnet of the beam line. Fig. 9.8a and b present the transmission rocking curve of one of the polarising wafers for both spin states and the corresponding polarisation efficiency, showing a value of about (80±4)% at the critical edge $q_c \approx 0.065$ Å^{-1}. The systematic error is due to the imperfect polarisation of the

---

[7] The beam divergence was determined by a 2θ-scan of the direct beam and corresponds to the FWHM of the measured intensity distribution.

incoming beam, which is different for the spin up and the spin down state.[8] The dip in the polarisation efficiency at $q \approx 0.056$ Å^{-1} is due to problems during the sputtering process of the multilayer system. From these measurements one can already estimate some properties of the polarisation device, as for example the cut-off wavelengths and the wavelength dependent transmission of the polarising wafers at a tilting angle of 1.07°:

- Below about 4 Å and above 20 Å the polarisation efficiency will drop to zero.
- The transmission of a single polarising wafer for an unpolarised neutron beam shows the expected linear behaviour as a function of the neutron wavelength λ, as presented in Fig. 9.8c. The transmission for unpolarised 5 Å neutrons is about 48%.

In Fig. 9.9 the transmission rocking curve of an absorbing wafer is plotted, showing that it is almost opaque for 5 Å neutrons with incident angles $\theta < 2.5°$. The peak at $\theta \approx 0°$ is caused by the direct beam, which passes by the wafer without penetrating the absorption layer. The transmission of less than 1% at the working point of $\theta \approx 2.2°$ ensures that in the polarisation device the reflected beam of the polarising wafers will get attenuated sufficiently for most applications.[9]

9.2.3. Performance Tests of the Polarisation Device

The performance of the transmission polariser has been tested with two neutron instruments - with the polarised neutron reflectometer Narziss and the polarised small angle neutron scattering facility SANS-I [Asw08], both at the spallation neutron source SINQ at the Paul Scherrer Institute.

The reflectometer was used to determine the spin-dependent transmission of the device versus its transverse position x with respect to the incoming neutron beam. Therefore the device was first aligned parallel to the beam by employing the specular reflection of the first polarising wafer. The neutron beam was collimated as stated in section 9.2.2, resulting in an approximately 0.6 mm wide and 30 mm high beam at the device position. The transversal position x was scanned in steps of 0.2 mm leading to the data shown in Fig. 9.10a. The spikes in the intensity of the spin down component are caused when scanning the finite width neutron beam over the 0.3 mm thin absorbing wafers and are therefore about 1 mm wide. They are separated by the same distance of 2.7 mm as the absorbing wafers in Fig. 9.7. The mean transmission for an unpolarised 5 Å neutron beam can be found to be about 44%, which is slightly less than the value of 48% without absorbing wafers in the beam, given in section 9.2.2. The corresponding polarisation efficiency is presented in Fig. 9.10b and shows an almost flat plateau over the whole cross-section of the device, leading to a mean polarisation efficiency of about $(78 \pm 4)\%$.

---

[8] This is caused by the fact that one does not use a spin flipper, but switches the magnetisation of the polariser of the beam line, to select between both spin states.

[9] The working point corresponds to twice the tilting angle of 1.07° of the polarising wafers, shown in Fig. 9.7.

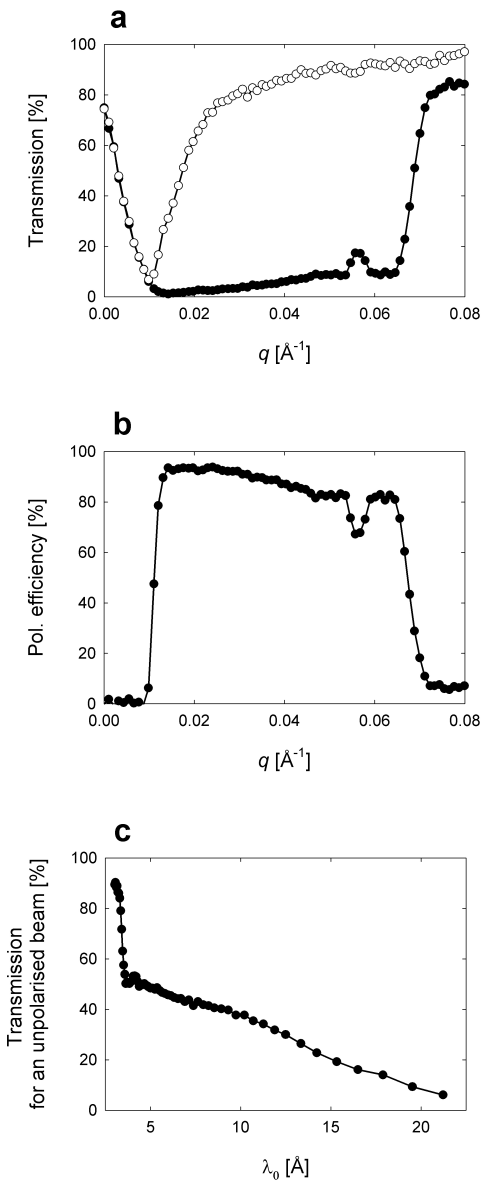

Figure 9.8: (a) Transmission rocking curve of a single polarising wafer with a $m = 3$ multilayer coating plotted versus q for both spin states: spin up (filled circles) and spin down (open circles). The applied magnetic field at the wafer position was about 450 G. (b) Polarisation efficiency of the wafer. The dip at $q \approx 0.056$ Å^{-1} is due to problems during the sputtering process of the multilayer system. (c) Calculated wavelength dependent transmission for an unpolarised neutron beam through a single polarising wafer at a tilting angle of 1.07°, using the data for both spin states shown in (a). Additional λ-dependent absorption has not been considered for this calculation.

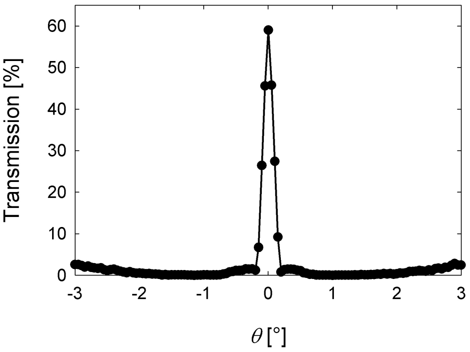

Figure 9.9: Transmission of a single absorbing wafer versus the rocking angle θ, measured in steps of 0.05°. The transmission at the working point $\theta \approx 2.2°$ is less than 1% for 5 Å neutrons.

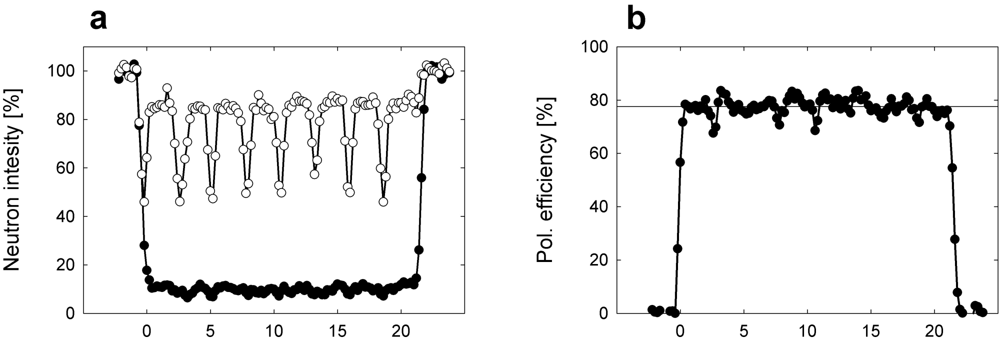

Figure 9.10: (a) Transmitted intensities of the polarisation device for 5 Å neutrons versus its transversal position x with respect to the incoming beam for both spin states: spin up (filled circles) and spin down (open circles). The intensities are normalised to the direct beam. The mean transmitted intensity for an unpolarised neutron beam is about 44%. (b) The corresponding polarisation efficiency. The horizontal line marks the mean polarisation efficiency of about (78 ± 4)%, averaged over the active cross-section of the device.

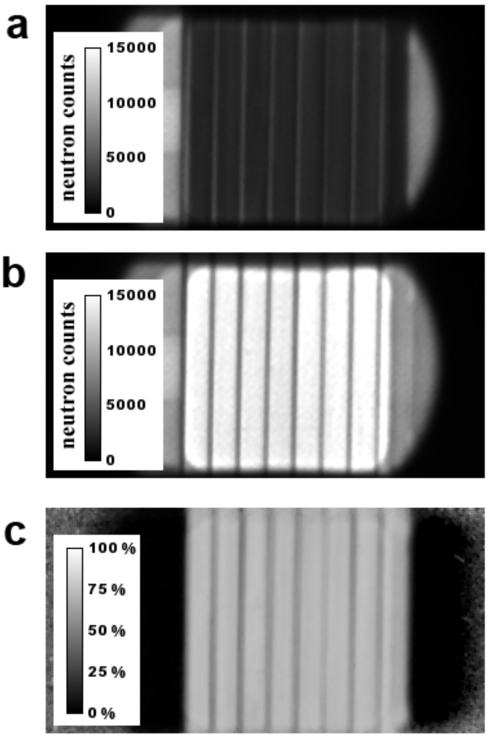

Figure 9.11: Neutron radiography images of the centre of the polarisation device, using the collimated neutron beam of the SANS-I instrument with $\lambda_0 = 5$ Å. Each image has a size of 340×175 pixels, which corresponds to an area of 44×23 mm^2. (a) and (b) show the dark-current corrected intensity images for spin up and spin down neutrons, respectively. The exposure time for one image is about 6 minutes, which equals to 7.5×10^5 counts on the monitor detector. (c) The resulting polarisation efficiency.

An often used figure of merit Q, which helps to compare polarisation devices, is defined as $Q = T \cdot P^2$, where T is the transmission and P is the polarisation efficiency of the device. Using the above stated values, Q of this device is 0.27 ± 0.03, which is of the same size as the Q of state of the art polarised ^{3}He gas cells [And05, Bat05].[10]

With a CCD-camera [Müh05], commonly used for neutron radiography, one can directly perform a two dimensional measurement of the spin-dependent transmission and the polarisation efficiency of the device. For this purpose a well collimated neutron beam with a large diameter is needed, which is available at the SANS-I beam line. With its 15 m long collimation length a beam divergence of about 0.2° can be achieved, i.e. about a factor 4 larger than at the Narziss reflectometer.
The polarisation device was placed at the usual sample position of the instrument, right in front of the neutron camera.[11] The incoming polarised neutron beam has a triangular shaped wavelength distribution with $\Delta\lambda/\lambda_0 \approx 10\%$, where λ_0 is the centre of gravity of the wavelength distribution. λ_0 is adjustable by means of a velocity selector and the beam polarisation can be flipped by an adiabatic high frequency spin-flipper with a flipping efficiency close to 100%. To take into account possible fluctuations of the neutron flux, the exposure time of the camera was correlated to a monitor detector

---

[10] We considered a ^{3}He nuclear spin polarisation of about 80%.

[11] The pixel-size of the camera is 0.13×0.13 mm^2.

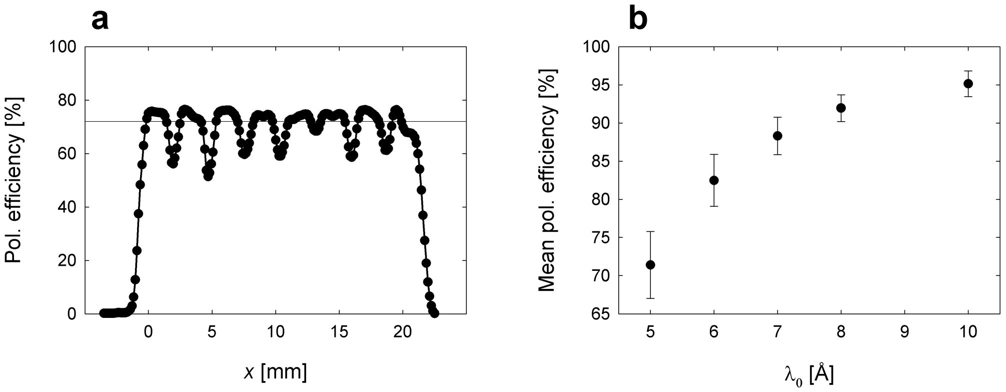

Figure 9.12: (a) Horizontal cut through the two dimensional polarisation efficiency shown in Fig. 9.11c. The horizontal line marks the mean value of about 72%. (b) The mean polarisation efficiency of the device averaged over an area of 18 × 18 mm^2 for different neutron wavelengths λ_0. Both plots have been corrected for an imperfect neutron beam polarisation of 98% of the SANS-I instrument.

placed in the monochromatic beam.

Fig. 9.11 presents images for the spin-dependent transmission and the resulting two dimensional polarisation efficiency. In Fig. 9.11b one can clearly recognize the eight vertical stripes with reduced transmitted intensity caused by the eight absorbing wafers of the device. Nevertheless at the position of the stripes the neutron intensity for an unpolarised beam is still approximately half of that at the residual polarising area. Further, it is important to emphasize that the polarisation efficiency is never below 50% over the whole cross-section of the device. This is visible by a horizontal cut of the polarisation efficiency of Fig. 9.11c, plotted in Fig. 9.12a. The plot is in accordance with the graph shown in Fig. 9.10b, except that the higher beam divergence produces more pronounced dips and also lowers the mean value to about 72%.[12]

Such images have been taken for different wavelengths λ_0 and the results are summarised in Fig. 9.12b. As expected from the measurement of one single polarising wafer, the polarisation efficiency rises with increasing λ_0 and reaches for 10 Å approximately 95%.

---

[12] These dips also appear, if the polarisation device is not aligned perfectly parallel to the neutron beam of the Narziss reflectometer.

9.3. The NSPI Setup at SANS-I at PSI

For a first test measurement the compact NSPI Ramsey apparatus was set up at the small angle scattering instrument SANS-I [Asw08] at the spallation neutron source SINQ at the Paul Scherrer Institute (see Fig. G.4 in the appendix). The reasons for choosing the SANS beam line are its following features:

- Its neutron wavelength spectrum is a triangular shaped distribution with a width of $\Delta\lambda/\lambda_0 = 0.10$. λ_0 is the centre of gravity of the spectrum, which can be adjusted by means of a velocity selector from 4.5 Å to 12 Å.
- The 15 m long collimation system.
- The polarisation option with an implemented adiabatic neutron spin flipper.

The beam size was restricted by a 20×20 mm^2 aperture and the beam divergence was measured to be 0.20°.[13] The sample to detector distance is limited to 225 mm by the length of the specially designed transmission spin analyser presented in section 9.2. This yields a geometrical resolution of 0.8 mm (FWHM of the point spread function), which is much larger than the pixel size of 0.13×0.13 mm^2 of the position sensitive detector used [Müh05]. Hence, the detector did not limit the resolution of the NSPI setup.

---

[13] The result for the beam divergence agrees well with the expected value, calculated assuming the 50×50 mm^2 aperture situated in front of the 15 m long collimation.

10. Results and Conclusion

In this chapter the first results obtained with the NSPI setup during one week of beam time at the SANS-I instrument are presented (compare section 9.3). They show the feasibility of the NSPI technique in three example measurements using thin ferromagnetic foils, a steel rod which produces a dipolar field and a small coil as a sample. A fourth example demonstrates the possibility of imaging paramagnetic and diamagnetic materials in a strong magnetic field of 2.5 Tesla, employing the Ramsey apparatus presented in section 5.1.

10.1. Example I: Thin Steel Foils

To demonstrate the technique, measurements were performed on two different ferromagnetic precision steel foils with thicknesses of (20 ± 2) μm and (40 ± 3) μm, respectively.[1] The foils were oriented along the magnetic field $\vec{B}_0$ perpendicular to the penetrating neutron beam, leaving a gap of about 4 mm between them. Fig. 10.1a-d show radiography images of the foils for four different spin flipper frequencies, where the 20 μm (40 μm) foil is situated on the left (right) side of the images. One can clearly recognise a position dependent modulation of the detected neutron intensity as a function of the spin flipper frequency. To illustrate this effect the intensities of three areas at different positions of the image have been averaged and plotted in Fig. 10.1e. Besides the phase shifts of the modulated signals one also observes a damping of the amplitudes, mainly caused by the finite width of the neutron wavelength spectrum [Pie082] and further by possible inhomogeneities of the magnetization of the foils. However, the decrease of the signal offset delivers the standard neutron attenuation image, i.e. the attenuation information of the sample is already included in these measurements. Fitting such signals with a sinusoidal function and plotting the phase values $\varphi(x, z)$ for each pixel, yields the so-called NSPI image. The phase shift $\Delta\varphi(x, z)$ due to the sample is obtained by subtracting the NSPI image of the empty beam from the one with the sample. The corresponding NSPI images of the ferromagnetic foils and of the empty beam are both generated from a set of eleven radiography images taken at different spin flipper frequencies from 545 to 555 kHz with an exposure time of about one minute each. This yields a statistical accuracy of the phase retrieval of about ±5° for each pixel. The resulting phase shift image modulo 360° is shown in Fig. 10.2. Note that the phase shift due to a ferromagnetic sample is always positive. To determine the exact phase shift one performs this measurement for different neutron wavelengths λ_0 and plots the phase shift as a function of λ_0, which yields a line through the origin, as presented in Fig. 10.3a. From the slope of the linear fit and the thickness of the foils one can determine the local magnetisation

---

[1] For further specifications see: *http://www.hs-folien.de.*

of the foils averaged along the neutron flight path. Equ. (8.1) leads for this example to a local magnetisation $\mu_0 M$ of $(1.08 \pm 0.08 \pm 0.11)$ Tesla for the 20 μm foil and $(1.81 \pm 0.02 \pm 0.14)$ Tesla for the 40 μm foil, where the errors are due to the linear fit and the thickness tolerances of the foils, respectively. These results can be compared with hysteresis curves of the shim steel foils taken with a physical property measurement system (PPMS), which are presented in Fig. 10.3b.[2] The magnetisations $\mu_0 M$ are about 0.82 Tesla and 1.55 Tesla at an external magnetic field of 19 mT (compare section 9.1). This is close to the values obtained with the NSPI technique. Possible reasons for the differences between the two methods are firstly that the NSPI technique determines the magnetisation locally and the PPMS averages over the whole sample. Secondly, the samples used for the PPMS have to be much smaller in size and have usually a different shape due to geometrical restrictions of the setup, which can cause deviations in the demagnetisation factors and the hysteresis curve. Lastly, in the neutron measurement the steel foils touched the ferromagnetic steel plates of the NSPI setup (like in an iron yoke) to reduce fringe fields of the sample and therefore might have been magnetized close to the saturation magnetisations $\mu_0 M_\mathrm{s}$ of about 1.08 Tesla and 1.93 Tesla, respectively.

10.2. Example II: Dipolar Magnetic Field by a Steel Rod

As a second example, a 9 mm long cylindrical ferromagnetic rod with a diameter of 2.2 mm was oriented parallel to the magnetic field and imaged as described before. Fig. 10.4a presents one of the eleven radiography images used to generate the NSPI image. In its centre, one can clearly recognise the strongly absorbing steel rod, which causes a dipolar magnetic field in its vicinity. Dark pixels indicate a lowered neutron intensity with respect to the empty beam image, due to a neutron spin phase shift $\Delta\varphi$ of about 180° modulo 360°. At the position of the bright pixels no net phase shift modulo 360° occurs, so there the intensity is of the same size as in the empty beam image. Moreover the lines of equal neutron intensity correspond to the magnetic field lines and show the typical dipolar shape. The NSPI image of the steel rod given in Fig. 10.4b shows three further characteristic features:

- The strong magnetic fields inside and very near the rod cause large phase shifts and therefore lead to a low S/N-ratio of the intensity modulation (compare Fig. 10.1e), due to the finite width of the wavelength distribution of the neutron beam. Hence, phase retrieval inside the rod is not possible and results in noise in the NSPI image.

- The phase jumps (black to white jumps) in the image indicate a spin precession of more than 360°. Further, the decreasing distance between the individual phase jumps implies that the field gradient increases with decreasing distance to the rod, just like expected for a dipolar field.

- The image shows no phase shift along the angle of $52 \pm 2°$, due to the angular dependent term of the dipolar field: $(3\cos^2\theta - 1)$. Theoretically for a point like dipole this angle would be 54.7°.

---

[2] Quantum Design: *http://www.qdusa.com.*

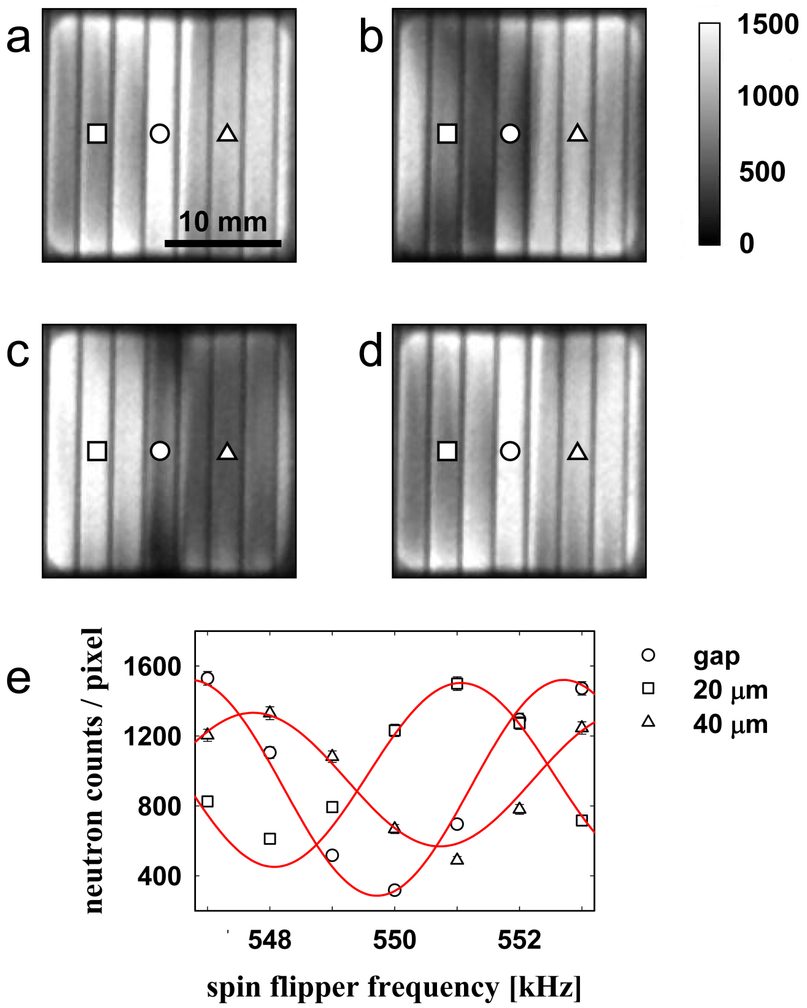

Figure 10.1: Radiography images of ferromagnetic steel foils using neutrons of $\lambda_0 = 6$ Å at different $\pi/2$-spin flipper frequencies: (a) 547 kHz, (b) 549 kHz, (c) 551 kHz and (d) 553 kHz. Each image has a size of 165×165 pixels, which corresponds to about 21.5×21.5 mm^2. The vertical stripes with lowered intensity result from the geometry of the transmission spin analyser. (e) Intensity modulation in three areas (averaged over 12×12 pixels) of the images as a function of the spin flipper frequency and sinusoidal fits: gap (circle), 20 μm foil (square) and 40 μm foil (triangle).

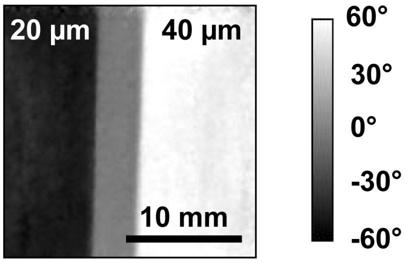

Figure 10.2: Resulting NSPI image of the two ferromagnetic steel foils.

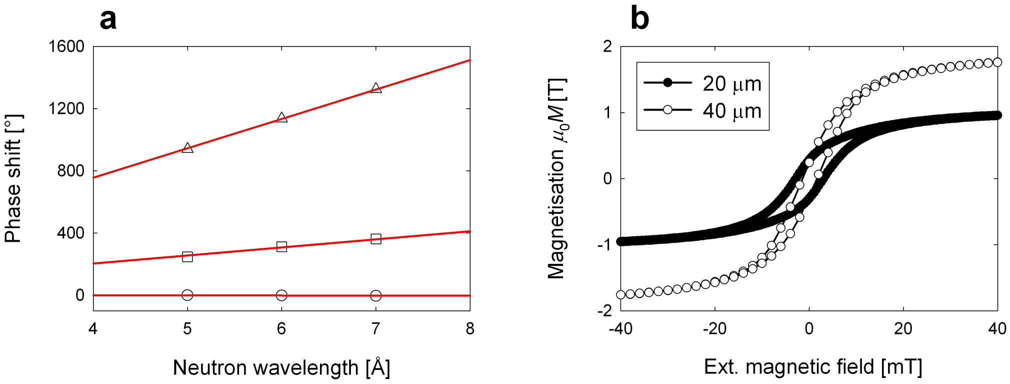

Figure 10.3: (a) Phase shift of the three areas (averaged over 12 × 12 pixels) of the NSPI images as a function of the neutron wavelength λ_0: gap (circle), 20 μm foil (square) and 40 μm foil (triangle). The lines are the linear fits through the data points. (b) Hysteresis curves of the two ferromagnetic steel foil materials measured with a PPMS.

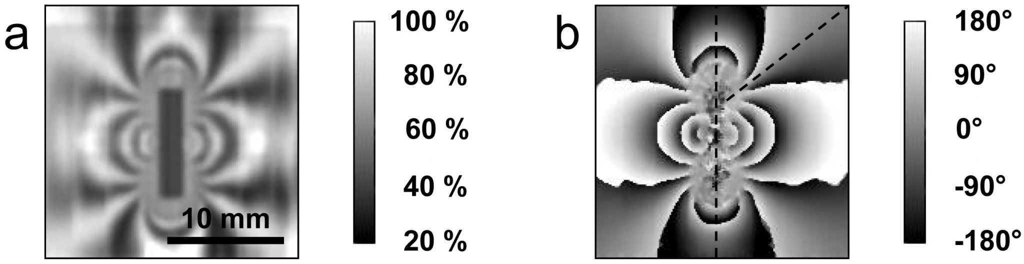

Figure 10.4: (a) Radiography image of the 9 mm long steel rod normalized with an empty beam image, taken at a $\pi/2$-spin flipper frequency of 550 kHz with neutrons of $\lambda_0 = 5$ Å. The size of the image is 21.5 × 21.5 mm^2. (b) NSPI image generated from a set of eleven individual images. The dashed lines mark the vertical magnetic field direction and the axis along which the spin phase shift is zero due to the vanishing dipolar field under the angle of 52 ± 2°.

10.3. Example III: The Magnetic Field produced by a Coil

In the following we are considering a very intuitive example, where the NSPI technique is used to image the magnetic field produced by a small coil.
Fig. 10.5 presents a picture and a standard absorption neutron radiography image of the 7 mm long coil.[3] In Fig. 10.6 the resulting neutron spin phase images at six different currents through the coil are presented. As expected, the phase shift inside the coil increases with the current and changes sign when the magnetic field produced by the coil is inverted. The observed phase shift as a function of the current is plotted together with a horizontal cut through one of the neutron spin phase images in Fig. 10.7.

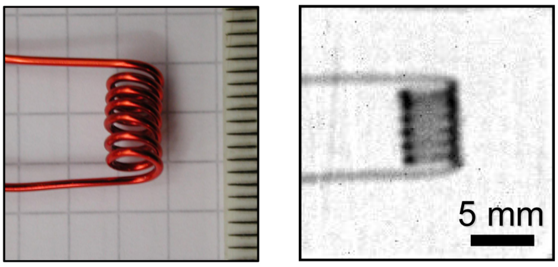

Figure 10.5: Photograph and absorption neutron radiography of a coil with 6 windings, a length of about 7 mm and an inner diameter of 3 mm made of 0.8 mm thick insulated copper wire.

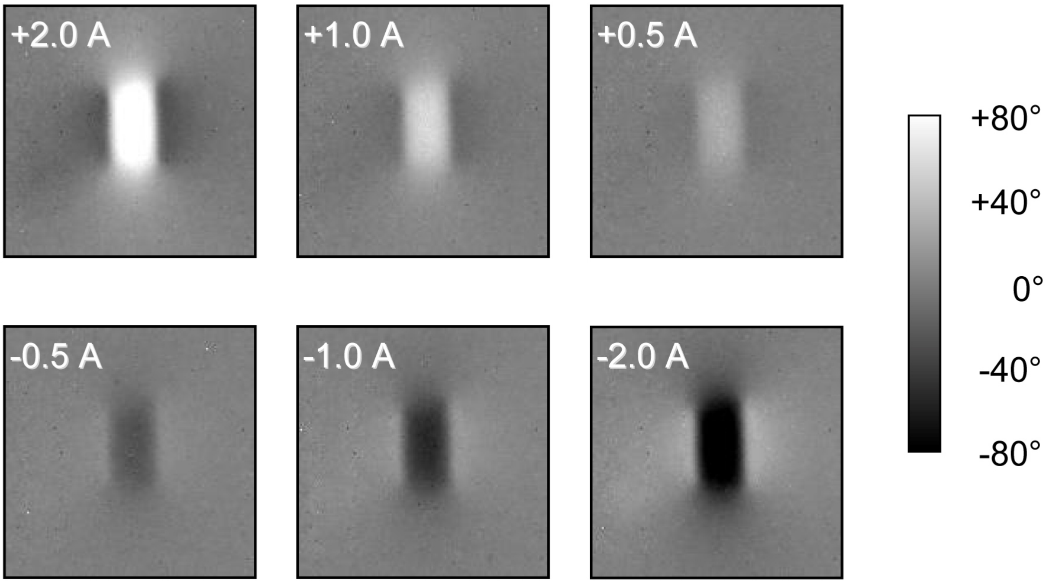

Figure 10.6: Neutron spin phase images of the magnetic field produced by the coil presented in Fig. 10.5 using currents between -2 A and +2 A. The calibration bar on the right gives the phase shift in degrees. Neutrons with a wavelength of λ_0 = 6 Å and $\Delta\lambda/\lambda_0$ = 10% have been used. All images have a size of about 20×20 mm^2, which corresponds to 150×150 pixels of the employed neutron camera.

---

[3] The absorption image is actually obtained from the NSPI data (offset of the Ramsey oscillation).

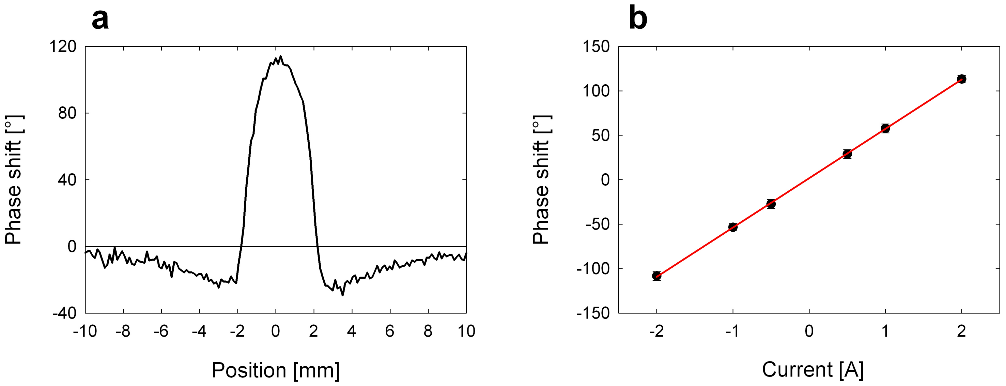

Figure 10.7: (a) Horizontal cut through the neutron spin phase image of the coil taken at a current of +2 A. The maximum phase shift in the centre of the coil is approximately 110°. (b) Neutron spin phase shift in the centre of the coil as a function of the coil current. The slope of the linear fit of (55.4 ± 0.3)°/A is in good agreement with the expected value of about 52°/A (obtained using Equ. (8.1)), which neglects the fringe fields.

10.4. Example IV: Test of Para- and Diamagnetic NSPI

The last example examines the possibility to image para- and diamagnetic materials using the NSPI technique. In general, the magnetic neutron spin interaction with para- and diamagnetic materials is a factor 10^{-5} weaker than with ferromagnetic samples, due to their tiny magnetic susceptibility χ_m. Hence, to observe a neutron spin precession the applied external magnetic field needs to be in the order of several Tesla to reach a sufficient magnetisation of the imaged object. The 2.5 Tesla field of the Ramsey apparatus presented in section 5.1 will thus yield a magnetisation of $\mu_0 M = \chi_\mathrm{m} \cdot 2.5$ T. With $\chi_\mathrm{m} = 10^{-5}$ this leads to $\mu_0 M = 25\ \mu$T and to an additional phase precession angle of about 0.3° per millimeter sample thickness for 5 Å neutrons (using Equ. (8.1)).

Reasonable sample materials need to be strongly para- or diamagnetic and possess a good neutron transmittance. A list of possible materials is given in table 10.1. For a first test we chose to image a 5 mm thick paramagnetic titanium block and a 30 mm thick diamagnetic lead block (Fig. 10.8). We employed neutrons with a wavelength of about 6.6 Å ($\theta_\mathrm{m} = 2.1°$, compare section 5.1.4) and the neutron analyser described in section 9.2. With the approximate divergence of 0.3° and a sample-detector distance of about 55 cm, a geometrical resolution of about 1.5 mm was achieved.[4]

The titanium sample causes a phase shift of (+34±3)°, which is in good agreement with the theoretical expected value of approximately +35°. This value already includes a negative phase shift of $\varphi_\mathrm{opt} = -3°$ due to the so-called *optical neutron spin precession*, which is caused by the de-/acceleration of neutrons passing through a refracting sample [Fra02].

On the other hand, a 30 mm long pure lead sample theoretically induces a phase shift of $\varphi = \varphi_\mathrm{dia} + \varphi_\mathrm{opt} = -23° + 27° = 4°$. However, the measured phase shift of $(-21 \pm 5)°$ is an indication that the used sample possesses a larger diamagnetic susceptibility

---

[4] The large sample-detector distance was necessary, as the CCD-chip of the neutron camera was not working correctly in the vicinity of the strong magnetic field. If the chip had not been affected, one could have reduced the distance to approximately 35 cm, yielding a geometrical resolution of about 1 mm.

Material	χ_m [10^{-5}]	density [g/ml]	1/e-length [mm]
Aluminium	+2.2	2.7	80
Titanium	+18.0	4.5	8
Chromium	+27.8	7.1	10
Vanadium	+34.8	6.1	7
Manganese	+87.1	7.5	3
D_2O	-0.9	1.1	15
Copper	-1.0	8.9	6
Lead	-1.8	11.3	26
Silver	-2.6	10.5	1
Antimony	-6.8	6.7	17

Table 10.1: Properties of para- and diamagnetic materials. The so-called 1/e-length is the theoretical thickness of a material that will attenuate a neutron beam to 1/e (about 0.37) of its incident intensity. Here it is calculated for neutrons with a wavelength of 5 Å.

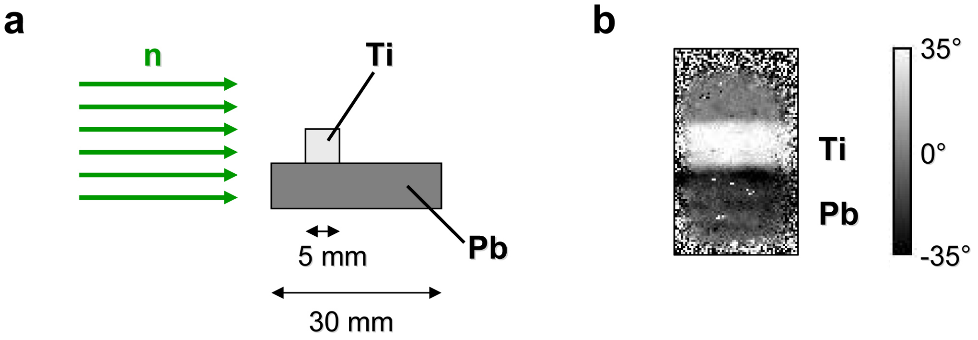

Figure 10.8: NSPI of paramagnetic titanium (Ti) and diamagnetic lead (Pb) blocks. (a) Sketch of the sample setup at the FUNSPIN beam line. The external magnetic field of 2.5 Tesla is perpendicular to the plane of projection. The titanium block has a height of 6 mm. (b) Neutron spin phase image with a size of 60 × 100 pixels, which corresponds to about 15.5×26 mm^2 (a binning of 2 × 2 pixels was used).

than expected. This might be due to admixed antimony, which serves to increase the hardness and mechanical strength in lead-antimony alloys.

In a further study the magnetic susceptibility of the lead sample needs to be measured separately with an independent technique.

10.5. Conclusion

The presented examples obtained with the novel neutron spin phase imaging technique show the feasibility of quantitative imaging of magnetic fields in- and outside magnetic materials with a sub-millimeter resolution. This is fundamentally different to another recently published approach [Kar08], which only determines the degree of beam depolarisation and therefore cannot deliver quantitative results about magnetic fields.

Furthermore, the NSPI technique also permits to apply any external magnetic field to the sample, which then for example allows to locally observe the magnetisation of magnetic objects as a function of the external magnetic field. Next steps will be to test other parameters, e.g. temperature, pressure and electric fields, and to perform three dimensional tomographies of magnetic fields and samples. Hence, the technique offers a wealth of new possibilities in real space condensed matter research.

Appendix

A. Green's Functions and Approximations

A.1. Green Function of the Helmholtz Equation

The inhomogeneous Helmholtz equation is given by $(\vec{\nabla}^2 + \vec{k}^2) h(\vec{r}) = f(\vec{r})$. The solution $h(\vec{r})$ is a sum of the solution of the homogeneous Helmholtz equation, where $f(\vec{r}) = 0$ and of a second part which is obtained using the Green's function $G(\vec{r}, \vec{r}')$ of the Helmholtz equation. The Green's function fulfils:

$$(\vec{\nabla}^2 + \vec{k}^2) G(\vec{r}, \vec{r}') = \delta(\vec{r} - \vec{r}') \ , \tag{A.1}$$

where $\delta(\vec{r})$ is the Dirac delta function, which is defined by:

$$\begin{aligned} \delta(\vec{r}) &= \begin{cases} 0, & \vec{r} = 0 \\ +\infty, & \vec{r} \neq 0 \end{cases} && \text{(A.2)} \\ \int_{-\infty}^{+\infty} d^3r \ \delta(\vec{r}) &= 1 \ . && \text{(A.3)} \end{aligned}$$

The Green's function of Equ. (A.1) is:

$$G(\vec{r}, \vec{r}') = -\frac{1}{4\pi} \frac{e^{ik|\vec{r} - \vec{r}'|}}{|\vec{r} - \vec{r}'|} \tag{A.4}$$

The solution of the homogeneous Helmholtz eqution is given by $h_0(\vec{r}) = e^{i\vec{k}\cdot\vec{r}}$, which leads to the total solution of the inhomogeneous Helmholtz equation:

$$\begin{aligned} h(\vec{r}) &= e^{i\vec{k}\cdot\vec{r}} + \int_{-\infty}^{+\infty} d^3r' \ G(\vec{r}, \vec{r}') \cdot f(\vec{r}') && \text{(A.5)} \\ &= e^{i\vec{k}\cdot\vec{r}} - \frac{1}{4\pi} \int_{-\infty}^{+\infty} d^3r' \ \frac{e^{ik|\vec{r} - \vec{r}'|}}{|\vec{r} - \vec{r}'|} \cdot f(\vec{r}') \ . && \text{(A.6)} \end{aligned}$$

A.2. Approximation of $|\vec{r}-\vec{r'}|$

The approximation used in section 3.2.1 can be derived using $\vec{r} = (x, y, z)$, $\vec{r'} = (x', y', z')$ and $r = |\vec{r}|$, $r' = |\vec{r'}|$.

$$\begin{aligned} |\vec{r}-\vec{r'}| &= \sqrt{(x-x')^2+(y-y')^2+(z-z')^2} && \text{(A.7)} \\ &= \sqrt{x^2+y^2+z^2+x'^2+y'^2+z'^2-2(xx'+yy'+zz')} && \text{(A.8)} \\ &= \sqrt{r^2+r'^2-2\vec{r}\cdot\vec{r'}} && \text{(A.9)} \end{aligned}$$

For $r \gg r'$ it follows:

$$\begin{aligned} |\vec{r}-\vec{r'}| &= r\cdot\sqrt{1+\frac{r'^2}{r^2}-2\frac{\vec{r}\cdot\vec{r'}}{r^2}} && \text{(A.10)} \\ &\approx r\cdot\sqrt{1-2\frac{\vec{r}\cdot\vec{r'}}{r^2}} && \text{(A.11)} \\ &\approx r\cdot(1-\frac{\vec{r}\cdot\vec{r'}}{r^2}) && \text{(A.12)} \\ |\vec{r}-\vec{r'}| &\approx r-\frac{\vec{r}\cdot\vec{r'}}{r} && \text{(A.13)} \end{aligned}$$

In Equ. (A.12) the Taylor expansion of the square root was employed.

A.3. Taylor Expansion

Taylor expansion of the function $f(x)$ in the vicinity of x_0:

$$T_n(x) = \sum_{k=0}^{n} \frac{f^{(k)}(x_0)}{k!}(x-x_0)^k \ , \qquad \text{(A.14)}$$

with $f^{(k)}(x_0)$ being the k-th derivative of the function at $x = x_0$.

B. Simulation of the Ramsey apparatus using time-evolution operators

The derivation given here differs slightly from that of N. Ramsey in [Ram50] and employs the method of the time-evolution operators[1]. Instead of solving the Schrödinger equation to calculate the development of a state $|\psi(t)\rangle$ under the action of a Hamiltonian, which consists of a stationary and a time-dependent part

$$\hat{H}(t) = \hat{H}_0 + \hat{V}(t) \ , \tag{B.1}$$

one can derive the time-evolution operator of the system [Sak95], using the equation of motion

$$i\hbar \frac{\partial}{\partial t} \hat{U}(t,t_0) = \hat{H}(t)\hat{U}(t,t_0) \ , \tag{B.2}$$

where $|\psi(t)\rangle = \hat{U}(t,t_0)\,|\psi(t_0)\rangle$ and $|\psi(t_0)\rangle$ is an arbitrary initial state. The general solution of Equ. (B.2) is given by

$$\hat{U}(t,t_0) = \exp\left(-\frac{i}{\hbar}\int_{t_0}^{t} \hat{H}(t')dt'\right) \ . \tag{B.3}$$

In our case we have a magnetic interaction of the magnetic moment of a spin 1/2 particle, the neutron, with a magnetic field $\vec{B} = (B_x, B_y, B_z)$, which can be written as

$$\hat{H}(t) = -\frac{\hbar}{2}\gamma_{\mathrm{n}}\vec{\sigma}\cdot\vec{B} = -\frac{\hbar}{2}\gamma_{\mathrm{n}}\begin{pmatrix} B_z & B_x - iB_y \\ B_x + iB_y & -B_z \end{pmatrix} \ , \tag{B.4}$$

where $\vec{\sigma}$ is the vector of the Pauli matrices and γ_{n} is the gyromagnatic ratio of the neutron. The Ramsey apparatus can be divided in three regions (see Fig. 3.3). In the first (I) and the third (III) region a circular oscillating field with the amplitude B_1 flips the neutron spin by $\pi/2$ into and out of the plane perpendicular to the steady magnetic field $\vec{B}_0 = (0,0,B_0)$. In the second (II) region the neutron spin precesses freely in this plane with the Larmor frequency ω_0 and inside the sample with the shifted angular frequency $\omega_0 + \Delta\omega^*$, respectively. The time each of the rf fields acts on the neutron spin shall be denoted as τ and the time the neutron spends between the flippers as T. φ^* is the wavelength dependent pseudomagnetic precession angle due to the polarised nuclei in the sample as defined in Equ. (3.37).

To simplify the problem we consider our system in the reference frame rotating with the angular frequency ω, which is the frequency of the two rf fields [Sli96]. One finds then for these three regions the following effective fields

$$\vec{B}_{\mathrm{I,eff}} = \frac{1}{\gamma_{\mathrm{n}}}(-\omega_1, 0, \Delta) \tag{B.5}$$

$$\vec{B}_{\mathrm{II,eff}} = \frac{1}{\gamma_{\mathrm{n}}}(0, 0, \Delta) \tag{B.6}$$

$$\vec{B}_{\mathrm{III,eff}} = \frac{1}{\gamma_{\mathrm{n}}}(-\omega_1\cos\vartheta, -\omega_1\sin\vartheta, \Delta) \ , \tag{B.7}$$

---

[1] An alternative derivation of this can be found in [Gol94].

where $\Delta = \omega - \omega_0$ and $\omega_1 = -\gamma_\mathrm{n} B_1$ and ϑ is a fixed phase angle between the two circular oscillating fields. These effective magnetic fields have to be inserted now in Equ. (B.3) and (B.4). If one takes also the additional precession angle φ^* into account one finds for the time-evolution operators setting $t_0 = 0$

$$\hat{U}_\mathrm{I}(\tau,0) = \begin{pmatrix} \cos\frac{\Omega\tau}{2} + i\frac{\Delta}{\Omega}\sin\frac{\Omega\tau}{2} & -i\frac{\omega_1}{\Omega}\sin\frac{\Omega\tau}{2} \\ -i\frac{\omega_1}{\Omega}\sin\frac{\Omega\tau}{2} & \cos\frac{\Omega\tau}{2} - i\frac{\Delta}{\Omega}\sin\frac{\Omega\tau}{2} \end{pmatrix} \tag{B.8}$$

$$\hat{U}_\mathrm{II}(T,0) = \begin{pmatrix} e^{+\frac{i}{2}(T\Delta+\varphi^*)} & 0 \\ 0 & e^{-\frac{i}{2}(T\Delta+\varphi^*)} \end{pmatrix} \tag{B.9}$$

$$\hat{U}_\mathrm{III}(\tau,0) = \begin{pmatrix} \cos\frac{\Omega\tau}{2} + i\frac{\Delta}{\Omega}\sin\frac{\Omega\tau}{2} & -i\frac{\omega_1}{\Omega}e^{-i\vartheta}\sin\frac{\Omega\tau}{2} \\ -i\frac{\omega_1}{\Omega}e^{i\vartheta}\sin\frac{\Omega\tau}{2} & \cos\frac{\Omega\tau}{2} - i\frac{\Delta}{\Omega}\sin\frac{\Omega\tau}{2} \end{pmatrix}, \tag{B.10}$$

with $\Omega = \sqrt{\Delta^2 + \omega_1^2}$. Without loss of generality we set $\vartheta = 0°$, so that $\hat{U}_\mathrm{I}(\tau,0) = \hat{U}_\mathrm{III}(\tau,0)$. The probability $\mathcal{W}$ for a transition from a spin state $|\uparrow\rangle = \begin{pmatrix} 1 \\ 0 \end{pmatrix}$ to $|\downarrow\rangle = \begin{pmatrix} 0 \\ 1 \end{pmatrix}$ is given by

$$\begin{aligned} \mathcal{W} &= \left|\left\langle\downarrow\left|\hat{U}_\mathrm{III}\cdot\hat{U}_\mathrm{II}\cdot\hat{U}_\mathrm{I}\right|\uparrow\right\rangle\right|^2 = \left|\left\langle\downarrow\left|\hat{U}_\mathrm{total}\right|\uparrow\right\rangle\right|^2 \\ &= \frac{4\omega_1^2}{\Omega^2}\sin^2\frac{\Omega\tau}{2}\left[\frac{\Delta}{\Omega}\sin\frac{\Omega\tau}{2}\sin\frac{T\Delta+\varphi^*}{2} - \cos\frac{\Omega\tau}{2}\cos\frac{T\Delta+\varphi^*}{2}\right]^2 . \end{aligned} \tag{B.11}$$

The condition for the spin flippers to induce $\pi/2$ flips is $\omega_1 = \pi/(2\tau)$.
Equ. (B.11) is identical to Equ. (12) in [Ram50] and applies to only a single neutron velocity and a fully polarised neutron beam. Since the times τ and T are proportional to the neutron wavelength one has to perform an average over the wavelength distribution[2] $p(\lambda)$ of the neutrons and one also has to take the imperfection of the neutron polarisation P_n into account. Then one finds the probability $\mathcal{W}'$ to detect the spin state $|\downarrow\rangle$ behind the Ramsey apparatus as

$$\mathcal{W}' = \int_0^\infty p(\lambda)\left[\frac{1+P_\mathrm{n}}{2}\left|\left\langle\downarrow\left|\hat{U}_\mathrm{total}\right|\uparrow\right\rangle\right|^2 + \frac{1-P_\mathrm{n}}{2}\left|\left\langle\downarrow\left|\hat{U}_\mathrm{total}\right|\downarrow\right\rangle\right|^2\right]d\lambda . \tag{B.12}$$

Additionally two approximations can be applied on Equ. (B.11). The first one considers only frequencies very close to the resonance, so that $\omega_1 \gg \Delta$:

$$\mathcal{W} \rightarrow \left[\frac{\Delta}{\omega_1}\sin\frac{T\Delta+\varphi^*}{2} - \cos\frac{T\Delta+\varphi^*}{2}\right]^2 . \tag{B.13}$$

From this, one can estimate the frequency distance Δf between two oscillation maxima, using only the first order term of the Taylor expansion of the tan-function around $\pi/2$. The result is given in Equ. (3.45) in section 3.3.
The other important approximation delivers the shape of the background resonance curve of the Ramsey signal (see Fig. 3.4), by substituting the fast oscillating terms $\sin\frac{T\Delta+\varphi^*}{2}$ and $\sin^2\frac{T\Delta+\varphi^*}{2}$ by their average values 0 and 1/2

$$\mathcal{W} \rightarrow \frac{2\omega_1^2}{\Omega^2}\sin^2\frac{\Omega\tau}{2}\left[\left(\frac{\Delta}{\Omega}\right)^2\sin^2\frac{\Omega\tau}{2} + \cos^2\frac{\Omega\tau}{2}\right] . \tag{B.14}$$

---

[2] Normalised wavelength distribution: $\int_0^\infty p(\lambda)d\lambda = 1$

C. Corrections

C.1. Correction due to the Magnetisation of the Sample

Besides the strong interaction also the magnetic interaction contributes to the spin precession of the neutron spin. Therefore, in this chapter we want to estimate the size of the magnetic fields produced by the nuclear spins and the electron spins of the paramagnetic centres in the polarised nuclear target.
Using magnetostatics [Jac83] and neglecting demagnetisation effects due to the sample geometry, i.e. assuming the worst case, we can estimate the total magnetisation of the polarised sample by the following formula:

$$\begin{aligned} \mu_0 M_{\mathrm{tot}} &= \mu_0 \cdot (M_{\mathrm{e}} + M_{\mathrm{p}} + M_{\mathrm{d}}) && \text{(C.1)} \\ &= \mu_0 \hbar \cdot \left(\frac{1}{2} \cdot \rho_{\mathrm{e}} \gamma_{\mathrm{e}} + \frac{1}{2} \cdot \rho_{\mathrm{p}} \gamma_{\mathrm{p}} P_{\mathrm{p}} + \rho_{\mathrm{d}} \gamma_{\mathrm{d}} P_{\mathrm{d}} \right) && \text{(C.2)} \end{aligned}$$

where $\mu_0 = 4\pi \times 10^{-7}\ \frac{\mathrm{Vs}}{\mathrm{Am}}$ and the electron polarisation is assumed to be unity. The number density of the electrons ρ_{e}, i.e. the paramagnetic centres is typically of the order $2{\times}10^{19}\ \mathrm{cm}^{-3}$. Hence, with $\rho_{\mathrm{p}} = 0.003\ \mathrm{mol/cm}^3$, $\rho_{\mathrm{d}} = 0.08\ \mathrm{mol/cm}^3$, $P_{\mathrm{p,max}} = 50\%$ and $P_{\mathrm{d,max}} = 20\%$, Equ. (C.2) leads to a maximum magnetisation of the sample of:

$$\mu_0 M_{\mathrm{tot}} \approx (-23 + 2 + 5) \times 10^{-5}\ \mathrm{Tesla} \tag{C.3}$$

The corresponding pseudomagnetic fields caused by the nuclear spins are $B^*_{\mathrm{p}} \approx 60$ mT for the protons and $B^*_{\mathrm{d}} \approx 120$ mT for the deuterons. This yields a relative correction due to the magnetic interaction of less than 4×10^{-4} for each nuclear species, which is more than a factor two smaller than our aimed accuracy goal.[1]
On the other hand, the electron magnetisation induces a phase shift of about -3° in a sample with a thickness of 1 mm employing 5 Å neutrons. But this phase shift can be assumed to be constant, as the we are mainly considering temperatures of less than 1 Kelvin, below which the electron polarisation is always above 90% (see Fig. 5.46). The only exception is the zero phase shift determination described in section 6.3, where one has to correct for this residual effect.

---

[1] Concerning the correction of the nuclear magnetic fields consult the appendix in Ref. [Zim02].

C.2. Correction due to the Polarisation of ^{13}C

Now we want to estimate the neutron spin precession angle in a polarised target due to polarised ^{13}C compared to protons and deuterons:
In the polarised target sample for the nd-experiment made from deuterated polystyrene (C_8H_8 and C_8D_8), the concentration c_p (c_d) of the protons (deuterons) is adjusted in the way that the phase shift due to both isotopes is approximately equal. This leads to $c_\mathrm{d}/c_\mathrm{p} \approx 25 - 30$, taking the lower maximum polarisation of deuterons compared to protons into account. The natural abundance of ^{13}C is about 1.1%. Using Equ. (3.38), this yields a ratio of the phase shifts of:

$$\frac{\varphi^*_\mathrm{C}}{\varphi^*_\mathrm{p}} \approx -0.22 \times 10^{-3} \cdot \frac{P_\mathrm{C}}{c_\mathrm{p} P_\mathrm{p}} \tag{C.4}$$

$$\frac{\varphi^*_\mathrm{C}}{\varphi^*_\mathrm{d}} \approx -1.1 \times 10^{-3} \cdot \frac{P_\mathrm{C}}{c_\mathrm{d} P_\mathrm{d}} \tag{C.5}$$

With typical values for polarisations in such a sample, i.e. $P_\mathrm{C}/P_\mathrm{p} \approx 1/4$, $P_\mathrm{C}/P_\mathrm{d} \approx 1$ and $c_\mathrm{p} \approx 0.03$, $c_\mathrm{d} \approx 1$, we end up with:

$$\frac{\varphi^*_\mathrm{C}}{\varphi^*_\mathrm{p}} \approx -2 \times 10^{-3} \quad \text{and} \quad \frac{\varphi^*_\mathrm{C}}{\varphi^*_\mathrm{d}} \approx -1 \times 10^{-3} \tag{C.6}$$

Hence, in deuterated polystyrene with the above given concentrations the neutron spin precession due to the natural abundance of ^{13}C is approximately 10^3 times smaller than the spin precession caused by the protons and deuterons.

D. Clausius-Clapeyron Equation

An universal equation for the vapour pressure of a liquid, which is in equilibrium with its own vapour shall be determined. For this equilibrium it holds that the temperature, the pressure and the chemical potentials μ_c of the liquid (l) and the gas (g) are equal:

$$T_\mathrm{l} = T_\mathrm{g} \ , \ p_\mathrm{l} = p_\mathrm{g} \ , \ \mu_\mathrm{c,l} = \mu_\mathrm{c,g} \tag{D.1}$$

To maintain the equilibrium also the changes in the chemical potentials must be equal:

$$d\mu_\mathrm{c,l} = d\mu_\mathrm{c,g} \tag{D.2}$$

Applying the Gibbs-Duhem relation: $0 = SdT - Vdp + Nd\mu_\mathrm{c}$ on the the previous equation leads to [Gre87]:

$$\frac{dp}{dT} = \frac{S_\mathrm{l} - S_\mathrm{g}}{V_\mathrm{l} - V_\mathrm{g}} = \frac{\Delta Q}{T(V_\mathrm{l} - V_\mathrm{g})} \tag{D.3}$$

The last step employs the second law of thermodynamics.[1] With the latent heat of evaporation $L_\mathrm{vap} = \Delta Q/n$, where n is the amount of matter in mol, it follows:

$$\frac{dp}{dT} = \frac{nL_\mathrm{vap}}{T(V_\mathrm{l} - V_\mathrm{g})} \tag{D.4}$$

The above equations even hold for other transformations, not only liquid to gas, but also the sublimation and the melting curve.

For example the horizontal melting curve in the p-T-diagram of helium implies that the superfluid phase has already the lowest possible entropy and that it does not further reduce when the helium becomes solid, i.e. $\Delta S = 0 \rightarrow dp/dT = 0$.

Another example is the special behaviour of the melting curve of ^{3}He, which is used for Pomeranchuck's solidification cooling. As $dp/dT < 0$ and $V_\mathrm{l} > V_\mathrm{s}$ at about 30 bar and below 320 mK, it follows that the entropy of the solid phase of ^{3}He is larger than the one of the liquid, i.e. a latent heat has to be applied to go from the liquid to the solid phase. Hence, under isentropic compression ($dS = 0$ - along the melting curve in the p-T-diagram) the system can be cooled down to a minimum temperature of about 2-5 mK. The first experimental realisation of cooling using this method can be found in Ref. [Anu65, Joh69].

Applying Equ. (D.4) to an ideal gas with $pV = nRT$ and $V_\mathrm{g} \gg V_\mathrm{l}$, where $R = 8.3145$ J K^{-1} mol^{-1} is the gas constant, it follows:

$$\frac{dp}{dT} = p \cdot \frac{L_\mathrm{vap}}{RT^2} \tag{D.5}$$

The solution of this differential equation is given by:

$$p(T) \propto e^{-\frac{L_\mathrm{vap}}{RT}} \propto e^{-1/T} \tag{D.6}$$

---

[1] $T \cdot dS \geq \Delta Q$, where dS is the change of entropy and the equal sign holds for reversible processes.

E. Samples of the nd-Experiment

no.	name	beam time	date of production	nomi. radical concentr. [10^{19} cm−3]	degree of deuteration [%]	size [mm^3]	mass [mg]	N_{16}	N_{106}
0a	-	-	2005	TEMPO: 2.5	0	$14 \times 15 \times 2$	606	5	1
0b	-	2nd	21.4.2005	d-TEMPO: 1.0	96	$14.4 \times 6.5 \times 2$	200	4	1
0c	d-PS + p-terphenyl	2nd	26.6.2005	d-TEMPO: 2.0	90	$13 \times 7 \times 1.5$	130	4	1
1	SANS sample	3rd	2000	TEMPO: 2.0	0	thickness: 3 mm	-	-	-
2	F92 (Glycerol+water)	3rd	2003	EHBA: 2.5	92	thickness: 3 mm	-	-	-
3	E98 (Glycerol+water)	3rd	5.5.2004	EDBA: 5.0	98	thickness: 3 mm	-	-	-
4	Glycerol+water	3rd	30.11.2005	d-TEMPO: 1.9	98	thickness: 2 mm	-	-	-
5a	-	3rd	1.12.2005	d-TEMPO: 2.2	>98	thickness: 0.4 mm	-	-	-
5b	-	3rd	1.12.2005	d-TEMPO: 2.2	>98	thickness: 0.7 mm	-	-	-
6	-	3rd	28.11.2005	TEMPO: 2.5	0	thickness: 0.5 mm	-	-	-
7	-	3rd	8.12.2005	d-TEMPO: 1.9	>98	thickness: 0.95 mm	-	-	-
8	-	3rd	8.12.2005	d-TEMPO: 1.9	>98	thickness: 2×0.95 mm	-	-	-
9	-	3rd	16.12.2005	d-TEMPO: 2.7	>98	thickness: 1.6 mm	-	-	-
10	-	3rd	18.12.2005	d-TEMPO: 2.9	96	thickness: 1.0 mm	-	-	-
11	-	3rd	20.12.2005	d-TEMPO: 2.5	92	thickness: 0.9 mm	-	-	-
12	d5-PS	3rd	21.12.2005	d-TEMPO: 2.6	94	thickness: 1.0 mm	-	-	-
13	-	4th	10.7.2006	d-TEMPO: 2.2	97	$13.9 \times 6.8 \times 1.2$	120	6	2
14	sample disc	5th, 6th	10.7.2006	d-TEMPO: 2.2	97	diam.: 5, thickn.: 1.2	25	8	2
15	M1	7th	5.6.2008	d-TEMPO: 2.0	97	$10 \times 8 \times 1.3$	110	10	4
16	M2	-	5.6.2008	d-TEMPO: 2.5	97	$14.3 \times 14.3 \times 2.8$	613	-	-
17	M3	-	6.6.2008	d-TEMPO: 1.5	97	$14.3 \times 14.3 \times 2.5$	540	-	-
18	M4	-	17.6.2008	d-TEMPO: 2.0	97	$14.3 \times 14.3 \times 2.9$	655	-	-

Figure E.1: During the nd-expermient several samples and sample materials have been tested. Their major characteristics are listed in this table. Samples no. 1-12 have the standard sample size of about 14 × 15 mm^2 with varying thicknesses.

F. Photographs: nd-Experiment

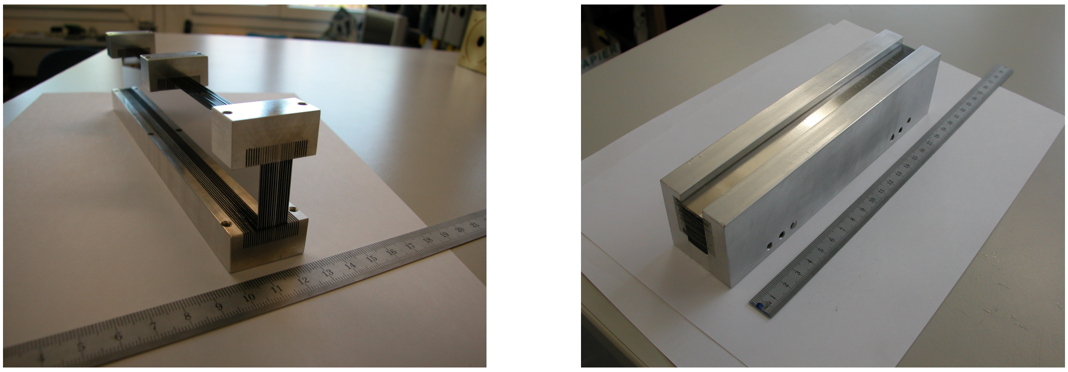

(a)

(b)

Figure F.1: Neutron collimators (each 200 mm long): (a) Silicon wafer collimator (b) Aluminium collimator. For more details see Ref. [Pie093].

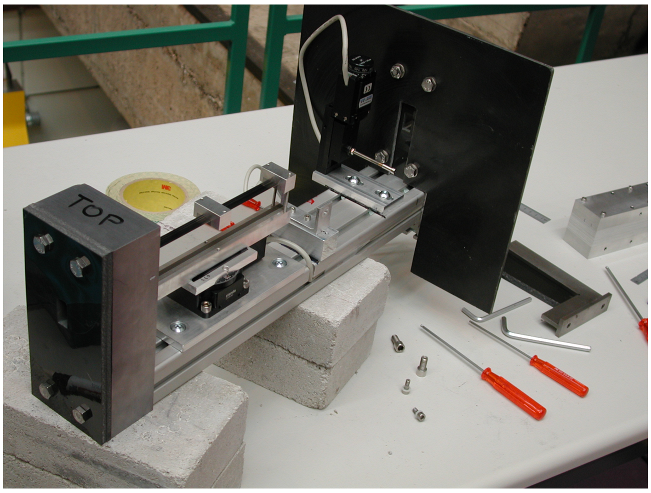

Figure F.2: Collimator mechanics with two controllable motorised stages (Vision GmbH: *http://www.optik-mechanik.de*). Only the silicon collimator is mounted. B_4C plates and lead bricks with holes (about 11×21 mm^2) for the neutron beam are placed before and after the collimators.

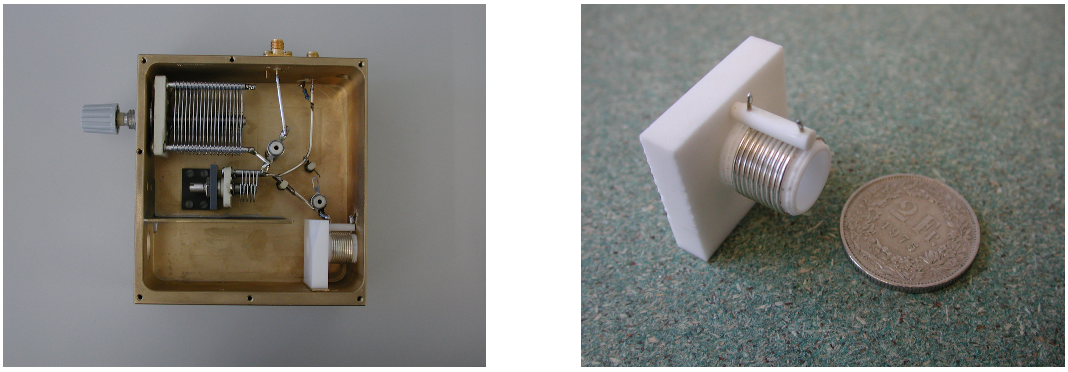

(a) (b)

Figure F.3: (a) Opened $\pi/2$-spin flipper (shielded brass case - size: 101.5 × 109 × 46 mm^3). Variable capacitors are used to tune the resonance circuit to about 73 MHz and to match it to 50 Ω. (b) The rf coil with an outer diameter of 14 mm and a length of 7 mm is consisting of 0.8 mm thick silver coated copper wire, which is wound on a *Macor*® cylinder with a pitch of one turn per millimeter (see Ref. [Sch05]). The hole for the neutron beam in the *Macor*® cylinder has a diameter of 11 mm. This spin flipper and this coil was used from beam time two until six. The pictures show a previous version with 10 windings and a length of 10 mm.

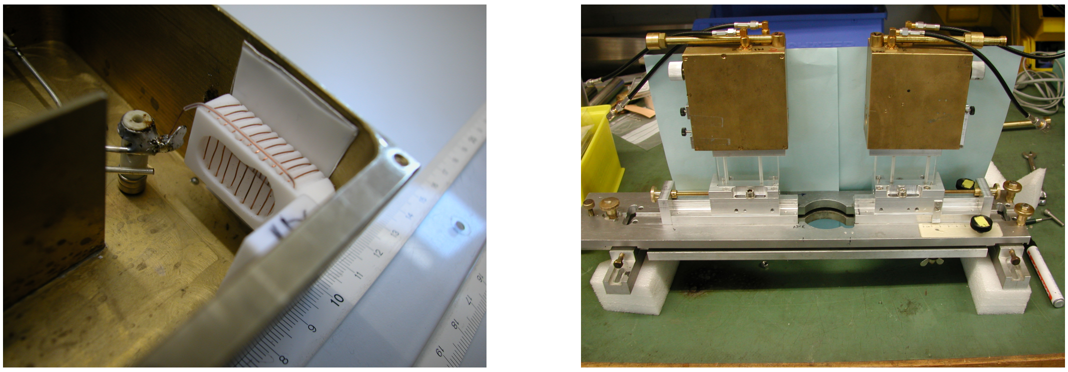

(a) (b)

Figure F.4: (a) Same spin flipper as in Fig. F.3, but with the L-shaped box coil used in beam time seven. The picture shows a version with copper wire, which was later replaced by a 0.5 mm thick silver coated copper wire (box coil size: 7 × 14 × 22 mm^3 with 11 windings with a pitch of one turn per 2 mm). Sheets of aluminium (thickness $= 2 \times 0.4$ mm) and PFTE (2×0.4 mm) were placed between the coil and the brass case wall to reduce the irradiated rf power and the associated heating of the cryostat - later the coils were further moved away from the walls by 6 mm to avoid spark-overs. (b) Spin flipper platform, which allows to adjust the position of the flippers in all three dimensions. Outside of the brass cases one can recognise the holding mechanisms for the Cd-apertures.

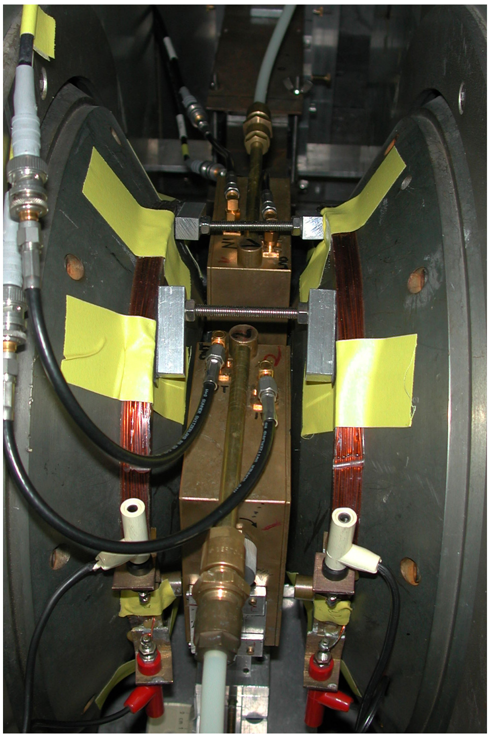

Figure F.5: Correction coils (red) with a diameter of about 25 cm are mounted on the two pole pieces of the 2.5 Tesla magnet and fixed by three C-shaped aluminium clamps (not by the yellow tape). They are separated by approximately 8 cm and have each an ohmic resistance of about 2 Ω. Each of them produces a field of about 0.8 mT/A at the sample position.

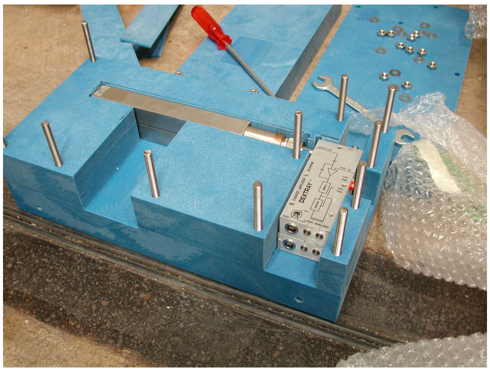

Figure F.6: Opened detector box with two box shaped ^{3}He gas tubes and preamplifiers.

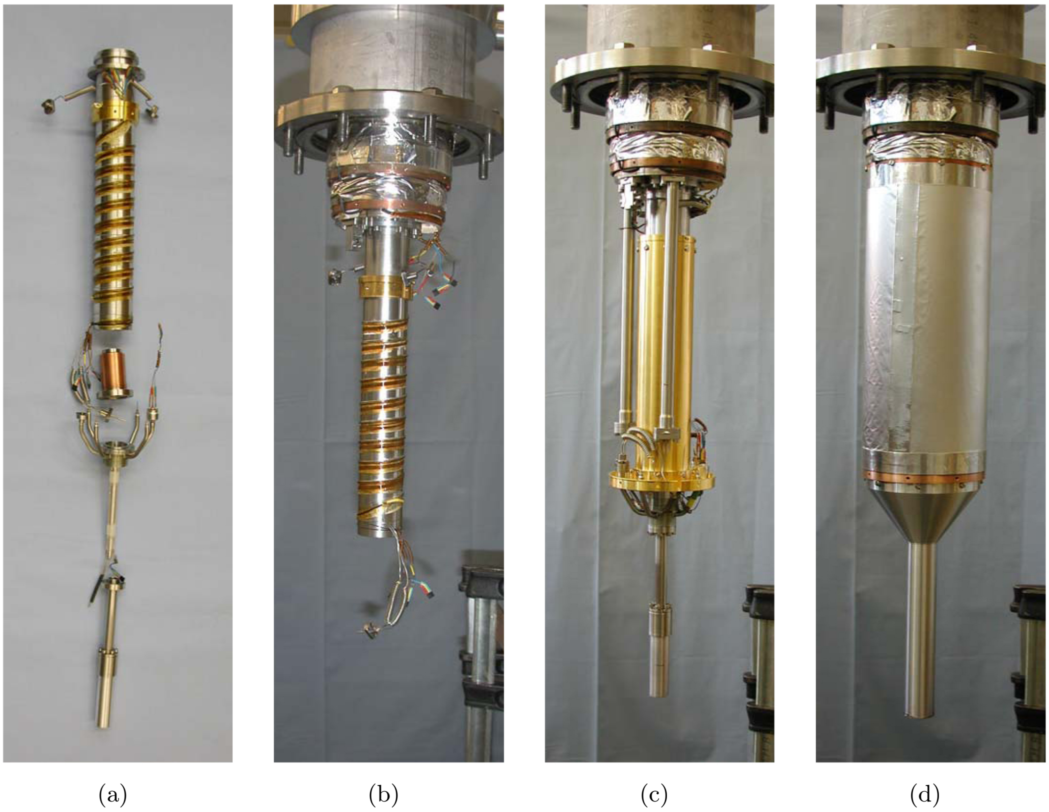

(a) (b) (c) (d)

Figure F.7: Step by step assembly of the nd dilution cryostat. (a) From top to bottom: cryostat vacuum tube (stainless steel: Ø 43 × 42 mm) with soldered ^{4}He capillaries and thermometer cables, heat exchanger (compare Fig. F.11), "spider" with NMR and thermometer feed-throughs and target cell (aluminium-stainless steel friction-weld: Ø 19 × 18 mm). (b) Vacuum tube mounted to the upper part of the cryostat. (c) Still heat shield (gold plated copper) and target cell with "spider" are mounted. (d) Aluminium and copper (with aluminium foil) heat shields.

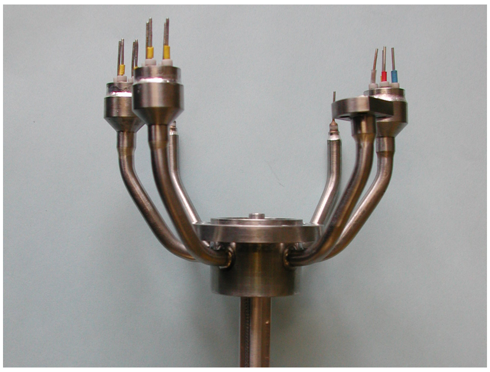

Figure F.8: The "spider" is mounted directly below the heat exchanger. It offers several feed-throughs for thermometers and NMR.

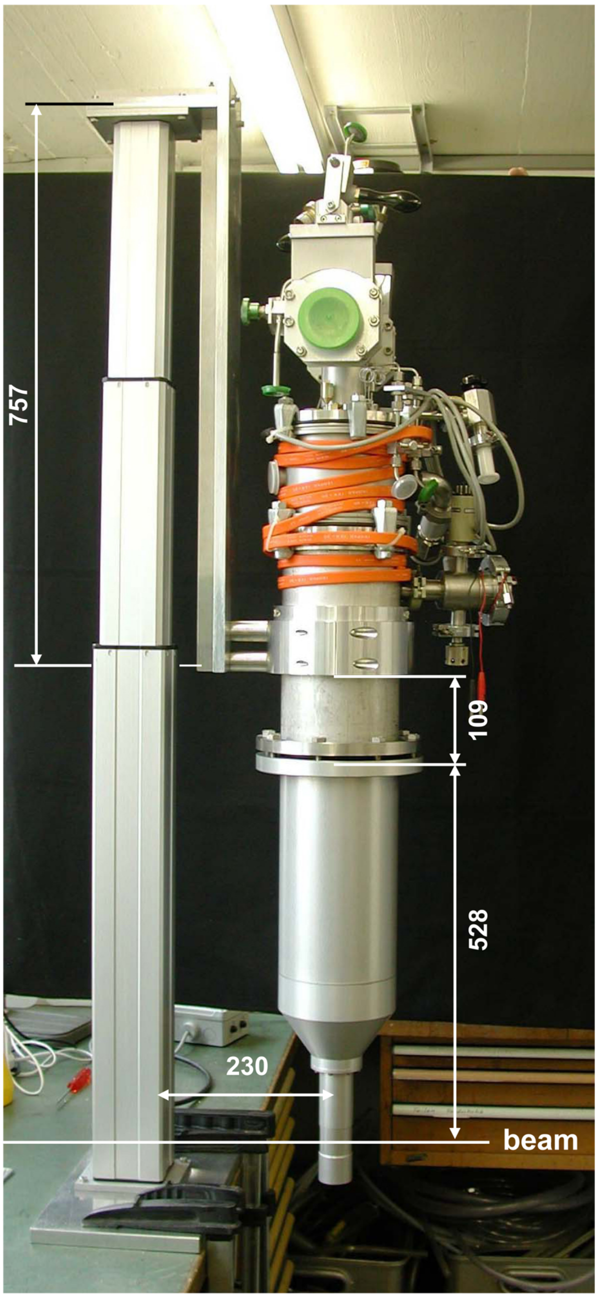

Figure F.9: Totally assembled cryostat with lifting apparatus.

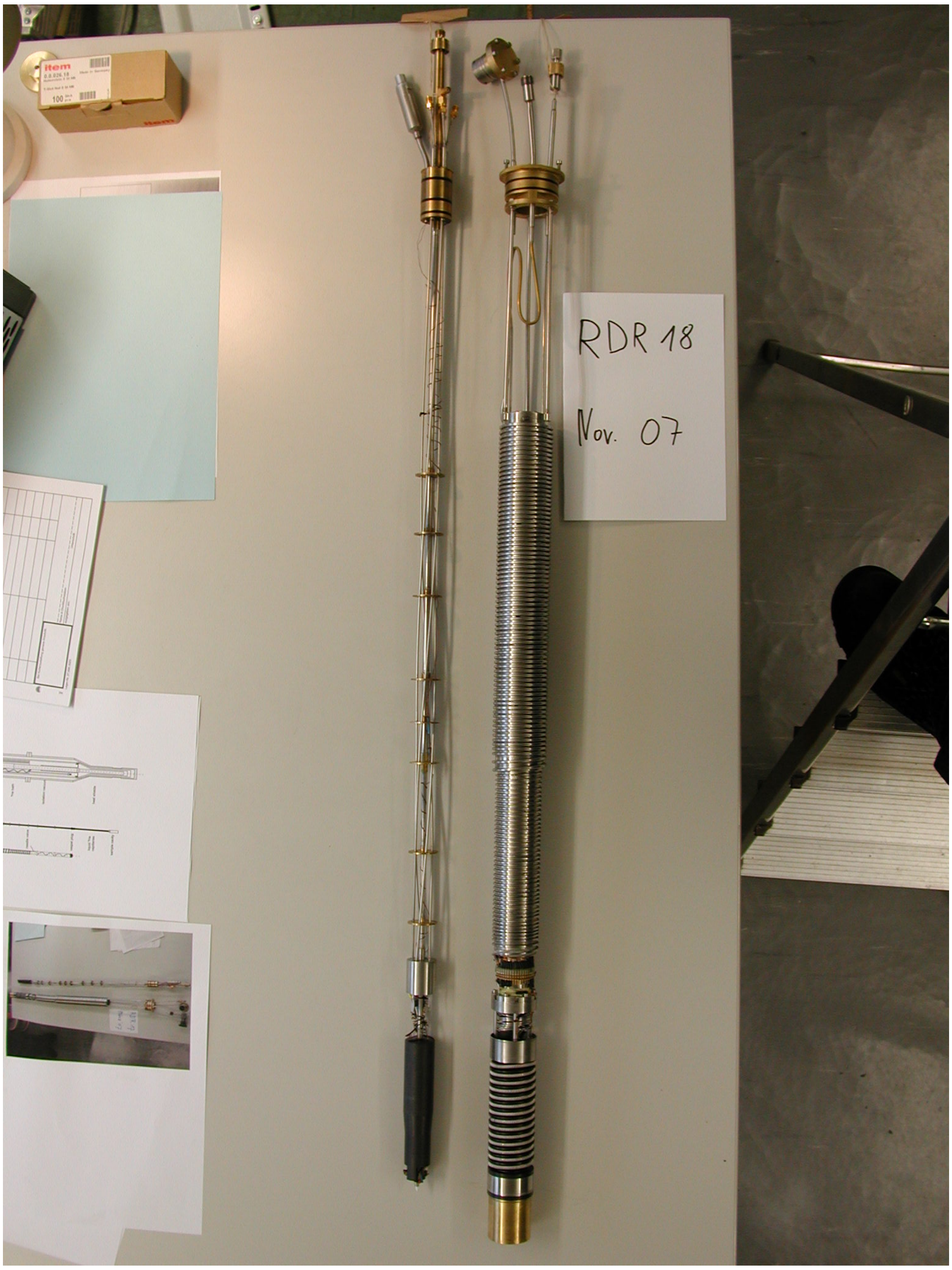

Figure F.10: Cryostat inserts (compare Fig. 5.18). Left: microwave insert. Right: dilution insert with a total length of approximately 96 cm (not including the parts on the top of the insert, i.e. needle valve, gas inlet etc.).

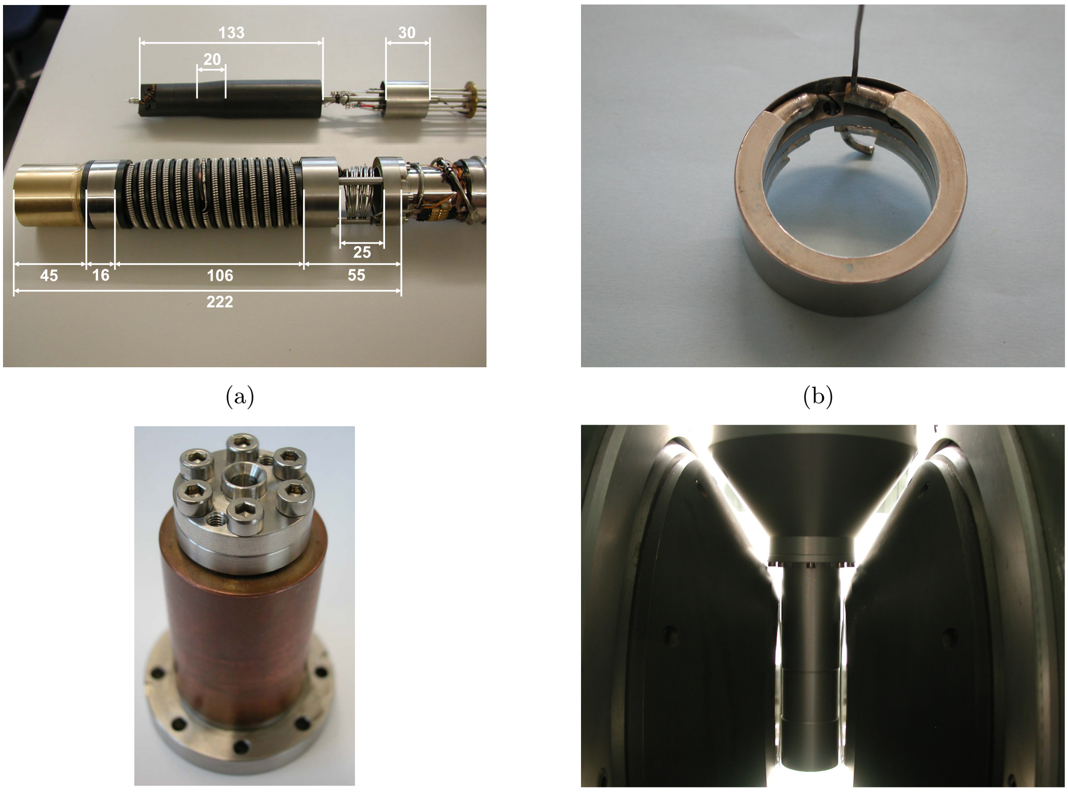

(a) (b)

(c) (d)

Figure F.11: (a) Lower parts of the cryostat inserts. Above: Vespel plug of the microwave insert. Below: liquid-liquid heat exchanger with secondary impedance, still and mixing chamber beaker made out of brass (Ø 38.8 × 37.8 mm, height: 41 mm). (b) Sintered silver heat exchanger situated after liquid-liquid heat exchanger. (c) Heat exchanger between mixing chamber and target cell with microwave socket: copper-stainless steel friction-weld (height: 47 mm and diameter of the copper cylinder: 28 mm). (d) Nose of the cryostat between the pole pieces of the magnet, which are separated by a distance of about 48 mm.

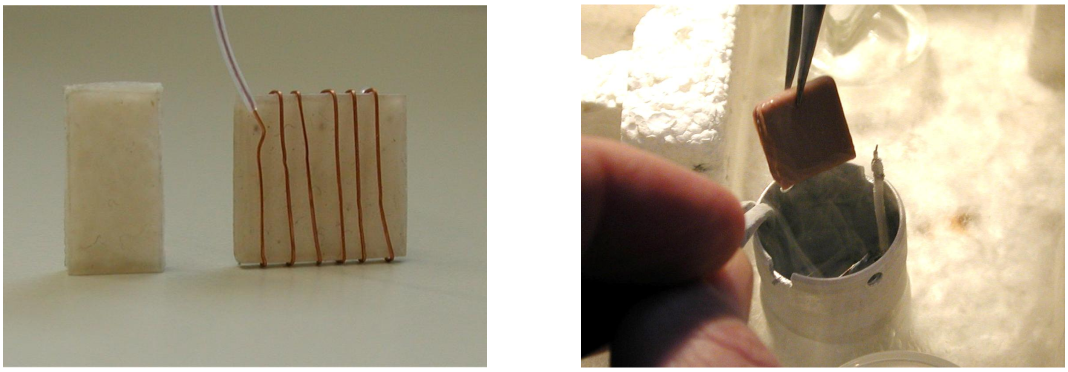

(a) (b)

Figure F.12: (a) Deuterated polystyrene platelets. The sample on the right has a size of $14\times14\times1.6$ mm^3. (b) Handling of a frozen alcohol sample under liquid nitrogen.

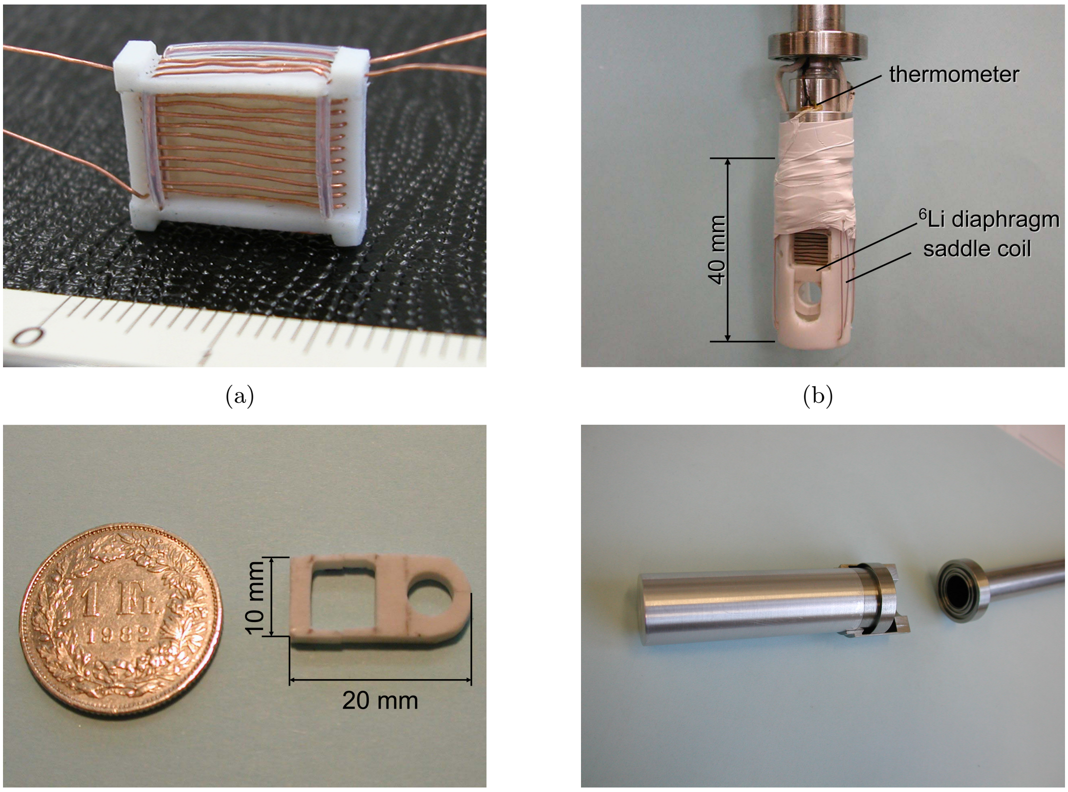

(a) (b)

(c) (d)

Figure F.13: (a) PTFE sample frame with two NMR coils (bare copper wire: Ø 0.25 mm). Sample size: $10 \times 8 \times 1.3$ mm^3. (b) PTFE sample holder (Ø 16 mm) inside the target cell. (c) ^{6}Li sample diaphragm with a thickness of 2 mm and $\chi_\mathrm{s}(8,7,4,5)$ (compare Fig. 5.13). (d) Target cell made from an aluminium-stainless steel friction-weld.

Figure F.14: Centre tube extension for the one Kelvin cryostat. The aluminium-stainless steel friction-weld has an inner diameter of 23 mm and an outer diameter of 25 mm (only 24 mm at the lower end, where the neutrons penetrate the tube).

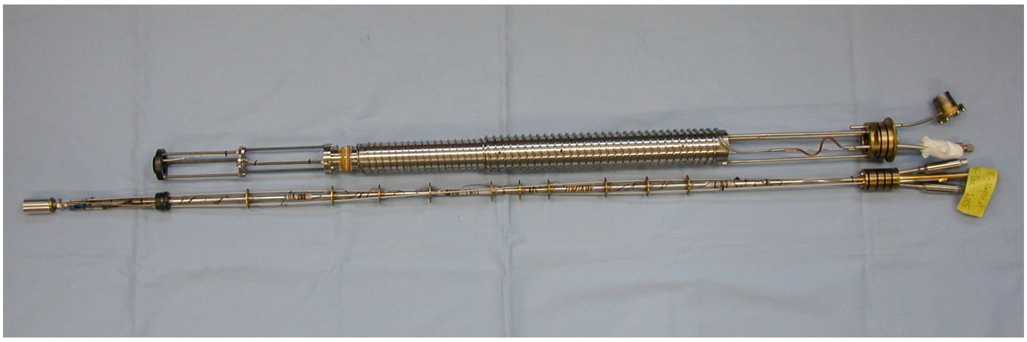

Figure F.15: 1 Kelvin ^{4}He evaporation cryostat inserts (compare Fig. 5.29). Above: evaporation insert with a total length of approximately 97 cm. Below: microwave insert with a total length of approximately 116 cm.

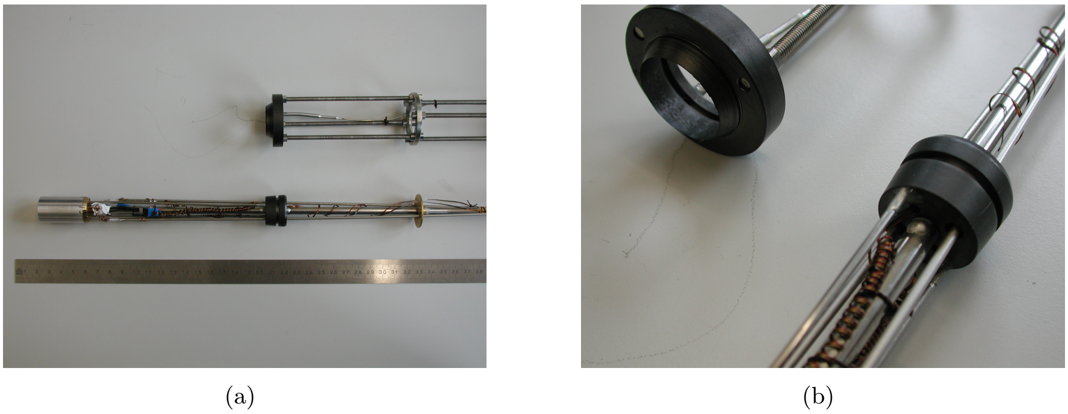

(a)

(b)

Figure F.16: Details of the 1 Kelvin ^{4}He evaporation cryostat inserts. (a) Lower parts of the cryostat inserts. Microwave insert with sample cavity (Ø 21 mm, height: 31 mm). (b) Vespel plug for the transfer of liquid ^{4}He from the evaporation insert to the microwave insert.

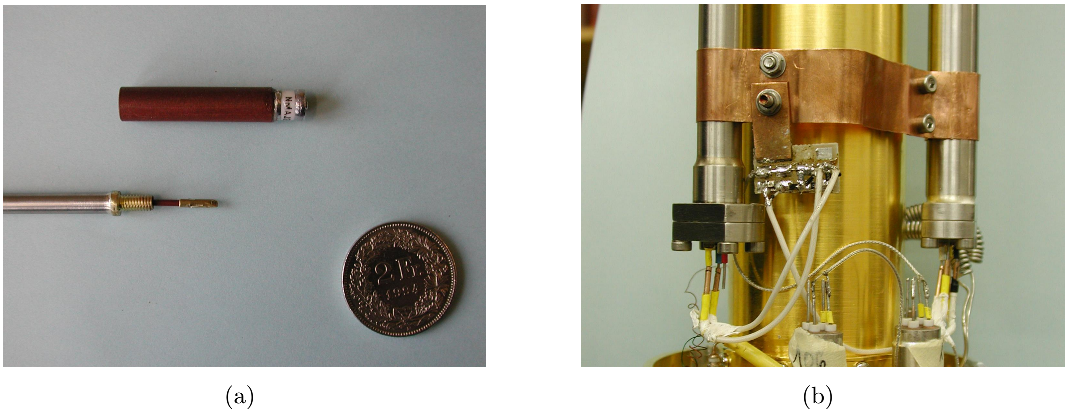

(a)

(b)

Figure F.17: (a) Tunable capacitor situated in the helium bath. The screw driver is used to remotely adjust the capacitance. (b) Circuit board of the LT NMR, thermally anchored to the helium bath. Later it was attached to the still shield.

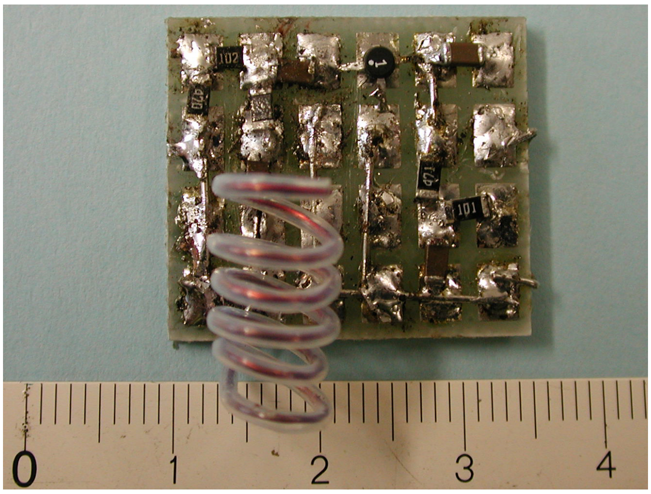

Figure F.18: Preamplifier circuit board for tests at 4 Kelvin using an ERA-1+ amplifier by *Minicircuits*®.

G. Photographs: Neutron Spin Phase Imaging

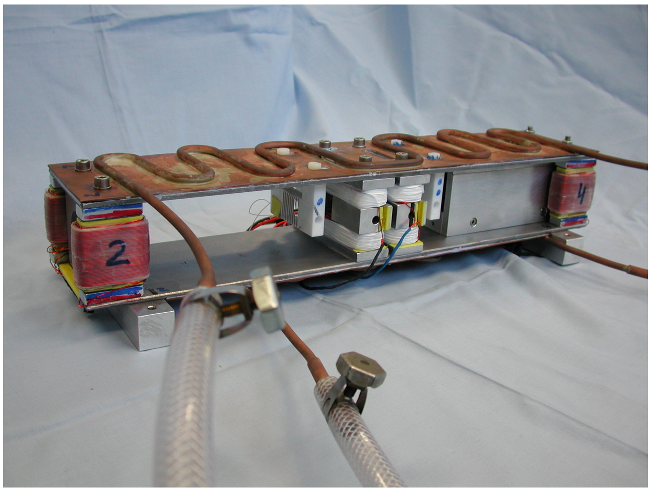

Figure G.1: Photograph of the NSPI Ramsey apparatus.

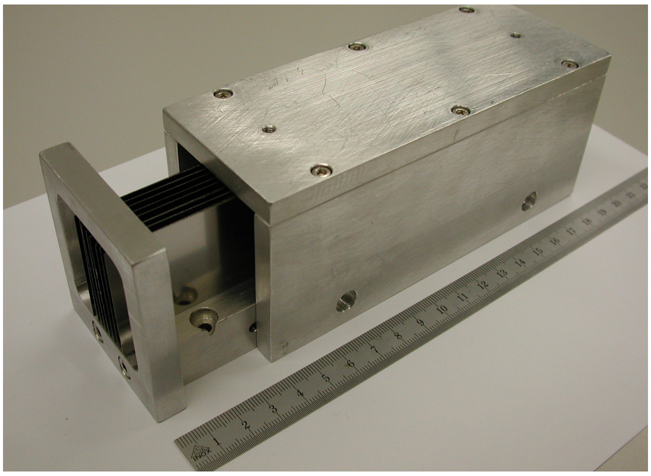

Figure G.2: Picture of the neutron polarisation device with partialy removed aluminium housing with the outer dimensions: $160 \times 58 \times 64$ mm^3. Eight repetitions of the N-shaped arrangement of the wafers were used to reach a polarisable beam cross-section of maximum 22×34 mm^2.

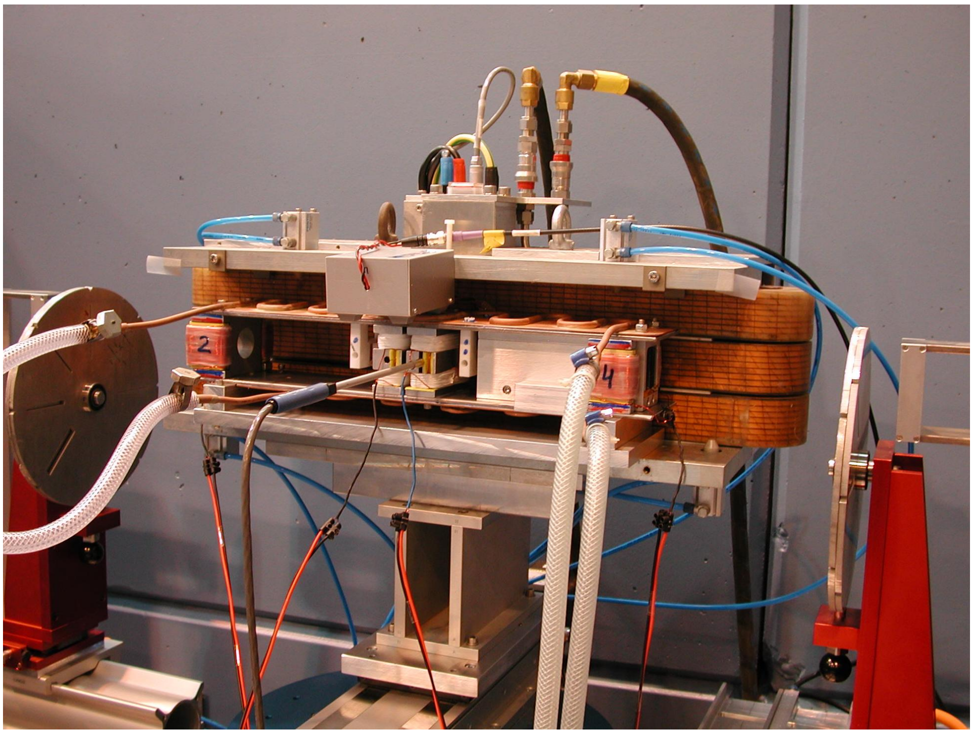

Figure G.3: For test purposes, the NSPI Ramsey apparatus has been set up at the cold reflectometer Narziss at PSI.

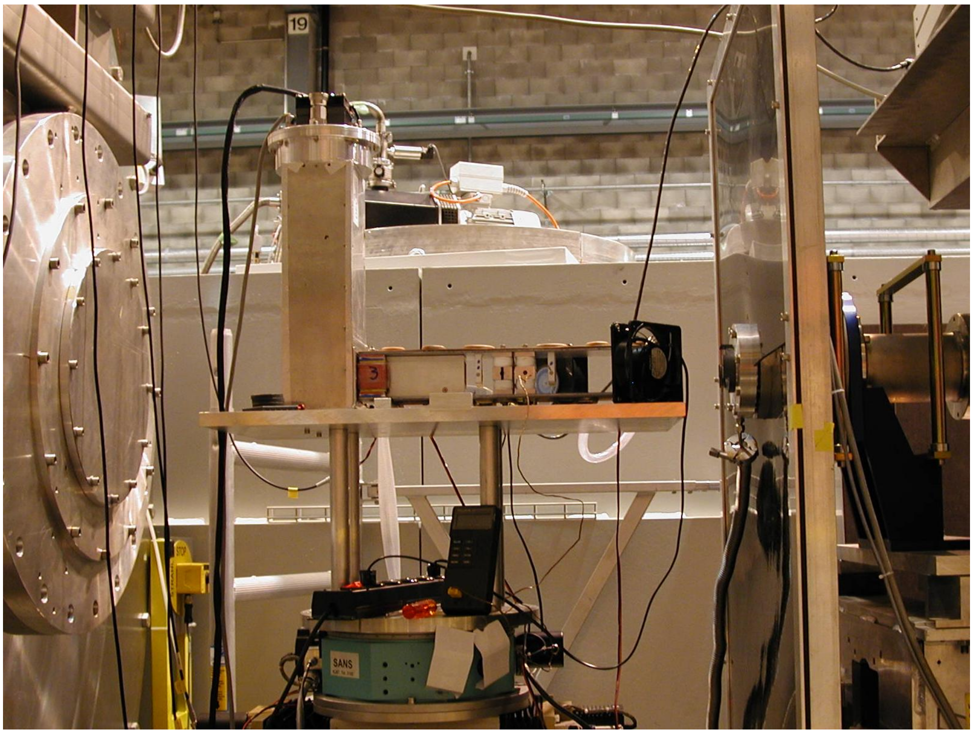

Figure G.4: The NSPI Ramsey apparatus at the small angle neutron scattering instrument SANS-I at PSI.

Bibliography

[Abe67] W.R. Abel, R.T. Johnson, J.C. Wheatley, W. Zimmermann *Phys. Rev. Lett.* **18** (1967) 737.

[Abe68] W.R. Abel, J.C. Wheatley, *Phys. Rev. Lett.* **21** (1968) 1231.

[Abr731] A. Abragam, *Trends in Physics*, European Physical Society, Geneva, Switzerland (1973) 177.

[Abr732] A. Abragam, G. L. Bacchella, H. Glätti, P. Meriel, M. Pinot, J. Piesvaux, *Phys. Rev. Lett.* **31** (1973) 776.

[Abr733] A. Abragam, G.L. Bacchella, H. Glättli, P. Meriel, J. Piesvaux, M. Pinot, P. Roubeau, *17th Congress Ampere* (1973) 1.

[Abr75] A. Abragam, G.L. Bacchella, H. Glättli, P. Meriel, J. Piesvaux, M. Pinot, *Journal de Physique Lett.*, **36** (1975) L-263.

[Abr78] A. Abragam, M. Goldman, *Rep. Prog. Phys.* **41** (1978) 395.

[Abr82] A. Abragam, M. Goldman, *Nuclear magnetism: order and disorder*, Oxford University Press (1982) ISBN 0-198-51294-5.

[Abr831] A. Abragam, *The principles of nuclear magnetism*, Oxford University Press (1983) ISBN 0-198-52014-X.

[Abr832] A. Abragam, B. Bleaney, *Proc. R. Soc. Lond.* A **387** (1983) 221.

[Ada99] D. Adams et al., *Nucl. Instr. Meth.* A **437** (1999) 23.

[Alb94] M. S. Albert, G. D. Cates, B. Driehuys, W. Happer, B. Saam, C. S. Springer, A. Wishnia, *Nature* **370** (1994) 199.

[And05] K.H. Anderson, R. Chung, V. Guillard, H. Humblot, D. Jullien, E. Lelièvre-Berna, A. Petoukhov, F. Tasset, *Physica* B **356** (2005) 103.

[Anu65] Yu.D. Anufriev, *JETP Lett.* **1** (1965) 155.

[Ari08] M. Arif (ed.), *Neutron Radiography: Proceedings of the eigth World Conference*, Destech Pubns Inc. (2008).

[Asw08] V.K. Aswal, B. van den Brandt, P. Hautle, J. Kohlbrecher, J.A. Konter, A. Michels, F.M. Piegsa, J. Stahn, O. Zimmer, *Nucl. Instr. Meth.* A **586** (2008) 86.

[Atc05] F. Atchison et al., *Phys. Rev.* C **71** (2005) 054601.

[Ay06] M. Ay, C. Schanzer, M. Wolff, J. Stahn, *Nucl. Instr. Meth.* A **562** (2006) 389.

[Bar65] V.G. Baryshevskii, M.I. Podgoretskii, *JETP* **20** (1965) 704.

[Bar82] *Neutron Radiography, Proceedings of the First World Conference.* Edited by John P. Barton et al., D. Reidel Publishing Company, Dordrecht, Holland (1982) ISBN 9-027-71528-9.

[Bat05] M. Batz et al., *J. Res. Natl. Inst. Stand. Technol.* **110** (2005) 293.

[Bay69] G. Baym, *Lectures on Quantum Mechanics*, W.A. Benjamin Inc. (1969) ISBN 0-805-30667-6.

[Bed02] P.F. Bedaque and U. van Kolck, *Ann. Rev. Nucl. Part. Sci.* **52** (2002) 339.

[Bed03] P.F. Bedaque, H.-W. Hammer, G. Rupak, H. Grießhammer, *Nucl. Phys.* A **714** (2003) 589.

[Bet76] D.S. Betts, *Refrigeration and thermometry below one Kelvin*, Sussex University Press (1976) ISBN 0-856-21028-5.

[Blo46] F. Bloch, W.W. Hansen, M. Packard, *Phys. Rev.* **70** (1946) 474.

[Bön97] P. Böni, *Physica* B **234-236** (1997) 1038.

[Bön99] P. Böni, D. Clemens, M. Senthil Kumar, C. Pappas, *Physica* B **267-268** (1999) 320.

[Bor68] M. Borghini, *Phys. Rev. Lett.* **20** (1968) 419.

[Bor71] M. Borghini, *Proc. of the 2^{nd} Int. Conf. on Polarised Targets* (1971) 1.

[Bra90] B. van den Brandt, J.A. Konter, S. Mango, *Nucl. Instr. Meth.* A **289** (1990) 526.

[Bra96] B. van den Brandt, P. Hautle, Yu.F. Kisselev, J.A. Konter, S. Mango, *Nucl. Instr. Meth.* A **381** (1996) 219.

[Bra00] B. van den Brandt, E.I. Bunzatova, P. Hautle, J.A. Konter, S. Mango, *Nucl. Instr. Meth.* A **446** (2000) 592.

[Bra04] B. van den Brandt, H. Glättli, H. Gießhammer, P. Hautle, J. Kohlbrecher, J.A. Konter, O. Zimmer, *Nucl. Instr. Meth.* A **526** (2004) 91.

[Bra061] B. van den Brandt, H. Glättli, H. Grießhammer, P. Hautle, J. Kohlbrecher, J.A. Konter, F.M. Piegsa, B.S. Schlimme, J.P. Urrego-Blanco, O. Zimmer, *AIP Conf. Proc.* **842** (2006) 814.

[Bra062] B. van den Brandt, H. Glättli, I. Grillo, P. Hautle, H. Jouve, J. Kohlbrecher, J.A. Konter, E. Leymarie, S. Mango, R.P. May, A. Michels, H.B. Stuhrmann and O. Zimmer, *Eur. Phys. Jour.* B **49** (2006) 157.

[Bra07] B. van den Brandt, H. Glättli, H. Grießhammer, P. Hautle, J. Kohlbrecher, J.A. Konter, F.M. Piegsa, J.P. Urrego-Blanco, O. Zimmer, *AIP Conf. Proc.* **915** (2007) 769.

[Bra091] B. van den Brandt, H. Glättli, P. Hautle, J.A. Konter, F.M. Piegsa, O. Zimmer, *Nucl. Instr. Meth.* A, Proc. of the Intern. Workshop on Particle Physics with Slow Neutrons, Grenoble (2008) – accepted for publication.

[Bra092] B. van den Brandt, P. Hautle, J.A. Konter, F.M. Piegsa, J.P. Urrego-Blanco, *Journal of Physics: Conference Series* **150** (2009) 012024.

[Buc61] M.J. Buckingham, W.M. Fairbank, *Prog. Low Temp. Phys.* **3** (1961) 80.

[Che99] J.-W. Chen, G. Rupak, M.J. Savage, *Nucl. Phys.* A **653** (1999) 386.

[Cou93] G.R. Court, D.W. Gifford, P. Harrison, W.G. Heyes, M.A. Houlden, *Nucl. Instr. Meth.* A **324** (1993) 433.

[Cou04] G.R. Court, *Nucl. Instr. Meth.* A **526** (2004) 65.

[Cus01] L.D. Cussen, C.J. Vale, I.S. Anderson, P. Hoghoj, *Nucl. Instr. Meth.* A **471** (2001) 392.

[Dav95] K. B. Davis, M. -O. Mewes, M. R. Andrews, N. J. van Druten, D. S. Durfee, D. M. Kurn, W. Ketterle, *Phys. Rev. Lett.* **75** (1995) 3969.

[DeB74] W. De Boer, M. Borghini, K. Morimoto, T.O. Niinikoski, *J. Low. Temp. Phys.* **15** (1974) 249.

[DeB76] W. De Boer, *J. Low. Temp. Phys.* **22** (1976) 185.

[Del71] L.E. DeLong, O.G. Symko, J.C. Wheatley, *Rev. Scien. Instr.* **42** (1971) 147.

[Dil71] W. Dilg, L. Koester, W. Nistler, *Phys. Lett.* B **36** (1971) 208.

[Edw65] D. Edwards, D. Brewer, P. Seligman, M. Skertic, M. Yaqub, *Phys. Rev. Lett.* **15** (1965) 773.

[Ens00] C. Enss, S. Hunklinger, *Tieftemperaturphysik*, Springer (2000) ISBN 3-540-67674-0.

[Epe02] E. Epelbaum, A. Nogga, W. Glöckle, H. Kamada, U.-G. Meißner, H. Witala, *Phys. Rev.* C **66** (2002) 064001.

[Fal06] P. Falus, A. Vorobiev, T. Krist, *Physica* B **385-386** (2006) 1149.

[Fis97] W.E. Fischer, *Physica* B **234-236** (1997) 1202.

[Fra02] A.I. Frank, I. Anderson, I.V. Bondarenko, A.V. Kozlov, P. Hoghoj, E. Ehlers, *Phys. Atom. Nucl.* **65** (2002) 2009.

[Fri07] J.M. Friedrich, *Eur. Phys. Jour.* A **31** (2007) 620.

[Fro78] G. Frossati, *Jour. Phys.* **C6** (1978) 1578.

[Glä79] H. Glättli, G.L. Bacchella, M. Fourmond, A. Malinovski, P. Mériel, M. Pinot, P. Roubeau, A. Abragam, *Jour. Phys.* **40** (1979) 629.

[Glä87] H. Glättli, M. Goldman, *Meth. Exp. Phys.* **23 C** (1987) Chapter 21.

[Gol91] R. Golub, D. Richardson, S.K. Lamoreaux, *Ultra-Cold Neutrons*, Adam Hilger, Bristol (1991) ISBN 0-750-30115-5.

[Gol94] R. Golub, R. Gähler, T. Keller, *Am. Jour. Phys.* **62** (1994) 779.

[Gol08] M. Goldman, *Appl. Magn. Reson.* **34** (2008) 219.

[Gre87] W. Greiner, L. Neise, H. Stöcker, *Theoretische Physik Band 9: Thermodynamik und Statistische Mechanik*, Harri Deutsch Verlag (1987) ISBN 3-871-44621-1.

[Gri05] H.W. Grießhammer, *Few-nucleon systems as microscope for the structure and dynamics of nucleons*, Habilitation TU München (2005).

[Gri06] H.W. Grießhammer, *Few Body Syst.* **38** (2006) 67.

[Gri08] H.W. Grießhammer, *Few Body Syst.* **44** (2008) 137.

[Grü07] C. Grünzweig, G. Frei, E.H. Lehmann, G. Kühne, C. David, *Rev. Sci. Instr.* **78** (2007) 053708.

[Grü08] C. Grünzweig, C. David, O. Bunk, M. Dierolf, G. Frei, G. Kühne, R. Schäfer, S. Pofahl, H.M.R. Ronnow, F. Pfeiffer, *Appl. Phys. Lett.* **93** (2008) 112504.

[Hau04] P. Hautle, *Nucl. Instr. Meth.* A **526** (2004) 76.

[Hei95] W. Heil, H. Humblot, E. Otten, M. Schafer, R. Sarkau, M. Leduc, *Phys. Lett.* A **201** (1995) 337.

[Hei99] W. Heil, J. Dreyer, D. Hofmann, H. Humblot, E. Lelievre-Berna, F. Tasset, *Physica* B **267-268** (1999) 328.

[Hen90] A. Henstra, *The integrated solid effect*, Ph.D. Thesis Leiden University (1990).

[Iin00] M. Iinuma et al., *Phys. Rev. Lett.* **84** (2000) 171.

[Jac83] J.D. Jackson, *Klassische Elektrodynamik*, 2.Auflage (1983) Walter de Gruyer Verlag ISBN 3-110-18970-4.

[Joh69] R.T. Johnson, R. Rosenbaum, O.G. Symco, J.C. Wheatley, *Phys. Rev. Lett.* **22** (1969) 449.

[Kam08] H. Kamerlingh Onnes, *Koninklijke Nederlandsche Akademie van Wetenschappen Proceedings* **11** (1908) 168.

[Kam79] D. Kamke, *Einführung in die Kernphysik*, Vieweg (1979), ISBN 3-528-03328-2.

[Kar08] N. Kardjilov, I. Manke, M. Strobl, A. Hilger, W. Treimer, M. Meissner, T. Krist, J. Banhart, *Nature Phys.* **4** (2008) 399.

[Ker54] E.C. Kerr, *Phys. Rev.* **96** (1954) 551.

[Ker57] E.C. Kerr, *J. Chem. Phys.* **26** (1957) 511.

[Ket04] W. Ketter, *Messung des Realteils der gebundenen* ^{3}*He-Streulänge*, Ph.D. Thesis J. Gutenberg Universität Mainz (2004).

[Kit04] C. Kittel, *Introduction to Solid State Physics*, Wiley (2004) ISBN 0-471-41526-X.

[Kle83] A.G. Klein, S.A. Werner, *Rep. Prog. Phys.* **46** (1983) 259.

[Kre05] M. Kreuz, V. Nesvizhevsky, A. Petoukhov, T. Soldner, *Nucl. Instr. Meth.* A **547** (2005) 583.

[Kri92] T. Krist, C. Lartigue, F. Mezei, *Physica* B **180-181** (1992) 1005.

[Kri00] T. Krist, F. Mezei, *Physic*a B **276-278** (2000) 208.

[Kri04] T. Krist, *Nucl. Instr. Meth.* A **529** (2004) 50

[Kri05] T. Krist et al., *Physica* B **356** (2005) 197.

[Kub04] K. Kubodera, T.S. Park, *Ann. Rev. Nucl. Part. Sci.* **54** (2004) 19.

[Lan74] L.D. Landau, E.M. Lifschitz, *Quantenmechanik*, Band 3, Paul Ziesche (1974) ISBN 3-817-11328-5.

[Leh07] E.H. Lehmann, G. Frei, G. Kühne, P. Boillat, *Nucl. Instr. Meth.* A **576** (2007) 389.

[Lid98] D.R. Lide (ed.), *Handbook of chemistry & physics*, 78th edition, CRC-Press (1998) ISBN 0-849-30488-1.

[Lou74] O.V. Lounasmaa, *Experimental principles and metods below 1 Kelvin*, Academic Press Inc. (1974) ISBN 0-124-55950-6.

[Mai63] H. Maier-Leibnitz, T. Springer, *J. Nucl. Energy* A/B **17** (1963) 217.

[Mal81] A. Malinovski, J. Coustham, H. Glättli, *Nucl. Phys.* A **365** (1981) 103-112.

[McC92] P.V.E. McClintock, J.K. Wigmore, *Low-temperature physics: an introduction for scientists and engineers*, Blackie (1992) ISBN 0-216-92979-2.

[Mez72] F. Mezei, *Z. Phys.* **255** (1972) 146.

[Müh05] M.J. Mühlbauer, E. Calzada, B. Schillinger, *Nucl. Instr. Meth. A* **542** (2005) 324.

[New76] R.G. Newton, *Am. J. Phys.* **44** (1976) 639.

[Pfe06] F. Pfeiffer, C. Grünzweig, O. Bunk, G. Frei, E.H. Lehmann, C. David, *Phys. Rev. Lett.* **96** (2006) 215505.

[Pie04] F.M. Piegsa, *Experimente mit einer Ramsey-Apparatur zur Präzisionsmessung der spinabhängigen Neutronenstreulänge des Deuterons und Beiträge zum Aufbau eines neuen polarisierten Protonentarget*, Diploma Thesis TU München (2004).

[Pie081] F.M. Piegsa, B. van den Brandt, P. Hautle, J.A. Konter, *Nucl. Instr. Meth.* A **586** (2008) 15.

[Pie082] F.M. Piegsa, B. van den Brandt, H. Glättli, P. Hautle, J. Kohlbrecher, J.A. Konter, B.S. Schlimme, O. Zimmer, *Nucl. Instr. Meth.* A **589** (2008) 318.

[Pie083] F.M. Piegsa, M. Schneider *Nucl. Instr. Meth.* A **594** (2008) 74.

[Pie091] F.M. Piegsa, B. van den Brandt, P. Hautle, J.A. Konter, *Nucl. Instr. Meth.* A, **605** (2009) 5.

[Pie092] F.M. Piegsa, B. van den Brandt, P. Hautle, J. Kohlbrecher, J.A. Konter, *Phys. Rev. Lett.* **102** (2009) 145501.

[Pie093] F.M. Piegsa, *Nucl. Instr. Meth.* A, **603** (2009) 401.

[Phi02] D. Phillips, *Czech. J. Phys.* **52** (2002) B49.

[Pob92] F. Pobell, *Matter and Methods at Low Temperature*, Springer-Verlag (1992) ISBN 3-540-53751-1.

[Pov01] B. Povh, K. Rith, C. Scholz, F. Zetsche, *Teilchen und Kerne*, Springer (2001), ISBN 3-540-65928-5.

[Pro08] Proceedings of the Dynamic Nuclear Polarisation Symposium 2007 in Nottingham (UK), *Appl. Magn. Res.* **34** 3/4 (2008).

[Pur46] E.M. Purcell, H.C. Torrey, R.V. Pound, *Phys. Rev.* **69** (1946) 37.

[Rab38] I.I. Rabi, S. Millman, P. Kusch, J.R. Zacharias, *Phys. Rev.* **53** (1938) 495.

[Ram50] N. Ramsey, *Phys. Rev.* **78** (1950) 695.

[Ram56] N. Ramsey, *Molecular Beams*, Oxford University Press (1956) ISBN 0-198-52021-2.

[Rek02] M.T. Rekveldt, W.G. Bouwman, W.H. Kraan, S.V. Grigoriev, O. Uca, T. Keller, *Appl. Phys.* A **74** (2002) S323.

[Rou74] P. Roubeau, A. Abragam, G. L. Bacchella, H. Glättli, A. Malinovski, P. Meriel, J. Piesvaux, M. Pinot, *Phys. Rev. Lett.* **33** (1974) 102.

[Rou76] P. Roubeau, Proc. of the 6th Int. Engineering Conf. in Grenoble, *IPC Scien. and Techn. Press* (1976) 99

[Rou78] P. Roubeau et al., *Jour. de Phys.* **39** (1978) C6-1146.

[Sak95] J.J. Sakurai, *Modern quantum mechanics*, 2nd edition, Addison-Wesley (1995) ISBN 8-177-58548-7.

[Sch65] T.J. Schmugge, C.D. Jeffries, *Phys. Rev.* **138** (1965) A1785.

[Sch88] F. Schwabl, *Quantenmechanik*, 1.Auflage Springer-Verlag (1988) ISBN 3-540-19476-2.

[Sch89] O. Schärpf, *Physica* B **156-157** (1989) 639.

[Sch00] F. Schwabl, *Quantenmechanik für Fortgeschrittene*, 2. Auflage Springer-Verlag (2000) ISBN 3-540-67730-5.

[Sch03] K. Schoen, D.L. Jacobson, M. Arif, P.R. Huffman, T.C. Black, W.M. Snow, S.K. Lamoreaux, H. Kaiser, S.A. Werner, *Phys. Rev.* C **67** (2003) 044005.

[Sch05] B.S. Schlimme, *Experimente zur Bestimmung der inkohärenten Neutron-Deuteron-Streulänge*, Diploma Thesis TU München (2005).

[Sea89] V.F. Sears, *Neutron Optics*, Oxford University Press (1989) ISBN 0-195-04601-3.

[Sea92] V.F. Sears, *Neutron News* **3** (1992) 26.

[Sen04] M. Senthil Kumar, V.R. Shah, C. Schanzer, P. Böni, T. Krist, M. Horisberger, *Physica* B **350** (2004) e241.

[Sli96] C.P. Slichter, *Principles of magnetic resonance*, 3rd edition, Springer Berlin (1996).

[Str07] M. Strobl, W. Treimer, P. Walter, S. Keil, I. Manke, *Appl. Phys. Lett.* **91** (2007) 254104.

[Tak04] K. Takeda et al., *Jour, Phys. Soc. Jpn.* **73** (2004) 2313.

[Tis38] L. Tisza, *Nature* **141** (1938) 913.

[Tre08] A.S. Tremsin, J.V. Vallerga, J.B. McPhate, O.H.W. Siegmund, W.B. Feller, L. Crow, R.G. Cooper, *Nucl. Instr. Meth.* A **592** (2008) 374.

[Ver90] P.F.A. Verheij, *MIONP in molecular crystals at mm-wavelength*, Ph.D. Thesis Leiden University (1990).

[Ver87] G.A. Vermeulen, G. Frossati, *Cryogenics* **27** (1987) 139.

[Wak05] T. Wakui et al., *Nucl. Instr. Meth.* A **550** (2005) 521.

[Wen69] W.Th. Wenckebach et al., *Phys. Rev. Lett.* **22** (1969) 581.

[Wen74] W.Th. Wenckebach et al., *Phys. Rep.* **14** (1974) 181.

[Wen95] W.Th. Wenckebach, *Nucl. Instr. Meth.* A **356** (1995) 1.

[Wen08] W.Th. Wenckebach, *Appl. Magn. Reson.* **34** (2008) 227.

[Wil67] J. Wilks, *The Properties of Liquid and Solid Helium*, Oxford Clarenden Press (1967) ISBN 0-198-51245-7.

[Wil72] W.R. Wilkes, *Cryogenics* **12** (1972) 180.

[Zej05] J. Zejma et al., *Nucl. Instr. Meth.* A **539** (2005) 622.

[Zim99] O. Zimmer, T.M. Müller, P. Hautle, W. Heil, H. Humblot, *Phys. Lett.* B **455** (1999) 62.

[Zim02] O. Zimmer, G. Ehlers, B. Farago, H. Humblot, W. Ketter and R. Scherm, *EPJ direct* A **1** (2002) 1.

[Zim07] O. Zimmer et al., *Phys. Rev. Lett.* **99** (2007) 104801.

List of Publications

During this work different projects were persued. Here the resulting publications are listed:

1. **A compact neutron Ramsey resonance apparatus for polarised neutron radiography**,
   Nucl. Instr. Meth. A, **605** (2009) 5,
   F.M. Piegsa, B. van den Brandt, P. Hautle and J.A. Konter.

2. **Highly collimating neutron optical devices**,
   Nucl. Instr. Meth. A, **603** (2009) 401,
   F.M. Piegsa.

3. **Quantitative radiography of magnetic fields using the neutron spin phase imaging-technique**,
   Phys. Rev. Lett. **102** (2009) 145501,
   F.M. Piegsa, B. van den Brandt, P. Hautle, J. Kohlbrecher and J.A. Konter.

4. **Dilution refrigerators for particle physics experiments: two variants with sample cooling by helium-4**,
   Journal of Physics: Conference Series **150** (2009) 012024,
   B. van den Brandt, P. Hautle, J.A. Konter, F.M. Piegsa and J.P. Urrego-Blanco.

5. **The measurement of the incoherent neutron scattering length of the deuteron,**
   Nucl. Instr. Meth. A – accepted for publication,
   B. van den Brandt, H. Glättli, P. Hautle, J.A. Konter, F.M. Piegsa
   and O. Zimmer.

6. **A short-length neutron transmission polariser for large beam cross-sections**,
   Nucl. Instr. Meth. A **594** (2008) 74,
   F.M. Piegsa and M. Schneider.

7. **A Ramsey apparatus for the measurement of the incoherent neutron scattering length of the deuteron**,
Nucl. Instr. Meth. A **589** (2008) 318,
F.M. Piegsa, B. van den Brandt, H. Glättli, P. Hautle, J. Kohlbrecher, J.A. Konter, B.S. Schlimme and O. Zimmer.

8. **Neutron spin phase imaging**,
Nucl. Instr. Meth. A **586** (2008) 15,
F.M. Piegsa, B. van den Brandt, P. Hautle and J.A. Konter.

9. **Characterisation of the polarised neutron beam at the small angle scattering instrument SANS-I with a polarised proton target**,
Nucl. Instr. Meth. A **586** (2008) 86,
V.K. Aswal, B. van den Brandt, P. Hautle, J. Kohlbrecher, J.A. Konter, A. Michels, F.M. Piegsa, J. Stahn, S. van Petegem and O. Zimmer.

10. **Polarised nuclei: From fundamental nuclear physics to applications in neutron scattering and magnetic resonance imaging**,
AIP Conference Proc. **980** (2008) 312,
B. van den Brandt, P. Hautle, J.A. Konter, F.M. Piegsa and J.P. Urrego-Blanco.

11. **An accurate measurement of the spin-dependent neutron-deuteron scattering length**,
AIP Conference Proc. **915** (2007) 769,
B. van den Brandt, H. Glättli, H. Griesshammer, P. Hautle, J. Kohlbrecher, J.A. Konter, F.M. Piegsa, J.P. Urrego-Blanco and O. Zimmer.

12. **Polarised solid targets at PSI: Recent developments**,
World Scientific **6466** (2007) 173,
B. van den Brandt, P. Hautle, J.A. Konter, F.M. Piegsa and J.P. Urrego-Blanco.

13. **A high-accuracy measurement of the spin-dependent neutron scattering length of the deuteron**,
AIP Conference Proc. **842** (2006) 814,
B. van den Brandt, H. Glättli, H. Griesshammer, P. Hautle, J. Kohlbrecher, J.A. Konter, F.M. Piegsa, B.S. Schlimme, J.P. Urrego-Blanco and O. Zimmer.

14. **High-accuracy measurement of the spin-dependent neutron scattering length of the deuteron**,
World Scientific **5812** (2005) 669,
B. van den Brandt, H. Glättli, H. Griesshammer, P. Hautle, J. Kohlbrecher, J.A. Konter, A. Michels, F.M. Piegsa and O. Zimmer.

Conferences and Talks

The progress and the results of this work have been presented by the thesis author at several international conferences and workshops. A complete list is given here:

1. **Neutron spin precession in samples of polarised nuclei and neutron spin phase imaging**, *invited talk* at Stanford University in the group seminar of Prof. G. Gratta, October 13th 2008 in Stanford, CA (USA).

2. **Polarised solid targets at PSI**, *invited talk and chair* at the 18th International Spin Physics Symposium, October 6th-11th 2008 in Charlottesville, VA (USA).

3. **Neutron spin phase imaging**, *talk* at the 6th International Topical Meeting on Neutron Radiography, September 14th-18th 2008 in Kobe (Japan).

4. **Neutron spin precession in samples of polarised nuclei and neutron spin phase imaging**, *invited talk* at the Excellence-Cluster Seminar, August 26th 2008 in Garching (Germany).

5. **An accurate measurement of the spin-dependent neutron-deuteron scattering length**, *invited talk* at the International Workshop on Particle Physics with slow Neutrons, May 29th-31st 2008 in Grenoble (France).

6. **First results of the neutron spin phase imaging technique**, *invited talk* at the Workshop on Neutron Wavelength dependent Imaging, April 20th-24th 2008 in Garching (Germany).

7. **Polarised solid targets at PSI**, *talk* at the 12th International Workshop on Polarised Sources, Targets and Polarimetry, September 10th-14th 2007 in Brookhaven, NY (USA).

8. **Dynamic nuclear polarisation in particle beam experiments at PSI**, *poster* at the Dynamic Nuclear Polarisation Symposium, August 29th -31st 2007 in Nottingham (UK).

9. **Neutron spin phase imaging**, *talk* at the European Workshop on Neutron Optics NOP, April 5th-7th 2007 in Villigen PSI (Switzerland).

10. **The nd-experiment**, *invited talk* at the Swiss Physical Society meeting, February 21st 2007 in Zürich (Switzerland).

11. **Neutron spin precession in samples of polarised nuclei**, *poster* at the Workshop on Precision Measurements at Low Energy, January 18th-19th 2007 in Villigen PSI (Switzerland).

12. **The nd-experiment**, *talk* at the 17th International Spin Physics Symposium, October 2nd-7th 2006 in Kyoto (Japan).

13. **The nd-experiment**, *invited talk* at the 3rd meeting "Polarised Nucleon Targets for Europe" in the 6th European framework program, February 2nd-4th 2006 in Rech (Germany).

14. **The nd-experiment**, *talk* at the Laboratory for Particle Physics seminar, January 18th 2006 in Villigen PSI (Switzerland).

15. **The nd-experiment**, *talk* at the 17th Particles and Nuclei International Conference, October 24th-28th 2005 in Santa Fe, NM (USA).

Acknowledgment

Finally, I want to thank those people, who made this thesis possible:

Kurt Clausen for welcoming me in the department of *Condensed Matter Research with Neutrons and Muons* of PSI and for supporting my research work.

Oliver Zimmer für die Möglichkeit an diesem interessanten und umfangreichen Projekt teilzunehmen, für das grenzenlose Vertrauen in meine Arbeit und dafür, daß er mich bereits zu Beginn meiner Diplomarbeit mit ans PSI genommen hat.

Ben van den Brandt für die richtigen aufmunternden Worte zur rechten Zeit, für fortwährende Unterstützung in allen Angelegenheiten, für den schier endlosen Quell an guten Ratschlägen während den Kaffeepausen und noch vielem mehr.

Patrick Hautle für das Schärfen des Blicks für die Präzision und der Zunge für die diplomatische Wortwahl, außerdem für unzählige prompte Modifikationen von LabView-Programmen, die Unterstüzung während so vielen Strahlzeiten, deren Nächte nicht all zu selten bis in die frühen Morgenstunden gingen und noch vielem mehr.

Ton Konter für das Weitergeben seines Wissens über die Tieftemperaturphysik, welches ich wahrscheinlich erst heute und nur zu einem Bruchteil nachvollziehen kann.

Paul Schurter dafür, daß er der beste schweizer Techniker der Welt ist und ein guter Freund, gerade dann wenn man mal von allem anderen die Nase voll hat.

Willi Arrigoni dafür, daß er der beste pensionierte schweizer Techniker der Welt ist und daß er sich gerade zu Beginn meiner Doktorarbeit viel Zeit genommen hat mir einige wertvolle technische Grundlagen beizubringen.

Hans Glättli, Harald Grießhammer, Joachim Kohlbrecher, Michael Schmutz und Juan-Pablo Urrego-Blanco.

Johann Gironnet for being the best office mate since the French-German-Friendship.

The Rinikens Murat Ay, Christian Grünzweig and Daniel dos Santos Covita for being the best flat mates someone can have. I would not like to imagine the time in Switzerland without you. I hope to see you all again soon.

Den Ehren-Rinikens Marc Janoschek, Christian Schanzer, Ela, Melanie und Ben.

Meinen Eltern, meinem Bruder und Nari.

"The graph on the wall tells the story of it all.
Picture it now, see just how the lies and deceit gained a little more power."

Depeche Mode – *everything counts*